Large Scale Manufacturing of WS_2 Nanomaterials and Their Application in Polymer Nanocomposites

Submitted by **Fang Xu** to the University of Exeter

as a thesis for the degree of

Doctor of Philosophy in Engineering

In January 2013

I certify that all material in this thesis which is not my own work has been identified and that no material has previously been submitted and approved for the award of a degree by this or any other University.

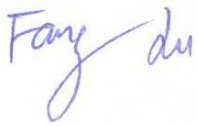

Signature: ……..

Abstract

With size down to nanoscale, nanomaterials exhibit novel properties exceeding or differing significantly from their bulk counterparts. In particular, amongst a wide range of interesting new nanostructures, tungsten based nanomaterials have demonstrated super physical, chemical, electronical and mechanical properties in a diverse range of applications which has been comprehensively reviewed. However, challenges still remain high on the effective processes to scale up the manufacturing of such nanomaterials, with desired shape, size and quality. These tungsten based nanomaterials are thus become the research subject of this project, and the study on continuous manufacturing of specifically inorganic fullerene WS_2 (IF-WS_2) nanoparticles, and their potential exploration as fillers to polymer matrix to fabricate nanocomposites with improved mechanical properties are the main objectives of this research.

After a thorough assessment of the extremely promising potentials of tungsten based nanostructures, and review of the current bottleneck for large quantity production of IF-WS_2, a generic experimental methodology and techniques used for the investigations have been described in experimental methodology part. In the following chapters, this thesis demonstrates the following research works:

A novel rotary furnace for continuous scaling up manufacturing of IF-WS_2 nanoparticles has been designed, constructed, tested and refined in this work. The new furnace consists of several key components: a tube furnace, self-contained rotary system, dynamic seal system, modified new tube with baffle, and a continuous gas-blow feeding system. Test results show that the rotary reactor has improved the lab scale manufacturing of IF-WS_2 from sub-gram to several tens of grams per batch without agglomeration, which makes this technique a promising alternative for the replacement of the existing tall fluidised tower processing in industrial level production.

As an important precursor for IF-WS_2 nanomaterials production, the synthesis of WO_x nanoparticles by high temperature thermal decomposition of Ammonium Paratungstate (APT) has been investigated, and the parameters have been optimised (with Ar flow at 6 L/min at 1350°C) for achieving desired sizes. Further studies on the creation of uniform and ultra-thin WO_x nanowires were carried out using solvothermal technique. The

solvent concentrations, reaction time and solvent types have been systematically investigated, and the resulting WO_x nanowires from tungsten chloride precursor in mixed cyclohexanol and ethanol solvent exhibited a record high specific surface area of 275 m^2/g. This is fundamentally significant for their applications in sensor and electro-chromic devices.

Reverse patterned growth of WO_x nanorods was realised for the first time on an Au-coated W foil by a simple W-water vapour reaction. The resulting nanorods of different diameters, lengths and patterns have been created by tuning the growth parameters. Further nitriding under NH_3 atmosphere at elevated temperature, converted the WO_x nanorods, as a template, to WO_xN_y nanorods. The WO_xN_y nanorods have been found to inherit the patterns on the substrate and kept the size and shape of WO_x nanorods. An interesting morphology revolution for the conversion of WO_x to WO_xN_y nanorods was observed, and a mechanism has been proposed accordingly to account for the growth. This result represents a simple, innovative and efficient process for the reverse-patterned growth of new nanomaterials.

Further development of the rotary furnace has led to a unique new class of core-shell composite nanoparticles, carbon (C)-coated IF-WS_2 hollow nanoparticles, by continuous chemical vapour deposition (CVD) production. The composite nanoparticles exhibited a uniform and adjustable C coating, with little or no agglomeration. Importantly, the thermal stability of the core-shell C-coated IF-WS_2 against oxidation in air has been improved by about 70°C, compared to the pristine IF-WS_2. This new material could find applications where thermal stability is critical.

Exploration of 0-4 wt% IF-WS_2 as reinforcement in nylon 12 matrix nanocomposites has been carried out for the first time, using a combination of ultrasonic dispersion and magnetic stirring technique to achieve excellent IF-WS_2 dispersion in the matrix. Tensile and bending test results showed moderate improvements of 27% and 28% respectively, with a 2 wt% IF-WS_2 addition, but a staggering 185% and 148% improvement in toughness for the addition of 0.25 and 0.5 wt% IF-WS_2 samples, against pure nylon 12, suggesting that such composites are promising candidates for structural and ballistic fibre applications.

Table of Contents

Publications

Journal papers

1. Fang Xu, Yanqiu Zhu etc. Preparation and Characterisation of IF-WS_2 impregnated Kevlar fibre. In preparation
2. Fang Xu, Yanqiu Zhu, etc. Synthesis, characterisation and mechanical behaviour of nylon 12 reinforced with IF-WS_2 nanocomposites. In preparation
3. Fang Xu, Yanqiu Zhu etc. Improving thermal properties of IF-WS_2 nanoparticles by carbon coating. In preparation.
4. Fang Xu, Amir Fahmi, Yimin Zhao, Yongde Xia, and Yanqiu Zhu, Patterned growth of tungsten oxide and tungsten oxynitride nanorods from Au-coated W foil, Nanoscale. **4**, 7031-7037(2012)
5. Hong Chang, Georgios Dimitrakis, Fang Xu, Chenbo Yi, Samuel Kingman, Yanqiu Zhu, Microwave dielectric properties of inorganic fullerene-like tungsten disulphide nanoparticles, Chemical Physical Letters. **555**, 159-163(2013)
6. Nicolas Cheval, Fang Xu, Nabil Gindy, Richard Brooks, Yanqiu Zhu, Amir Fahmi, Morphology, crystallinity behaviour and thermal properties of polyamide 66/polyoxometalates nanocomposites synthesised via the in-situ Sol-Gel method, Macromol. Chem. Phys. **212**, 180–190(2011)
7. Nicolas Cheval, Fang Xu, Nabil Gindy, Richard Brooks, Yanqiu Zhu, Amir Fahmi, Reinforcement of Polyamide 66 with Polyoxometalates Nanoparticles through the In Situ Sol-Gel Method, Key Engineering Materials. **450**, 169-172 (2011)

Conference presentations

8. Fang Xu, Nicolas Cheval, Hong Chang, Amir Fahmi, Richard Brooks and Yanqiu Zhu, Scaling up the synthesis of WS_2 nanomaterials, EUROMAT, France, 2011, Montpellier.

9. M.N.M. Hatta, Fang Xu, Yongde Xia and Yanqiu Zhu, Deposition of bamboo-shaped carbon nanostructures on carbon fibre, NANOSMAT, Poland, 2011, Karkow.
10. Fang Xu, Yimin Zhao, Nicolas Cheval, Hong Chang, Amir Fahmi, Richard Brooks and Yanqiu Zhu, Influence of growth parameters on morphologies of tungsten oxide nanostructures prepared by solvothermal synthesis, 1st International Conference on Advanced Material Research (ICAMR), China, 2011, Chongqing
11. Hong Chang, Fang Xu, Yanqiu Zhu, Microstructure of Metal Toughened Ceramic Nanocomposites, 1st International Conference on Protective Structures (ICPS), UK, 2010, Manchester.

List of Figures

List of Tables

Acknowledgement

I would like to express my sincere thanks to Prof. Yanqiu Zhu, my supervisor, for his continuous guidance, support and encouragement throughout my PhD studies. He led me into the forefront of the research field of nanomaterials. His attitude, enthusiasm and insight in research will always be my sources of inspiration and support. I would also like to thank Dr. Richard Brooks (University of Nottingham) and Dr. Liang Hao, who partly involved supervision of my PhD work along with Prof. Zhu. Their advice, guidance and valuable suggestions have been much appreciated.

I would like to appreciate the friendship and constant help from the group members Dr. Yimin Zhao, Dr. Trevor Almeida, Dr. Zhuxian Yang, Dr. Hong Chang, Dr. Iftikhar Ahmad, Dr. Chunze Yan, Mr Hamed Parham, Mr Mohamed Nasrul, Mr Charlie Carpenter, Dr. Nicolas Cheval, Dr. Fenghua Bai, Miss Lijie Hu, Mr Yan Wen and many others. Thanks also go to Mr Qi Wang for his friendship and help with schematic drawings.

I wish to thank Prof. Amir Fahmi from university of Rhine-Waal University of Applied Sciences, Dr. Yongde Xia and Prof. Shaowei Zhang for their constant help and valuable advice and guidance.

I would like to thank Mr Peter Gerry and Mr Matthew Wears from Harrison workshop, and Mr David Weightman from Harrison store for their help with machining parts and delivery. Thanks to Mr Peter Splatt from Bioscience for help with SEM and TEM; Dr. Ellen Green from Physics for Raman characterisation; Dr. Lesley Wears for XRD, SEM and Micro-CT analyses; and Drs. Yina Guo from University of Birmingham and Michael Fay from the University of Nottingham for high-resolution TEM characterisation.

I also wish to thank the technical staffs in the Advanced Materials group in University of Nottingham. Special thanks are given to Mr. Keith Dinsdale and Dr. Nigel Neate for their expertise and constant help in various characterisation techniques, including TEM and XRD etc. Thank Mr Thomas Buss for his assistance on all the furnaces. Thanks to Mr. Martin Roe and Mrs. Nicola Weston for their help in SEM. Thanks are also given to Mrs. Julie Wells for her help in developing the TEM images.

I also would like to take the opportunity to thank the ORSAS (Overseas Research Students Awards Scheme), the University of Nottingham and University of Exeter for the provision of scholarship.

Last but not least, my deepest gratitude goes to my parents and my husband for their love, understanding and support.

List of Symbols and Abbreviations

0D	Zero-dimensional
1D	One-dimensional
2D	Two-dimensional
2θ	2 theta (degree)
2H-WS_2	Two-layer hexagonal WS_2
3D	Three-dimensional
AFM	Atomic force microscopy
Al	Aluminium
APCVD	Atmospheric pressure chemical vapour deposition
APT	Ammonium paratungstate
Ar	Argon
BET	Brunauer-Emmett-Teller
BJH	Barret-Joyner-Halenda
C	Carbon
CNTs	Carbon nanotubes
CVC	Chemical vapour condensation
CVD	Chemical vapour deposition
DMA	Dynamic mechanical analysis
DSC	Differential scanning calorimetry
EDX	Energy-dispersive X-ray spectroscopy
FWHM	Full width half maximum
GIXRD	Grazing incidence X-ray diffraction
H_2	Hydrogen
HRTEM	High-resolution TEM

H_2S	Hydrogen sulphide
IF	Inorganic fullerene-like particle
INT	Inorganic nanotube
IPP	Isotactic phlypropylene
JCPDS	Joint Committee on Powder Diffraction
MOCVD	Metal-organic chemical vapour deposition
MS_2	M=Mo or W, including MoS_2 and WS_2
MX_2	M=Mo or W, X=S, Se etc.
NH_3	Ammonia
NWs	Nanowires
OPA	Octadecyl phosphonic acid
PA 12	Polyamide 12
PEEK	Polyetheretherketone
PMMA	Polymethylmethacrylate
PPS	Polyphenylene sulphide
PS	Polystyrene
S	Sulphur
TEM	Transmission electron microscopy
TGA	Thermogravimetric analysis
W	Tungsten
WO_x	Tungsten oxide
WN_x	Tungsten nitride
WO_xN_y	Tungsten oxynitride
WS_2	Tungsten disulfide
XRD	X-Ray diffraction

Chapter 1 Introduction

Nanoscience and nanotechnology have attracted a large amount of research interests in the last two decades and the study will be further strengthened in the future.

As the foundation of nanoscience and nanotechnology, nanomaterials are defined as materials of less than 100 nm at least in one dimension, including zero-dimensional (0D) quantum dots, one-dimensional (1D) nanowires and nanotubes, two-dimensional (2D) nanosheets, and three-dimensional (3D) nanospheres and nanoparticles. Because of their extremely small size, these nanomaterials exhibit not only new crystalline order but also various new properties, promoting numerous potential applications that could not be realised from their corresponding bulk forms. Potential applications typically range from miniaturized nanodevices across diverse industries, such as miniature batteries, solar cells, sensors biomedical actuators, packaging films, super absorbants, nanocatalysts, components of armour and automobile.

One of the most vigorous research areas concerns MX_2-type inorganic nanostructures, in which M=W, Mo and X=S, Se etc. Different forms of such nanomaterials [1-6], e.g. particles, rods, fibres and bundles, have been synthesised in laboratories after the initial success pioneered by Tenne et al in 1992 [1]. Multi-layered WS_2 nanostructures are classified into 1D elongated nanotubes and 0D near-spherical nanoparticles according to their geometry. Recently, studies on inorganic MX_2 nanostructures have showed that tungsten disulphide (WS_2) and molybdenum disulphide (MoS_2) fullerene-like structures, in addition to their significant mechanical and electronic properties, are excellent solid lubricants [7-12]. The incorporation of these nanomaterials into a proper matrix in composites may lead to new products with hugely improved physical and mechanical properties. Another extraordinary property of WS_2 nanostructures is their superb shock absorbing performance [13-15], which suggests a potential application in lightweight and high performance protective composites. This suggestion was underlined by a recent article published in Science [16]. Such applications will obviously demand large amounts of WS_2 supply, however their synthesis has been only obtained in laboratory in gram level which is far too less for any practical work. More recently, an Israeli group led by Tenne has produced such inorganic fullerenes in large quantity by using very

complicate high tower reactors [17]. A simple and yet effective process remains highly desirable for these nanomaterials.

Therefore, to develop an innovative, simple and scalable technique that is suitable for the continuous manufacture of WS_2 inorganic nanomaterials in large scale becomes the primary aim of this PhD project. Having achieved this, research using these nanomaterials in the fabrication of lightweight and high performance polymer matrix nanocomposites will be reported as a further objective of this work. In the meanwhile, the extension of new technique for continuous production of other novel nanostructures, for example, the first creation of a new class of C-coated IF-WS_2 composites nanoparticles, forms another research focus of this thesis.

Among the diverse synthesis approaches of WS_2 or MoS_2 nanomaterials, the sulphidisation from their oxide counterparts has been proved very successful [1, 6, 18-20]. While being considered as the most important precursor for WS_2 nanomaterials, tungsten oxide (WO_x) nanostructures also demonstrate significant potentials in numerous applications such as electro-chromic devices, gas sensors, catalysts and electrochemical devices etc. [21-28].

With high aspect ratio, unique electrical and chemical properties have been exhibited by 1D WO_x nanowires/nanorods, while intense research effort has been focused on their preparation by different methods [29-34]. It is widely acknowledged that the properties of nanowires are closely related to their morphology. However, it is still a challenge to produce WO_x nanostructures with desired size and shape, or controlled pattern, which becomes another objective of this PhD project. In this work, 0D and 1D WO_x nanostructures would be produced using effective methods, while systematic studies will be carried out to investigate the growth mechanism and to achieve materials with desired morphology, especially aiming for 1D nanowires of high aspect ratio and high surface area. In addition, an effective way to produce patterned 1D WO_x nanorods will be explored, for potential device construction.

As an analogy to WO_x nanomaterials, nanostructured WN_x also attracted considerable research interests due to promising application as catalyst, semiconductor devices electrodes and microelectronic barriers [35-39]. However, there are relatively less studies involving the preparation of 1D WN_x nanostructures [35, 40, 41], compared to

1D WO_x nanostructures, thus investigation is requested on their growth, especially for controlled pattern growth. Therefore, research to achieve 1D tungsten nitride (WN_x) nanostructures through nitridation of our previously produced WO_x nanorods as a template become an extended objective, in which the morphology evolution would be characterised and the growth mechanism will be discussed.

The thesis has been presented as 8 chapters. Chapter 1 introduces the motivation, objectives and organization of the thesis. Chapter 2 presents the research background and literature review for inorganic MS_2 (M=W, Mo) fullerenes and nanotubes, as well as nanocomposites reinforced by MS_2 nanostructures. Chapter 3 describes the materials and preparation techniques for nanomaterials and nanocomposites, in addition to the structural and property characterisation methods employed. Chapter 4 demonstrates design, modification and initial investigation of a rotary furnace aiming to scaling up manufacturing of WS_2 nanoparticles. Chapter 5 describes the preparation and characterisation of precursors for WS_2 nanomaterials, different tungsten oxide/nitride nanostructures, including tungsten oxide nanoparticles by high temperature thermal decomposition, tungsten oxide nanowires through solvothermal method, besides, and, the patterned growth of tungsten oxide and tungsten oxynitride nanorods using chemical vapour deposition technique have also been presented in Chapter 5. Chapter 6 presents the synthesis of IF-WS_2 through different method, and the parameter optimization towards scaling up manufacturing of WS_2 from WO_3 precursors and H_2S gas, based on the designed rotary furnace described in Chapter 4. Furthermore, thermal stability improvement of WS_2 by carbon coating has also been investigated. Chapter 7 describes the preparation process, structural and mechanical properties characterisation of nylon 12 matrix impregnated with IF-WS_2 nanoparticles. Conclusions of the thesis are summarised in Chapter 8, as well as some recommendations for future development in related research areas.

Chapter 2 Background and literature review

2.1 Large scale manufacturing of WS_2 fullerene-like nanomaterials

Introduction

Inorganic nanotubes (INTs) and inorganic fullerene-like (IF) structures of WS_2 were first discovered by Tenne et al. in 1992 [1], which has opened a challenging field for the synthesis and application of numerous INTs and IF structures, such as WS_2 [1], MoS_2 [2, 3], BN [42], $NiCl_2$ [4], and etc. These nanostructures are generally produced from layered (2D) materials and are similar to fullerenes and carbon nanotubes (CNTs) in structure, with shapes of multi-walled quasi-spherical cages, nano-octahedra [43], or nanotubes.

After their first discovery, intense studies have been carried out on various synthesis methods, and numerous potential applications of the INTs and IFs nanostructures are proposed due to their distinguished properties [10, 12, 15, 17, 18, 44-48]. This part of the review introduces the synthesis methods, crystal structures, properties and potential applications of these IFs and INTs.

2.1.1 Crystal structure of INTs and IF nanostructures

Layered compounds, such as graphite or MS_2 (M=Mo, W), are typified by their very anisotropic 2D layered characteristics. In the case of graphite, within the layer (*ab* plane), the carbon atoms are covalently bonded, while along the *c* axis, weak Van der Waals forces are responsible for the stacking of these molecular slabs (Figure 2-1a) [49]; whilst in MS_2 (M = Mo, W) (Figure 2-1b), in contrast to graphite, each molecular sheet consists of a tri-layer structure made of a M layer sandwiched between two S layers, within which different atoms chemically bonded together. As shown in Figure 2-1b, a trigonal biprism is formed by binding one M atom with six S atoms [50, 51]. Similarly, the S-M-S layers are also stacked together by weak Van der Waals forces (Figure 2-1a) [49, 52].

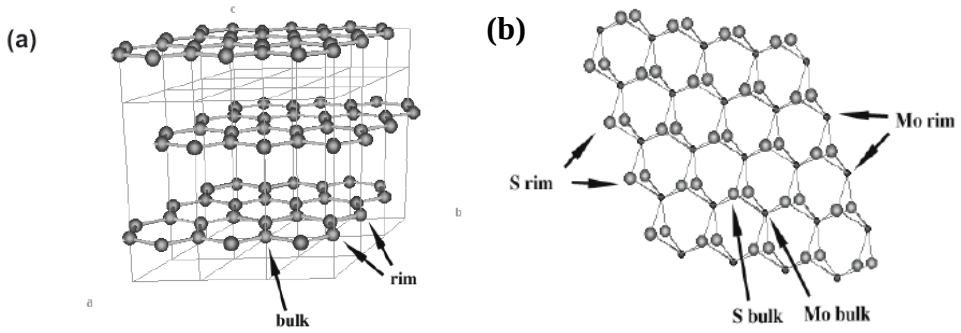

Figure 2-1 (a) A schematic drawing of graphite. The surface energy is concentrated in the 2-fold coordinated carbon atoms on the rim of the layer. (b) A schematic drawing of a MoS_2 nanocluster showing the Mo and S rim atoms with their dangling bonds (adapted from Ref. [49]).

Figure 2-2a shows a high-resolution transmission electron microscopy (HRTEM) image of a typical WS_2 nanotube obtained using precursor of WO_x ($2 \leq x \leq 3$) [49], and Figure 2-2 b is a schematic presentation of a single-walled WS_2 nanotube with W and S atoms, each shell consists of three layers, in contrast to the single layered structure in the case of graphite [53]. That is how the name of inorganic fullerene comes from.

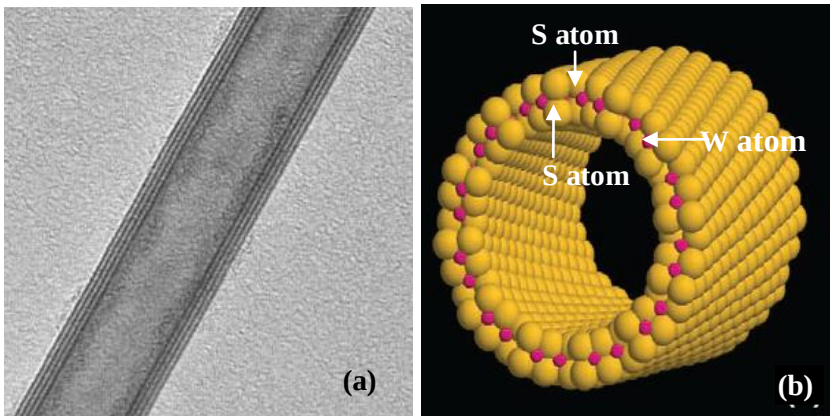

Figure 2-2 TEM image of a multiwall WS_2 nanotube (a) and Model of WS_2 nanotube (b) (adapted from Ref. [49, 53]).

2.1.2 Properties and potential applications of INTs and IF nanostructures

2.1.2.1 Mechanical and tribological properties

To date, mechanical properties such as tensile, buckling, compression and bending properties of multi-walled MS_2 (M = Mo, W) nanotubes have been briefly studied [10, 11, 41, 54]. Figure 2-3 displays a WS_2 nanotube compressed against the surface of a Si wafer within a high resolution scanning electron microscope (HRSEM), and the average

bending modulus value was measured to be 217 GPa using the electric-field-induced resonance method [41]. The experimentally determined tensile stress-strain plots show that the nanotubes deform elastically almost until their failure [10], which is very impressive. According to the measurement, the Young's modulus, yield strength and elongation values are measured to be 150 GPa, 3-16.3 GPa and 5-14%, respectively. The yield strength to Young's modulus ratio is 0.11, which is exceedingly high in comparison with other high-strength materials [11].

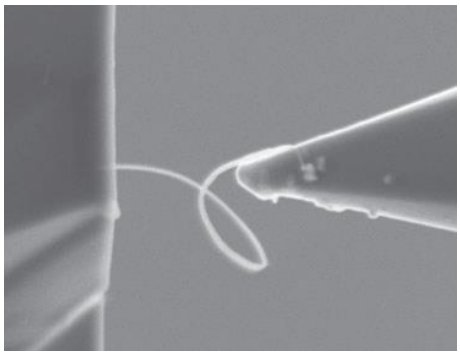

Figure 2-3 SEM picture of a WS_2 nanotube under axial compression (adapted from Ref. [41])

Accordingly, uniaxial compression test have been carried out for an individual IF particle, by using an AFM within HRSEM, as shown in a schematic diagram Figure 2-4 [55]. The stiffness for an individual IF was measured to be 350-360 Nm^{-1}, and it possessed a compression failure strength as high as 1-2.5 GPa [55]. It is also found that the stiffness of a spherical nanoparticle is higher than a faceted one, probably due to the lower stress concentration at the corners. This could explain the fact that IF-MoS_2 which are generally more spherical than IF-WS_2, has a higher stiffness than that of the WS_2 counterpart.

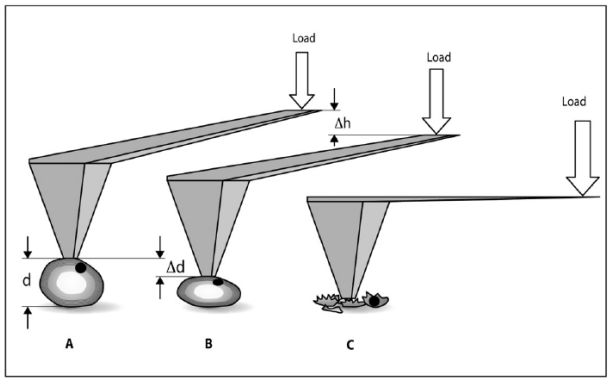

Figure 2-4 Schematics showing the multi-layered polyhedral IF nanoparticle pressed by an AFM cantilever probe in HRSEM [55]

Tribological properties of IF-MS_2 have attracted numerous research interests as additives to lubricant fluids since its first report in 1997 [12], due to their quasi-spherical shape and inert terminated surface. Recently, in a macroscopic friction experiment, IF nanoparticles were added to oil under severe contact conditions, and the friction coefficients were measured as low as 0.03 [56]. Cobalt films impregnated with IF-WS_2 nanoparticles (Co+IFs) were successfully deposited onto a stainless steel substrate and the films showed a lower friction and wear, which indicated an efficient lubrication obtained by the dry metallic film embedded with IF-WS_2 [57]. In addition, the friction coefficients in dry tests were generally higher (ca. 0.1) than in oil-lubricated surfaces (no more than 0.06).

Accordingly, intensive studies have been carried out to understand the lubricant mechanism for these MS_2 materials [56, 58-62]. Generally, three main lubrication mechanisms have been proposed and discussed, include rolling, sliding and exfoliation and transfer of films (third body) (Figure 2-5). When rolling dominates [7, 12], the IF particles act as a ball bearing; when sliding dominates, low friction and shearing are provided by IF particles working as a separator between the two weakly interacted coupling surfaces; and whilst exfoliation mechanism works, the exfoliated layer would be deposited on the asperities of the mating surfaces [58].

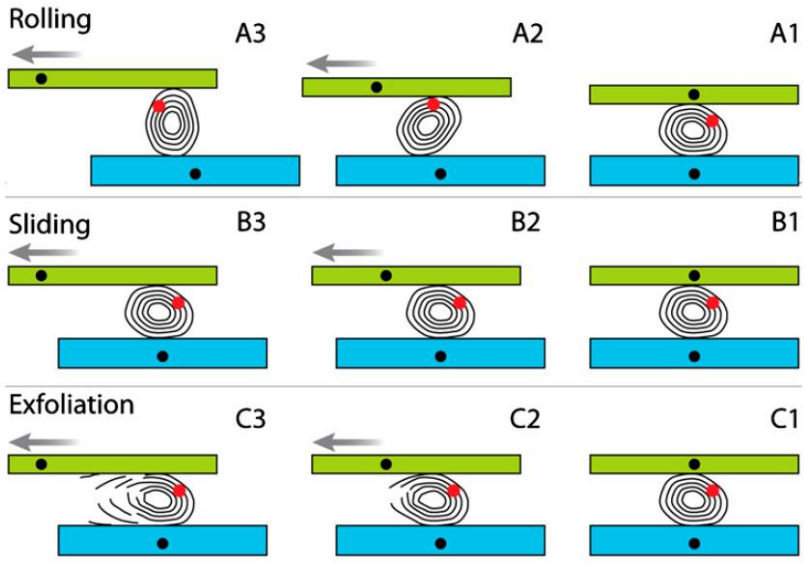

Figure 2-5 Three main friction mechanisms for IF MS_2 nanoparticles: rolling (A), sliding (B) and exfoliation (C), demonstrated with reference particle (red mark). The bottom surface was kept stationary while the top surface is moving from right to left [59]

Of these three main mechanisms which are believed to contribute to the excellent tribological behaviour of IF nanoparticles, the exfoliation of nanosheets from IF nanoparticles is considered to be predominant. Under intensive loading, the exfoliated nanosheets will be deposited onto the coupling surface forming a tribofilm which reduces both friction and wear. This mechanism has been illustrated in Figure 2-6.

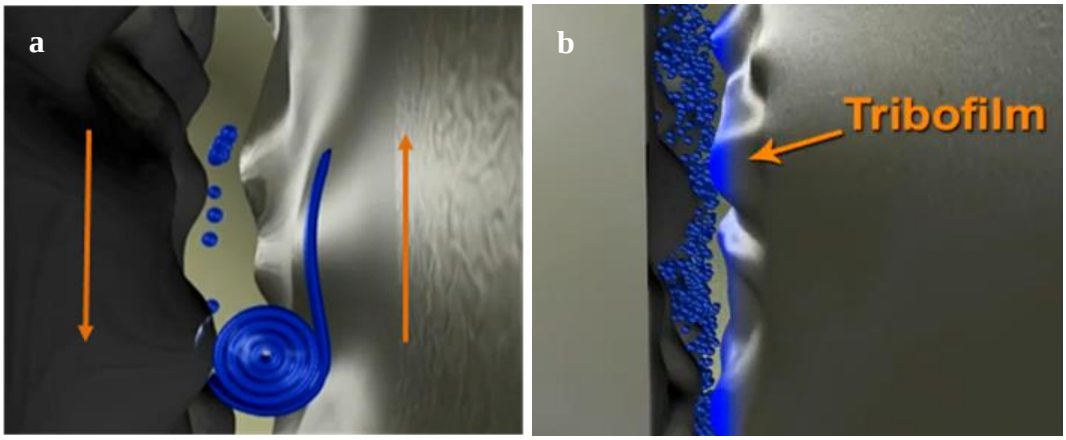

Figure 2-6 Sketch of IFs work as lubricant. The exfoliation of the nano IF (a) leads to the formation of a tribofilm, (b) which decreases the friction and wear dramatically (adapted from video of NanoLub Engine Oil Additive on Youtube)

A series of images captured by a video during a nanocompression test for a single IF nanoparticle were shown in Figure 2-7, which have further confirmed the exfoliation mechanism. The faceted IF-WS_2 particle was attached to the diamond tip and compressed onto the Si substrate. It deformed as soon as the load was applied (8 s): the lower layers of the particles further deformed and the hollow core disappeared with time (11 s), then the particle started to tear and debris of nanosheets were resulted from the exfoliation of the nanoparticles with further loading, followed by a sudden drop of force from 2.8 to 1 μN accompanied with the morphology change at 15 s, and the particles continued to exfoliate with further loading, finally the WS_2 layers became well-separated and the particles were completely crushed at 45 s. Comparison experiment has been carried out for an IF-MoS_2, which is without a hollow core and better crystallized. It was showed that hollow particles are more prone to exfoliate compared to more spherical and well-crystallized particles. This might also give explanation to the fact that, a perfectly crystallized spherical particles was found to have poorer tribological behaviour than those of hollow faceted structures [63].

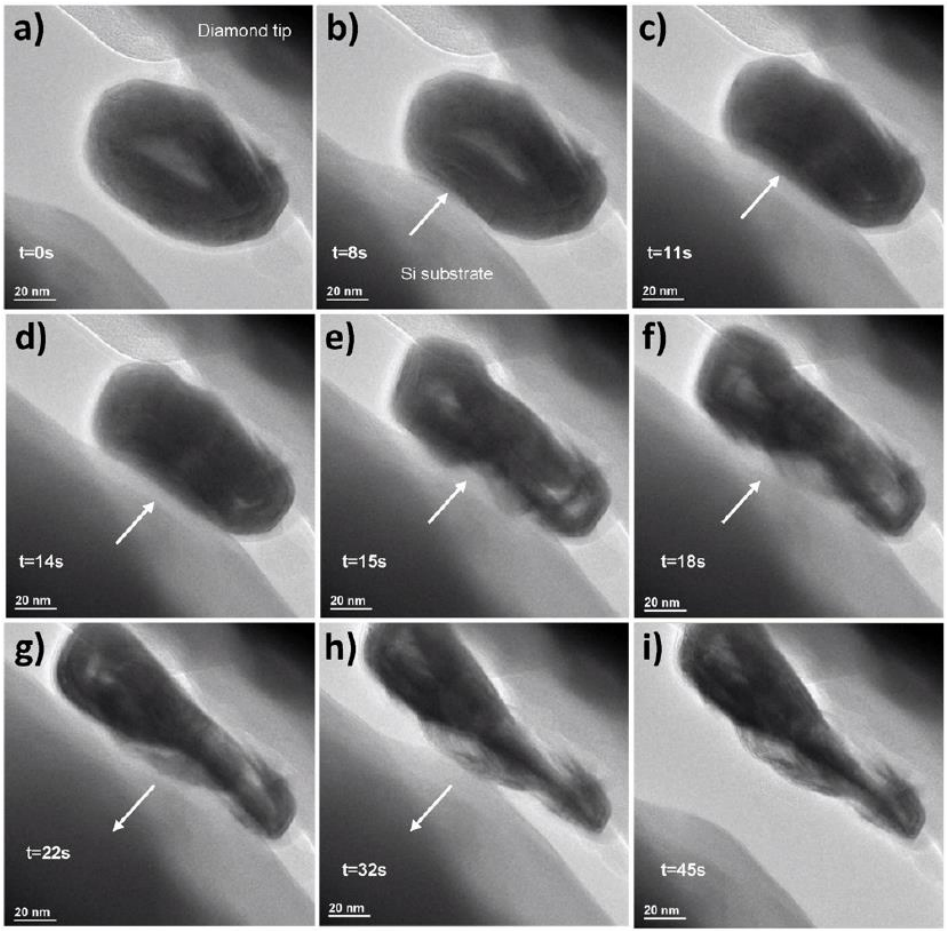

Figure 2-7 Snapshot images from a video recorded during a compression experiment carried out with a single WS_2 particle [61]

It was thus suggested that the IF-MS_2 particles could be used as superior solid lubricants in vacuum, space and other applications where the use of liquid lubricants are impractical. Further efforts have been made to applications in aerospace [64], medical [65], machining [57] and other industries [12], as self-lubricating coatings. For an example, during an outgassing screening test for space applications, the IF-WS_2 powder has significantly surpassed the minimum requirements [64]. The first medical application--alleviating friction in orthodontic wires was also reported [65, 66], and the IF-WS_2 nanoparticles are confirmed as safe under toxicological tests [67], which makes them promising for numerous medical applications.

In addition, porous composites produced by impregnating the IF nanoparticles into an porous matrix exhibited low friction coefficients and reduced wear loss even under high loads [68]. Similarly, self-lubricating polymer coatings have been reported by incorporation of IF-WS_2 nanoparticles into polymer matrices [45]. The addition of small

amounts of IF nanoparticles into isotactic Polypropylene (iPP) matrix improved the thermal stability of the polymer and also significantly influenced the crystallization rate of the polymer, reported by Naffakh et al [69]. More discussion about polymer impregnated with IF-WS_2 nanocomposites will be presented later in Section **2.2**.

2.1.2.2 Shock absorbing properties and potential application

Zhu et al. have first reported the extraordinary shock absorbing performance of the IF MS_2 [13-15].

Figure 2-8 illustrates the shock recovery experiments. When the high-speed projectile hits the sample container, shock waves transmit and propagate within the sample, resulting in high shock wave pressures and very high temperatures, with temperature reaching 1000°C under high pressures more than 20 GPa. Due to the limitation of thermal diffusivity, the decay of thermal spikes of the sample lasts much longer than the shock wave reverberation.

Results showed that the IF-WS_2 nanoparticles exhibited significant shock absorbing properties, survived shockwave pressures up to 25 GPa and concurrent temperatures close to 1000°C, and is probably the toughest cage molecules known to date. These cage-like spherical particles can also sustain static pressures up to 30 GPa [14], whilst their tube form (elongated hollow particles) have tensile strengths approaching 16 GPa [13], which is nearly twice the strength of the best impact resistant materials (e.g. SiC) used in protective armour applications and five times that of high tensile steel [15].

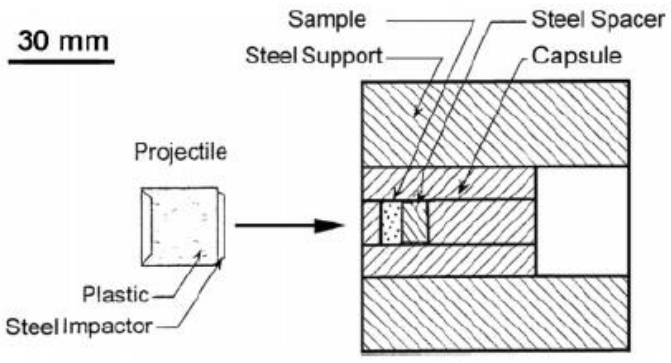

Figure 2-8 Shock recovery sample assembly for a single-stage gun experiment, IF-WS_2 withstand 25 GPa shockwave pressure [15]

Based on the results and the high pressure and high temperature arisen from the shock wave recovery experiments, two possible destructive mechanisms have been proposed,

a direct stresses-induced breakage failure and a diffusion-controlled oxidation, either separately or combined. Furthermore, several IF nanoparticle models are also proposed to demonstrate the likelihood damage under shock wave (Figure 2-9), by taking several different factors into account: exterior geometry, inner oxide fillings (residues), and overall dimensions. According to the two possible destructive mechanisms, the shock absorbing property of these model particles are expected to increase remarkably from (a) to (d). The perfectly spherical small model particle is supposed to exhibit the best anti-shock performance [14, 15].

It is also worthy to note that, in terms of structural failure, many common features were found between tribologically tested IFs and post-shock samples, including the surface splintering feature, the ovoid-shaped elongated IFs, as well as the similar oxidation occurred during both processes. This similarity in failure structure and the excellent performance of IF nanoparticles in both lubrication and shock wave absorption process, suggest that IFs are valuable materials for a diverse range of applications where dynamic pressures concomitant with high temperatures are involved [15].

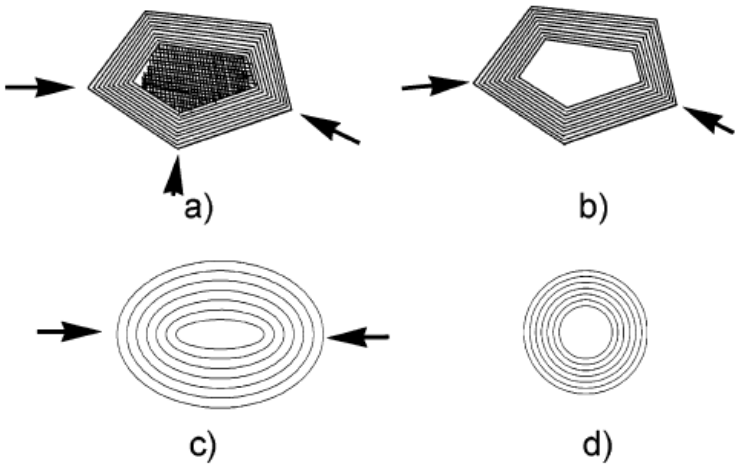

Figure 2-9 Schematic illustration of the likelihood damage of IFs under shock wave pressure [15]

The above results suggest that IF-MS_2 can be combined with other matrix to produce ultra-high strength and high impact resistance nanocomposites, which could find wide applications in the automotive, aerospace and personal safety and defence industries [16]. For example, the current generation of ballistic armour gives some level of protection by using strong materials only to stop bullet penetration, not shock absorbing

and unable to dissipate concurrent high temperatures generated by shockwaves. Further study in this field will be extremely exciting.

2.1.2.3 Thermal properties of IF nanoparticles

Since high temperature is involved in many applications, thermal stability is of significant importance for IF nanoparticles. In a study with microtribology properties of the layered MoS_2 nanoparticles, the thermal stability of MoS_2 in air atmosphere was also analysed [70], and the results were showed in Figure 2-10. The oxidation of 2 μm and 50 nm particles started at 400°C and 250°C respectively. The weight loss of 2 μm MoS_2 finishes by 600°C, with 20% weight loss in this temperature range, which is consistent with a conversion of MoS_2 to MoO_3 and gaseous SO_2; whilst a 30% weight loss was observed for 50 nm nanoparticles during 250-500°C.

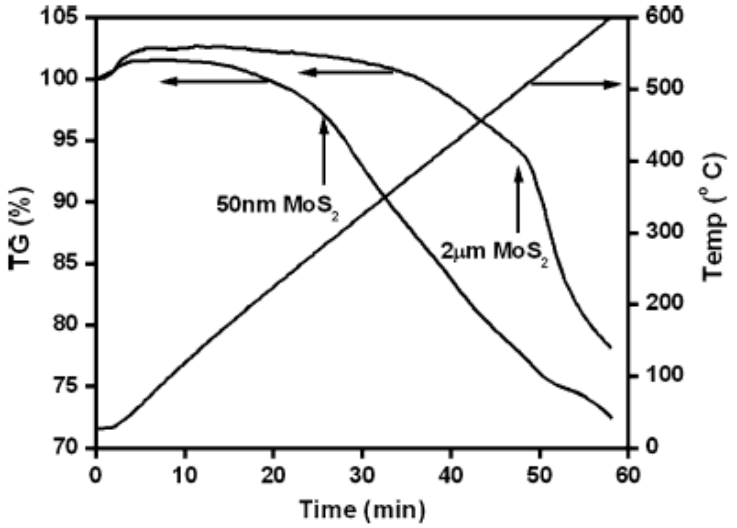

Figure 2-10 TGA results for MoS_2 with size of 2 μm and 50 nm respectively [70]

Similarly, in a study using IF nanoparticles as additives to lubricant, the oxidation temperatures for IF nanoparticles (ca. 120 nm) and 2H (2 hexahedron) WS_2 platelets (4 μm) were found to be about 320°C and 420°C respectively, reported by L. Rapoport and co-workers [7]. This result indicates that the macroscopic (4 μm) platelets are chemically more stable than the IF nanoparticles. However, another studied platelets with smaller size (ca. 0.5 μm) exhibited poorer chemical stability and lower oxidation temperature 250°C. By comparing the XPS analyses of the wear track surfaces of the IF-WS_2 nanoparticles and 2H-WS_2, it is notable that, despite the different initial oxidation temperature, during the tribological process, 2H-WS_2 exhibited a remarkably

higher rate of oxidation and left more severe wear tracks on the surface than those of IF particles. The advantage of IF nanoparticles is probably owing to their round shape and absence of dangling bonds [7, 71].

Thermal stability of a range of inorganic nanomaterials (IF-NbS_2, IF-MoS_2, and IF-WS_2) in both oxidizing and inert atmosphere, in comparison with their bulk counterparts, were studied systematically in another work [72]. In O_2 atmosphere, the oxidation resistant was found mainly depending on particles size, with oxidation of nanosized IF particles (100 nm) occur from 295°C compared to 440°C for large micron sized particles (3 μm). The order of stability for the investigated materials descended in the following order 2H-MoS_2 > 3R-$Nb_{1+x}S_2$ >2H-WS_2 > IF-WS_2 > IF-MoS_2> IF-NbS_2. The oxidation occurred through sulphates and lower oxides at lower heating rates, whilst almost through a one-step oxidation to highest oxides at higher heating rates.

WS_2 coated CNTs were produced by Raymond and co-workers [73], and their thermal stability has also been studied. The results reveal that pure INT-WS_2 possess a higher oxidation temperature in air compared to pure CNTs and WS_2-coated CNTs, as displayed in Figure 2-11.

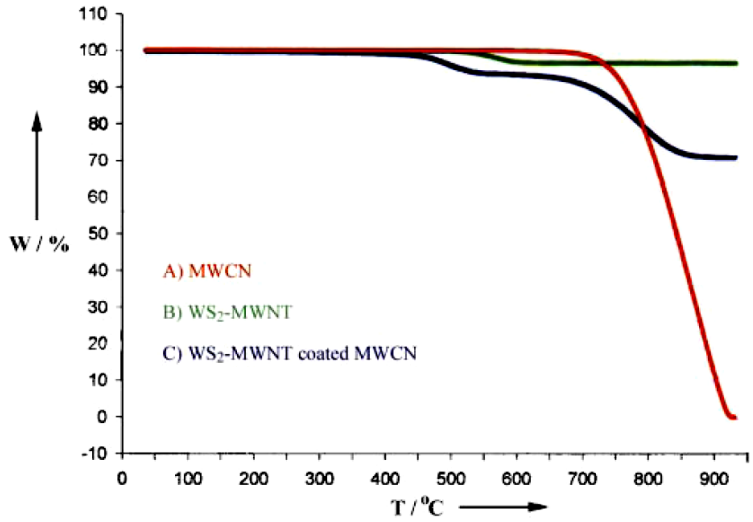

Figure 2-11 TGA analysis of CNTs, INT-WS_2 and WS_2-coated CNTs [73]

To summarise, though many excellent properties are exhibited by IF nanoparticles, the thermal stability of IFs are inferior to their bulk counterpart. Further efforts need to be focused on improvement of thermal properties of IFs, for applications which involve critical temperature environment. Some initial effort has been invented to coat MWCNT

with INT-WS_2, where higher thermal stability is shown compared to pure MWCNT. Thus it is inspired that, a coating layer outside IFs might confer to their thermal stability.

2.1.2.4 Other properties and applications

Numerous different properties and applications of the IF nanostructures have been reported [8, 46, 47, 74-85]. The thermal properties of these IFs have been studied recently [46, 74]. In one of those studies, low temperature specific heats of bulk platelets and IF-WS_2 were found significant different from below 9 K [46]. Because of finite size effects, the specific heats of nanoparticles deviated from the usual T^3 dependence below 4 K [46], and similar phenomena were also observed for carbon and TiO_2 nanotubes [20, 86]. It is therefore not difficult to presume that the thermal effect of the IF-WS_2 in nanocomposites would be significant.

The use of INT-WS_2 as tips for scanning probe microscopy has been accomplished by A. Rothschild et al. [75]. Both ends of the INT-WS_2 are closed due to the formation of triangular and rhombohedral defects, leading to an extremely sharper end than those of CNTs, which only consist of pentagonal defects [76]. INT-WS_2 can be easily sensitized by visible and infrared light and are therefore promising for carrying-out photo-stimulated processes on surfaces, as they have similar optical properties to the 2H-WS_2 [77]. These robust and inert tips could be used in imaging rough surfaces with high aspect ratios, such as in biologically significant systems.

Furthermore, Chen et al. have applied MoS_2, TiS_2 and WS_2 INTs for catalytic methanation of CO [78, 79], and used them as cathode materials for Li intercalation batteries [80-82].

These various INTs also possess significant electronic and optical properties, according to theoretical and experimental reports [8, 47, 83-85]. For an example, unlike quantum dots, the band gap of semiconducting nanotubes shrinks with decreasing diameter of the nanotubes, such as MoS_2 and WS_2 [8, 47], although IF-MS_2, even with only a single-layer, preserve the semi-conductivity of the bulk material. This could help with new optical observations for the study of structure-property relationship and for the exploration of the optical properties for specific applications, e.g., for photocatalysis. By intercalation of alkali metal atoms, the Fermi level, i.e. the conductivity of

semiconducting IF nanoparticles, could be tuned [83]. Furthermore, it was suggested that INTs could also be metallic [84] and even superconductive [85].

2.1.3 Synthesis of WS_2 nanostructures

All these excellent properties of IF particles and INTs, especially WS_2-IFs (or INTs) have initiated an immense amount of efforts to synthesise them. Up to now, WS_2 nanostructures have been prepared by several processes, as follows.

2.1.3.1 Direct oxide-sulphide conversion

The first method applied for IF nanoparticles and INTs of WS_2 synthesis was sulphidising a WO_3 precursor in H_2 atmosphere at high temperature (850ºC) [1-3]. After that, oxides continue to be used as the precursor for the large scale synthesis of IF nanoparticles in a reducing atmosphere [18, 87, 88]. As an example, Figure 2-12 shows some IFs achieved by this process. The hollow core in the centre of the nanoparticle is formed due to the lower density of oxide precursor (WO_3) than that of sulphide product (Figure 2-12a) [53]. An INT-WS_2 with eight cylindrical and concentric layers is shown in Figure 2-12b, the separation between each layer is 0.62 nm [89].

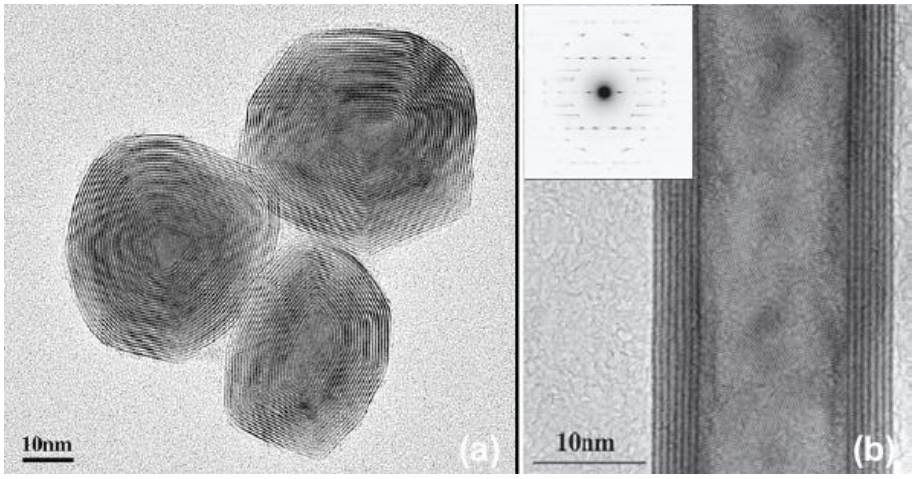

Figure 2-12 TEM image of (a) IF-WS_2 nanoparticles and (b) INT-WS_2 produced by sulphidisation of oxide precursors (adapted from Ref. [53, 89, 90]).

2.1.3.2 Gas phase synthesis

IF-WS_2 and INTs have also been obtained by a gas phase reaction starting from various WCl_n (n=4, 5, 6) and WO_xCl_y with H_2S in a horizontal or vertical reactor (Figure 2-13) [44, 90]. As shown in Figure 2-13, the reducing gas H_2, together with N_2 gas, will carry the metal chloride precursors into the main reactor which will be reduced completely

and react with the sulphidising agent H_2S (in form of N_2 and H_2S gas mixture) coming from the other end of the reactor [44]. The effect of the various WCl_n (n = 4, 5, 6) precursors on the formation of the products has been investigated [44], and WCl_4 and WCl_5, were the most suitable ones. Figure 2-14 illustrates the formation mechanism of the IF-WS_2 and INT-WS_2 synthesised by these reactors [44].

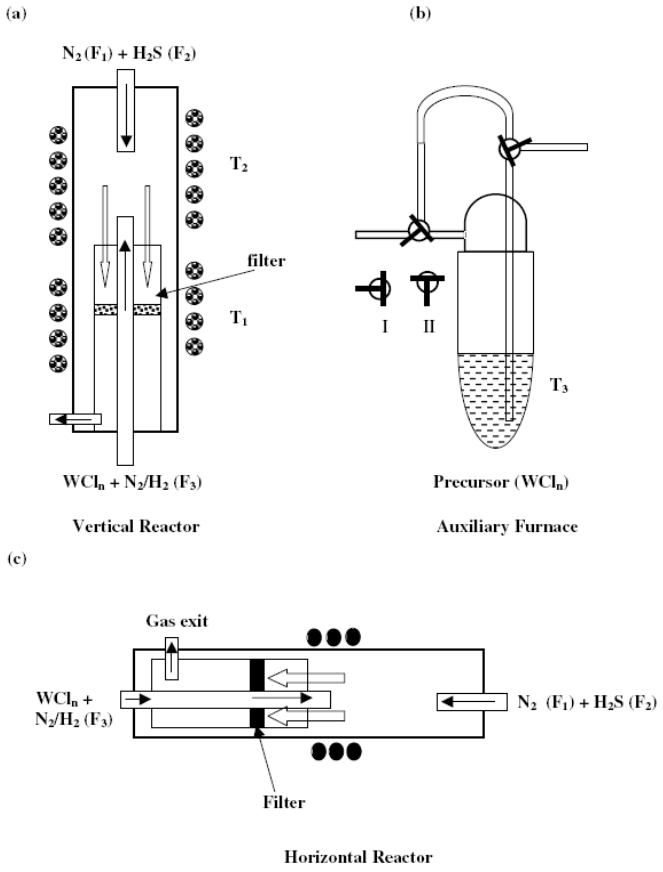

Figure 2-13 Schematic presentation of (a) a vertical reactor, (b) an auxiliary reactor which produces the WCl_n vapours, and (c) an horizontal reactor (adapted from Ref. [44]).

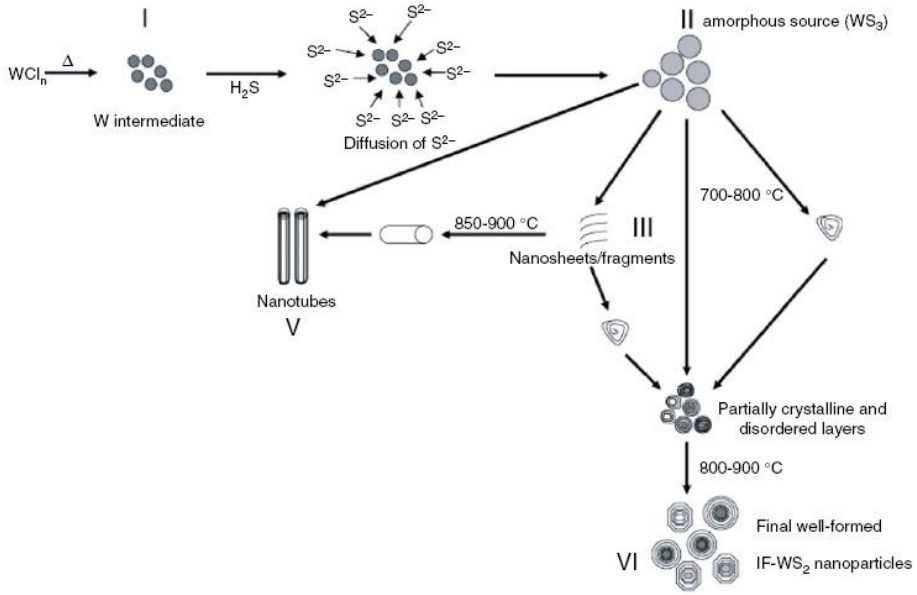

Figure 2-14 A mechanism for the formation of IF-WS_2 and INT-WS_2 in the gas phase reaction (adapted from Ref. [44])

Interestingly, this method could open up a technique for doping the IFs and INTs, however a disadvantage is the high sensitivity of the metal halides to water and oxygen.

2.1.3.3 Metal-organic chemical vapour deposition (MOCVD) method

Other precursors have been applied to the synthesis of IF-WS_2 by a MOCVD method using metal carbonyl precursor [$W(CO)_6$] and elemental S [91, 92]. Either a one-step or a two-step process can be employed in this reaction. In the two-step process, amorphous WS_2 nanoparticles were first formed during the high-temperature reaction of W with S, and they were isolated and converted into IF-WS_2 in a separate annealing step [91, 92].

2.1.3.4 Atmospheric pressure chemical vapour deposition (APCVD) method

An alternative APCVD route using metal chloride precursors for the large scale synthesis of IF-WS_2 has been developed by Li et al [93]. With this method, under controlled reaction conditions, the reaction of chlorides (WCl_6) and S has produced IFs, as well as elegant 3D nanoflowers [93].

2.1.3.5 Other synthesis methods

Other methods include a direct pyrolysis from artificial lamellar mesostructures WS_4^{2-} and Cetyltrimethyl Ammonium Bromide (CTAB) to form INT-WS_2 [94], a microwave treatment of tungsten carbonyl and H_2S [95], a direct heating at 800°C of ultrasonic

irradiated $W(CO)_6$ solution mixed with diphenylmethane and S [96], an activation of a commercial WS_2 sample [97], the iodine transport technique [5], a Chemical Vapour Condensation (CVC) of tungsten hexacarbonyl over S vapour in an inert gas flow [98], and a thermal decomposition of ammonium thiomolybdate and thiotungstate at higher temperatures to form MoS_2, WS_2 and a host of other transition metal dichalcogenide INTs [48, 99, 100]. However, these techniques, suitable for lab scale study, do not appear to be able to achieve large scale production.

Until now, the most suitable technique for large scale manufacturing seems to be the oxide-to-sulphide conversion by using H_2S at high temperature up to 1000°C under a reducing atmosphere [1, 6, 19], which has been explained in **2.1.3.1.**

2.1.3.6 Tungsten oxide precursor

In addition to being considered as the most favourable precursor for synthesis of WS_2 IFs and INTs [1, 6, 18-20], nanostructured WO_x ($2 \leq x \leq 3$) also have many other promising applications, such as in electric field emitters [101], catalysts [21, 102], gas sensors [22-25], and in electro-chromic [26] and electrochemical devices (such as Li-Ion lithium battery) [27, 28].

Recently, many studies have focused on the production of 1D WO_x nanowires/nanorods using a variety of different approaches, similar to those for WO_x nanoparticles growth [29-31]. Hydrothermal reactions starting with W-containing salts such as WCl_6, $W(CO)_6$ and WCl_4 in solvents including ethanol, water, cyclohexanol and their mixture etc., with or without the addition of acids and surfactants [32-34] have also been reported.

Amongst the numerous applications, the size and specific area of tungsten oxide nanostructures seem to play an important role in many of them. For example, in the application as gas sensor, the reduction/oxidation reactions guide the sensing signals are mainly affected by the surface area of oxides, thus increase of the specific surface area is an effective way to enhance sensing performance [25, 103, 104]. Similarly, studies on electro-chromic properties have suggested that high surface area and porosity of tungsten oxide film contributed to enhanced electro-chromic properties, such as better response time and coloration efficiency [25, 103, 105, 106].

Promising properties of WO_x nanowires with high surface area for potential application have been reported by our group, as gas sensor for NH_3 [24] and as liquid crystal electro-chromic materials. For these applications, high surface area is the key to achieve revised properties [25, 103-106]. Thus, to achieve nano-sized tungsten oxide with high surface area is fundamentally essential and becomes one of the research interests in this PhD programme.

2.1.4 Detailed growth mechanism of WS_2 nanostructures

Before it is possible to manufacture WS_2 nanostructures by oxide-to-sulphide conversion in large scale, the growth mechanism has been intensely investigated [6, 18, 52, 53, 90]. The knowledge of the growth mechanism of IF-WS_2 nanoparticles, starting from the trioxides, would help to achieve relatively high quality products with good size distribution and shape. The model used to illustrate the oxide to sulphide conversion has been described previously, and is represented in Figure 2-15 [53, 90].

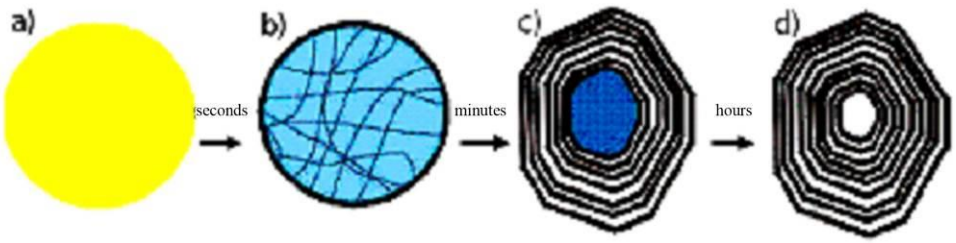

Figure 2-15 Schematic drawing of the growth mechanism of IF-WS_2 nanoparticles produced from WO_3 particulate precursor. (a) The starting WO_3 nanoparticles; (b) partly reduced suboxide encapsulated with several (1–2) layers of WS_2; (c) the suboxide core within the envelope of more disulphide layers; and (d) the final quasi-spherical closed-cage hollow IFs (adapted from Ref. [53, 90])

At the first step, which is very fast lasting only a few seconds or less, the surface of a tungsten oxide (WO_3) nanoparticle is reduced, and the atomic planes at the surface shears and reacts with H_2S immediately forming a closed sulphide layer and leaving the oxide core. This inert sulphide layer prohibits the fusion of neighbouring reactive oxide nanoparticles thus preventing the growth of a large tungsten oxide which would eventually lead to the formation of 2H-WS_2 [18, 53]. The first stage will make sure the final products being IFs, rather than 2H-WS_2 particles.

The second stage lasts several minutes. During which, the completely radial reducing of the incipient oxide core into $W_{18}O_{49}$ occurs. After this process, the oxide particle would be encapsulated by more and more layers of WS_2 [18, 88].

In the last step, the oxide core is gradually sulphidised into respective sulphide layers of the IFs, by the diffusion of sulphur through the preformed WS_2 layers inwards. According to different nanoparticle size and different reaction temperature, the whole sulphidisation time may vary from 30 to 300 min. For nanoparticles smaller than 100 nm, 60-120 min was considered to be enough. The resulting IFs would be left with a hollow core (5-10% of the whole IF's volume) due to the differences in the density between the starting material WO_3 and the produced WS_2 (5%) [53, 90]. Because the shell formed during the first stage follows the shape of the initial WO_3 nanoparticles, the size and geometry of the IF is thus determined by the size and geometry of precursor used.

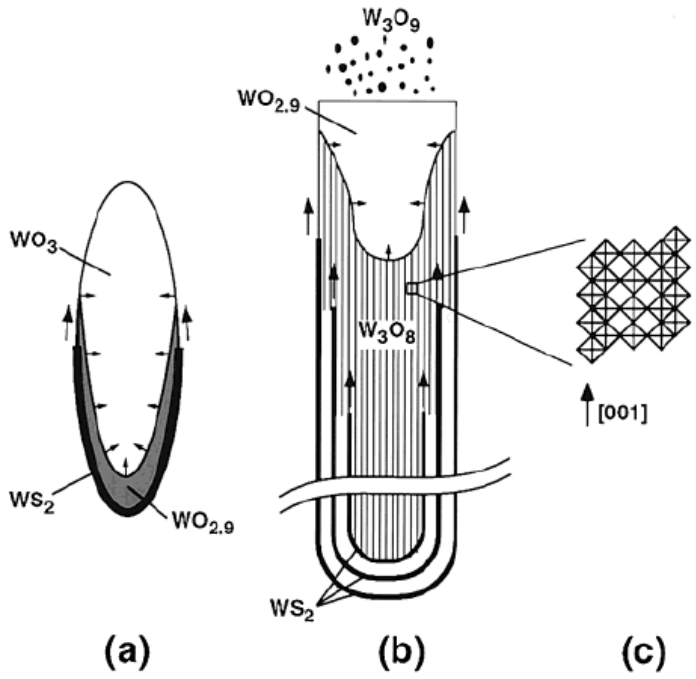

Figure 2-16 Schematic drawing of a growth mechanism for INT-WS_2 produced from WO_3 nanoparticles precursor. (a) The enfolding of the elongated suboxide nanoparticles by the sulphide layers; (b) the growth of a long sulphide/oxide encapsulated nanowhisker; and (c) enlargement of the CS (crystallographic shear) planes exhibiting within one CS plane region of an edge sharing octahedra (adapted from Ref. [6]).

Researchers have also proved that the growth mechanism for INTs is similar, but not identical, to the growth mechanism of IFs, as the final geometry is determined by the initial geometry of the reacting WO_3 precursors [6, 18, 53].

In these studies, it is found that within the first a few seconds of the INT-WS_2 formation (Figure 2-16a), needle-like oxide nanoparticle reacts with H_2S and partly forms a protective tungsten disulphide monomolecular layer, preventing direct contact of this nanoparticle with neighbouring oxide nanoparticles, similar to the particulate conversion stage. The most striking different is that the whisker tip remains open due to the rapid whisker growth, so that the $(WO_3)_n$ or $(WO_x.H_2O)$ clusters could be condensed on the open tip and subsequently be reduced by hydrogen, resulting in a continuous growth of the sulphide-covered oxide nanowhiskers. Subsequently these nanowhiskers would be gradually sulphidised into INTs [6, 53]). Finally, higher oxide vapour pressure ensure restricting the reduction and sulphidisation reactions and promoting the tip growth, thus leading to long INTs, as shown in Figure 2-16b [6].

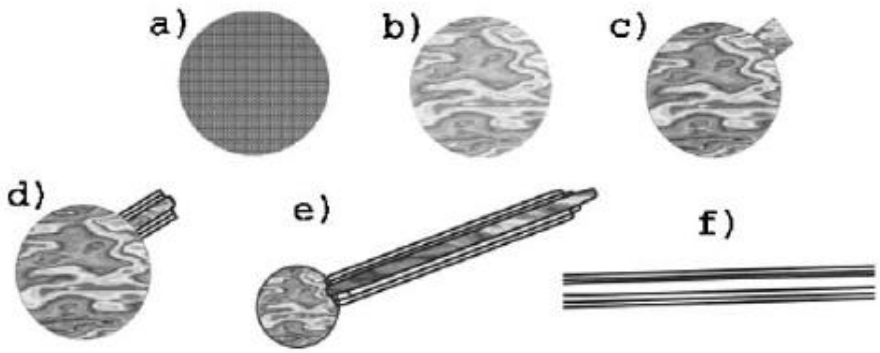

Figure 2-17 Schematic drawing of a growth mechanism for INT-WS_2, (a) The starting oxide nanoparticle precursor; (b) the reduced particle with a volatile oxide phase enveloped; (c) the break-through of the volatile phase through the encapsulating surface; d) the formation of the root of a nanotube on the top surface of the particle; (e) further growth of the nanotube: the volatile oxide that is emitted from the nanotube's hollow core. Reacting with H_2S, WS_2 is formed at the tip of the tube ; and (f) the final INT (adapted from Ref. [53]).

A more visual scheme is shown in Figure 2-17 to illustrate the growth of INT-WS_2 [53]. In this mechanism, the authors believed that the oxide powder (Figure 2-17a) would firstly be reduced with a volatile oxide phase surrounded. A root for nanotube growth started to form from the oxide protrusion, at the same time, the reduced oxide vapour (Figure 2-17b) reacts with the H_2S gas, and WS_2 would be formed at the tip of the

nanotube. Thus the continuous nanotube tip growth would be accomplished by the emission of the reduced oxide–hydrate vapour from the core of the nanotube and its rapid sulphidisation into WS_2 at the tip [53], although there is no solid evidence for the emission of the oxide-hydrate through the core.

2.1.5 Scale up of the manufacturing of WS_2 nanostructures

The scale up of the synthesis of IFs and INTs has been hindered by the powder agglomeration which causes reaction to occur only on surfaces in a static gas-solid reaction setup used by many.

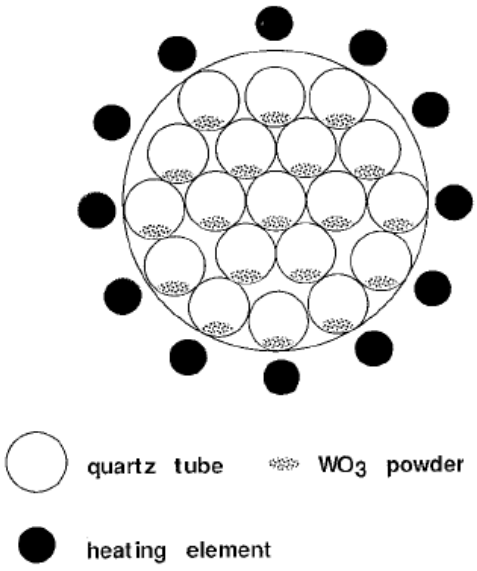

Figure 2-18 Cross section of a modified multiple reactor used for the synthesis of IF-WS_2 (adapted from Ref. [18])

The first gas-solid reaction (GSR) reactor for the synthesis of relatively large quantities of IF-WS_2 was built in 1996 based on the principles of the above reaction mechanism [18]. This reactor, shown in Figure 2-18, consists of a bundle of small tube reactors with a diameter of 7 mm inside a large working tube of 40 mm in diameter. The precursor oxide powder was placed very loosely in these small tubes, to separate the precursor and increase the gas-solid reactive surface. After standard gas-solid reaction with H_2/N_2 +H_2S at around 850°C, 1 g of IF-WS_2 could be produced from each single batch (3 h) [18], which represented the best result at that time.

After years of study, the same Israeli group developed the falling bed reactor and fluidised bed reactor, as illustrated in Figure 2-19, which have significant advantages over the previous static process [17, 107]. In this design, the top of the reactor is the

vibro-electromagnet set-up with the aid of N_2 for co-feeding the WO_3 powder into the reactor. It is formed by two glass beakers with a mesh at the bottom, which makes it a semi-continuous process, as shown in Figure 2-20a [17, 107].

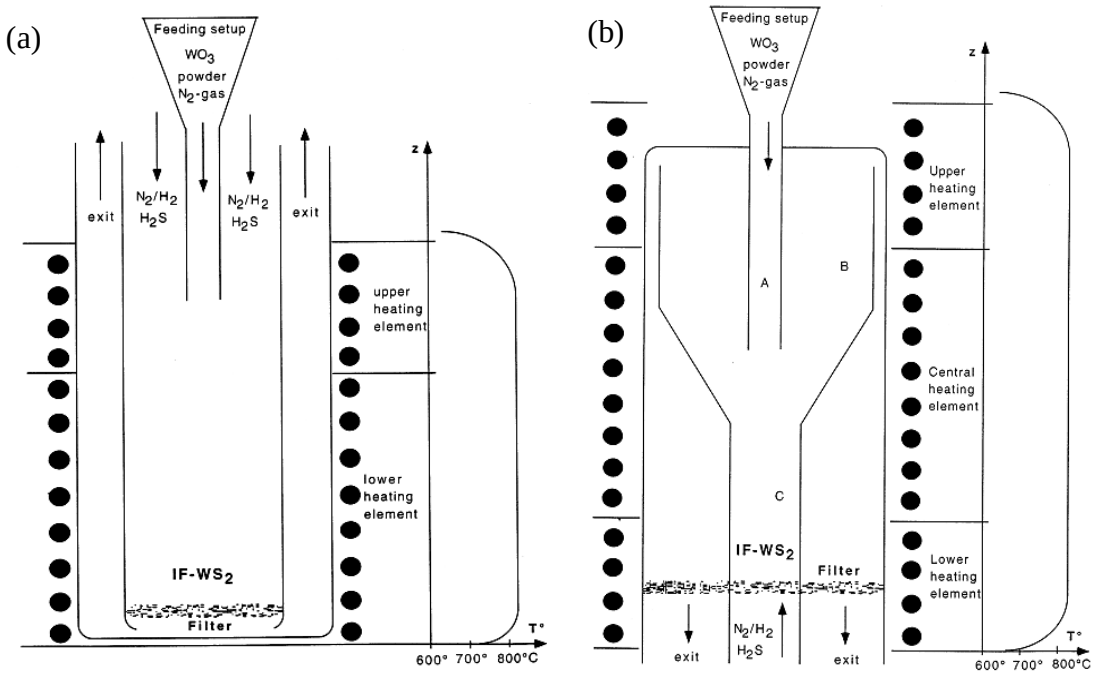

Figure 2-19 A schematic drawing of the falling bed reactor (left) and fluidised bed reactor (right); with the temperature profile along furnace (Z) axis presented respectively (adapted from Ref. [17, 107])

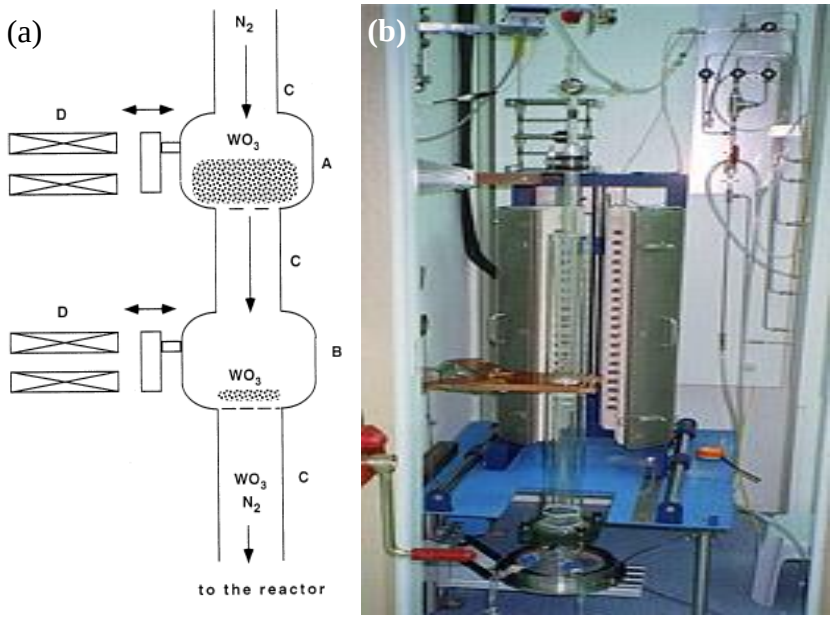

Figure 2-20 (a) A schematic drawing of two stage vibro-electromagnetic feeding set-up and (b) photo of the fluidised bed reactor used to produce IFs at ApNano's laboratories (adapted from Ref. [17, 108])

Another advantage of the design is that the reaction path extends along the falling path of the oxide powder, and the collector is located at the bottom of the reactor. The first closed atomic WS_2 would have formed on the top surface during the time lapse between the beginning of the forced fall of the WO_3 nanoparticles from the topmost of the reactor and land on the filter, which is essential for the successful synthesis of IF nanoparticles [53]. Compared with the falling bed reactor, in which the reacting gas inlet is placed at the top of the reactor, the agglomeration of the oxide particles could be better avoided in a fluidised bed reactor, in which the inlet of reacting gasses is located at the bottom of the reactor, these nanoparticles were blew by the mixed gas all the time. The temperatures of the reaction area are quite similar in both cases, remaining constant between 750°C to 850°C. Generally, the maximum production yield of the fluidised bed reactor is 50 g of IF-WS_2 per batch [90, 107].

However, as we can see from the above pictures (Figure 2-19 and Figure 2-20), the patented fluidised bed reactor is rather high and complicated, and demands huge energy to maintain the constant temperature for the whole high vertical reactor. Therefore, a simple and effective process remains a great challenge for further research.

From above discussion, the key technical barrier for the scale up of the IF-WS_2 nanostructures can be identified as the powder agglomeration and superficial reaction. To avoid the extended physical contact of the particles during the heating stage holds the key to avoid agglomeration-a forced physical movement; and a sufficiently long reaction time at proper temperatures would make sure the particles to be converted thoroughly.

Bearing this in mind, we intend to modify the common tube furnace into a rotary tube furnace, which have been widely used in industry for micron sized particulates reaction (Figure 2-21), some are designed especially for superior gas-solid contact. The advantages of this process are: the constant tumbling action of the product within the rotary tube would result in high degrees of temperature uniformity and improved gas-solid contact areas, resulting in more homogenous product at reduced processing times and increased production rates. Thus, this would be energetically efficient and technically reliable, and easy to scale up to a continuous process [109-111]. Therefore, the tumbling of WO_x inside the rotary tube would expect to minimise the agglomeration

and avoid superficial reaction in one go. If it is successful, this will extend the existing conventional rotary synthesis facilities into a new era of nanomaterials research.

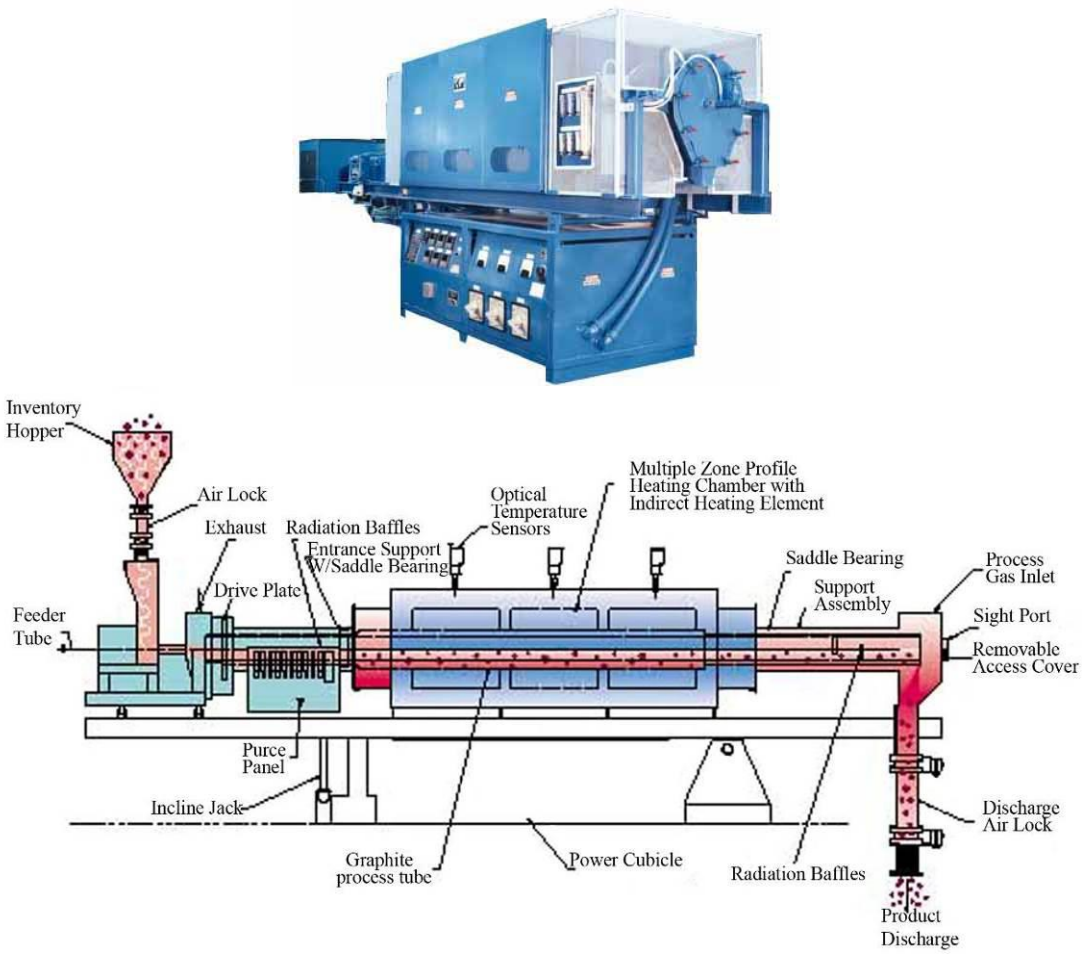

Figure 2-21 A rotary furnace used in industry (top image); a sketch of a whole industrial rotary process system (bottom image)

In short, the rotary furnace concept could be applied to the IFs and INTs regime by offering the two main characteristics of constant movements of the nanoparticles and controllable reaction time. Of course, many importantly scientific and technical challenges remain to be tackled in the course of the development towards a simple and effective rotary processing technique suitable for large scale manufacturing of WS_2 nanostructures. These challenges therefore become the main tasks of this PhD programme.

2.2 Nanocomposites based on polymer impregnated with WS_2 nanostructures

Introduction

Following the discussion in Section **2.1.2**, these excellent properties of IF-WS_2 suggest that when they are combined with other matrices, they could form bulk ceramic, metal and polymer matrix composites, or form various composite coatings, with outstanding tribological performance and ultra-high strength and high impact resistance for shock absorbing.

Due to the relatively easier preparation process, IF-WS_2 has indeed been widely introduced into a wide range of different polymer matrices and the resulting composites have showed significant improvements in their properties. This part of the review introduces the preparation and characterisation of polymer nanocomposites based on IF-WS_2 as reinforcement, the performance will also be summarised.

2.2.1 The dispersion of nanomaterials

The main challenge in nanocomposites preparation is to obtain a good dispersion of IFs in a matrix and a strong bonding between them. Example procedures to achieve good dispersion of nanoparticles in a matrix include: (1) surface treatments before casting [112, 113]; (2) sonication of nanoparticles with polymer in solution, followed by casting [114]; and (3) melt mixing with [115] or without [116, 117] surface pre-treatments.

Regarding the dispersion of transition metal dichalcogenides, initial research was focused on functionalization of nanostructures [118, 119]. For example, organosilane coating have been applied on surface of IF-WS_2 nanostructures to reduce agglomeration, thus improved the stability of the IF-WS_2 solid lubricant oil suspensions [118]. In another study, the solubility of IF-MoS_2 nanoparticles in water have been improved by functionalise the surface with polymeric chelating ligands [119].

Some novel work towards dispersion and further exfoliation of different transition metal dichalcogenides, without any surface pre-treatment, has been done by Coleman et al. [120, 121], based on the Hildebrand solubility parameter (HSP) theory, which is used to predict the dispersion efficiency of materials in either single or mixed solvent [122]. Around 25-30 solvents were tested for each material and the successful solvents were

found for each material, the Hansen parameters of successful solvents for each materials were found to be within a well-defined ranges as given [120]. This is very useful to find new solvents or develop successful solvent blends for these materials.

Another interesting work has been done by Zhou *et al* [123], to demonstrate how ethanol and water mixture could be designed to give high solubility to different inorganic graphene analogues (MoS_2, WS_2 and BN), with different volume fraction of ethanol in water. The best dispersion of MoS_2, WS_2 and BN are obtained at 45, 35 and 55 vol% ethanol/water respectively. This opens up numerous possibilities to combine two 'poor' solvent into a 'good' solvent mixture for specified materials.

In short, the dispersion of nanomaterials could be controlled and evaluated, but the selection of solvent in each case should be considered according to the process applied.

In the case of polymer reinforced with WS_2 nanomaterials, the dispersion of nanostructures in polymer matrix become critical during the preparation. So far, in order to combine the flexibility of polymer with special properties of IFs such as high modulus, high impact resistance and low friction etc., different thermoset and thermoplastic polymers were studied as the matrices for nanocomposite fabrication [45, 69, 124-135].

Various techniques were applied to incorporate IF and INT-WS_2 nanostructures into various polymer matrices, normally without modifier or surfactant, such as mixed into epoxy resin by stirring [124], high shear mixing [125], or a combination of both magnetic stirring and ultrasonic mixing [126]; melting mixing has been a popular technique to mix IF-WS_2 and INT-WS_2 into numerous polymer matrices, such as iPP [69, 127], Polyphenylene sulphide (PPS) [128, 129], Polyetheretherketone (PEEK) [130, 131] and nylon 6 [132, 133]. Aerosol-assisted deposition process has also been employed to introduce IF-WS_2 nanoparticles into PEEK for self-lubricating composite coating in another study [45].

Electron spinning, as a popular method to prepare 1D polymer or composites fibers [136], has been applied to mix INT-WS_2 into a PMMA nanofiber matrix [135]. Sometimes, WS_2 nanostructures were functionalised first before adding to some specific polymer matrices. For example, functionalised INT-WS_2 have been added to an immiscibly blended PS/PMMA system [134]. The functionalization was done by

coating INT with octadecyl phosphonic acid (OPA) by ultrasonic irradiation of nanotubes in OPA, with a WS_2–acid ratio of 10:1 (by weight) in 50 ml toluene. The functionalised INTs helped to achieve a good dispersion of the INTs in the blend matrix, and the phase-separated domain size and surface roughness of the nanocomposite films were reduced relative to the pure homo polymer blend.

2.2.2 Properties of polymer matrix embedded with IF/INT-WS_2

By incorporation of WS_2 nanostructures, the properties of polymer nanocomposites, such as tribological, mechanical and thermal properties have been remarkably improved.

Enhanced tribological properties have been achieved for WS_2 nanostructures reinforced polymer composites [45, 124, 126]. For example, with the addition of 10 wt% IF-WS_2 into epoxy resin by stirring, the composites exhibit only a third of the average friction coefficient, and half of the maximum friction force in comparison to the reference pure epoxy resin sample (0.02 vs 0.06 and 2 N vs 4.4 N, respectively) [124].

In a recent study, INTs-WS_2 were mixed into Epon 828/Versamide140 epoxy resin by a combination of both magnetic stirring and ultrasonic mixing [126], and 53% and 88% huge reduction of wear for 1 wt% IF and 0.5 wt% INT composites were achieved, as shown in Figure 2-22. From 1.8 down to 0.22, the wear rate of INTs-WS_2 reinforced epoxy nanocomposites is 8 times better than that of the neat epoxy.

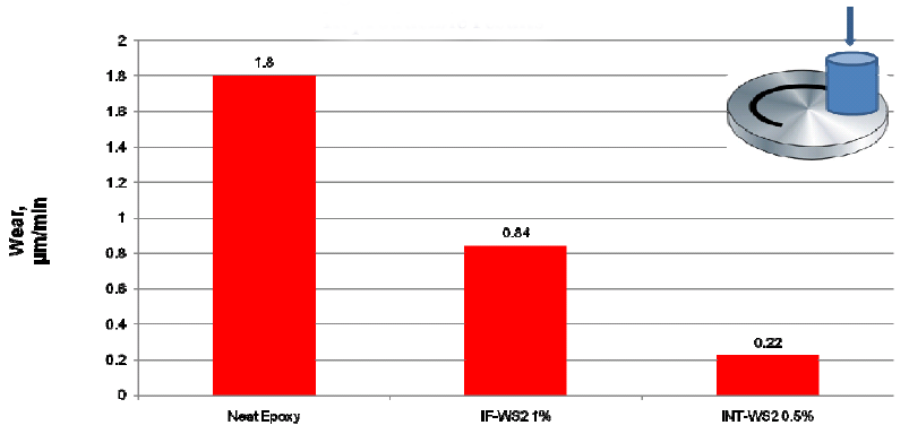

Figure 2-22 Histogram summarizing the wear measurements of Epon 828/Versamide140 epoxy compounded with INT-WS_2 and IF-WS_2 [126]

Up to 70% reduction of friction coefficient was also achieved by the addition of 2.5 wt% IF-WS_2 to PEEK, whilst no further reduction was observed with higher IFs

contents above 5 wt%. This reduction also led to a remarkable improvement in the wear resistance [45].

Significant improvement in mechanical properties of polymer/WS_2 has also been demonstrated in numerous researches. With very low concentration of WS_2 (0 wt%, 0.3 wt%, 0.5 wt% and 0.6 wt%) added in epoxy resin, there is a remarkable simultaneous increase of both the shear and peel strength, with >100% increase at 0.5 wt% (Figure 2-23), which has potential applications as high performance additive in structure and ballistic fibre composites [125].

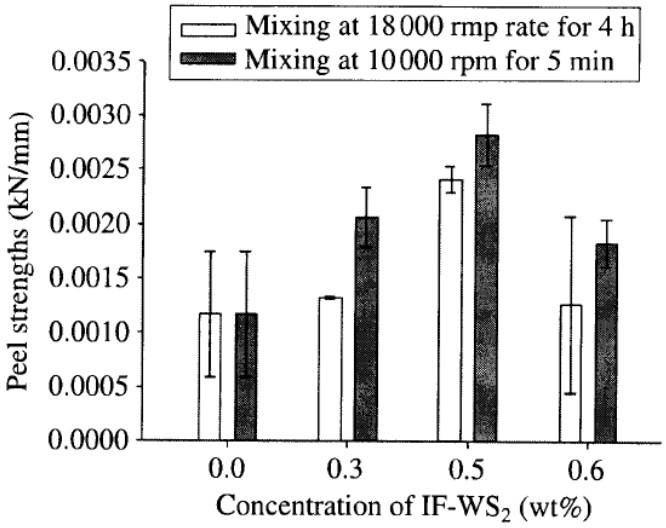

Figure 2-23 Peel strengths of epoxy resin reinforced with IF-WS_2 [125]

It is worthy to note that, about 10 and 22 times increases in elastic modulus with 1 and 2 wt% INTs have been exhibited in the INT-WS_2/PMMA composites fiber, against the pure PMMA. Meanwhile, the tensile strength and toughness of composite fiber have also been increased by 35% and 30%, respectively, in addition to a 61% improvement in the dielectric constant.

Dynamic Mechanical Analysis (DMA) were carried out for many IF-WS_2 reinforced polymer composites, and the results showed improvement in dynamic mechanical performance [128-130, 133]. At a 20 wt% IF concentration, the hardness and modulus of the PEEK/IF-WS_2 coating were increased by as much as 60%; 31% storage modulus and 17°C of Tg increases were observed for 2 wt% and 1 wt% composites, respectively [130]. IF-WS_2 reinforced iPP nanocomposites showed an increase in the storage modulus of the nanocomposites with the filler content of 0.1, 1, 2, 4 and 8 wt% by the nucleation effect of the IFs. For PPS nanocomposites embedded with IF-WS_2 [128, 129],

an increase in the storage modulus was observed. High concentration of IFs had led to an improvement of 40-75% in the dynamic mechanical performance of PPS composites.

Thermal stability for WS_2 reinforced polymer composites has also been improved [69, 127, 131, 135]. For example, for PEEK impregnated with IF-WS_2 self-lubricating composite coating, the temperature of maximum decomposition rate improved by 20-30°C with 1 wt% IF addition and the initial and final degradation temperatures increased by 55- 60°C for 2 wt% IFs [131]. The electro spun INT-WS_2 reinforced PMMA composites fiber exhibited a 23°C thermal stability improvement compared to pure PMMA fiber [135].

These remarkable improvements of thermal, mechanical properties should be attributed to well-dispersed nanoparticles within the polymer matrix, due to strong adhesion or interfacial interaction between nanoparticles and the matrix [125], nucleation efficiency of added nanostructures, and promoted crystallization with addition of nanostructures [69, 127-129].

For example, in IF-WS_2 toughened epoxy resin nanocomposites, the strong surface adhesion between IF-WS_2 nanoparticles and epoxy resin was observed under TEM, with the interfacial layer around 20-40 nm, while chemical interaction between IF-WS_2 and epoxy was evidenced by detection of R-SO_3 or R-SO_3H band at 1249 cm^{-1} in a FTIR spectrum, by preparing 20 wt% WS_2 in epoxy, indicating the formation of a C-O-S bond [125].

In nylon 6/IF-WS_2 nanocomposites, the presence of IFs caused a strong nucleation effect for nylon-6. The high nucleation efficiency of IF-WS_2 on nylon-6 resulted in lower fold surface free energy (σ_θ) of nylon-6 chains with increased IF-WS_2 contents [132]. Addition of IF-WS_2 has also improved the crystallization behaviour of the iPP matrix [69, 127], while increasing IF content in PPS matrix had resulted in a dramatic change from retardation to promotion of the crystallization [128, 129], whereas this promotion has increased the glass transition temperature and the dynamic mechanical properties.

In summary, the impregnation of IF-WS_2 and INTs into polymer matrices have led to improved performance in mechanical properties including toughness, strain and Young's modulus, while other properties such as thermal properties and tribological

properties are also improved to some extent. These results have showed that IFs and INTs are ideal candidates for reinforcing various thermoset and thermoplastic polymers, for wide applications in automotive, aerospace and personal safety and defence industries. The exploration of the resulting IFs in relevant areas is thus becomes another objective of this PhD programme.

2.3 Summary

In this chapter, the synthesis, crystal structures, properties and potential applications of the MS_2 IFs and INTs, and the preparation and properties of polymer nanocomposites reinforced by these IFs and INTs, were reviewed. The excellent performance and application prospects require the supply of these IFs and INTs in large quantity, for which a simple and yet effective process remains highly desirable for these nanomaterials.

Based on the research background, the research in this PhD programme is aimed to scale up the synthesis of these IFs, improve the thermal stability, and explore further application of IFs in polymer nanocomposites. The objectives of this PhD thesis are summarised below:

- Design and modify a novel rotary reactor suitable for continuous scaling up synthesis of IF-WS_2
- Synthesis of precursor of WS_2, tungsten oxide nanostructures, in different forms, such as nanoparticles, nanowires, as well as patterned growth of tungsten oxide and tungsten oxynitride nanorods from W foil
- Prepare tungsten oxide nanowires with higher surface area, for improved properties for gas sensor and electro-chromic applications
- Optimise parameters for large scale manufacturing of IF-WS_2 based on designed rotary process
- Realise continuous rotary process by further modification
- Create new C/WS_2 nanocomposite fullerene particles, to achieve improved thermal stability of IFs by applying a carbon coating
- Incorporation of IF-WS_2 into nylon 12 matrix to achieve improved properties

Chapter 3 Experimental methodology

3.1 Introduction

This chapter introduces the materials and methods applied to synthesise several types of tungsten related nanomaterials and techniques used for the preparation of WS_2 reinforced nylon 12 nanocomposites.

The synthesis of tungsten related nanomaterials has been described first, including the preparation of precursors for WS_2 nanomaterials, such as production of WO_x nanoparticles by decomposition of APT, synthesis of WO_x—nanowires through solvothermal, growth of WO_x nanorods and WO_xN_y nanorod by a Chemical Vapour Deposition (CVD) method. The synthesis of IF-WS_2 based on the designed rotary reactor through a gas-solid reaction were introduced, as well as applying a carbon coating on the surface of IF-WS_2 nanoparticles to the improvement of thermal stability. The preparation procedure of IF-WS_2/nylon 12 nanocomposites was also demonstrated subsequently.

In addition, a generic description of the complementary techniques used to appraise the chemical, structural and morphological features of the resulting nanomaterials and nanocomposites samples, as well as the mechanical measurement processes for the nanocomposites, will be provided.

3.2 Preparation procedure

3.2.1 Materials

Ar (zero grade, 270050-L), NH_3 (99.98%), H_2 (Research grade N5.5, 290629-L) and H_2S (Tech grade N2.5, 100%, 289377-F) gases were purchased from BOC.

Tungsten chloride (WCl_6, >99.9%) and Cyclohexanol (ReagentPlus, 99%) for solovthermal synthesis of WO_x nanowires were bought from Sigma Aldrich UK.

Tungsten trioxide powder used as precursor for IF-WS_2 nanomaterials was purchased from Changsha Nanina Advanced Materials Co. Ltd (China) and commercialised as

nano monoclinic WO_3 powder (light yellow powder, with size from 20-100 nm, purity 99%).

PS-b-P4VP was purchased from Polymer Source, Inc. The molecular weight for PS and P4VP was M_w 41300 and 1900 g/mol, respectively, with a polydispersity index of Mw/Mn =1.07. $HAuCl_4$ was purchased from Aldrich.

W foils with thickness of 0.05 mm (267538-9.6 g) used for WO_x nanorod growth was purchased from Sigma-Aldrich.

Zinc pieces (Zn, 2-14 mesh, 99.9%) used to in wash bottle to absorb residue H_2S gas were bought from Sigma-Aldrich.

Ammonium paratungstate (APT, $(NH_4)_{10}H_2(W_2O_7)_6 \cdot xH_2O$, 99.99%) particles used to produce WO_x nanoparticles were bought from Sigma-Aldrich.

Sulfur powder (S, sublimed, 100 mesh, 99.5%) were bought from Cole Parmer.

Nylon 12 ($[--NH-CH_2-(CH_2)_9-CH_2=O--]_n$) powders were kindly provided by X-at group (PA2200 Polyamide powder, EOS, Germany), is also named polyamide 12 (PA12) in this context.

Styrene (S4972, molecular weight 104.15) was bought from Sigma Aldrich (UK).

Acetone (laboratory regent grade), ethanol (laboratory regent grade) and hydrogen chloride (36 wt%) were bought from Fisher Scientific (UK).

3.2.2 Synthesis of tungsten based nanomaterials

3.2.2.1 WO_x nanoparticles produced by the decomposition of APT

A tube furnace with temperature up to 1600°C is used for this experiment (Figure 3-1). APT particles were firstly located in the hot zone of the quartz tube, and a collector was placed in the downstream 40 cm away from the APT source. Ar gas was flushed through the quartz tube at a rate of 50 ml/min for 30 min to remove air inside, before the furnace was switched on, the Ar flow was kept until the target temperature was reached. This procedure was repeated for all the experiments involving reaction in a tube furnace, to make sure there is no air in the working tube when reaction starts. In this experiment, Ar gas flushed at a flow rate of 50 ml/min before the target temperature was reached

(1350 to 1400°C), and then increased the flow rate to 2-6 L/min for about 30-45 min during reaction. Finally, the furnace was turned off and cooled down to room temperature with the flushing Ar back to a flow rate of 50 ml/min. The particles were collected separately from different areas.

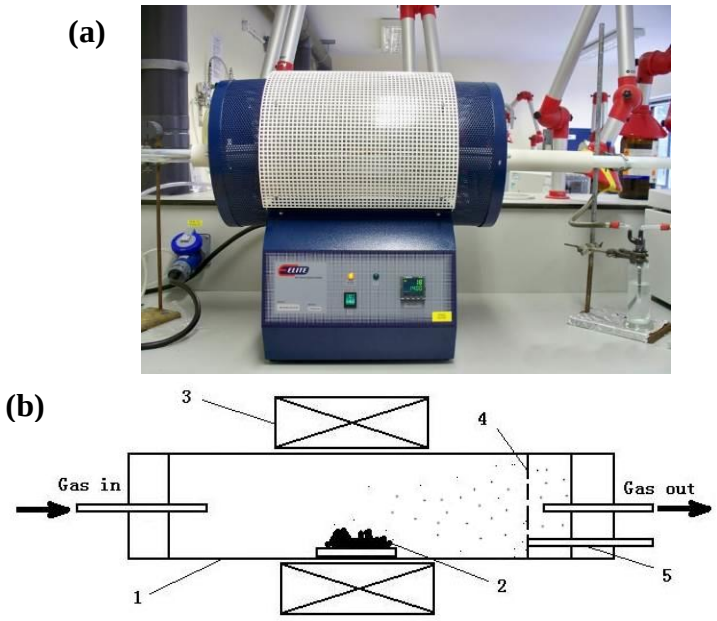

Figure 3-1 Experimental set up, (a) photos of furnace employed, (b) Sketch of the experimental set up: 1- Quartz tube; 2- APT source; 3- Furnace; 4- collector; 5- thermal couple

3.2.2.2 Solvothermal synthesis of WO_x nanowires

The experimental set ups are shown in Figure 3-2. Basically, 40-80 mg of WCl_6 were slowly dissolved in 50 ml of solvent to obtain uniform solution. The solution was then transferred to a 125 ml Teflon-lined stainless-steel pressure vessel for reaction at 200°C for several hours (2-6.5 h) in a cubic furnace. After reaction, the precipitate was centrifuged and washed with deionized water and acetone several times respectively. Samples then dried and prepared for SEM observation, XRD detection, TEM characterisation and BET measurement.

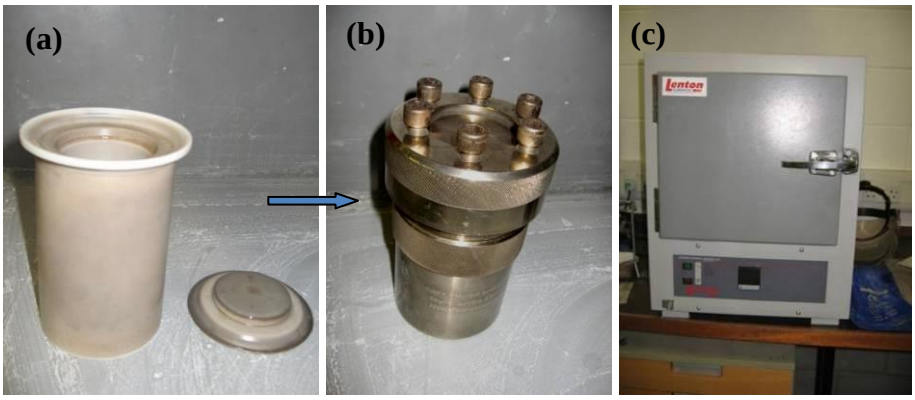

Figure 3-2 Teflon-line stainless-steel pressure vessel (a and b) and cubic furnace (c)

3.2.2.3 Patterned growth of WO_x and WO_xN_y nanorods

10 ×10 mm square W foils were subjected to two different surface treatments in order to create desired surface patterns: Au coating and blade engraving.

For the creation of Au coating, there are several steps involved as following [137]: at first, spherical micelles with a P4VP core and a PS corona would be formed by dissolving 5 mg of PS-b-P4VP in 1 mL of toluene, and $HAuCl_4$ was then added in stoichiometric amounts with respect to the P4VP block. Stoichiometric amounts of LiBH4 solution in THF were subsequently added to reduce the precursor. Hence, NPs with diameter of ca. 2.5 nm were formed within the micelle core (P4VP) and stabilized by the surrounding PS shell. At last, a non-selective solvent (THF) was added to the solution (ratio THF/toluene=1:2) prior to deposition. The solution was finally spin-cast on pre-polished W foil substrates at 3000 rpm for 120 s. Plasma etching was then applied to remove the copolymer (polystyrene-b-polyvinyl pyridine, PS-b-P4VP), leaving only Au patterns on the surface of W foil [137].

A letter "T" was engraved on the tungsten foil by a blade. Besides these two types of pattern pre-treatment, a third type of W foil is treated with acid (immersed into 1M HCl for 1 min), to study the influence of W substrate. The W foil was then placed in the centre of a quartz tube located in a horizontal tube furnace. After flushing with high purity Ar for 30 min, the furnace was raised to target temperature (600-750°C), and high purity Ar was then bubbled through a wash bottle at a flow rate of 50 ml/min. The reaction lasted for 5-40 min, for the creation of the WO_x nanorod templates. The experimental set up is shown in Figure 3-3.

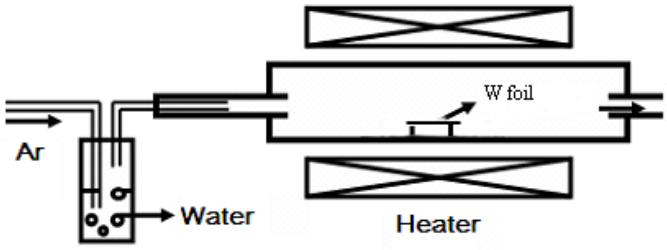

Figure 3-3 Chemical vapor deposition (CVD) setup for synthesis of 1D nanostructures

Further raising the temperature to 650°C and replacing the Ar with NH_3 at a flow rate of 100 ml/min, without bubbling through wash bottle, we carried out the oxide-nitride conversion for 6-12 h, for the WO_xN_y nanorod growth from WO_x template.

The resulting nanorods on W foils were appraised by XRD, SEM, Raman, AFM and TEM respectively.

3.2.2.4 Gas-solid reaction for WS_2 nanomaterials

As discussed in literature review part **2.1.3**, oxide-to-sulfide gas-solid reaction has been proven to be the most suitable approach for synthesis of WS_2 nanomaterials starting from oxide precursor. However, an efficient and yet simple process for scale up synthesis of IF-WS_2 remains a challenge.

Accordingly, in this work, a novel rotary reactor has been designed for scaling up manufacturing of IF-WS_2 nanomaterials. The rotary reactor was designed based on a conventional tube furnace with length of 1 m and temperature up to 1200°C, which ensures a long enough heated zone for a complete reaction and required temperature.

The synthesis of WS_2 nanomaterials were carried out in the designed rotary furnace (Figure 3-4). WO_3 precursor from (6 g to 30 g) was put into the quartz tube (40 mm OD, 36 mm ID, 2000 mm length), the furnace was turned on after purging the air out of quartz tube by high purity Ar for 30 min, and then the H_2S and/or H_2 gas was introduced upon temperature reached 550°C, the motor was started to rotate the working quartz tube simultaneously, before target temperature reached (800-900°C). The following chemical reaction would take place in the working quartz tube: $WO_3 + H_2S \rightarrow WS_2 + H_2O$ and the reaction would be kept at target temperature for a required time depending on the precursor amounts. The furnace were then switched off and cooled down to room temperature with flushing Ar.

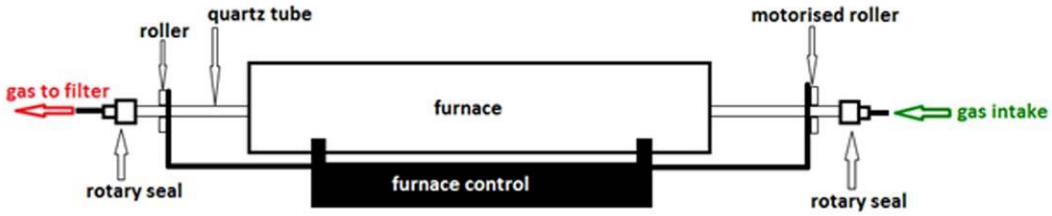

Figure 3-4 Sketch of the modified furnace, in a traditional furnace, the WO_x particles stay still in the quartz tube at high temperature (800-900°C), which leads to 2H-WS_2 dominating in the final products, whilst in the modified furnace, the quartz tube together with WO_3 nanoparticles and WS_2 formed, are rotating and moving in the whole process, which leads to forced movement, resulting in better separated IF- WS_2 products at minimal agglomeration

The parameters for this experiment were optimized through a series of experiments, such as different reaction temperatures, reaction time, reaction gas atmosphere, modification of working tube as well as a new feeding system.

With the new feeding system fitted, 50-100 g WO_3 nanoparticle precursor was fed directly into the hot zone gradually using a syringe after the temperature reached 650°C, rather than being pre-placed at the inlet end of quartz tube. Other parameters remain similar to those used in previous investigations without feeding system.

The products were collected from different area separately. The morphology and chemical composition of produced IF-WS_2 nanoparticles were analysed by XRD, SEM and TEM.

3.2.2.5 Other method for synthesis of IF-WS_2 nanoparticles

Synthesis of IF-WS_2 nanoparticles from mixed WO_3 and S powder with H_2

WO_3 and S powder were first weighted at a mole ratio of 1:10, and mixed by dissolving them in ethanol and dispersing ultrasonically for 30 min, the composite powder was then ready for use after drying. Around 6 g composite powder was placed into the quartz tube in the inlet area, and Ar gas was used to purge the air inside quartz tube at 50 ml/min for 30 min, after the system was properly assembled and sealed. The furnace was started with Ar flow continued. Set the motor in motion to drive the working tube upon the temperature was raised to 600°C, introduce of the H_2 (80 ml/min) and Ar (30 ml/min) gas was then started. During this period, the inclination angle was set to ensure the powder in the working tube was delivered into the hot zone when temperature

reached 800°C. The reaction at 800°C was lasted for 1 h, then the H_2 was switched off, and the reaction was kept at 800°C for another one hour before the furnace was turned off. Ar was continued to flow at a rate of 50 ml/min to cool the furnace down.

Synthesis of IF-WS_2 nanoparticles from APT with H_2S gas

During this experiment, 6 g APT particles were placed into the centre of the quartz tube, Ar flow at rate of 50 ml/min were flushed for 30 min before furnace switched on, H_2S flow rate of 12 ml/min start from 550°C. The whole reaction lasted for 2 h at 800°C, at a fixed Ar flow rate of 50 ml/min throughout the whole process. After the reaction, the products were collected from different area and characterised with both SEM and XRD. Two types of SEM sample were prepared: the as-produced particles directly on carbon film stickers and ultrasonicated deposited on a Si wafer.

3.2.2.6 Carbon coated IF-WS_2 nanoparticles

At the beginning of the experiment, IF-WS_2 nanoparticles were produced using the rotary furnace by reaction of WO_3 precursor and H_2S gas as described above. Upon the completion of oxide to sulphur reaction, turn off the H_2S gas and set the furnace to desired temperature (700-800°C), start to inject carbon source (20 vol% styrene with 80 vol% acetone) at the rate of 1.2-2.4 ml/h for 10-30 min, the carbon source was brought into the hot zone by 100 ml/min Ar carrier gas. The morphology, chemical composition and thermal stability of carbon coated IF-WS_2 nanoparticles were appraised by TEM, Raman and TGA-DSC respectively.

3.2.3 Preparation of IF-WS_2 reinforced nylon 12 nanocomposites

IF-WS_2 nanoparticles were synthesised by the gas-solid reaction starting with WO_3 nanoparticles precursor and H_2S reaction gas, as described in Section **3.2.2.4.** The as-produced WS_2 were first dispersed in ethanol solvent using ultrasonic probe (UP200S ultrasonic processor from Hielscher ultrasound technology) for 100 min to obtain a well-dispersed WS_2 ethanol suspension, then mixed with nylon 12 powders by intensive stirring by stir bars at 90°C in a water bath until all ethanol vaporized. The composite powders were then dried in the oven at 120°C for 12 h.

To prepare mechanical samples, an Al mould was designed and manufactured, as shown in Figure 3-5. Four samples could be prepared each time using this mould, with 2 dog-bone tensile samples and two rectangular flexural samples. The dried composite

powders were filled and pressed into this produced mould and then placed in an oven at 220°C for 2 h. Subsequently the bulk composites samples for tensile and bending mechanical test were produced.

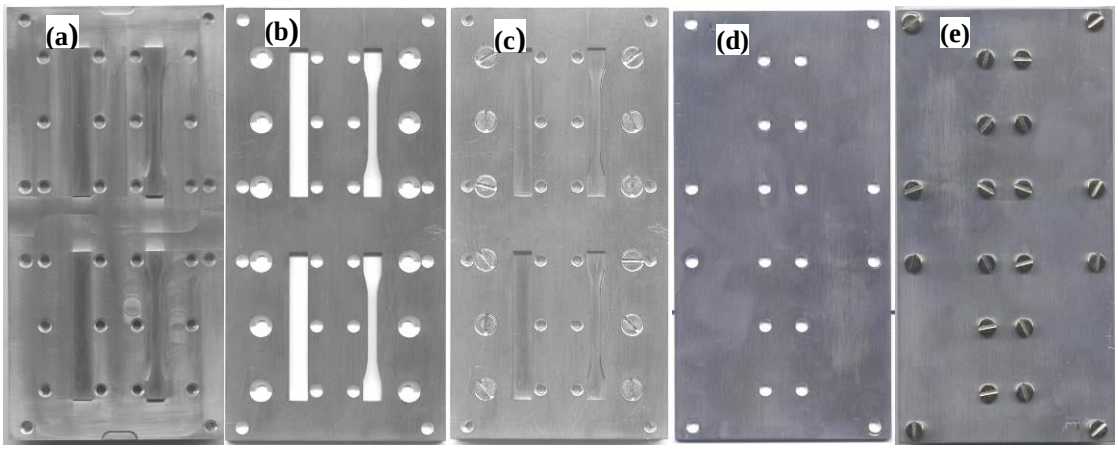

Figure 3-5 Al mould for mechanical testing samples (a, bottom plate with 2 dog-bone shape for tensile and 2 rectangular for bending protruding; b, middle plate with 2 hollow dog-bone and 2 rectangular shape; c, assembled bottom and middle plate, with 2 dog-bone and 2 rectangular hole, which the polymer would be poured into; d, top plate to press the sample and seal the mould; e, fully assembled mould)

The concentrations of IF-WS_2 in nanocomposites were ranged from 0 wt%, 0.1 wt%, 0.25 wt%, 0.5 wt%, 2 wt% to 4 wt%. The composite powder and bulk composites were characterised by XRD, SEM, TEM, Raman, Micro-CT and FTIR. The tensile and bending mechanical properties of bulk composites were also tested.

3.3 Materials characterisation techniques

To fully appraise the nanostructures, understand the growth mechanism and investigate the relation between the functionality and structural characteristics, a combination of complementary chemical, structural and surface characterisation techniques have been used to examine the produced nanomaterials and related nanocomposites. In this work, structural characterisation involves transmission electron microscopy (TEM), powder X-Ray diffraction (XRD), Grazing Incidence X-Ray diffraction (GIXRD) and Raman spectroscopy, morphological characterisation uses scanning electron microscopy (SEM) and X-ray microtomography (Micro-CT), surface characterisation employs atomic force microscopy (AFM). Energy dispersive X-ray analysis (EDX) was used to do elemental analysis. Brunauer-Emmett-Teller (BET) gas-sorption measurements were used to study

the surface area. TGA-DSC, tensile and bending test were employed to study the thermal and mechanical properties respectively.

3.3.1 X-Ray Diffraction

XRD technique is normally used to characterise the crystallographic structure, crystallite size (grain size) of bulk or powder sample. X-ray diffraction occurs only when Bragg's law is satisfied condition for constructive interference from planes with spacing d.

$$n\lambda = 2d\sin\theta \qquad \text{Equation 3-1}$$

where λ is the wavelength of the x-rays, d is the inter-lattice spacing, θ is the incident angle and n is an integer [138]. Samples were examined by plotting the angular positions (2θ) and the intensities of the resultant diffracted peaks of radiation, resulting in diffraction patterns characteristic to individual or mixed phases. Information content from diffraction patterns is available from peak position, intensity and profile.

Particle size of the nanostructure could be calculated by measuring the peak breath (Full Width at Half Maximum, FWHM) and applying the Debye-Scherrer formula:

$$\tau_{hkl} = \frac{K\lambda}{\beta_{hkl}\cos\theta_{hkl}} \qquad \text{Equation 3-2}$$

Where K is a constant or normally called shape factor (0.89<K<1), λ is the wavelength of X ray, β is the peak width at half maximum intensity in radians, θ is the peak position and τ is the crystallite size. With increasing of particles size, β will decrease. But the β needs to be corrected as it also increases by instrumental broadening. By subtract the measured β of the sample with the value of a standard reference sample, which is assumed to comprise infinitely thick particles, the instrumental broadening could be corrected.

In this thesis, finely milled powder sample were normally flatly pressed onto a glass slide while pre-polished bulk flat sample such as IF-WS_2/nylon 12 composites could be used directly for XRD analysis. For those WO_x nanoparticles and nanowires, where there is not enough sample available, the nanomaterials were normally dispersed into acetone first and then several drops of nanomaterials suspension were pipetted onto a Si wafer substrate, the Si wafer covered with nanomaterials layer was dried before XRD

analysis. XRD investigations were performed using a Siemens D500 and Bruker D8 Advanced x-ray diffractometer working at 40 kV and 20 mA and with a CuKα radiation source having a wavelength (λ) of 0.154 nm. Analysis data were collected at step intervals of 0.02 over a 2θ range of 5-80° with a dwell time of 2 seconds at room temperature.

In this context, average sizes of different WO_3 nanoparticles were calculated based on Debye-Scherrer formula and measured FWHM of some typical XRD peaks including 2θ angles at 26.7, 47.2 and 48.3. Al_2O_3 particles with size of 1 μm were used as standard reference sample.

For thin films and surface, GIXRD is an ideal structural probe, which combines the power of conventional XRD for determining bulk structure with refraction effects to probe the interface structure, normally use small incident angles from the incoming X-ray, the penetration depth of x-rays inside the slab is reduced by three orders of magnitude, compared to other diffraction scheme-- typically from 1-10 μm to 1-10 nm (10-100 Å). The resulting nanostructures on W foils (Section **3.2.2.3**) were appraised by Grazing Incident XRD on a Bruker D8 Advanced x-ray diffractometer, with a CuKα radiation, a step size of 0.05° and a scan rate of 10 s.

3.3.2 Scanning Electron Microscopy

Scanning Electron Microscopy (SEM) is a technique commonly employed to characterise the surface morphology with high magnification images, and elements composition in combination with Energy Dispersive X-ray spectroscopy (EDX).

Compared to optical microscopy, the SEM uses electrons instead of light to form an image. The electron beam is produced by heating of a metallic filament from the top of the microscope and follows a vertical path through electromagnetic lenses which focus and direct the beam down towards the sample.

Once the electron beam interacts with the sample surface, a range of photon and electron signals are emitted (Figure 3-6). Many of these signals can be used for imaging, *e.g.* secondary electrons and backscattered electrons in SEM or elastically scattered electrons in TEM; or chemical analysis, *e.g.* characteristic X-rays in EDX analysis.

Within SEM, Secondary Electrons and Backscattered Electrons were collected by detectors and converted into signal that sent to a cathode ray tube (CRT) image.

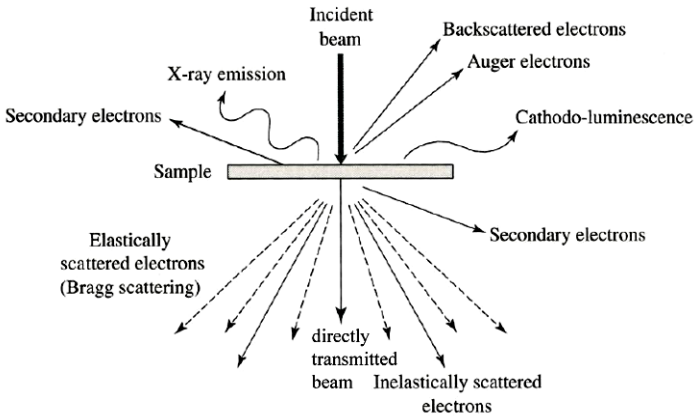

Figure 3-6 Electron beams/specimen interaction

The secondary electron images will provide the topography of the specimen surface as the secondary electrons are emitted from the very top layer (10 nm) of the specimen. The backscatter electrons are reflected from sample by elastic scattering and is very sensitive to the atomic number (Z) of the specimen, thus the distribution of different elements in the sample could be achieved by the backscattered electron images, providing distinguishable difference in atomic number. Further compositional information of the sample could be achieved while EDX is equipped within SEM, by collecting the X-Rays produced from the electrons/samples interactions (Figure 3-6), which will be described later.

In our work, powder samples including tungsten oxide and tungsten disulphide particles were prepared by either being dispersed in acetone and pipetted a few drops onto Si wafer and dried for observation by mounting the Si wafer onto sample holder by a conductive tape, or dispersed on the conductive tape (carbon) sticking to sample holder directly. Nylon 12/WS_2 composites powders were observed under BSE mode, to avoid any coating required in SE mode and get correct EDX information. The nanostructures on W foil samples were mounted on sample holder using conductive carbon tape. SEM characterisations were carried out using either a FEG-ESEM Philips/FEI XL30 or a JEOL JSM-6390LV SEM, operated at 20 kV.

3.3.3 Transmission Electron Microscopy

Transmission Electron Microscopy (TEM) enables detailed crystal structure, crystal quality, grain size and crystal orientation study for electron transparent specimens (<100 nm for inorganic specimen, could be a little bit thicker for polymer specimen), the resolution of TEM approaches atomic scale. Normally a TEM is composed of several basic components as shown in Figure 3-7.

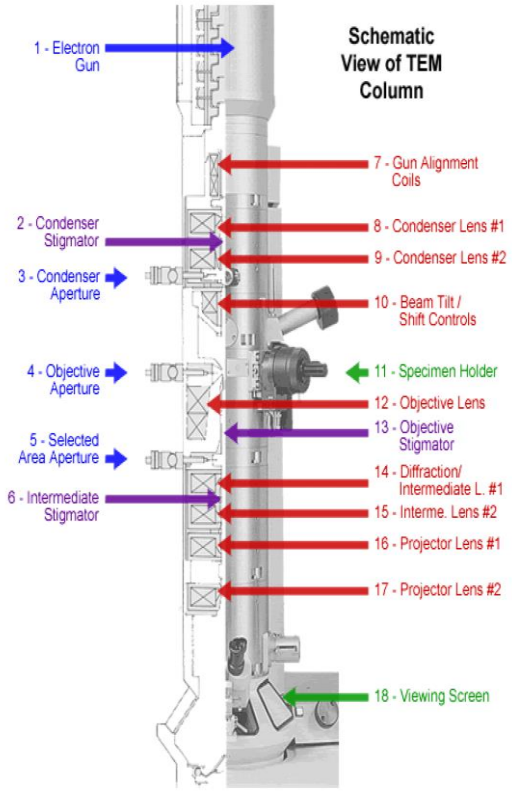

Figure 3-7 Schematic diagram of the basic components of a TEM

The electron beam normally generated by thermionic emission of tungsten or LaB_6 filament or by field emission of a single tungsten crystal, is accelerated through an electromagnetic field that also narrowly focuses the beam. The beam then will pass through the ultra-thin sample, producing transmitted electrons, elastically and inelastically scattered electrons (Figure 3-6). The specially prepared thin specimen with thickness <100 nm is inserted on a plane normal to the optic axis and located close to the focal plane of the objective lens. The objective aperture is located in the back focal plane of the objective lens, transmitted electrons with a large scattering angle will be blocked, enhancing the contrast of the projected image. The image is projected onto an electron sensitive florescent screen or a charged couple device (CCD) camera by the

projector lens. Images could either be recorded on photographic film or digitised to be stored on computer [139]. High-resolution transmission electron microscopy (HRTEM) allows the imaging of the crystallographic structure of a sample, can reveal lattice with atomic resolution. During TEM investigation, selected area electron diffraction (SAED) could be used to identify the crystal structural, measure lattice parameters and study crystal orientation of the sample as well as imaging based on diffraction contrast.

Most TEM and HRTEM characterisation in this thesis were performed on JEOL 2000-FX microscope and 2100-F TEM microscopes, with a LaB6 filament operated at 200 kV. The nanoparticles and nanorods are naturally thinner than 100 nm, which are ideal for TEM analysis. To prepare sample, a small amount of (about 1 mg) the nanomaterials powder was dispersed into 5 ml acetone and vibrated for 5 min by ultrasonic probe to obtain a uniform suspension. One or two drops of the suspension were dropped onto a 3mm diameter holely carbon coated Cu TEM grid (300 mesh, Agar). To prepare TEM sample for the nanorods grown from W foil, an ultrasonic probe treatment was applied for the W foil for 10 min in acetone, then pipetted 1 or 2 drops onto the holey carbon coated copper TEM grid. The acetone was thoroughly evaporated at room temperature before the sample was inserted into the TEM. The carbon coated WS_2 nanoparticles were examined by Jeol 1400 TEM at 120 kV for TEM images and by FEI Tecnai T20 G2 microscopy at 200 kV for HRTEM images.

The preparation of TEM sample for WS_2 reinforced nylon 12 nanocomposites includes several procedures as following: first, flat embedded small pieces of polymer composites into TAAB Low Viscosity Hard resin (TAAB Laboratories Equipment LTD) and polymerised at 60℃ for 22 h. Individual sample pieces were cut out of the resin and glued to a blank resin stub using Araldite Epoxy Resin and left to cure at room temperature for 24 h. Samples were then mounted in a Reichert-Jung Ultracut Microtome and trimmed with a single edge razor blade before final sectioning with a Diatome Diamond knife. Sections cut were in the order of 100 nm thick which were then floated onto Formvar coated 300 mesh copper grids and allowed to air dry. Samples were imaged with a Jeol 1400 TEM at 120 kV.

3.3.4 EDX

Energy dispersive X-ray analysis (EDX) is normally used for local elemental identification, equipped within an SEM and TEM. When the incident electron beams interacts with the specimen, intense bombardment of high energy electrons on the inner most electron shell of an atom will results in the escape of high energy electrons and an escape vacancy is generated. An electron from the outer orbit shell then jumps into the empty electron shell, emits energy in the form of an X-ray photon (Figure 3-6). The energy of the X-rays arises from the difference in energy between the two shells, and is characteristic to the atomic structure of the element from which they were emitted, therefore can be used to ascertain the elemental composition of the specimen [139]. The number and energy of the X-rays emitted from a specimen can be measured by an energy-dispersive spectrometer. The element-specific spectral lines are identified to give the elemental composition of the incident area.

In the present work, EDX analysis was performed using the energy dispersive system from Oxford Instruments, UK, for detailed compositional analysis combined with SEM (Philips XL 30) observation. This equipment is suitable for qualitative and quantitative chemical analysis of the samples down to the atomic number 5 (boron).

3.3.5 Raman spectroscopy

Raman spectroscopy is a spectroscopic technique to study vibrational, rotational, and other low-frequency modes in a system. Raman effect occurs when the laser light impinges upon a molecule and interacts with the electron cloud and the bonds of the molecule [140]. Both inelastic scattering and Raman scattering are excited during the interaction. Most photons are elastically scattered and thus possess same energy (frequency) and wavelength as the incident photons, while small fraction of light (approximately 1 in 107 photons) is scattered at optical frequencies different from, and usually lower than, the frequency of the incident photons [140]. The energy difference between the incident photon and the Raman scattered photon is equal to the energy of a vibration of the scattering molecule. A Raman spectrum is obtained by plotting intensity of scattered light versus energy difference. The vibration information is characteristic of specific chemical bonds in molecules, thus the molecule could be identified. Since it is a

scattering technique, Raman spectra can be collected from a very small volume (< 1 μm in diameter).

In this work, Raman spectra were acquired using a Renishaw RM1000 Raman microscope (RENISHAW, Wooton-Under-Edge, UK) equipped with a 1200-line/mm grating providing a spectral resolution of 1 cm^{-1}, a diode laser providing excitation at 532 nm/785 nm with up to 300 mW power, and a 40× microscope objective lens was used to focus light onto the substrate. For powder form sample, the powders were first flatly pressed onto a Si wafer substrate before placed under the microscopy while bulk form sample such as nanorods on W foil and bulk IF-WS_2/nylon 12 composites were placed under the microscopy directly. The system was calibrated using the Raman band of a silicon wafer at 520 cm^{-1}. Spectral data was acquired using Renishaw v.1.2 WiRE software.

3.3.6 Micro-CT

Microtomography, works the same as tomography, uses X-rays to create cross-sections of a 3D-object that later can be used to recreate a virtual model without destroying the original model, but is able to produce cross-sections image with the pixel sizes in the micrometer range. In this work, a Micro-CT scanner (Benchtop CT 160Xi, X-Tek) was utilized to analyze the porosity of prepared nanocomposites.

3.3.7 AFM

Atomic force microscopy is a popular technique for studying surface properties of materials, from micro scale down to nano scale. As two fundamental components, the probe is the point of interface between the AFM and the sample while the scanner controls the precise position of the probe in relation to the surface, both vertically and laterally. Tapping mode, contact mode, non-contact mode, and torsional resonance mode are four primary imaging mode of AFM. An AFM (Bruker Veeco di-innova) was used to reveal the morphology of Au coating on W foil substrate, operated in tapping mode.

3.3.8 Ultrasonic processing

Ultrasonic is an efficient technique for dispersing and de-agglomeration of powders into liquid, it is thus important for the separation of nanomaterials and preparation of

nanostructures reinforced nanocomposites. Ultrasonic probe used in this work is UP200S ultrasonic processor from Hielscher ultrasound technology, with S14 probe tip (Max. depth 90 mm, tip diameter 14 mm, Max. amplitude 125 μm). In the preparation of nanocomposites, the nanoparticles IF-WS_2 were first measured and mixed with ethanol, then dispersed using ultrasonic probe for desired time, to get uniform suspension of IF-WS_2 in ethanol before mixing with the nylon 12 powder. Ultrasonic probe were also applied to disperse nanostructures into acetone, to prepare nanostructure suspensions for TEM and SEM sample.

3.3.9 BET

The Brunauer-Emmett-Teller method (BET) is used to determine the total surface area of solid materials with complicated shapes, such as porous materials. In BET, adsorption and desorption isotherms are used to identify the number of gas molecules adsorbed on the material surface and thus lead to the surface area providing the size of the gas molecule is known [141]. In this thesis, the surface area of WO_{3-x} nanowires were calculated based on nitrogen adsorption-desorption isotherms measured using the BET method. Pore size distribution was analysed based on the Barret-Joyner-Halenda (BJH) method [142].

3.4 Properties characterisation

3.4.1 Thermal stability analysis

Thermal analyse (TGA-DSC)

In material science, thermal analyse is carried out to study the difference of material properties with the temperature change. Among a range of ways used for thermal analyse, differential thermal analysis (DTA), differential scanning calorimetry (DSC) and thermogravimetric analysis (TGA) are the most commonly used ones. The properties measured in these methods are temperature difference, heat difference and mass difference respectively. In detail, DSC measures the energy required to keep both the reference and the sample at the same temperature whereas DTA measures the difference in temperature between the sample and the reference when they are both put under the same heat. Unlike DTA and DSC, TGA involves the determination of the change in weight of the sample in relation to the change in temperature.

Q600-SDT (TA instrument) was used to study the thermal properties of IF-WS_2 and related nanocomposites. Both TGA-DSC curves were obtained from the results, for each run, around 20 mg of a dried sample, has been heated at a rate of 10°C /min from room temperature to 1000°C under air/Ar atmosphere. The acquired thermal data were analysed using Universal Analysis 2000 computer software provided by TA Instruments, USA.

3.4.2 Mechanical test

Mechanical properties of the resulted IF-WS_2/nylon 12 composites were evaluated by tensile and flexural testing.

Tensile test

Tensile (pull to break) samples were finished and tested according to ASTM D638 standard, using a Lloyd Instrument EZ20 and a 10 KN load cell, with test performed at a speed of 2 mm/min. 3 samples were prepared for each concentration of IF-WS_2/nylon 12 composites, size of sample along the loading direction is shown in Figure 3-8. All samples were polished using 1200 sandpaper before subject to test.

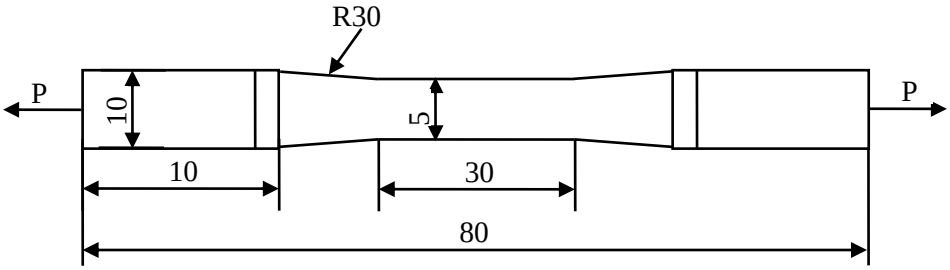

Figure 3-8 Loading geometry and dimensions of tension specimen at room temperature

Defined as stress, tensile strength is measured as force per unit area.

$$\sigma_t = \frac{F}{bd}$$ Equation 3-3

Where F is the maximum load, b is the sample breath and d is the sample thickness.

Young's modulus, which also commonly known as tensile modulus, E, can be calculated by dividing the tensile stress by the tensile strain in the elastic (initial straight-line) portion of the stress-strain curve:

$$E = \frac{\sigma}{\varepsilon} = \frac{F/bd}{\Delta L / L_0} = \frac{FL_0}{bd\Delta L}$$ Equation 3-4

Where E is the Young's modulus (modulus of elasticity), F is the force exerted on an object under tension; L_0 is the original length of the object; ΔL is the amount by which the length of the object changes; b is the sample breath and d is the sample thickness.

Bending test

Three-point bending testing was conducted in accordance with ISO178 [143] using a Lloyd Instrument EZ20 and a 1 KN load cell. 3 samples were tested for each type of polymer nanocomposite sample, different in concentration of IF-WS_2 nanoparticles, the sample size was 80×10×4 mm (Figure 3-9). All surfaces of sample was polished using polishing paper 1200. The bending span and the load speed were 64 mm and 2 mm/min respectively.

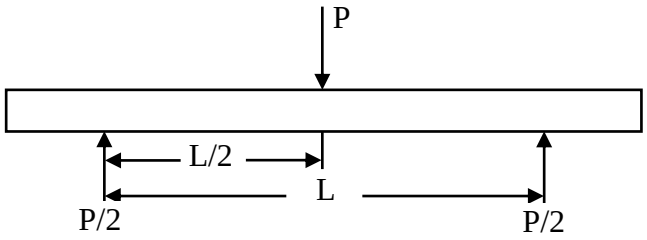

Figure 3-9 Configuration of three point bending specimen at room temperature

Flexural strength is defined as the strength of a material in bending at the instant of failure and is expressed by Equation 3-5, for three-point bending over a sample with rectangular cross section:

$$\sigma_f = \frac{3FL}{2bd^2}$$ Equation 3-5

Where σ_f represents flexural strength F is the load at the fracture point, L is the span length, b is the sample breath and d is the sample thickness.

Flexural modulus of elasticity is linear to the gradient of the initial straight-line portion (elastic portion) of the load-deflection curve, and could be calculated by

$$E_f = \frac{\Delta PL^3}{4bd^3\Delta f}$$ Equation 3-6

Where E_f is the flexural modulus of elasticity, ΔP is the load increase of the elastic portion of the load deflection curve, Δf is the deflection increase of the elastic portion of the load deflection curve, while L, b and d represents span length, sample breath and sample thickness respectively.

Modulus of toughness is defined as the ability of material to absorb energy prior to fracture, or the energy needed to break a unit volume of material. One way to measure toughness of materials is to calculate the entire area under the stress-strain curves (i.e. take the integral), the unit for toughness is energy per volume (J/m^3).

3.5 Summary

The materials, experimental procedures for fabrication and characterisation of the resulted nanostructures and nanocomposites have been presented in this chapter.

A rotary reactor was designed and modified for continuous large scale synthesis of IF-WS_2 nanomaterials, with rotating system, seal system and feeding system properly designed and fitted. An Al mould was designed and manufactured for fabrication of IF-WS_2 reinforced polymer composites.

A combination of XRD, SEM/EDX, TEM, Raman and Micro-CT etc. techniques were used to characterise the resulting nanostructures and nanocomposites, to obtain their morphology, structure and chemical composition information. The thermal stability and mechanical properties were analysed by TGA/DSC and tensile/bending test respectively.

Chapter 4 Rotary reaction furnace design and modification

4.1 Introduction

As discussed earlier, the large scale manufacturing still remains as the biggest challenge for the wide applications of this class of MS_2 (M=W, Mo, Nb) materials. Using the initial growth mechanism of oxide to sulphide conversion using WO_x as the precursor, Tenne's group realised a batch yield up to 1 g in 1996 [18]. Years later, the use of falling bed reactor and fluidised bed reactor have made the large scale synthesis of WS_2 and MoS_2 nanoparticles possible, with significant advantages over the previous static process [17]. However the fluidised bed reactor is rather high and complicated to construct, with huge energy consumptions (to maintain the constant temperature for the entire vertical reactor during a lengthy reaction period). A new, continuous, scalable, simple and economical process for the production of WS_2 remains a great challenge.

Given the fact that, the key technical barrier for the scale up of the WS_2 nanostructures is the agglomeration and superficial reaction which could not be avoided in a static solid-gas reaction, thus, in the alternative new process, effective measures needs to be taken to avoid extended physical contact of the particles during the heating stage, to minimise the particles agglomeration.

Rotary kiln have been widely used in industry, for chemical and mechanical engineering, such as for mixing, drying [144-146]. Beside the traditional applications in industry for rotary kilns, rotary dryers and coolers, and mixing drums, the rotary bed reactor has recently been developed for nanomaterials production based on gas solid reaction, in which a controlled atmosphere and agitation of particle could be achieved simultaneously, having combined all the advantages of the fluidised bed furnace and the rotary kiln [147]. The rotation of the reactor has led to no-agglomeration and good mixing of bed particles. It has also been reported that best gas-solid contact has been assured by the flow regime in a rotary bed reactor, which consequently leads to a faster and complete conversion from precursors to product [148]. Thus the rotary bed reactor has been considered as a promising technique in the manufacturer of various nanomaterials, especially for carbon nanofibres or carbon nanotubes [147-150], as an

alternative method to replace the fluidised bed reactor [151, 152]. This technique can therefore be applied to the synthesis of WS_2 nanomaterials.

In this chapter, an innovative, simple and continuous rotary processing technique suitable for the manufacture of WS_2 inorganic nanomaterials at a large scale will be developed. The design and modification of a rotary furnace based on a traditional static tube furnace has been described in detail. Initial validation of the rotary furnace design based on WO_x nanoparticles, as well as the dynamic particle movement in the rotary reactor, will also be discussed.

4.2 Objectives and technical requirements

In the reactor, the following chemical reaction will take place in the reaction tube: $WO_3 + H_2S \rightarrow WS_2 + H_2O$, as already described in Section **3.2.2.4**. For a thoroughly efficient reaction and to prevent the sintering occurrence of the WO_3 precursor and of the newly formed WS_2 particles, the working tube should be kept in a rotary motion---either at a constant or a variable speed, to allow the precursor to mix well with the gas for reaction and to prevent the particles agglomeration. At the same time, while rotating, the inlets and outlets of the working tube containing the mixture gases need to be sealed against any leakages, since a toxic gas H_2S is involved. Accordingly, the new rotary reactor should satisfy the following technical criteria:

1. Versatile speed control: allow the speed to be adjustable within a range from 0 up to 300 rpm.
2. Precise temperature control: allow for accurate temperatures for the reaction to take place.
3. Sufficient reaction time: ensure the WO_3 precursor to be completely converted into WS_2. This includes enough heat length (hot zone) and sufficient residence time.
4. Multiple gases supply: suitable for inert, corrosive and toxic gas operation.
5. Proper seal for the rotary quartz tube. Make sure the toxic gas contained in the rotary quartz tube sealed against any leakage, during the whole reaction time at high temperature.
6. Efficient mixing. Minimise the agglomeration of precursor and the formed WS_2 nanoparticles.

7. Continuous feeding. A mechanism allows for the WO_3 precursor to be introduced into the reactor continuously, easy to be scaled up.
8. Compact. The overall dimension of the whole system should be compact, capable of large scale production and proper for lab use.
9. Low cost. Cost effective refers to reactor construction cost and overall running cost, an important factor for future industry production.
10. Healthy and Safety. Any potential healthy safety issue needs to be considered throughout the design, manufacture, assembly and testing process.

The design concept of the rotary tube furnace reactor for the production of IF-WS_2 nanomaterials is shown in Figure 4-1a. A traditional tube furnace could be adopted as the basic element for further design and modification (Figure 4-1b), in which a working tube of a required size normally sits stationary inside the furnace, and contains a temperature controller as well. To make sure a complete reaction, sufficient reaction time is needed, thus a very long tube furnace with a hot zone of 950 mm was selected. The diameter of selected reaction working tube can be up to 75 mm.

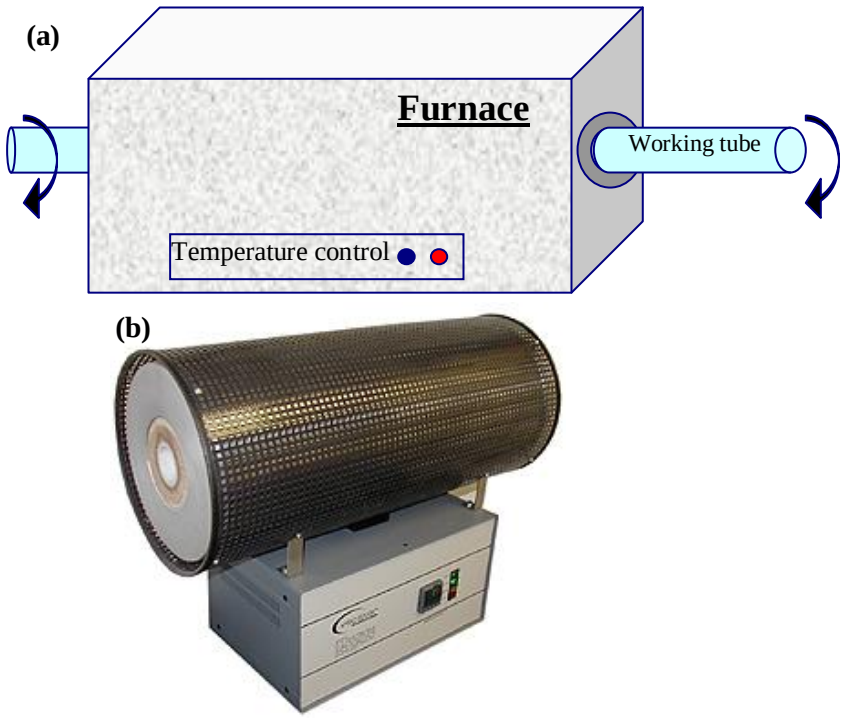

Figure 4-1 A diagrammatic of the rotary furnace reactor (a) and a real furnace purchased (b). Arrows indicate the desired rotation effect of the working tube, whist keeping the entire furnace itself stationary.

To achieve the above technical criteria/requirements base on this static tube furnace, several key design stages were identified:

1. Set the working tube into rotary motion. This could be realised by driving the working tube using a rotary motor, which is more energy effective than driving the whole furnace. The design of a supporting frame and a complete transmission system is required.
2. Allow the speed of rotation to be controlled within a reasonable range. A motor equipped with an appropriate speed controller needs to be selected and assembled.
3. Dynamic seal system design and evaluation. Whilst the tube is in motion, the working tube containing the reaction gas needs to be sealed to prevent any leakage of H_2S and other gases. A dynamic seal system is required which connects the rotary working tube and the static gas supply pipes together. This includes seal selection and materials evaluation, shaft design and manufacturing, housing design and manufacturing, the evaluation of the system, against leakage whilst rotating.
4. The design of a continuous feeding system. Design, evaluation and selection of a proper feeding system with easy handling and reliable features are important for future scale up.

These aims were split into a number of objectives that would be finished gradually. A range of factors would be considered during the design, such as materials selection for frame, pulley, roller, seal, shaft, etc. low cost, easy machining, widely available, safe and easy to operate, under the environment of corrosion, high temperature, and should be wear resistant, reliable and easy to modify and maintain for further improvement—versatile.

4.3 Rotary furnace transmission system design

To set the working tube into rotary motion, several transmission designs were considered and finally the design shown in Figure 4-2 was selected. It is easy to realise and appears to satisfy all the required functions with high efficiency.

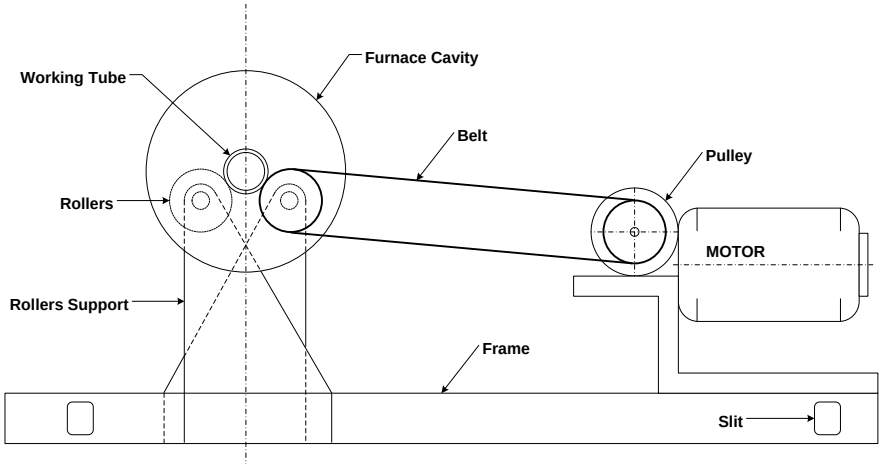

Figure 4-2 Frame mount with belt around free moving rollers transmission design

The design makes use of the basic concept of turning mechanical energy provided by the motor into rotational energy for the working tube (Figure 4-2). The base frame consists of 4 'L' brackets which are fixed to the furnace to hold the quartz working tube in place, as shown in top of Figure 4-3. According to the length and bore diameter of the furnace, as well as the length of the base frame, a quartz tube with o. d.40 mm, i. d. 36 mm, and length of 2000 mm was chosen for working tube.

Two metal rollers are held in a supporting frame mounted to the L bracket base frame, at both ends. There are slits and additional holes in the supporting frame allowing adjustable roller height, which enables to tilt the working tube at small angles (Figure 4-3).

At the active end, the motor which drives the pulley and belt is mounted to the base frame. The belt loops around one free moving roller, driving it to rotate. In this case, the belt tension could be adjusted by changing the roller height. Since the working tube sits in between the two rollers, once the rollers rotate the friction between the rollers and the quartz tube will drive the working quartz tube to rotate, in the opposite direction. This design is simple and straightforward, could easily be machined and a motor can be easily assembled onto the base frame (Figure 4-3, Figure 4-4 and Figure 4-5).

In this transmission system, these 'L' bracket are made of steel due to their high stiffness and strength as they are going to support the whole transmission system and the working tube in action. To lighten the burthen for the 'L' bracket base frame, all the other parts are made of Al, including all rollers, the supporting frame they are mounted to, and the frame holding the motor, attributed to their low density. All rollers are

covered with a rubber layer to protect the quartz tube which will be driven, and to increase the friction.

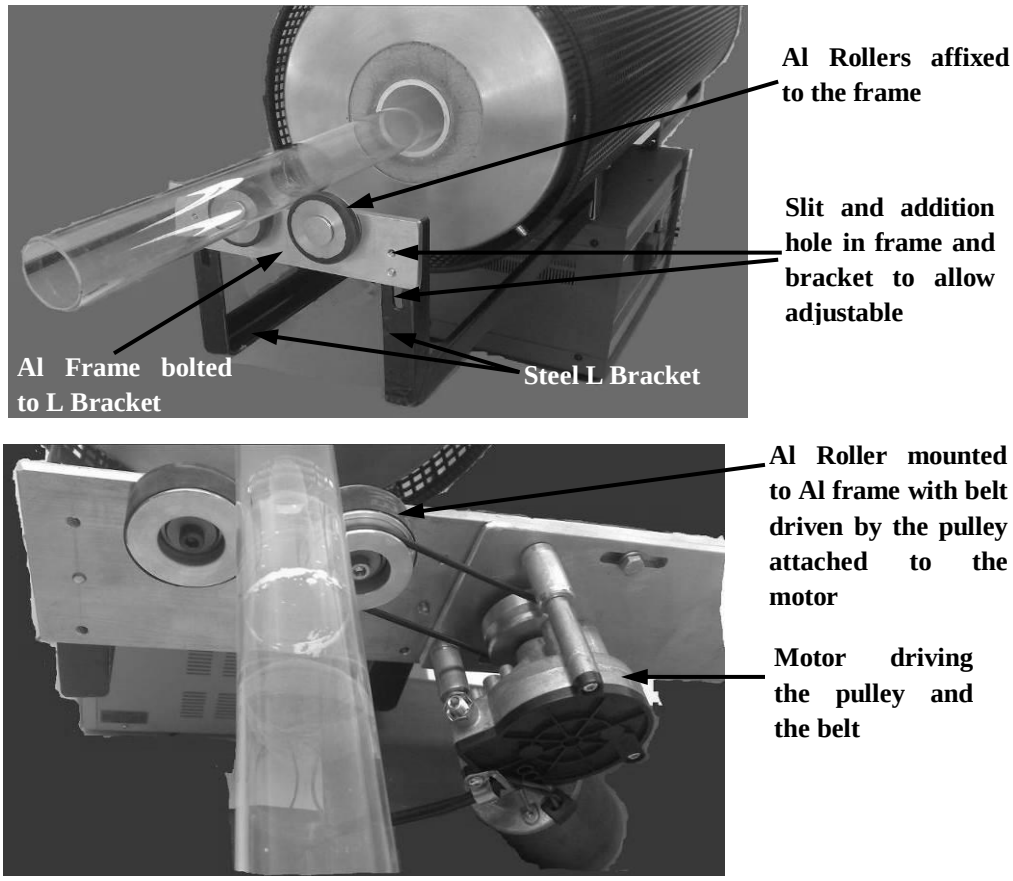

Figure 4-3 Transmission system to drive the working tube, with base frame, supporting frame, pulley, roller and motor from the passive end view (top image), the active end view (bottom image)

In order to rotate the tube in a proper speed range, A RS motor (Type III geared DC motor, 240 rpm, 24 V, 38 W from RS as shown in Figure 4-5) was chosen. With a DC motor speed controller (Regulated Laboratory Power supply from Telonic instruments limited, Output Voltage 0 - 30 V, Output Current 0 - 5 A, Figure 4-5), the pulley speed ranges from 0 - 240 rpm. Due to the smaller circumstance of the quartz tube than the pulley (d_{tube}: d_{pulley} = 40:58), the maximum speed for the quartz tube could reach 350 rpm ($\omega_1 r_1 = \omega_2 r_2$ when share the same linear velocity, thus $\omega_2 = \omega_1(r_1/r_2)=240\times(58/40)$), which allows for speed testing at a desired range. For safety reason, this maximum speed should not be improved further owing to the brittle feature of the quartz tube.

Figure 4-4 Photos for the assembled rotary system (left image) and details of driving part (right image)

Figure 4-5 Motor (left image) and the motor speed controller (right image)

4.4 Dynamic seal system design and evaluation

The next challenge is to design an appropriate dynamic seal system which connects the rotary working tube and the static gas pipes together, realising gas tight at high temperature under dynamic movement, corrosion environment and atmosphere pressure.

4.4.1 Dynamic seal system design

As discussed previously, the main purpose of the rotary seal is to seal H_2S, a colourless, hazardous, highly toxic, and highly corrosive and flammable gas. According to the manufacture's safety data sheet, it can be identified in relatively low concentrations, by a characteristic of rotten egg odour. Although very pungent at first, it quickly deadens the sense of smell, so potential victims may be unaware of its presence until it is too late. This toxic gas is considered a broad-spectrum poison, meaning that it can poison several different systems in the body causing instant paralysis and death in severe cases.

For all the above safety reasons mentioned, it is of inherent importance that the seal is of exceptional quality, and that there are good quality air ducts to suck away any waste of the sulphide gas, at the inlet or outlet ends of the tube, to maintain human safety.

For a normally static furnace, the working tube can be sealed by silicon stoppers (for small diameter tube) or by metal plates to which the gas tube was weld, together with O-ring, the difference in the required rotary system is that the gas tube is stationary but need to be connected to the rotating working tube, the essential issue is the sealing of the joint point of the static part (gas tube) and rotary part (working tube), so a rotary seal is needed to avoid gas leakage. As the reaction temperature ranges 800-1000°C, the working temperature for the seal at the end of quartz tube would be up to 200°C at the outlet end.

There are two design concepts for the seal system. The first design as shown in Figure 4-6 top, the rotary seal could be put into the tube connector (Figure 4-6 bottom), the rotary tube connector keeps the part connected with the housing unit rotating while the other parts connected with gas tube remain static.

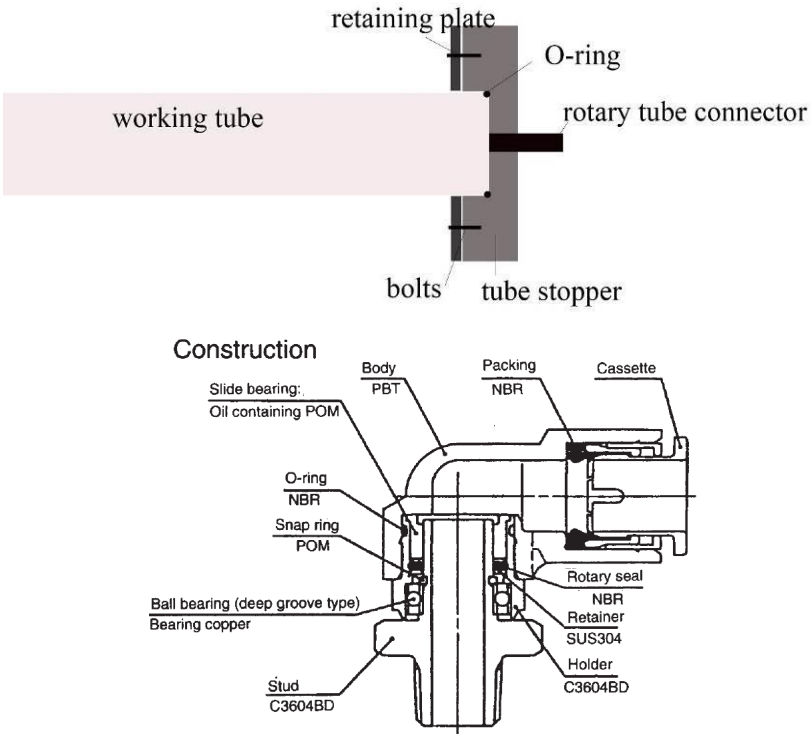

Figure 4-6 Top: The 1st design concept of rotary seal system; bottom: the construction of the rotary tube connector (from SMC website)

In the second design, the seal is placed between the shaft (stationary with the gas tube) and the housing unit (rotating with the working tube), as shown in Figure 4-7, and the whole seal unit will be set in motion except the shaft. The rotary seal is compressed between a rotating housing and a stationary shaft. The retaining plate in the left holds the shaft and housing together with the rotary seal, the right plate holds the housing and working tube rotating together using an O-ring. The tubes carrying the reaction media (gas and particles) will be welded into the holes through the shaft.

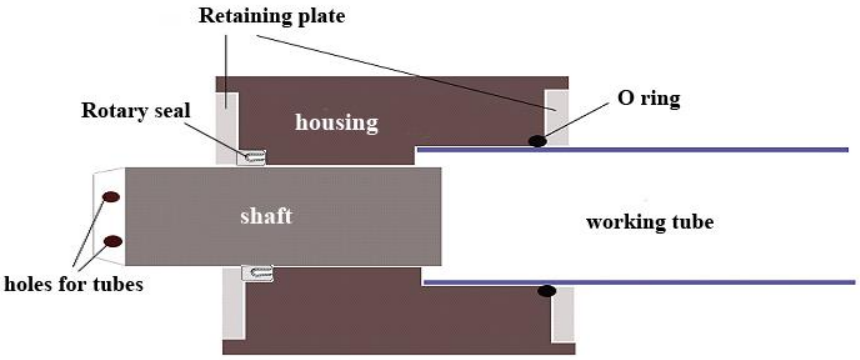

Figure 4-7 Second design concept of rotary seal system

In the case of the 1st design, commercially available rotary tube connectors are mostly for compressed air or water, and the rotary seals inside the connectors especially the copper bearing are not suitable for sealing H_2S gas (copper is going to react with H_2S gas) and cannot survive the high temperature applied. Furthermore, it is also not practical to manufacture such a small tube connector in our own workshop. Therefore, the second design is selected, although it seems more complicated than the first one, and there are various rotary seals commercially available for easy selection.

4.4.2 Seal evaluation and selection

Based on above discussions and after comparing several possible materials, a modified PTFE is chosen, owing to its outstanding chemical resistance, good lubricating qualities and low thermal conductivity. It is however less resilient than elastomeric materials and has poor resistance to thermal cycling. The resilience can be improved by using a PTFE coated/ energised springs in encased seals.

Seals that are generally available made from encased PTFE materials are usually radial lip seal and rod seals for rotating shafts. Comparing the size range of these rotary seals,

the following rod seals were chosen since they have size appropriate to the current circumstance.

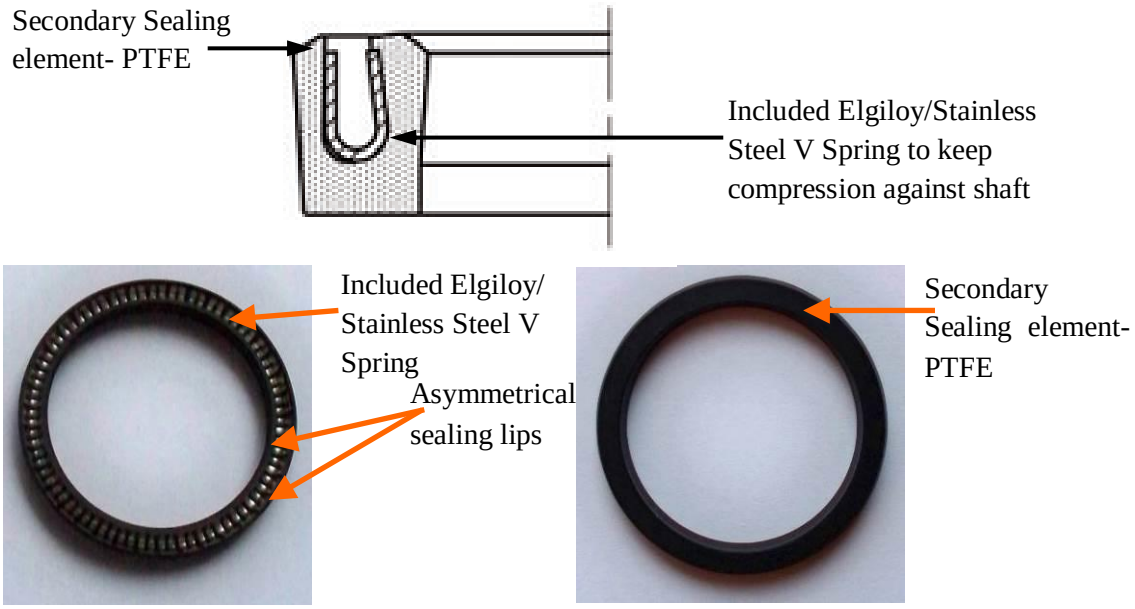

Figure 4-8 V spring Rod Seal as received (SNI 43 from Dichtomatic Ltd.)

This particular U-ring rod seal (SNI 43 from Dichtomatic Ltd., Figure 4-8) is a single-acting PTFE seal in the form of an inner sealing U-ring. The steel (non-corrosive, acid resistant steel) V-spring activates the sealing lip permanently so that even in a non-pressurized state, good sealing performance can be achieved. As a result of the asymmetrical sealing lips, the sealing force is optimised and the friction behaviour is improved, thus the service life is substantially extended. This seal also incorporates all the advantages of PTFE, as the entire secondary sealing element is made from enhanced PTFE (PTFE/carbon compound). In addition, it satisfies the operational application limits of pressure up to 35 MPa, temperature from -150 to + 250, running speed up to 15 m/s.

4.4.3 Seal shaft and housing design and assembly

a. Seal shaft design

As discussed earlier, the seal needs to be fitted around a stationary shaft. The feed of H_2S and WO_3 particles will travel in the steel tubes which will be welded to the main shaft. The housing unit and the shaft have been designed after considering the following seal profile (Figure 4-9).

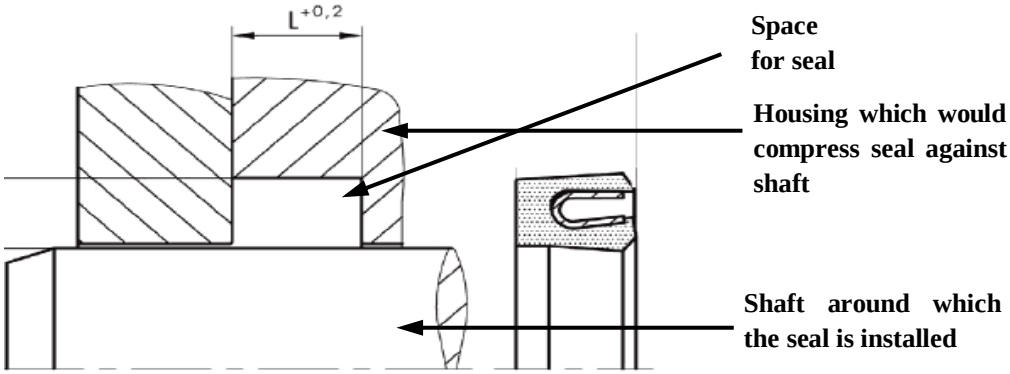

Figure 4-9 Rod Seal profile for housing and shaft (from website of Dichtomatic Ltd.)

All the dimensions have been detailed as part drawings according to the working tube and the seal profile. These drawings will be used in the manufacture of the parts, and are attached in the Appendix (Appendix A and B for the seal shaft housing respectively).

Two feeding holes are drilled through to the outlet end of the shaft to allow for the material feed to travel into the working tube safely and smoothly. Two feeding tubes will be welded to the two holes shown in the model (Figure 4-10). The inlet ends of the shaft are chamfered to allow a sharp grip at the area of contact with the seal (Figure 4-10 top image), while the diameter of the shaft should be determined according to the inside diameter of the rotary rod seal.

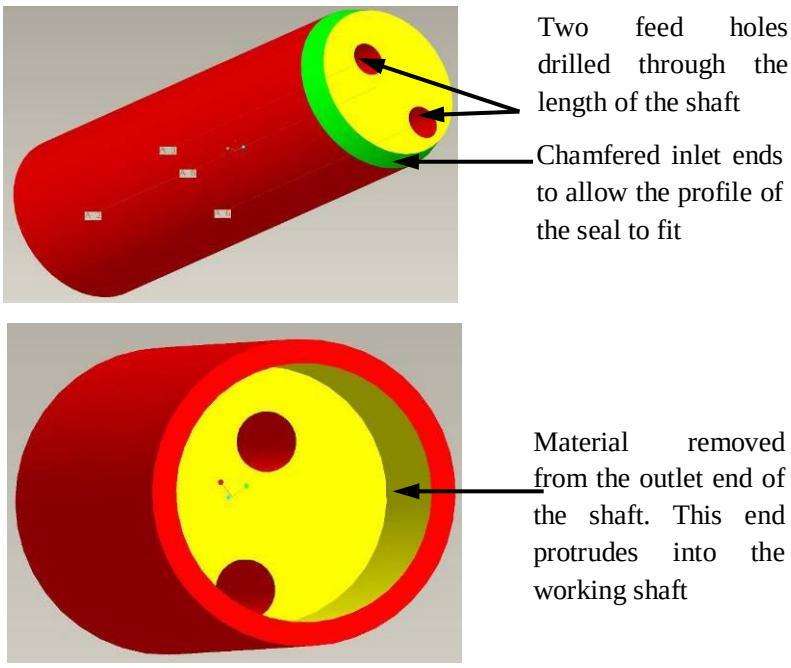

Figure 4-10 Shaft model – stainless steel (top image, inlet view; bottom image, outlet view)

Material from the outlet end was removed to make the shaft lighter in weight, so that the shaft can be easily supported by the housing, to improve the system service life. This also improves the manufacturing process, as the shaft is very long, drilling a thin hole through would be very difficult (Figure 4-10 bottom image).

b. Seal housing design

A step housing model was designed, to allow for the working tube, shaft and seal of different diameters to be compatible with the same housing. For detailed Housing drawings, refer to Appendix. The housing is designed to fit with both the shaft and working tube (Figure 4-11 and Figure 4-12). For the end which will be sealed with the shaft by a rotary sealing (Figure 4-11), the inside diameter of the grey part should be the same as the outside diameter of the shaft, in which the shaft will be inserted. Then the seal needs to be fitted into the blue part, onto the shaft and compressed by the housing, and a retaining plate will be bolted with the housing in the yellow area, to fix the rotary seal.

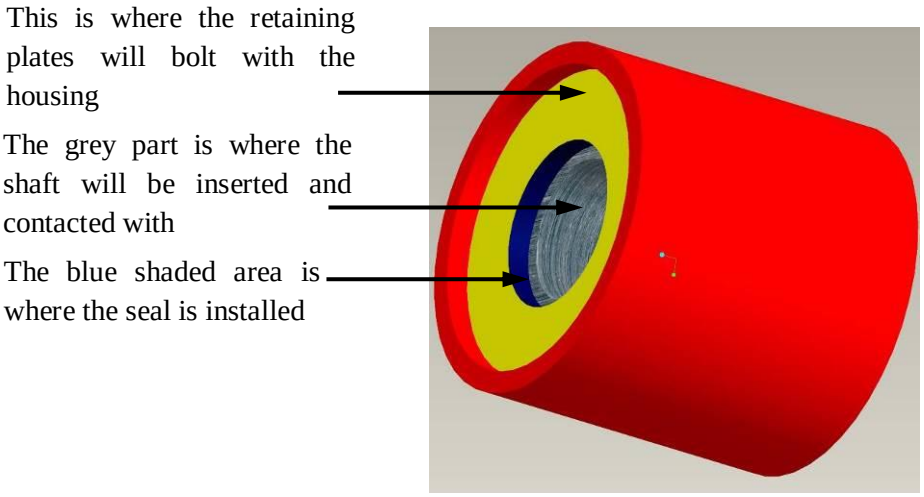

Figure 4-11 Housing model- Al- seal with shaft end

It is not that complicated at the other end (Figure 4-12). At this stage for small amount of sample synthesis only a static sealing is needed between the housing and the working tube. The diameter at this end is designed within a tolerance fitting with the outside diameter of the working tube, which will be inserted till the blue end of this part. An O-ring will be pressed onto the quartz tube at the red shaded step down, then compressed by a retaining plate in the yellow area.

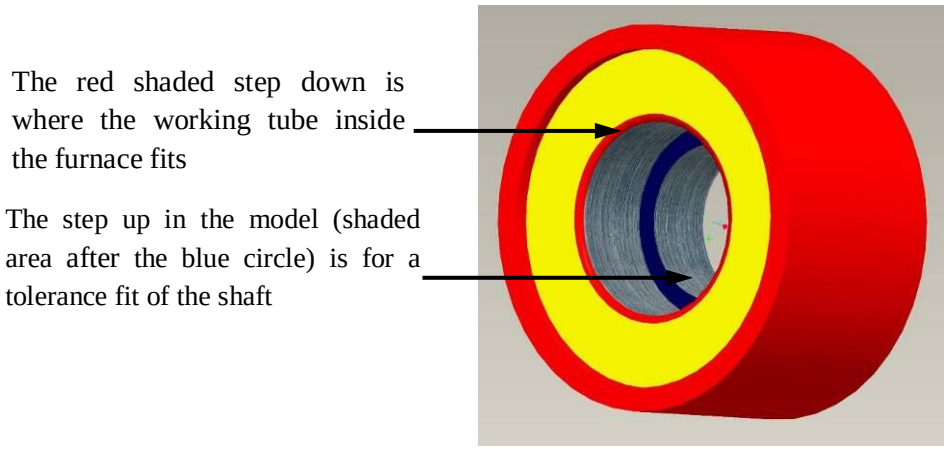

Figure 4-12 Housing model- Al-seal with working tube end

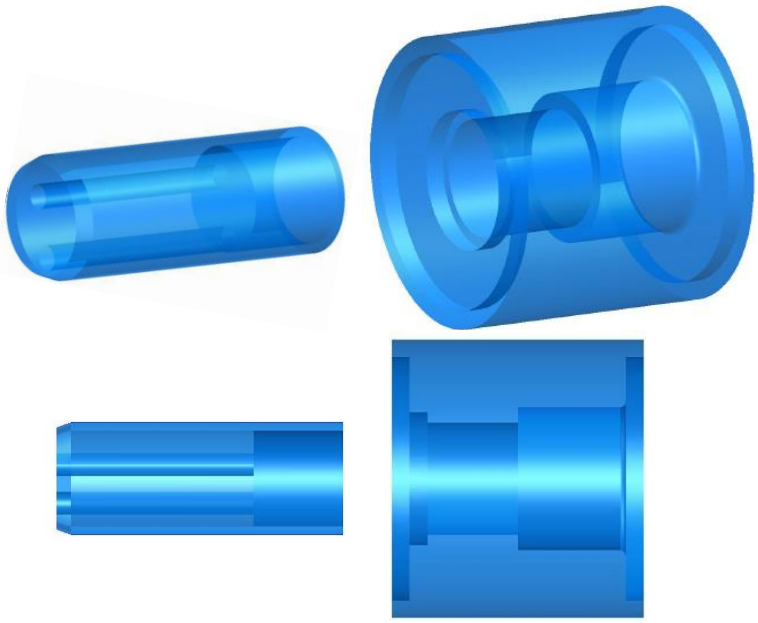

Figure 4-13 Shaft made of stainless steel (left image), and housing made of aluminium (right image)

To help gain a clear understanding, the shaft and housing are also shown in a transparent view, and placed in a way the shaft to be fitted to the housing, leaving the other end of the housing with a bigger diameter for the working tube (Figure 4-13). The material for the shaft is stainless steel, owing to its robustness, to ensure the wear resistant against friction between the rotary seals. As the housing is fixed to both ends of the quartz tube and supported by the frame, i.e. no direct contact with the corrosive gas, Al is chosen for the housing material to reduce the overall weight.

c. Shaft and housing manufacturing and assembly

Figure 4-14 shows the assembly of the modelled parts briefly, with all parts representing relevant elements as shown below:

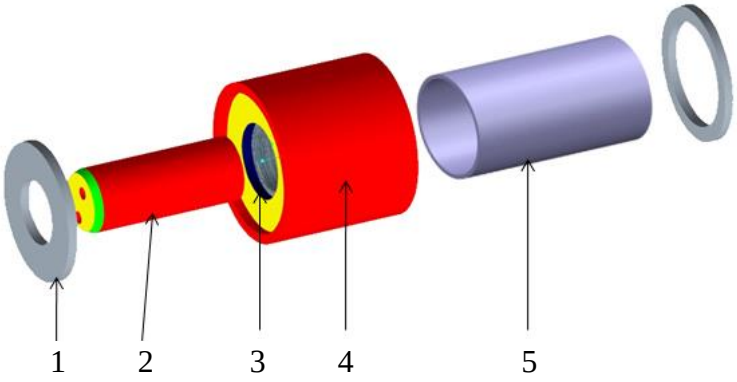

Figure 4-14 Exploded assembly view for the whole seal system: (1) Retaining plate that compresses the seal between the housing and the shaft. The retaining plate is bolted onto the outer edge of the housing; (2) Shaft, to which the feed pipes are welded, and surrounded by rotary seal; (3) The contact surface where the seal fits around the outer surface of the shaft and inner surface of the housing; (4) Housing; (5) Working tube

The shaft and housing were manufactured according to above design. Surface finish and tolerance were carried out following the installation instruction (Figure 4-15) for the particular seal (SNI 43).

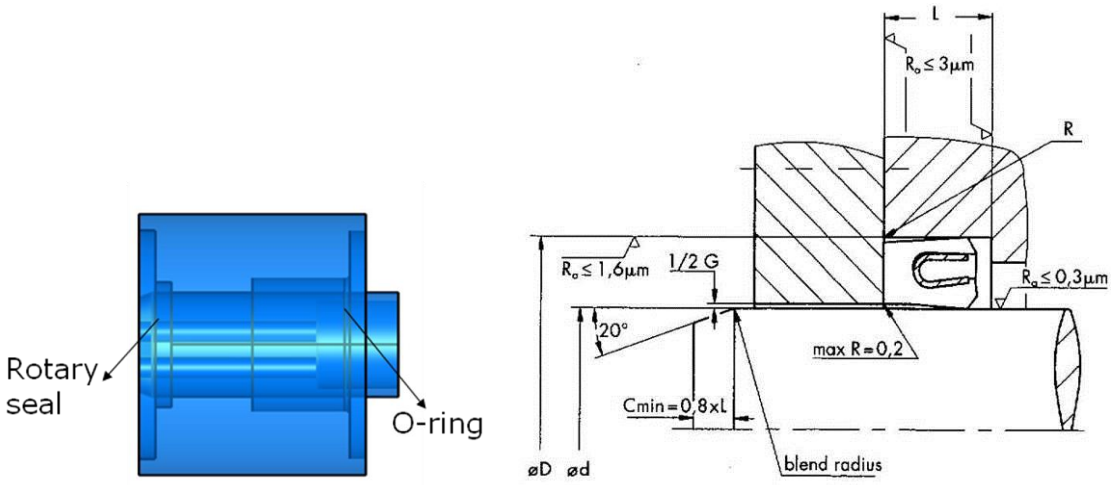

Figure 4-15 Installation instruction for the seal (left image, transparent model; right image, surface finish and tolerance instruction for the seal)

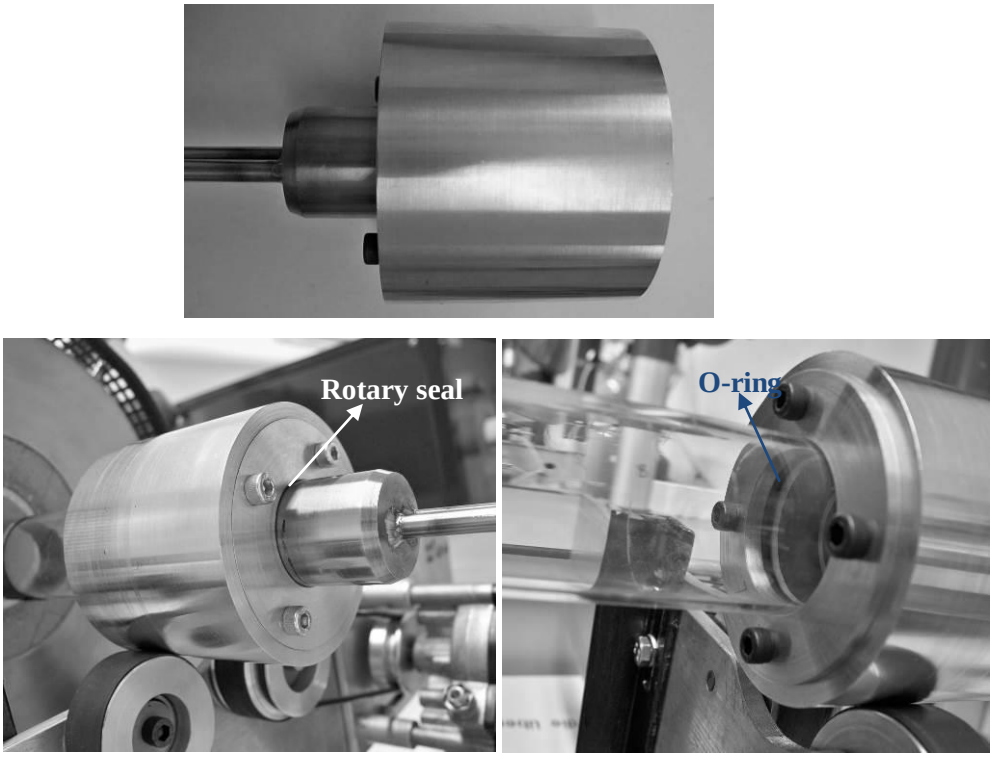

Figure 4-16 Picture of assembled shaft and housing (top: assembled housing and shaft, bottom: assembled whole seal system from different view)

Figure 4-16 shows the picture of the final assembled seal system. The shaft and housing need to be assembled together first (Figure 4-16 top), with the rotary seal compressed between them with the help of a retaining plate being bolted to the housing (Figure 4-16 bottom left). Then the assembled housing will be fitted to the end of the quartz tube, and an O-ring would be compressed to seal between the quartz tube and the housing, also by a retaining plate (Figure 4-16 bottom right). In this way, the O-ring plays an role of static seal, when the housing is being driven, the quartz tube would rotating together with the housing, whilst the shaft remains stationary as it is only connected with the rotating housing by a rotary seal.

4.4.4 Rotating test of the rotary seal design

Rotary tests have been carried out upon the rotary seal system were assembled. However during the test, the housing and shaft tend to rotate or stay still together, which means if the shaft is not fixed, both housing and shaft would be in a rotary motion driven by the motor, otherwise if the shaft has been fixed tightly to a stand frame, neither the working tube nor housing could rotate by the driving force provided by the roller. This happened due to insufficient driving force in the motor transmission system,

and the resulted friction between the driving roller and the housing is not big enough to overcome the large frictions between the seal and the housing, especially when the two heavy housing units are attached to the long quartz tube, making it more difficult to rotate.

a. Modified rotary system design

To increase the driving force, a modified rotary transmission system was designed accordingly (Figure 4-17).

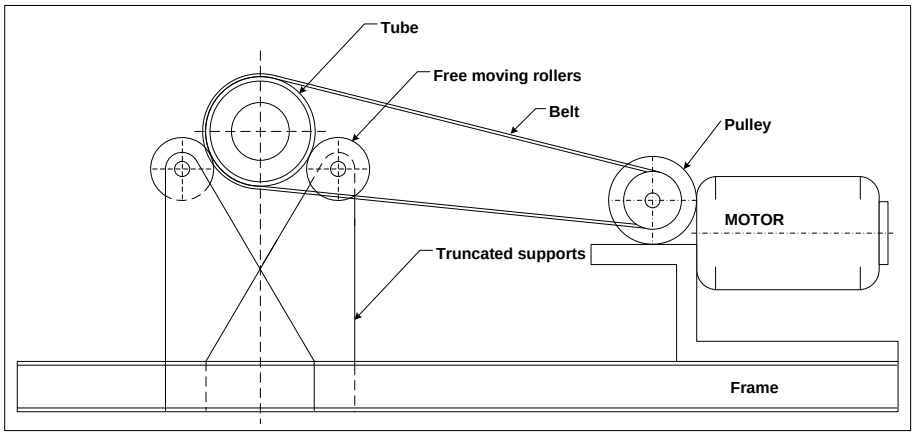

Figure 4-17 Frame mount with truncated support rollers

This design is similar to the previous one in the sense of making use of the same base frame which is mounted onto the furnace. Mechanical energy provided by the motor will be used to rotate the pulley which will drive a belt looping around the working tube directly and rotating the working tube at desired speeds. The working tube will be supported by free moving rollers on which it sits. These rollers are held in place by being mounted onto a truncated support, which is bolted to the base frame.

The significant difference between this design and the previous one is that, it drives the working tube directly (Figure 4-19) rather than driving the tube by friction (Figure 4-18). Furthermore, in order to increase the driving force given by the pulley, the driving pulley of the motor has been changed from a common light duty pulley to a teethed timing belt pulley, and the diameter of the timing belt pulley is a little smaller than the previous one, which means the rotary speed provided by this pulley will be slightly decreased. Further, as the timing belt could not drive the working tube directly, as the torsion is not large enough, it is decided to drive the housing directly, which is compressed together with the working tube.

Figure 4-18 Photo of the first transmission system

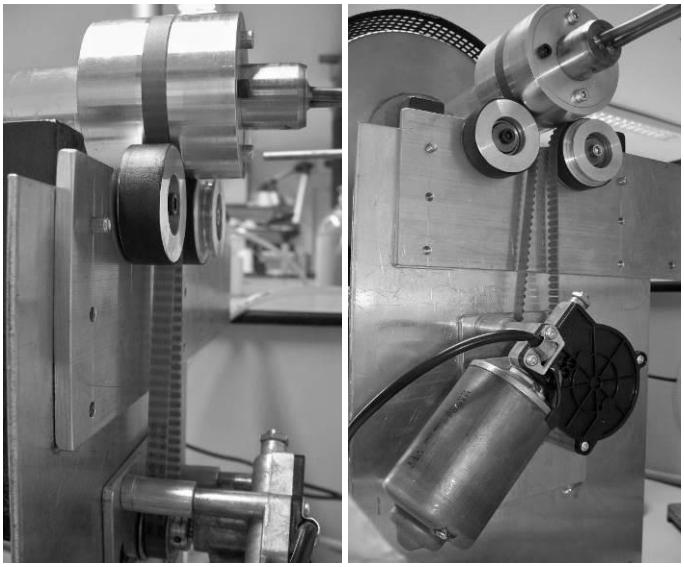

Figure 4-19 Photo of new transmission system

In this case, a 2 mm groove was machined on the housing located at the active end of the transmission system, to fit the timing belt in, as shown in Figure 4-19. With the modified transmission system, the rotary system works well finally.

b. Transmission agent

As the transmission system has been changed from driving the working tube directly to driving the rotary seal housing, which has a diameter (80 mm) twice of that of working tube (40 mm), the maximum rotary speed then decreased to half of the previous maximum speed ($\omega_1 r_1 = \omega_2 r_2$ when share the same linear velocity). At the same time, as the housing now set on the wheels, the end of the tube has been restricted to the roller position.

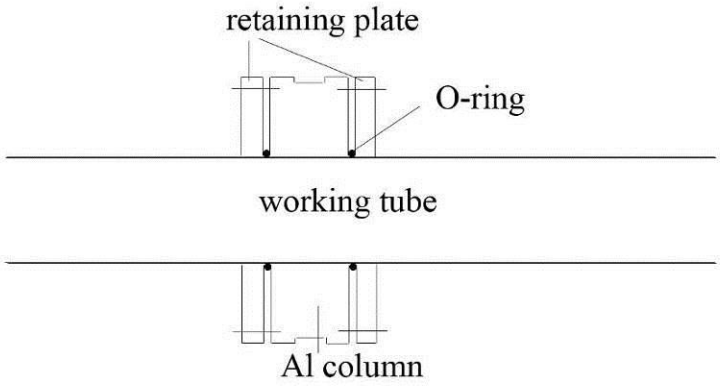

Figure 4-20 Sketch of the transmission agent used to get a larger driving force

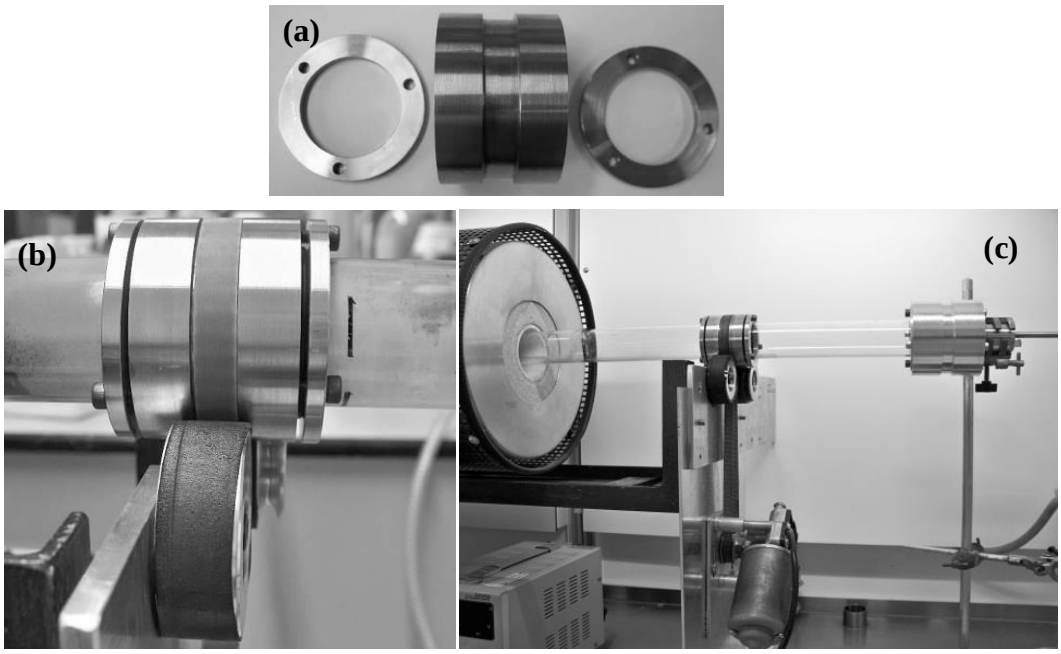

Figure 4-21 Manufactured aluminium transmission agent (a) and assembled working transmission agent (b) and the whole modified rotary system (c)

In order to solve this problem, and to avoid decreasing the rotary speed and the restriction to the working tube, a transmission agent was added to the working tube. As shown in the drawing (Figure 4-20), an Al column will be installed to the working tube, using O-rings and retaining plates to hold them together with the working tube (Figure 4-21). In this way, the tube can move freely and be balanced at each end. Moreover, the Al column has a bigger diameter than the working tube, which allows for a larger torsion than working tube; and is smaller than the housing diameter, which allows for a higher rotary speed to be achieved than driving the housing.

As safety is the most critical issue in the application, gas leakage test has been carried out after the system is properly installed. During the detection, a mild drift between the

shaft and housing was observed, and this drift might get worse and potentially result in leakage during the experiment. Thus, further improvement is required.

c. Further shaft modification

In order to avoid any potential danger of gas leakage, the drift between the housing and the shaft needed to be prevented. A new shaft has been designed, on which a retaining plate has been added compared to the previous shaft, as shown in the sketch below (Figure 4-22). By fixing the two shafts at both ends, the housing and tube were thus restricted of any movement between the shafts, no drift could occur at either end. As shown in Figure 4-23, the gas tube will be connected to the long stainless steel tubes on the shaft using tube connectors.

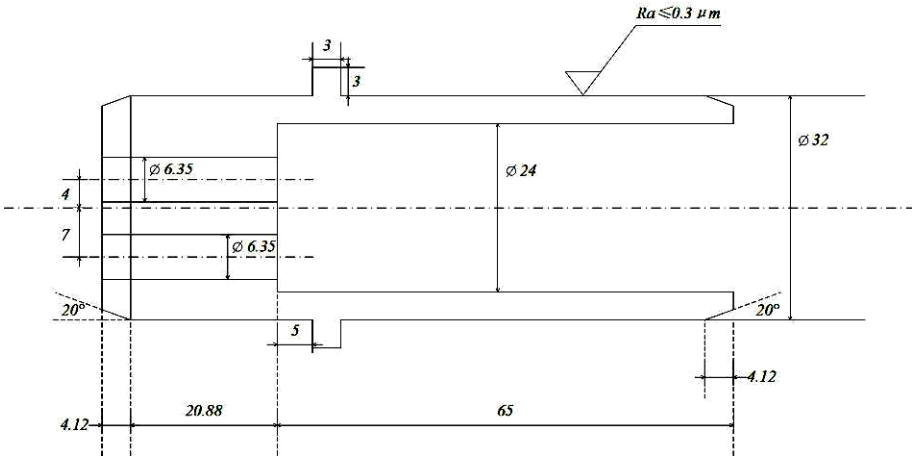

Figure 4-22 Sketch of modified new shaft

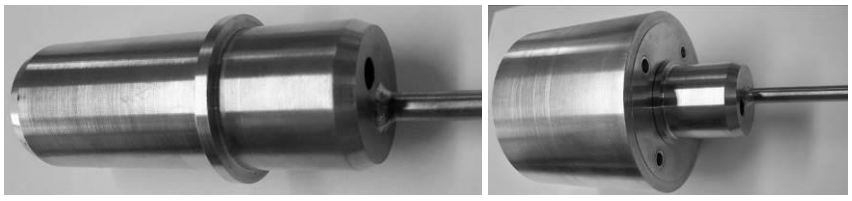

Figure 4-23 Manufactured new shaft (left) and assembled housing with the modified new shaft (right)

To realise the multi-gas supply, 3 branches were connected from the H_2S, H_2 and Ar supply pipelines respectively, united together by using L, T and U connectors to a special anti-corrosive and reinforced plastic tube A, and the other end of which is led to the stainless steel tube welded to shaft (Figure 4-24). Another hole on the shaft was left and temporarily sealed with silicon stopper, for later connection for the continuous powder feeding.

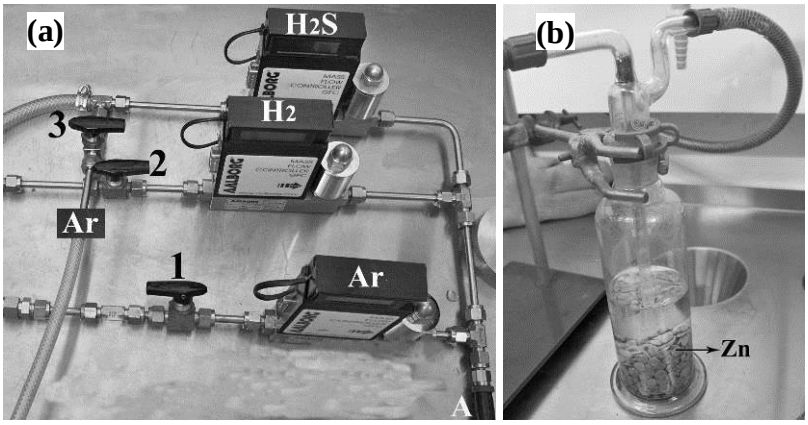

Figure 4-24 Picture of multi-gas supply at inlet (a) and outlet end (b)

In this supply system (Figure 4-24), 3 different flow meters are fitted to control the gas ratio of H_2S, H_2 and Ar gas during the reaction. Several valves are also fitted, of which valve 1 and 2 are normally switched on during the reaction, while valve 3 would only be open after the reaction finished, using flushing Ar to purge residue H_2S out of the H_2S pipeline. Also for safety reason, some Zn particles were placed in the wash bottle at the outlet end, as shown in Figure 4-24b, to absorb unreacted H_2S gas in case there is any, though theoretically H_2S would have completely decomposed at high temperature.

4.5 Validation of the rotary furnace design via basic speed investigation using WO_x nanoparticles

In order to study the influence of the rotary speed on the particle size after exposure to high temperatures (800°C or 600°C) in air/Ar, some basic investigations were carried out as below.

4.5.1 Experimental

The furnace is set up ready for rotary process. In order to let the powders travel through the tube quickly, the working quartz tube was placed with a slope rather than parallel to the base horizontal line. The angle between the working tube and the horizontal line is well-known as the inclination angle. All experiments in this chapter were carried out with a very small inclination angle ($\tan \theta = 0.008 \sim 1.5^o$). The furnace was turned on first, upon the temperature reached the target temperature (600°C or 800°C), WO_3 nanoparticles (3-6 g) were placed at the inlet end, with motor being switched on subsequently, the working tube started to rotate at the speed of 120-260 rpm. 2-5 min later, some of the WO_3 particles started to reach the other end, whilst 10-15 min was

taken for most of them (1-3 g) to reach the other end. However, due to the very low inclination angle and low filling percentage, not all of the input particles travelled through the tube to reach the exit, up to half of them were left inside the centre of the tube.

The parameters such as rotational speed, atmosphere and temperature applied are shown in Table 4-1.

4.5.2 Results and discussion

All the particles which went through the quartz tube were collected from the outlet end. To study the influence of different speeds, temperatures and atmosphere on the agglomeration of those WO_x nanoparticles, SEM and XRD analyses were applied for all the collected particles and the average size of WO_x nanoparticles were calculated by FWHM of XRD peaks using Derby-Scherrer Equation.

$$\tau_{hkl} = \frac{K\lambda}{\beta_{hkl}\cos\theta_{hkl}} \qquad \text{Equation 4-1}$$

The SEM images showed the size of collected WO_3 nanoparticles from different processes, the results are consistent with the average value calculated from XRD data, as summarised in Table 4-1 and Figure 4-25.

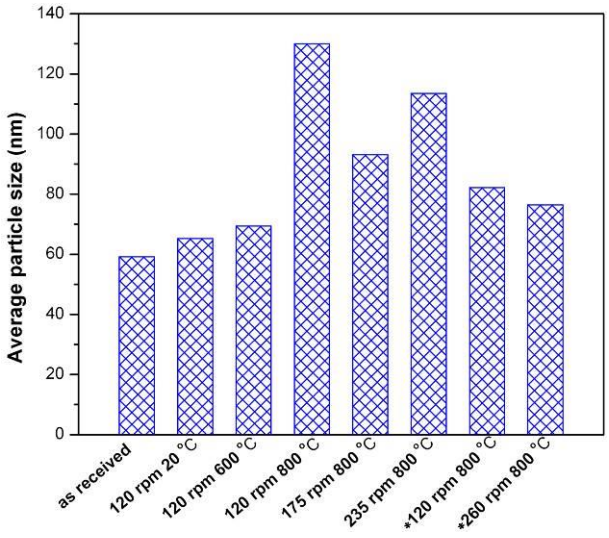

*: proceed in Argon while others proceed in air

Figure 4-25 Average particle size comparison of WO_3 nanoparticles after proceed with different paramete

Table 4-1 Experimental parameters for the study of speed influence

	Speed (rpm)	Temperature (°C)	Atmosphere	Powder filled (g)	Powders come out (g)	Time start to come out (minute)	Time stop to come out (minute)	Size of particles out (nm)
1	120	20	Air	6	3	5	15	65.2
2	120	600	Air	3	1.6	5	15	69.4
3	120	800	Air	6	3	5	15	130
4	175	800	Air	3	1.5	3	10	93.1
5	235	800	Air	3	1	3	10	113.5
6	120	800	Ar	3	1.3	5	15	82.2
7	260	800	Ar	3	1	3	9	76.4
8		particles as received						59.8

Average size of WO_x nanoparticles as received was also calculated, as ca. 59.8 nm, which could also be confirmed by SEM pictures (Figure 4-26). SEM images for all the particles experiment 1-7 are listed below from Figure 4-27 to Figure 4-33, with 2 different magnifications for each.

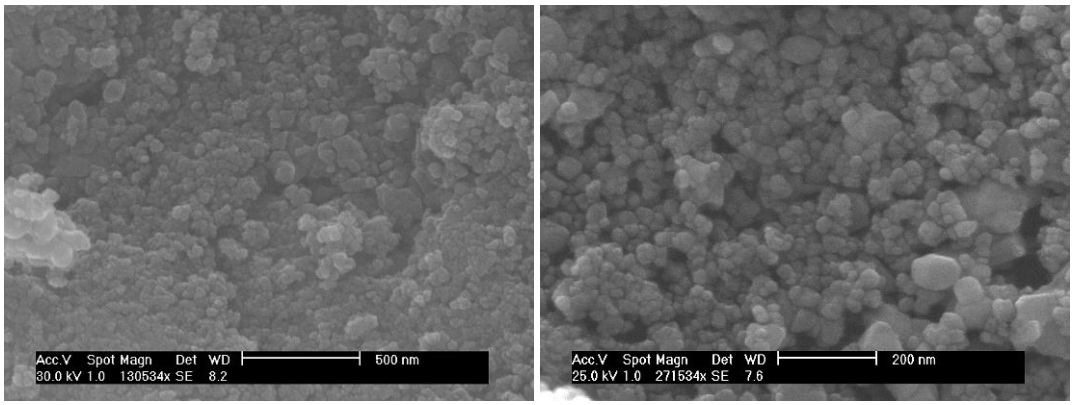

Figure 4-26 Images of as received WO_3 nanoparticles (59.8 nm)

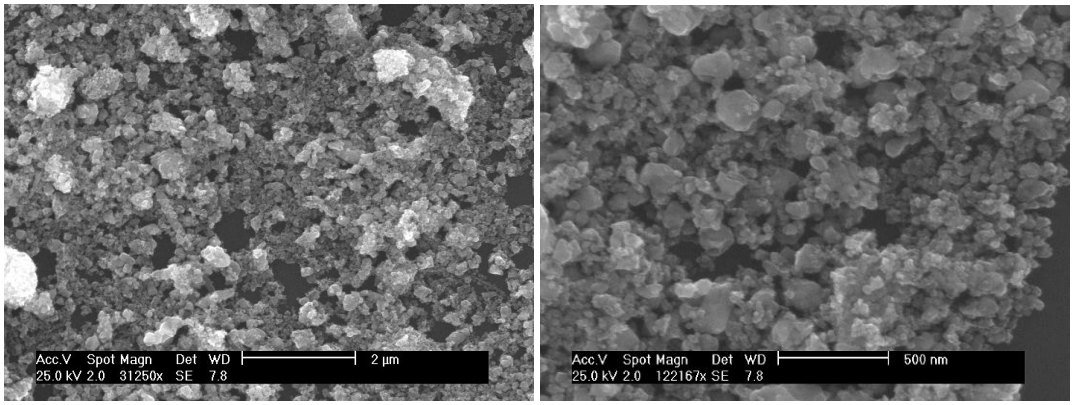

Figure 4-27 WO_x particles collected from experiment 1 (120 rpm at room temperature in air, 65.2 nm)

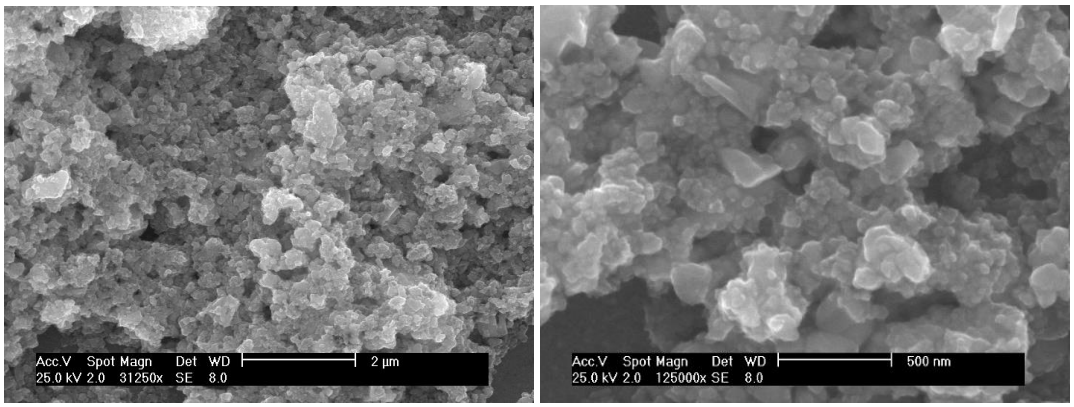

Figure 4-28 WO_x particles collected from experiment 2 (120 rpm, 600°C in air, 69.4 nm)

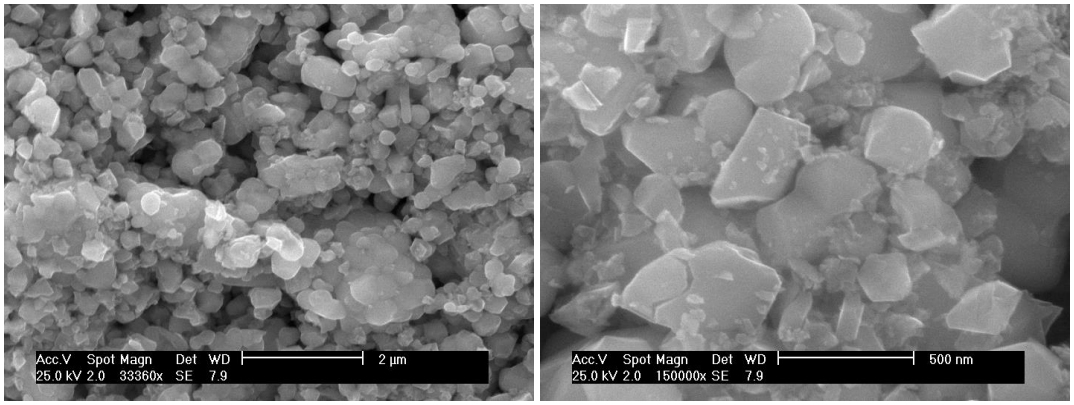

Figure 4-29 WO_x particles collected from experiment 3 (120 rpm, 800°C in air, 130 nm)

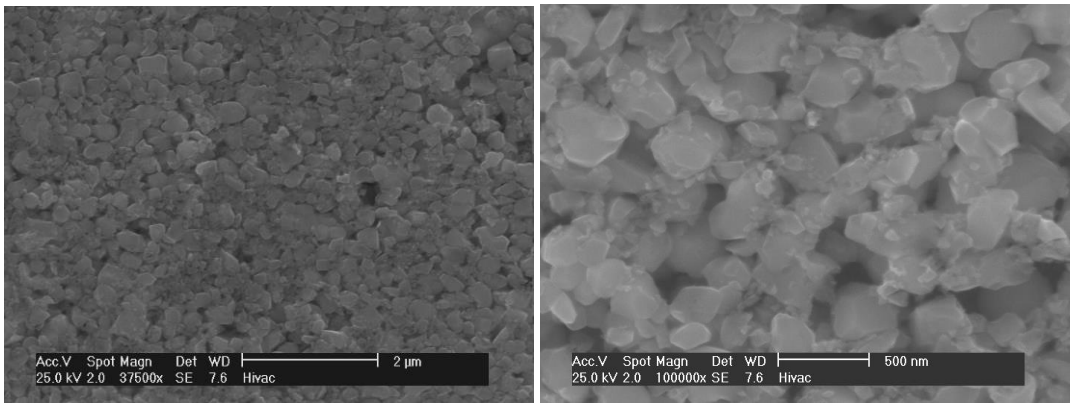

Figure 4-30 WO_x particles collected from experiment 4 (175 rpm, 800°C in air, 93.1 nm)

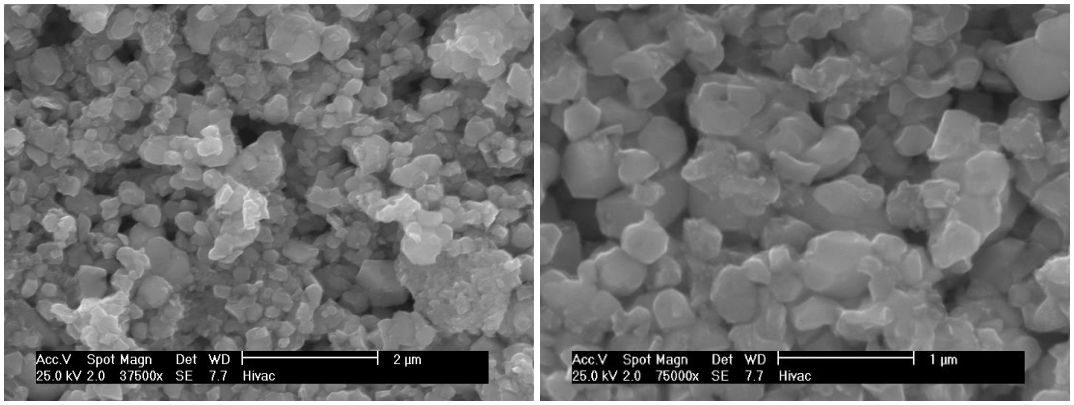

Figure 4-31 WO_x particles collected from experiment 5 (235 rpm, 800°C in air, 113.5 nm)

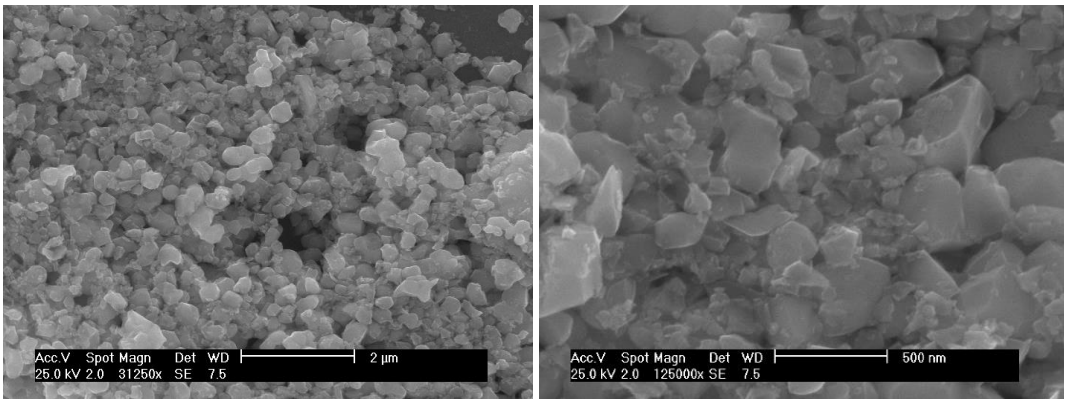

Figure 4-32 WO_x particles collected from exit of experiment 6 (120 rpm, 800°C in argon, 82.2 nm)

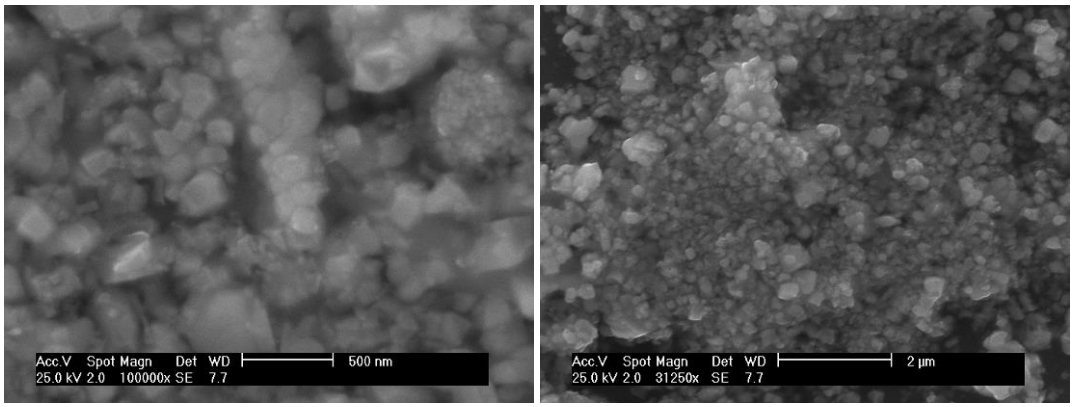

Figure 4-33 WO_x particles collected from experiment 7 (260 rpm, 800°C in argon, 76.4 nm)

From the results, some trends could be found. Particles went through in argon (120 rpm, 800°C in argon, 82.2 nm, Figure 4-32) are much smaller than particles obtained in air (120 rpm, 800°C in air, 130 nm, Figure 4-29). Particles came through under 600°C (69.4 nm, Figure 4-28) are smaller than under 800°C (130 nm, Figure 4-29). These results also revealed a higher effect of temperature on particles size than that of atmosphere.

The comparison of average particles size between as-received WO_3 nanoparticles (59.8 nm) and those collected from experiment 1 (120 rpm, room temperature, 65.2 nm) showed that the average particles size collected from exit were larger than the overall average size. This implied that the bigger particles were more favourable to travel through the working tube, or in other words, smaller particles have a longer residence time, thus particles left in the centre zone are smaller. This might be due to the contribution of gravity originated from the inclination angle.

With the rotational speed increases, the average particle size was decreased first then followed by an increase. For the experiment carried out in air, with rotation speed increased from 120 to 175 and further to 235 rpm, the average particle sizes first decreased from 130 nm at 120 rpm to 93.1 nm at 175 rpm, but an unexpected increase to 113.5 nm was observed when speed was increased to 235 rpm. This might be explained by the travelling speed of particles went through the working tube, which could be reflected by residence time. With the rotary speed increasing, the minimum residence time of the particles decreased from 5 to 3 min and maximum residence time decreased from 15 to 10 min. However, after the speed reached a very high value as 235 and 260 rpm, most of the particles tended to just roll inside the tube rather than to move forward. Thus, at the speed of 235 rpm (800°C in air, 113.5 nm) and 260 rpm (800°C in Ar, 76.4 nm), only 33% of the particles reached the exit, compared to 50 % at speed of 120 rpm and 175 rpm (800°C in air, 93.1 nm).

With knowledge gained previously that it is easier for larger particles to reach the exit, it is not difficult to understand that the average particle size of the top 33% big particles in experiment 5 (235 rpm, 800°C in air, 113.5 nm, Figure 4-31) would be larger than that of top 50% big particles in experiment 4 (175 rpm. 800°C in air, 93.1 nm, Figure 4-30) if there is no huge difference in the overall average size.

The results also indicated that a higher rotation speed did not always lead to less agglomeration. Detailed discussion will be introduced later in Section **4.5.3**. Another conclusion to be drawn from experiments 1, 2 and 3 is that temperature has less effect over the residence time than that of the rotary speeds.

As the actual experiment condition is quite different from the experiments above, practical investigation should base on the real experiments conditions. But the above experiments also offered some assistance for the real experiments, for example, as to how to keep the powders in the working tube area for desired time. It is likely that a higher rotation speed and a smaller inclination angle could be applied at the very beginning, and then switches to lower and zero angle or even to negative angles, which will allow for controlling the particles moving forward and backward, according to different situations. In addition, the travel direction could also be controlled by the rotating direction, either clockwise or anticlockwise in turns. Useful information has been obtained from these simple simulations and validation experiments.

4.5.3 Dynamic particle movement

The particle movement within the rotary tube will be discussed based on the above speed investigations.

In the rotary furnace, the precursor WO_3 particles are set into motion by the rotation of the quartz working tube (kiln). The bed motion in rotary cyclinders/kilns have been intensively studied, both theoretically and experimentally [144-146, 153-155]. The dynamic similarity of the rotary kiln behaviour has been indicated by Rutgers in 1965; and the type of transverse bed motion is established by the rotational Froude number [155], which is defined by:

$$F_r=\omega^2R/g \qquad \text{Equation 4-2}$$

where ω is the rotation rate (s^{-1}), R is the inside radius of the cylinder (m) and g the acceleration rate due to gravity (9.81 ms^{-2}). Thus, for a given system, with the rotation speed ω increasing, F_r is increased, which leads to the occurrence of several different flow patterns in a rotary kiln [145, 146, 153, 156], as shown in Figure 4-34.

These flow patterns were displayed in the order of slipping, slumping, rolling, cascading, cataracting and centrifuging. Generally, in a given system, they take place in an ascending order with increasing the rotation speed or in other words, F_r.

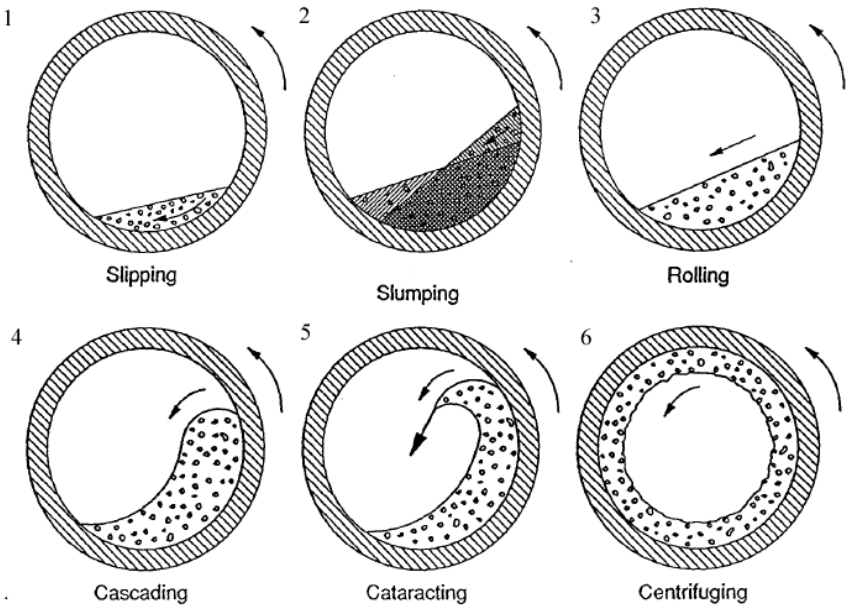

Figure 4-34 Basic flow patterns of the granular bed in a rotary cyclinder [144, 156]

Slipping occurs at very low rotation speed, with the absence of shear rate in the granular bed. With the rotaional speed progressively increased, the motion of the bed will turn over from slipping to slumping, where in the former case, the majority of the particles slip against the wall; whilst in the latter, particles moves down discontinuously at the free surface of the bed. There is a very thin layer formed of particles moving down discontinuously; whilst a very thick zone below still consisted of particles move upward.

Rolling will take place with further increasing the rotational speed, in which the discharge of the particles onto the free bed surface becomes continuous and steady, though all particles are still in the lower half of the transverse plane of the tube [157]. The flow will transfer to the cascading mode, when the bed surface starts to arch as the rotational speed further increases. Some particles would be transported upwards to the upper half of the transverse plane of the tube before they are moved down to form the top layer.

At very high rotational speed, individual particles are detached from the bed and ejected into the free space of the cylinder, which is a characteristic feature of a cataracting motion. The centrifuge motion would occur in the case of further increases of the rotational speed, and is characterised by the particles on the outer paths starting to adhere to the wall. Normally in a ball mixing application, cataracting always dominates. However, both the cataracting and centrifuge mode are not a relevant form in rotary kilns.

The transverse flow motion also varies for different materials [158]. The motion of carbon in a rotating drum has been studied in a report, and the bed behaviour diagram shows that the motion performance of CNTs is similar to sand; whilst the catalyst exhibits a similar motion to limestone [148].

In practice, the slumping, rolling and cascading mode dominate in the application of the rotary kilns and reactors, rotary dryers and coolers, mixing drums and etc. [144, 146, 157]. However the slipping mode has no use at all. In a slipping mode, no particle mixing would occur. Hence this flow pattern is undesired though it is difficult to be avoided in every case, and may at least take place partially in some production processes. In most of the applications, slipping could be prevented in practice through the application of rough walls or rods attached to the wall.

In the present work, the inside wall of the working quartz tube is very smooth, further modification will be made by attaching rods to its inside wall (Figure 4-36), to increase the friction between the particles and the tube, thus preventing the unfavourable slipping mode.

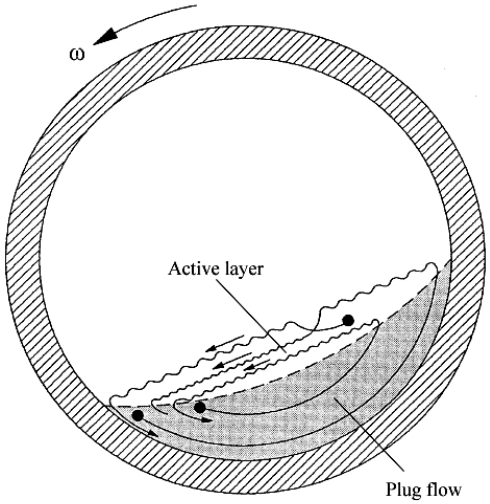

Figure 4-35 A rolling bed motion consisting of two distinct regions [144, 156]

In the rolling mode, which is prefered in most kiln operations, there are two distinct regions (Figure 4-35): the thinner shear region (active layer) which is formed by particles flowing down the sloping upper bed surface, and the thicker non-shearing (plug flow) region formed by the remainder of the particles carried upwards by the rotating wall of the cyclinder [146]. All the particles are involved in plug flow and then active layers consequently take places in turns. As discussed above, the active layer has also occurred in the slumping mode, though it is not a continuous layer yet. In this way, the energy imparted by the cylinder's rotation will be continuously fed into the plug flow region as potential energy, which will then subsequently be released and dissipated in the active layer. The rolling mode provides best conditions for the heat transfer in high temperature processes, even in high filling percentage, a uniform, high quality of the product could be achieved [144, 156, 159, 160].

This work provides a vivid example of rotary bed reactor applied in the large scale manufacturing of nanomaterials, as an alternative to the huge fluidised bed reactor. During the process, similar to other rotary kiln applications, it is believed that rolling and cascading motions dominant for nanoparticles, as the applied rotational speed is very high (no less than 120 rpm). This would enable a uniform heat transfer in addition

to a sufficient and uniform exposure/contact of the WO_3 with the reaction gas H_2S, and well-mixed precursors and products in progress, leading to minimized agglomeration and nano-sized IF- WS_2 products.

In addition, the particles residence time, or it could be called reaction time in this rotary tube reactor, is determined by both the rotation speed and the inclination angle [150, 161]. During measurements, the residence time is defined by the average time needed for the product to reach the reactor exit. In the experiments carried out in Section **4.5.1**, the inclination angle was fixed to tan θ=0.008~1.5^o, while a decrease in the residence time of the particles was observed with the increase of the rotational speeds. In the reactor, the inclination angle could be varied both by adjusting the height of the supporting frame thus height of the quartz tube at the passive transmission end, as discussed in Figure 4-3 in Section **4.3**, and by tilting the furnace with an underlay beneath the bottom of the furnace at one end.

The above discussion as to how the transverse cross section behaviour changes with the increase of rotary speeds has further confirmed our basic speed investigations in Section **4.5.2**. In addition, it implies that further modification would improve the performance of the reactor.

4.6 Further modification of the rotary system

4.6.1 Modified tube for increased friction

To improve the batch yield and quality of this rotary reactor, several modifications were attempted. For an example, high frequency and low amplitude vibration generator has been considered, but the noise and environmental unfriendly feature makes it not a preferred technique here.

Based on the study of the transverse dynamic particle movement in a rotary bed reactor (Section **4.5.3**), to avoid prevent the unfavourable slipping mode and improve the mixing performance of particles, it is decided to increase the friction of the inside tube wall. This can be realised either by rougher the wall or add baffles. In this circumstance, adding rod within the rotary tube as baffles would be a feasible and preferred choice.

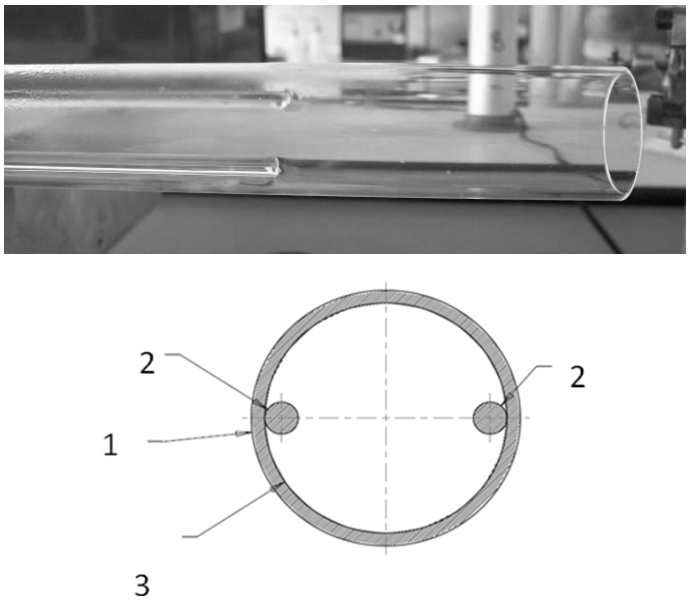

Figure 4-36 Image (top) and sketch (bottom) of a new tube with baffles inside, created by adding two quartz rods inside the normal quartz tube

Herein, a change in the reaction quartz tube itself was made. As shown in Figure 4-36, on top of a normal quartz tube (i. d. 36 mm, o. d. 40 mm) (1), two small quartz rod blades with diameter of 5 mm (2) have been oppositely attached to the inner wall, to force the movement of powders inside reactor. This may help separate the particles from agglomeration. In fact, this newly designed quartz tube has led to the yield increase from around 5 to 15 grams of WS_2 per batch, without obvious compromising in the quality of the products. The results will be presented later in Chapter **6**.

Actually, with the attachment of the two quartz rods as a baffle in the inside wall, the movement of particles would be a mixture of rolling and cataracting (Figure 4-37). When the baffle travels away from the particles, the movement of particles follows the pattern of rolling, with all the particles involved in the plug flow fused into the active layers consequently in turns (Figure 4-37a). Even the plug flow would become more active when the baffle was knocked into the plug flow. At the moment the baffles run against the upper part of the plug flow, the particles would be separated from the wall and thrown down to the free space, which means a cataracting mode has occurred (Figure 4-37b) though it is a discontinuous and localized process.

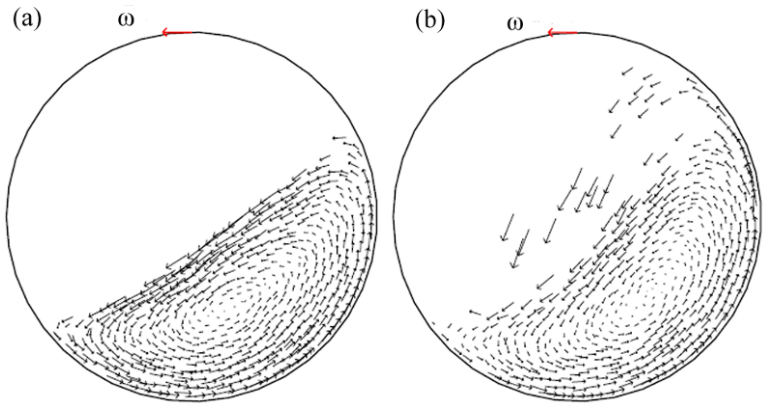

Figure 4-37 Velocity of particles in a transverse cross-section (a) rolling regime (b) cataracting regimes, for visual clarity, magnitude of velocity vectors has been scaled (adapted from [153]).

In this way, when the filling degree is increased, a uniform heat transfer, sufficient H_2S-WO_3 contact, and a well-mixed precursor, partially or completely sulphidised products can be obtained. All these functions will avoid the sintering of WO_x and lead to the desired nano-sized WS_2 products, at high batch yield.

4.6.2 New feeding system

By introducing the baffled new tube, the batch yield has been improved to 15 grams for the IF-WS_2 final products per batch. However as the mixing efficiency drops with the increase of filling degree [153], a higher amount of WO_3 precursor input would leads to less effective mixing and thus compromise in quality of final product. Thus the batch yield is limited by the quantity of feeding precursor at the beginning of each batch.

In order to move the batch process to a continuous production, a continuous feeding system is required. Two types of feeding mechanism had been considered, either feed by screw or by piston mechanism [162-164]. However a screw feeder, possibly could do, is not cost effective in the current laboratory scale trial.

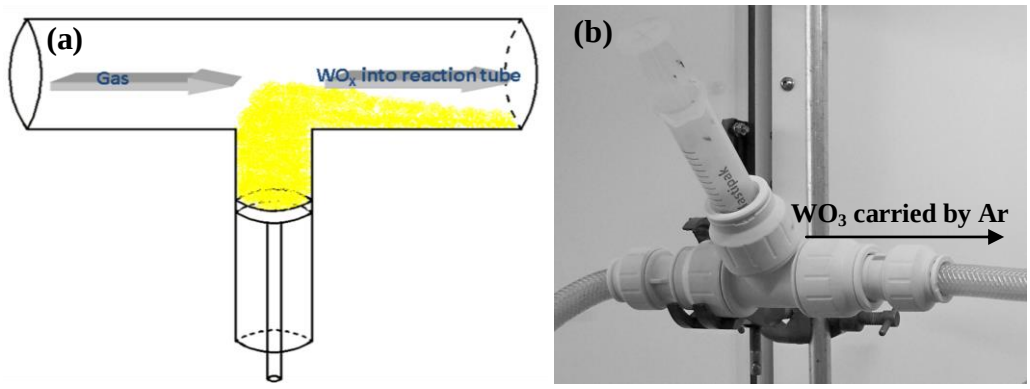

Figure 4-38 Sketch (a) and picture (b) of a new gas blow feeding system, aiming to continuous production

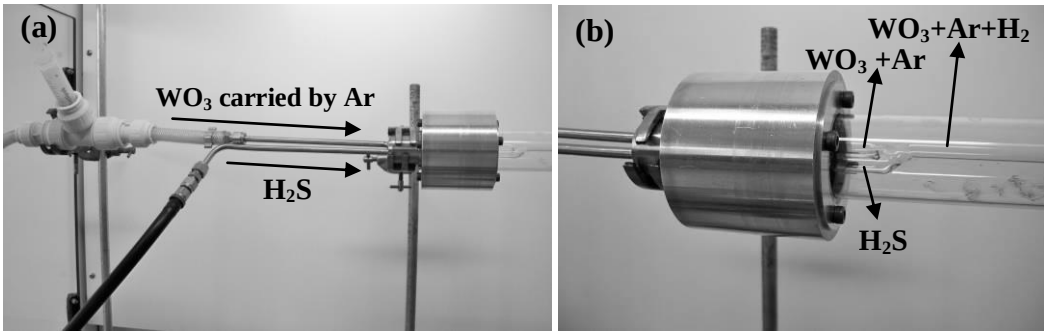

Figure 4-39 Assembled gas blow feeding system. (a) Assembled feeding system and (b) extended V shape leading tube

A syringe piston feeder has been designed as shown in Figure 4-38, made of a syringe of 20 ml connected to a push type 'T' push junction.

Figure 4-39 shows the assembled gas blow-piston feeding system. A stainless steel tube was connected to the second hole left on the shaft for material feeding. The syringe feeder is connected between the gas inlet and the stainless steel tube, and the compressed Ar will be introduced to blow the particles from the nozzle of the feeder into the furnace. In order to lead the feeding powders directly to the hot-zone, a v-shape quartz tube connector is designed to extend the outlet end of the shaft, being the pathway for both the precursor WO_3 and H_2S gas (Figure 4-39). Thus, WO_3 have been mixed with reaction gas before entering the hot-zone, allowing for reaction to take place as soon as it reaches the required temperature, and avoiding agglomerates.

Figure 4-40 has shown the modified gas supply system. Based on the gas supply shown in Figure 4-24, a new gas channel for Ar connected by valve 4 was added to the system, to introduce high flow rate of Ar gas to blow the WO_3 nanoparticles into the furnace, thus valve 4 is only switched on during material feeding period.

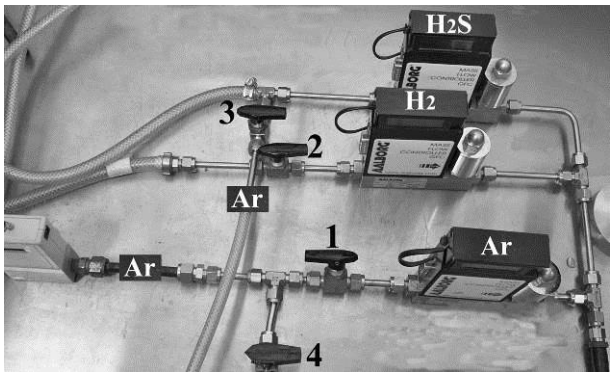

Figure 4-40 Modified gas supply system with gas blow branch added

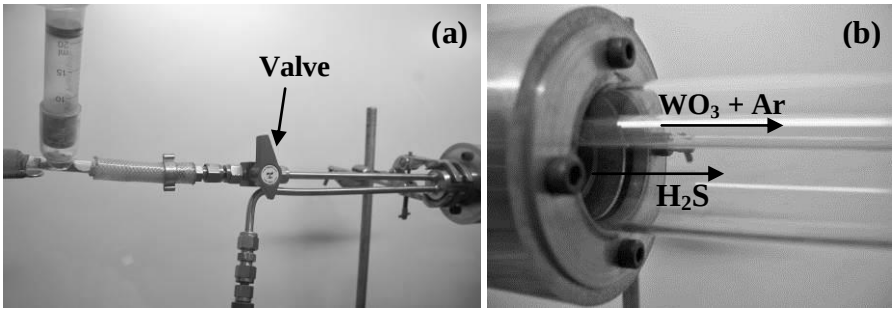

Figure 4-41 Modified feeding system. (a) Valve added for multi-syringe feeding and (b) straight extended leading tube for precursor

Further modification was made to the gas blow feeding system as shown in Figure 4-41 during the optimization for the production of IF-WS_2 nanoparticles, such as an added valve between the syringe and the shaft, and the v shape leading tube changed to straight, the reason for which will be discussed in Chapter **6**.

By applying this gas blow-piston feeding system, WO_3 precursors could be fed gradually into the furnace, which could avoid agglomeration before the first WS_2 layer forms [53, 90]. Compared with all the powder being introduced into the reactor in a batch process, the quality of products will expect to be further improved. The plastic syringe has a volume of 20 ml, contains about 50 g WO_3, which can easily be replaced to contain more and realise continuous production. In fact, by simply adding a valve between the feeder and shaft (Figure 4-41a), the empty syringe had been easily replaced with full ones to realise the 'continuous' feeding during our laboratory trail.

Overall, by combining the baffled tube with the feeding system, the yield was increased to several tens of grams for one run, and could be higher with continuous feeding of precursor. More importantly, this set-up could be easily adopted for continuous industry manufacturing. Of course, the collection of the products at the other end of the reactor

needs to be considered, however, there are numerous examples for such collections [147, 150, 165]. As there is nothing special comparing with existing micro-sized particle collection in this case, therefore no further investigation was focused on this aspect.

4.7 Summary

1. A completely new rotary tube furnace for nanomaterial production has been designed, machined and assembled, which satisfies all the technical requirements, such as speed variation, inclination angle control, proper sealing, sufficient reaction time, multi gases supply etc..

2. Initial validation using WO_3 nanoparticles under conditions similar to real reaction has been carried out and the related dynamic particle movement has been discussed accordingly, which helped to achieve efficient mixing of the particles during the rotary process.

3. Further modification and assessment confirm that this rotary furnace is capable of continuous IF-WS_2 production, and most significantly, this could be easily enlarged to realise scale up.

4. The continuous feeding system and the baffled reaction tube design appear to allow this technique a true contender/alternative process for replacing the tall fluidised reactor, which needs final validation.

Chapter 5 Synthesis of tungsten oxide and tungsten oxynitride nanomaterials

5.1 Introduction

Nanostructured tungsten oxides, WO_x ($2 \leq x \leq 3$), are very promising for applications in electric field emitters [101], catalysts [21, 102], gas sensors [22, 23, 166], and in electro-chromic [26] and electrochemical devices (such as Li-Ion lithium battery) [27, 28]; In particular, WO_x has been considered as the most efficient precursors for another type of very useful materials, namely the WS_2 IFs or INTs [1, 6, 18-20].

Accordingly, diverse approaches have been investigated for the WO_x growth, typical examples including a direct heating of W wire/tips/foil with SiO_2, O_2, and water vapours under N_2, Ar or vacuum, such as heating a tungsten wire partly wrapped with B_2O_3 in N_2 atmosphere at 1600°C [167], heating an electrochemical etched W tip at 700°C in an Ar atmosphere [30], heating a W foil, partly covered by a SiO_2 plate, in an Ar atmosphere at 1600°C [29], oxidizing W filaments and in-situ evaporating via an infrared irradiation heating at 950-1000°C [31], simple electric heating the carbon-covered W under a vacuum of 5×10^{-4} Pa [168], as well as hydrothermal reactions starting with W-containing salts, for example, solvothermal treatment of WCl_6 with ethanol [32], pyrolysis of $NaWO_4$ with $(C_3H_7NO_2)_n$ [169], and microwave decomposition of APT [170].

In short, earlier efforts have been focused on using metallic W or W salt to produce appropriate forms of WO_x, nanospheres or nanorods/wires. In our work, studies would be focused on the production of 0D, 1D WO_x nanostructures using simple, effective methods, with better quality, and on the investigation into the growth mechanism to gain a deeper understanding and to achieve materials with desired morphology.

5.2 WO_x nanoparticles produced by the decomposition of APT

In this part, WO_x nanoparticles, as an important precursor for IF-WS_2 nanoparticles, will be produced by the decomposition of APT at high temperatures.

5.2.1 Experimental

APT was firstly located in the hot zone of the quartz tube, and a collector was placed in the downstream 40 cm away from the APT source. Kept flushing Ar gas at a flow rate of 50 ml/min before the temperature reached 1350°C, and then increased the flow rate to 2-6 L/min for about 30-45 min during reaction. Finally, the furnace was cooled down to room temperature with the flushing Ar. The particles were collected separately from different areas.

Different reaction temperatures (1350°C and 1400°C), quartz tube with different lengths (1 and 1.5 m), different Ar flow rates (2-6 L/min) as well as different reaction time (30-45 min), have been applied to investigate the decomposition of APT.

5.2.2 Results and discussion

The reaction happened within the furnace at high temperature (1350-1400°C) is shown as following: $(NH_4)_{10}[H_2W_{12}O_{42}]\bullet 4H_2O \rightarrow 12WO_3 + 10NH_3 + 11H_2O$

During the heating process, the APT will start to decompose into WO_3 at 500°C, following the above reaction. WO_3 will start to melt and vaporise in the central area upon temperature reaches 1200°C and 1250°C respectively, and the WO_x vapour would be brought downstream by Ar flow and deposited at the inner wall of the quartz tube.

The particles collected from different areas of the inner wall of the quartz tube were examined carefully under SEM. 3 different areas are studied, sample holder in hot-zone- Zone O; area 30-40 cm away from central hot zone- zone B; and area 40-50 cm away from central hot zone- zone A.

SEM images for WO_x particles collected from different areas of the quartz tube are presented in Figure 5-1. Black powders collected from zone O were shown in Figure 5-1a and b, and those powders are micro-sized, with some of them reach 50 μm. Figure 5-1c and d showed the particles collected from zone B the size of which ranged from very fine nanoparticles around 50 nm to very coarse polyhedrons up to 500 nm. However the particles collected from zone A are of very uniform size, with the majority less than 50 nm, though very few particles have size up to 150 nm could still be observed (Figure 5-1e and f). Thus a clear trend has been indicated that the closer the deposition area to the hot-zone, the bigger the particle size. This is because at the area

closer to hot-zone, the high concentration of WO_3 vapour and high temperature is favourable for WO_3 to nucleate and grow. However for those vapour brought far away from the hot zone, it is more difficult for them to grow bigger after deposit on the low temperature area.

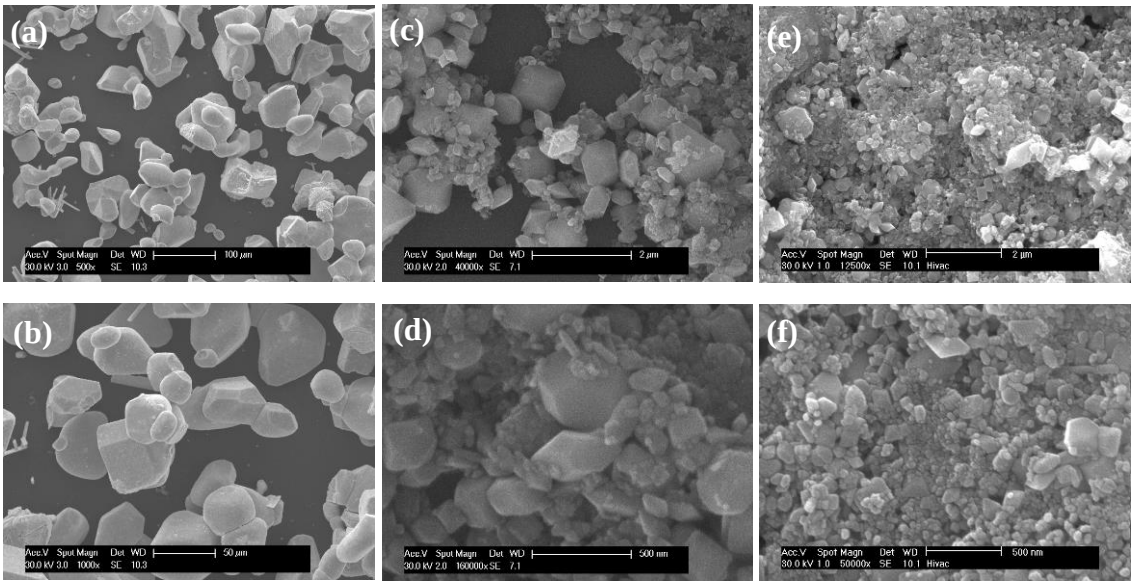

Figure 5-1 SEM images of WO_x nanoparticles collected from different deposition areas, under the condition of 1350°C, 1 m, 45 min, 2 L/min. (a) and (b), black powders left in the holder at hot-zone (zone O); (c) and (d), collected from area 30-40 cm away from hot-zone (zone B); and (e) and (f), particles collected from area 40-50 cm away from hot-zone (zone A). Scale bar: 100 μm for (a), 50 μm for (b), 2 μm for (c) and (e), and 500 nm for (d) and (f)

SEM images for WO_x nanoparticles produced under different gas flow rates were shown in Figure 5-2, and the particles size has been decreased significantly from around 100 nm to around 50 nm with gas flow rates increased from 2 L to 6 L, as well as the uniformity of size distribution. As there are some coarse particles with size of 300 nm among those fine particles in Figure 5-2a, while only uniform, round particles were observed from Figure 5-2c. Similar to the influence of temperature zones (deposition areas) on the particles size, the higher flow rate could carry more WO_3 vapour away to the low temperature area, less vapour was thus left in the high temperature area to grow into big agglomerates, hence the more finer of the particles resulted.

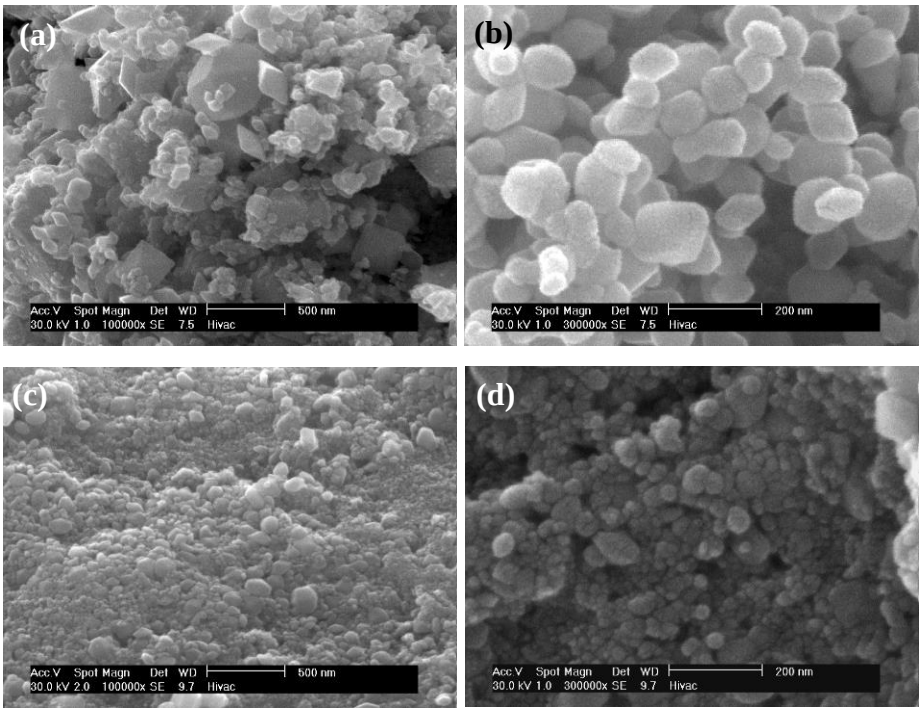

Figure 5-2 SEM images of WO_x nanoparticles produced by using different gas flow rates (1350°C, 1.5 m, 30 min; (a) and (b), from gas flow rate at 2 L/min, (c) and (d), from gas flow rate at 6 L/min)

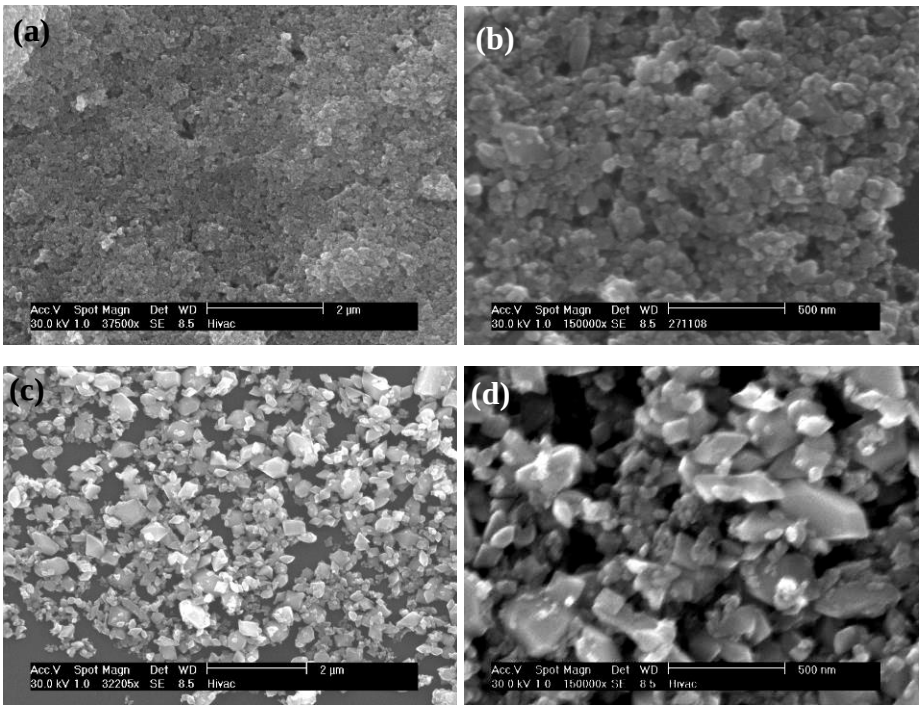

Figure 5-3 SEM images of WO_x nanoparticles produced by different reaction time (a and b, 30 min; c and d, 45 min; 1400°C, 1.5 m, 5 L), collected from zone B

WO_x nanoparticles produced by different reaction times were demonstrated in Figure 5-3. The particles synthesis after 30 min (Figure 5-3a and b) possess much smaller size

than particles produced from 45 min reaction time (Figure 5-3c and d), especially more polyhedral particles with size over 300 nm in the maximum dimension present after longer reaction time. This indicates the continuous growth of tungsten oxide particles during the whole reaction period.

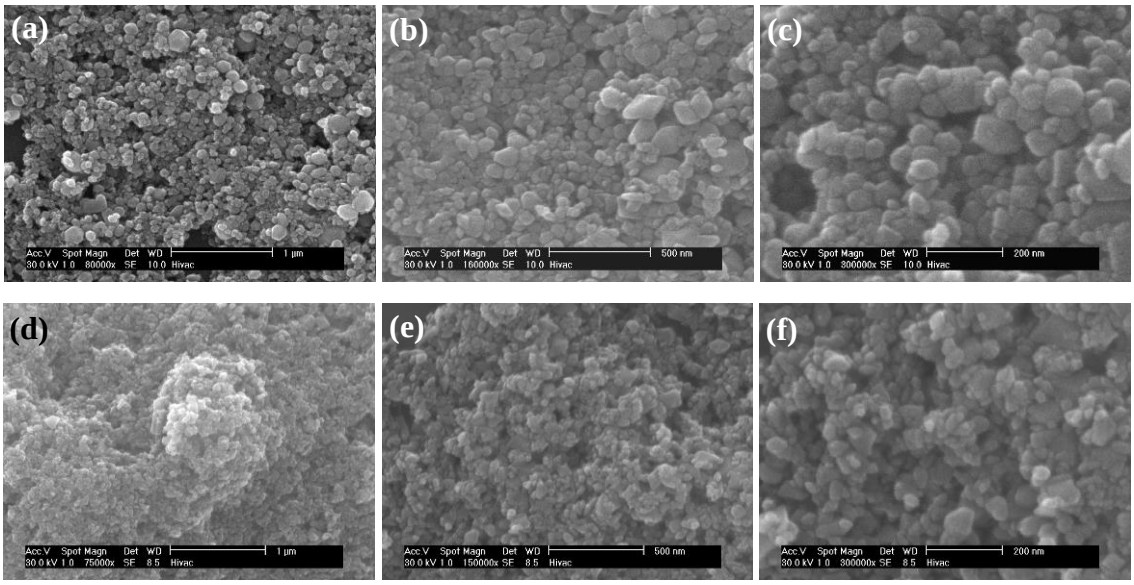

Figure 5-4 SEM images of tungsten oxide nanoparticle (a, b and c, 1400°C, 6 L/min, 30 min, 1.5 m) and (d, e and f,) (1350°C, 6 L/min, 30 min, 1.5 m). Scale bar: 1 μm for (a) and (d), 500 nm for (b) and (e), 200 nm for (c) and (f)

All these SEM photographs in Figure 5-4 show spherical nanoparticles within 100 nm, mostly around 50 nm. Maybe the proportion of smaller particles in Figure 5-4d, e and f is slightly higher than that in Figure 5-4a, b and c, at the same time. Polyhedral particles present in all images but more was observed in Figure 5-4a, b and c. This indicated that more small spherical particles and less polyhedral particles have formed at lower temperature 1350°C than that at higher temperature 1400°C.

The temperature increase showed not only increased particles size, but also decreased yield. This is because, as temperature increasing, the evaporation of WO_3 increased, higher concentration or saturation is favourable for WO_3 to nucleate and grow in high temperature area. Thus more microsized particles would form in hot-zone, and even those deposited onto the low area have bigger size.

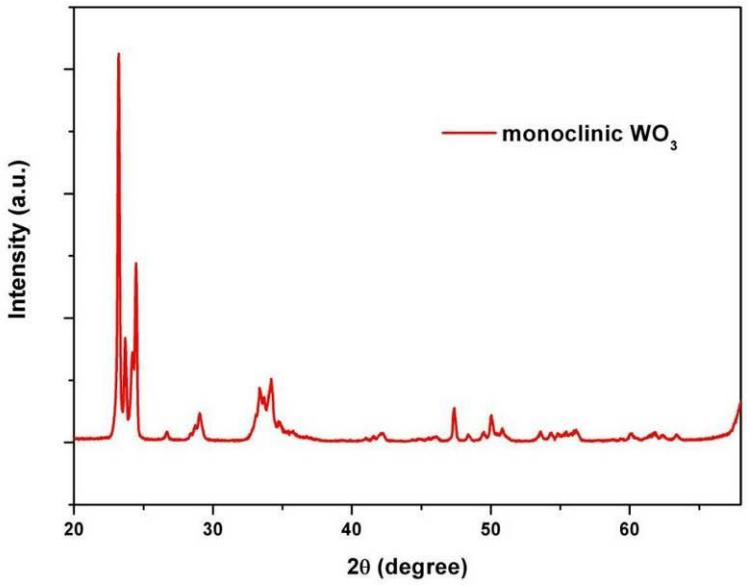

Figure 5-5 XRD profile for WO_3 from decomposition of APT (1350, 1.5 m, 6 L/min, 30 min)

XRD has been applied to analyse the products from the decomposition of APT, and a typical profile is shown in Figure 5-5, which matches very well with monoclinic WO_3 (JCPDS No. 43-1035), with the strongest peaks appear at 23-25 degree.

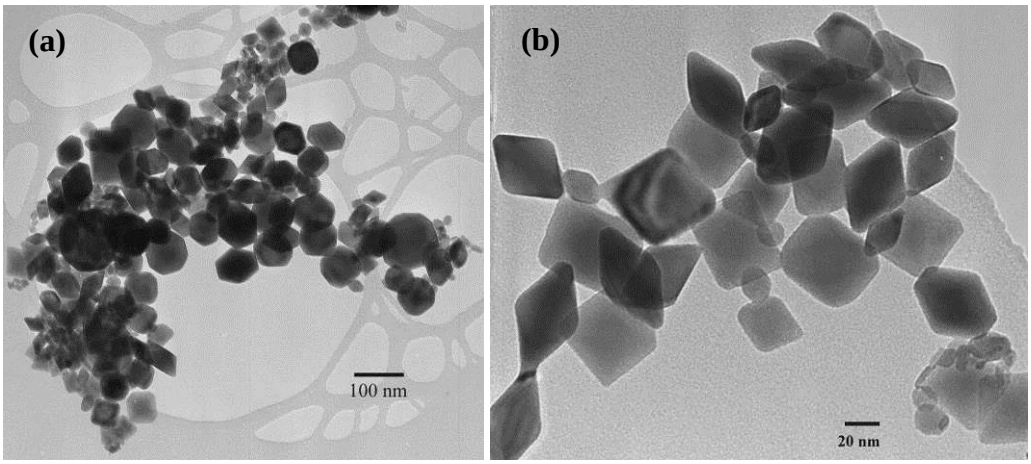

Figure 5-6 TEM images of WO_3 from decomposition of APT (1350, 1.5 m, 6 L/min, 30 min)

Figure 5-6 shows the TEM images of WO_3 nanoparticles from the decomposition of APT. The majority of nanoparticles are of a polyhedral shape, with the size uniformly distributed around 50 nm.

Table 5-1 Influence of different parameters on the product

Parameters	Change	Yield	Quality
Flow rate (L/min)	2-6 ↑	Increase(s)	Increase(s)
Length of quartz tube (m)	1-1.5 ↑	Increase(m)	Increase(s)
Reaction time (minute)	30-45 ↑	Increase(w)	Decrease(w)
Reaction temperature(°C)	1350-1400 ↑	Decrease(s)	Decrease(w)

*: (s) strong effect; (m) moderate effect; (w) weak effect

As summarised in Table 5-1, the increase of Ar flow rate and length of quartz tube will lead to increase of both quality of nanoparticles and batch yield, however with the increase of the reaction time, the yield will be increased with decreasing in particles quality. With the increase of reaction temperature, the quality has not been improved further, but the yield has been decreased dramatically.

5.3 WO_x nanowires prepared by solvothermal method

5.3.1 Experimental

Different parameters were used for our solvothermal experiments: temperature was fixed at 200°C based on previous studies, reaction time varied from 2 to 6.5 h, the concentration of WCl_6 varied from 0.002-0.004 M. The solvents used include cylcohexanol, ethanol and mixture of both. Table 5-2 has summarised the experimental parameters used for all the solvothermal synthesis of WO_x nanowires.

Table 5-2 Experimental parameters for solvothermal synthesis of WO_x nanowires

Sample names	Solvent 50 ml	Concentration of WCl_6 (M)	Time of reaction (hour)
A	Cyclohexanol	0.002	2
B			3
C			4
D			5
E			6
F		0.003	2
G			3
H			4
I			5
J			6
K			6.5
L		0.004	2
M			3
N			4
O			5
P			6
Q	Ethanol	0.002	5
R			7
S			8
T			9
U	Cyclohexanol 50 ml + ethanol 25 ml	0.002	5.5

5.3.2 Results and discussion

5.3.2.1 WCl_6 as precursor and cyclohexanol as solvent

As listed in Table 5-2, experiments A-P were carried out using WCl_6 and cyclohexanol as precursor and solvent, based on WCl_6 concentration from 0.002-0.004 M, and reaction time from 2-6 h. Figure 5-7 are typical EM images of the as-synthesised solvothermal nanowires from WCl_6 and cyclohexanol precursor. The SEM image of $W_{18}O_{49}$ nanowires is shown in Figure 5-7a, highly pure and uniform nanowires were produced, with a high aspect ratio. These nanowires are proved to be bundles comprising of nanowires with diameter of 2-5 nm, under TEM characterisation (Figure 5-7b). The characterisation is similar to the results reported in our previous publications [33, 41]. Large surface area contributes to this bundled feature, as often observed in thin and long 1D nanostructures [170].

Individual nanowires within the bundle are parallel to each other and adopt the same growth direction. This is further confirmed by the SAED pattern (top right inset, Figure 5-7c), in which a typical characteristic of bundled 1D nanostructured materials, broadened and stand spots, is exhibited. The growth direction of the nanowire is perpendicular to the broadened spots. High-resolution TEM (HRTEM) images of the nanowires are presented in Figure 5-7c and d. The lattice spacing along the growth direction is measured to be about 0.38 nm, in excellent agreement with interplanar distance of the (010) plane in monoclinic $W_{18}O_{49}$.

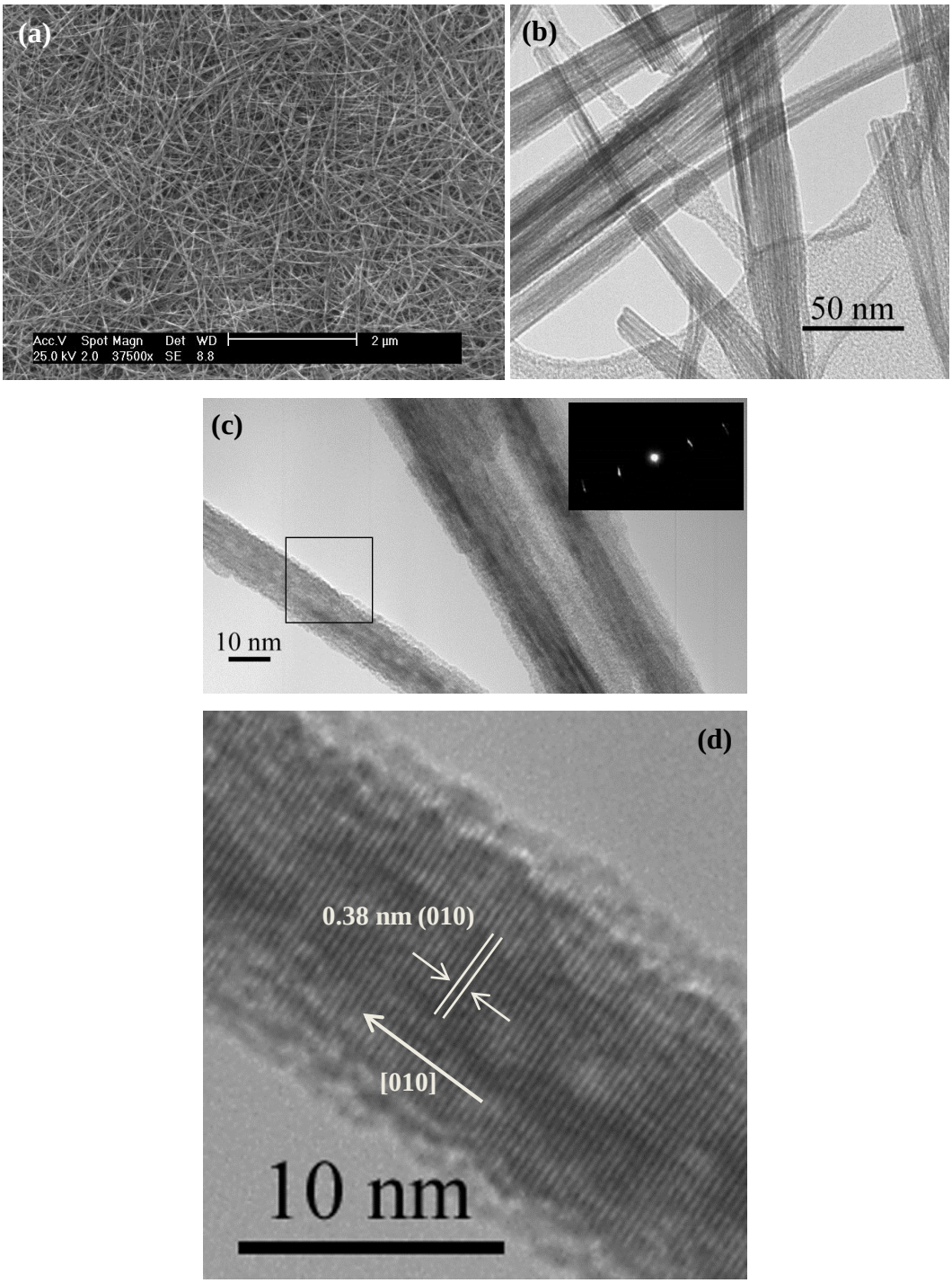

Figure 5-7 (a) SEM, (b)-(c) TEM and (d) HRTEM images of bundled $W_{18}O_{19}$ nanowires from cyclohexanol solvent

XRD diffractions were also carried out for these tungsten oxide nanowires, and a typical result is shown in Figure 5-8. Similar to those from previous works [33, 41], all major peaks assigned to the monoclinic $W_{18}O_{49}$ (JCPDS No. 71-2450). Despite the overall low intensity of the diffraction peak, the (010) peak at 23.49 degree is sharp and the most intense, as the nanowire grows along the [010] direction and the close-packed plane

(010) is perpendicular to nanowire axis direction. Some peaks of the $W_{18}O_{49}$ nanowires are broadened due to very small diameter of the nanowires.

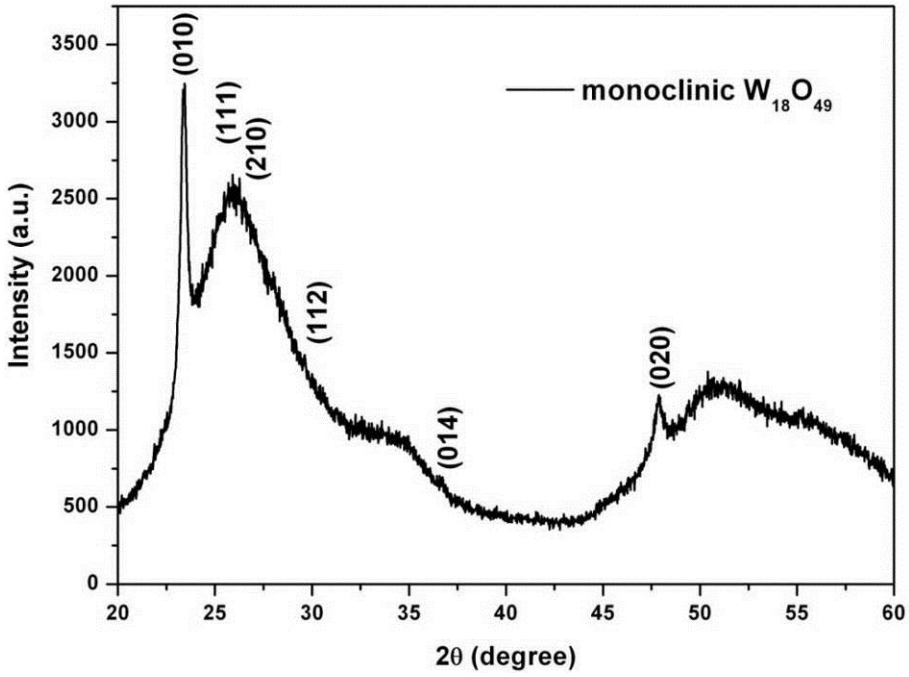

Figure 5-8 XRD patterns of the bundled $W_{18}O_{19}$ nanowires

The influence of time and precursor concentration on morphology of WO_x nanowires has been systematically studied. Figure 5-9 to Figure 5-13 have shown the SEM images of nanowires, based on the order showing comparison of concentration variations at fixed reaction time from 2 to 6 h.

Figure 5-9 shows products after 2 h reaction at 200°C, with WCl_6 concentration of 0.002 M (Figure 5-9a and b), 0.003 M (Figure 5-9c and d) and 0.004 M (Figure 5-9e and f). It is noted that the WO_x nanowires become shorter in length with increased concentration. The average length drops from around 2 μm at 0.002 M to just over 1 μm at 0.003 M, then less than 1 μm with 0.004 M. Though some very short nanowires less than 300 nm are presented in all these samples as well.

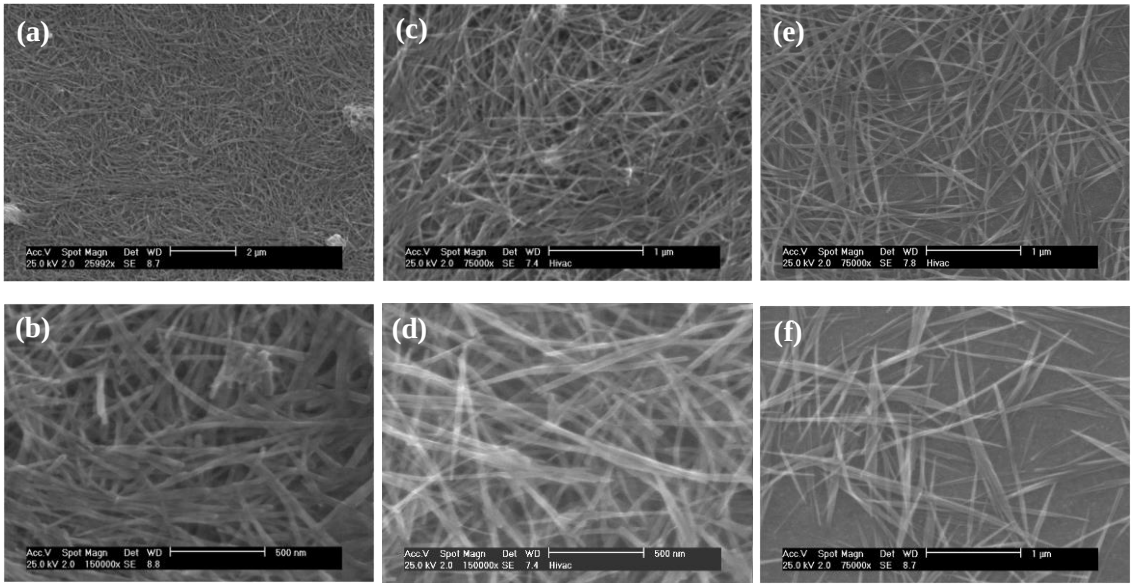

Figure 5-9 SEM images for the nanowires produced after 2 h. (a) and (b) from concentration 0.002 M; (c) and (d) from concentration 0.003 M; (e) and (f) from concentration 0.004 M. Scale bar: 2 μm for (a), 1 μm for (c), (e) and (f), 500 nm for (b) and (d)

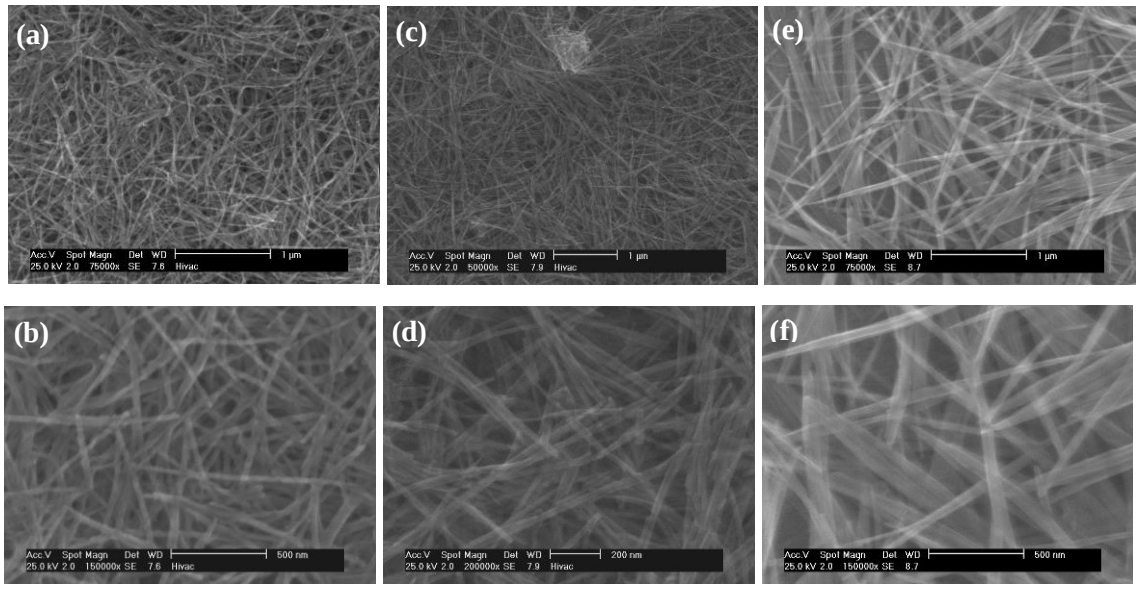

Figure 5-10 SEM images for the nanowires produced after 3 h. (a) and (b) from concentration 0.002 M; (c) and (d) from concentration 0.003 M; and (e) and (f) from concentration 0.004 M. Scale bar: 1 μm for (a), (c) and (e); 500 nm for (e) and (f); 200 nm for (d)

SEM images for products after 3 h reaction are shown in Figure 5-10. The length of nanowires with different precursor concentrations also shows a descendent order with concentration increasing, while the nanowires diameter seems increased with higher

concentration. Though over all the length at each concentration is longer than nanowires from 2 h reaction.

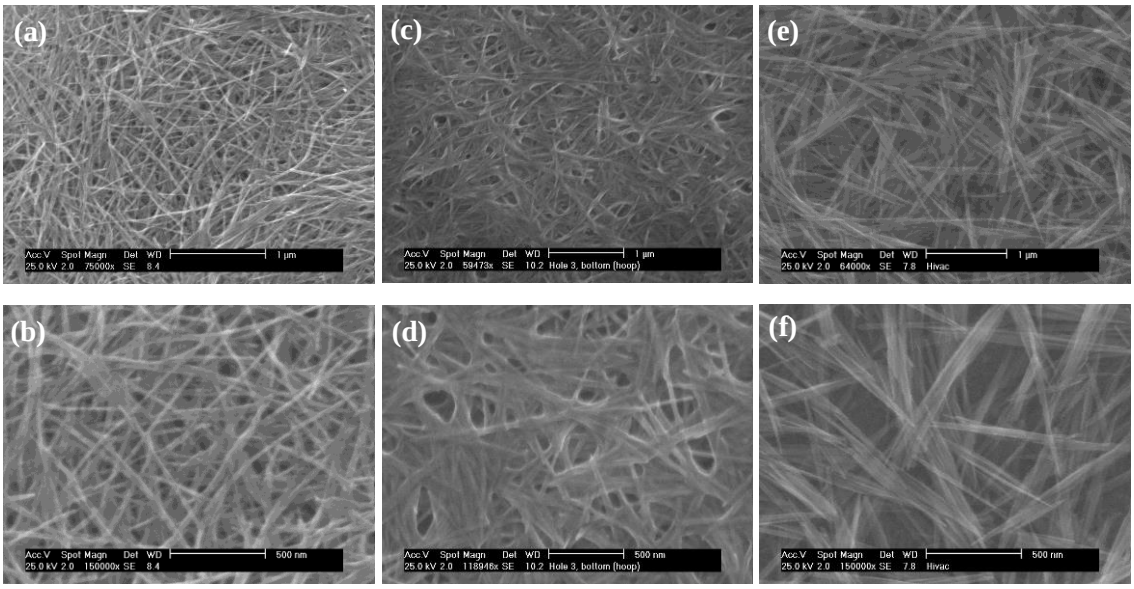

Figure 5-11 SEM images for the nanowires produced after 4 h. (a) and (b) from concentration 0.002 M; (c) and (d) from concentration 0.003 M; (e) and (f) from concentration 0.004 M. Scale bar: 1 μm for (a), (c) and (e); 500 nm for (b), (d) and (f)

The same behaviour has been exhibited by products from 4 h, 5 h and 6 h reaction time as well. That is the descendant of nanowire length and ascendant of nanowires diameter, while increasing precursor concentration from 0.002 M to 0.004 M.

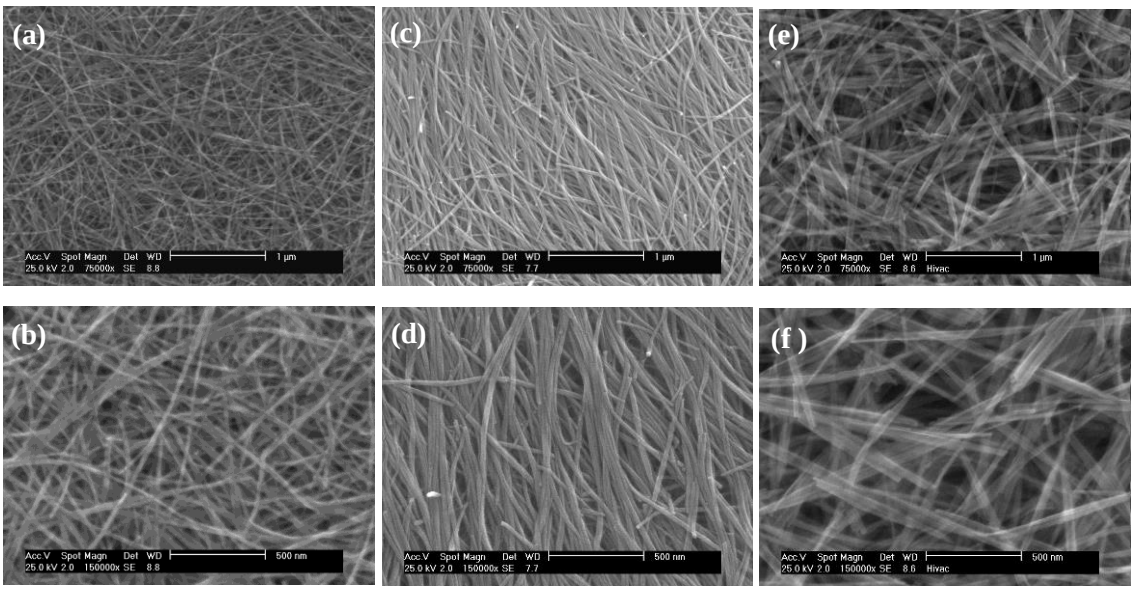

Figure 5-12 SEM images for the nanowires produced after 5 h. (a) and (b) from concentration 0.002 M; (c) and (d) from concentration 0.003 M; (e) and (f) from concentration 0.004 M. Scale bar: 1 μm for (a), (c) and (e); 500 nm for (b), (d) and (f)

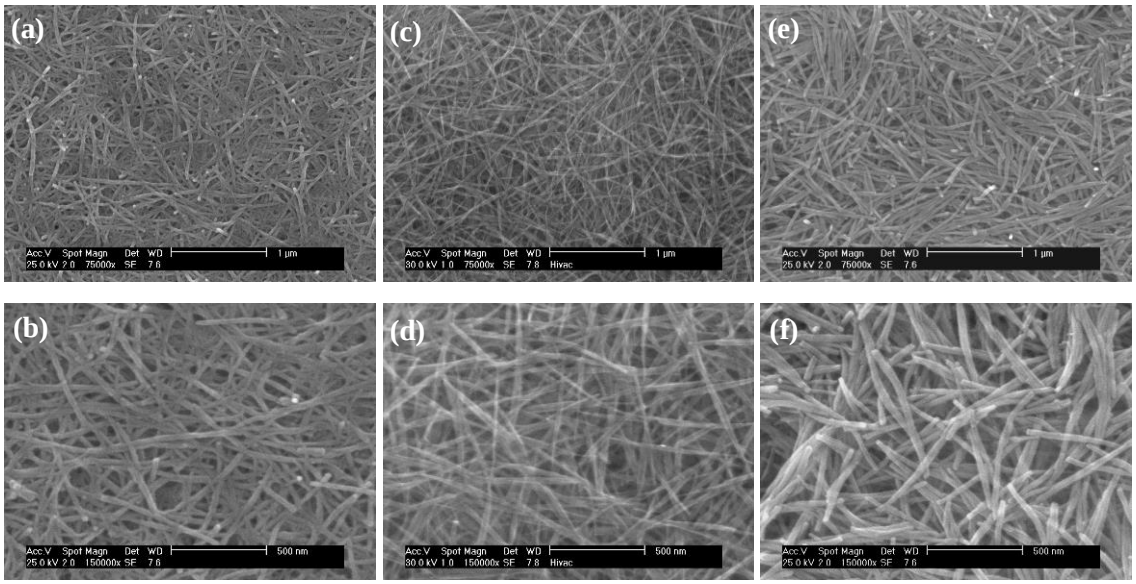

Figure 5-13 SEM images for the nanowires produced after 6 h. (a) and (b) from concentration 0.002 M; (c) and (d) from concentration 0.003 M; (e) and (f) from concentration 0.004 M. Scale bar: 1 μm for (a), (c) and (e); 500 nm for (b), (d) and (f)

It is noted that from all the results, after same reaction time, nanowires bundles resulted from different WCl_6 concentrations exhibit very different morphologies. The same phenomenon has been observed for all 5 reaction times, that is, when concentration of tungsten increases, the bundles diameter increases, but the length decreases. Previous reports have revealed that the morphology of hydrothermal products is greatly influenced by the concentration of the precursors, and this dependence behaviour could be explained by supersaturation of precursor WCl_6 [32, 171]. It was reported that the difference in the relative growth rates of individual crystal planes determines the shape of a crystal, under certain supersaturation, and the resulting products are normally bounded by facets with lowest growth rate [171]. Indeed supersaturation hinders the growth of nanostructures. An increase of tungsten concentration led to increase of supersaturation of tungsten source in solution, which restrained the growth rate. Length growth is slowed down at higher concentrations thus resulting in shorter nanowires, while the bundle diameter increase should attribute to a phenomenon of agglomeration.

Meanwhile, the influence of reaction time on the nanowires has also been investigated when the concentration of WCl_6 is fixed. For each concentration, samples after 2, 3, 4, 5 and 6 h reaction were prepared and observed under SEM, as shown in Figure 5-14 to Figure 5-16.

The products with concentration of 0.002 M after different reaction times are shown in Figure 5-14. The nanowires grows longer and thicker from 2 h to 5 h, but the length decreased for products after 6 h reaction. The same was observed from Figure 5-15 for products from 0.003 M and Figure 5-16 for products from 0.004 M.

For all the three concentrations, the same growth behaviour has been found with increased reaction time. Two growth steps could be defined based on the observation: the first step lasts until 5 h; while the second step starts upon 5 h of heating treatment. At the first step, when reaction the increases, the diameter and length both increase. But at the second step, a dramatic length decrease was observed for nanowires, whilst further increase was kept for the diameter of nanowires bundles.

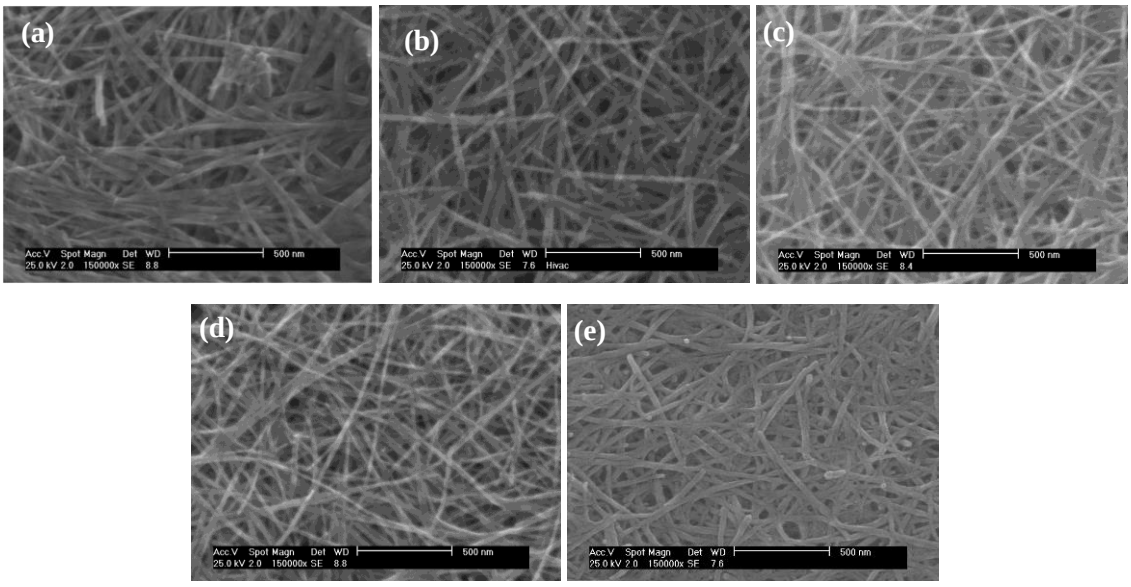

Figure 5-14 SEM images for the nanowires with WCl_6 concentration at 0.002 M, after a reaction time of (a) 2 h, (b) 3 h, (c) 4 h, (d) 5 h and (e) 6 h. Scale bar: 500 nm

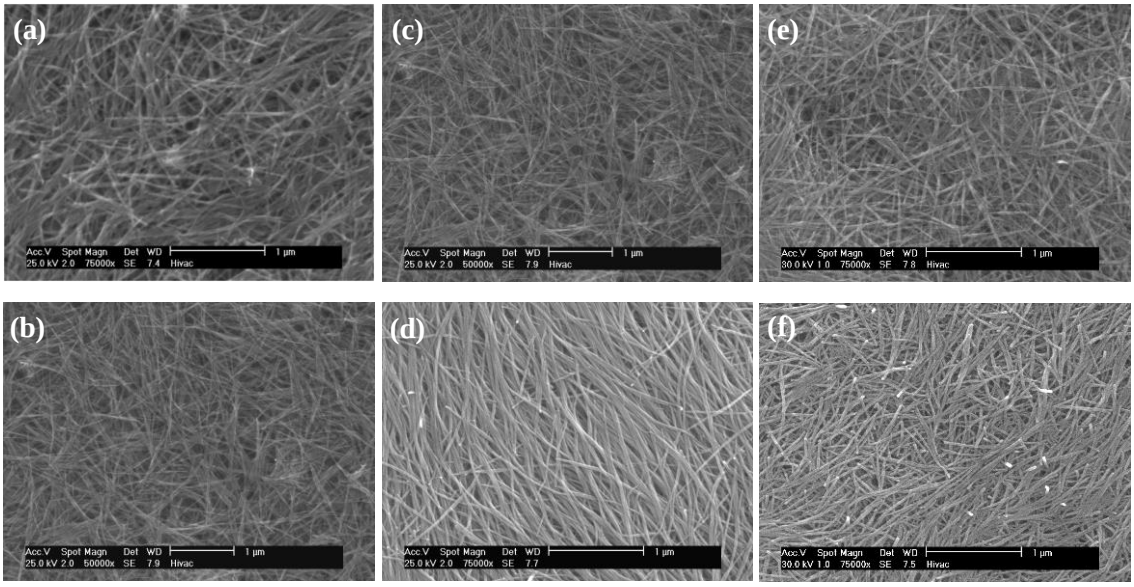

Figure 5-15 SEM images for the nanowires with WCl_6 concentration at 0.003 M, after a reaction time of (a) 2 h, (b) 3 h, (c) 4 h, (d) 5 h, (e) 6 h and (f) 6.5 h. Scale bar: 1 μm

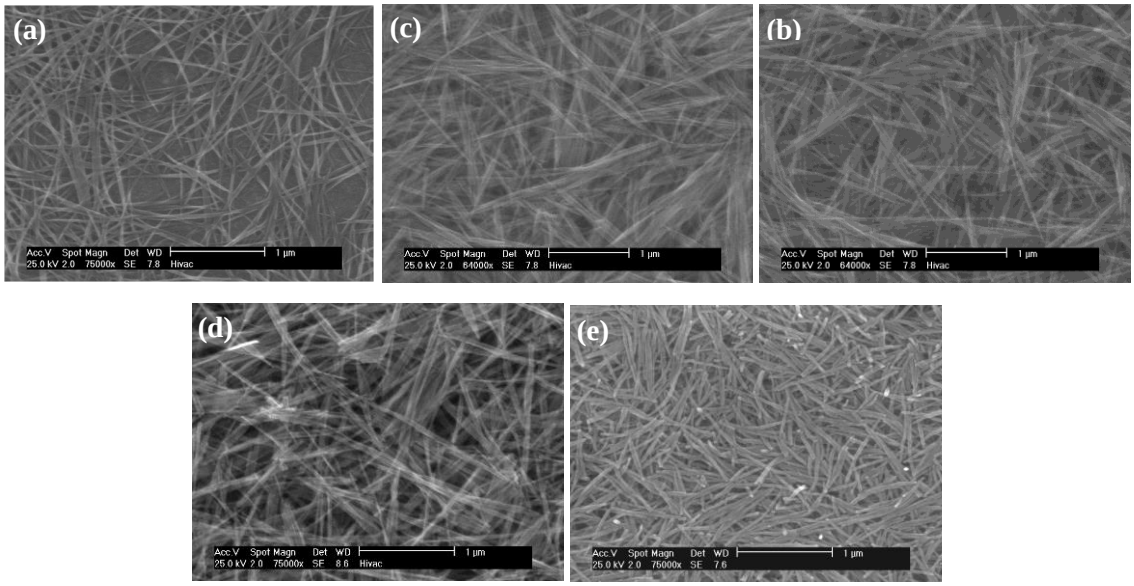

Figure 5-16 SEM images for the nanowires with WCl_6 concentration at 0.004 M, after a reaction time of (a) 2 h, (b) 3 h, (c) 4 h, (d) 5 h and (e) 6 h. Scale bar: 1 μm

The first step occurs up to 5 h which may show an experimental evidence for the growth mechanism. Nothing seems to have hindered the growth. Because the increasing of length (from several hundreds of nanometer to several micrometers) is much more tremendous than that of diameter (ten or so nanometers), the growth can be considered occurring in only one dimension, which is along the axis of nanowires. As revealed by the XRD (Figure 5-8) and TEM results (Figure 5-7), these monoclinic $W_{18}O_{49}$

nanowires grow along <010> direction, which is perpendicular to close-packed plane (010).

At the second step, the decrease of nanowires length has occurred, which is a really interesting phenomenon. This could suggest that the one dimensional growth mechanism was still in control, except the nanowires were broken into shorter ones from a certain length. It implies that a critical length may exist for the nanowires. The breakage could be explained by the defects present in the nanowires, as shown in TEM images (Figure 5-17). Indeed, in a long nanowire, planar defects and shear planes increase with length increasing, and would finally cause the breakage of nanowires when they are too long.

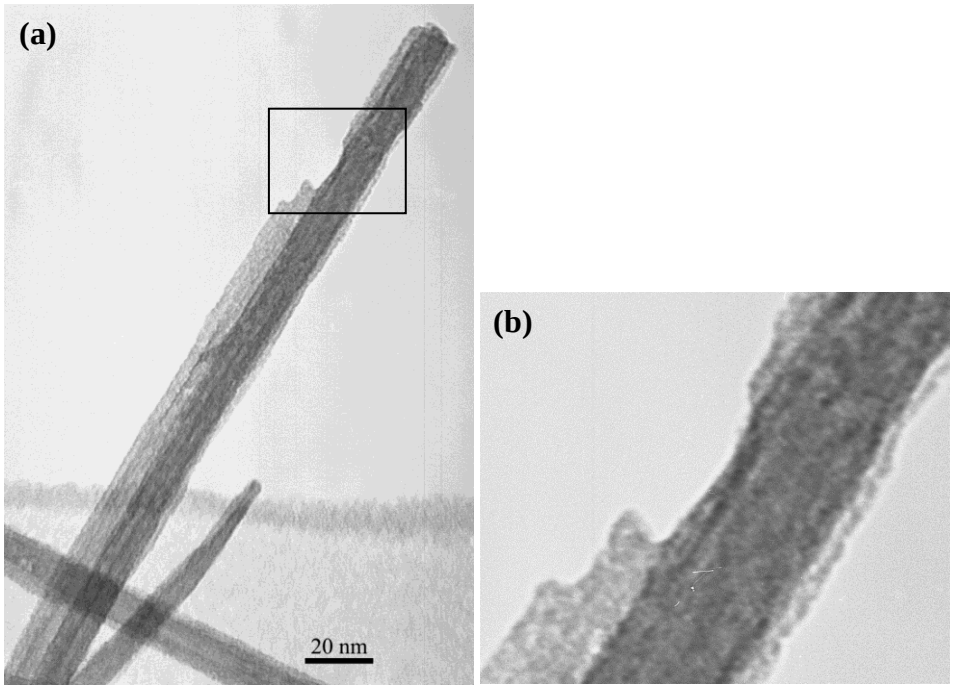

Figure 5-17 TEM images showing the defect in WO_x nanowires, (b) is a zoom in image of the framed area in (a)

Figure 5-17 shows a TEM image of tungsten oxide bundle, very obvious defects could be observed close to the end of the bundles, shown clearly in (b), which is an enlarged image of the frame area in Figure 5-17a. This finding provides evidence for the breakage during their growth for longer than 5 h, where nanowires from 6 h growth are found shorter in length than those from 5 h growth. Though in this particular circumstance, this structure defect could also be resulted from damage introduced during ultrasonic process for TEM sample preparation, as the planar defect within the

nanowires could be promoted by ultrasonic which caused the breakage of long nanowires.

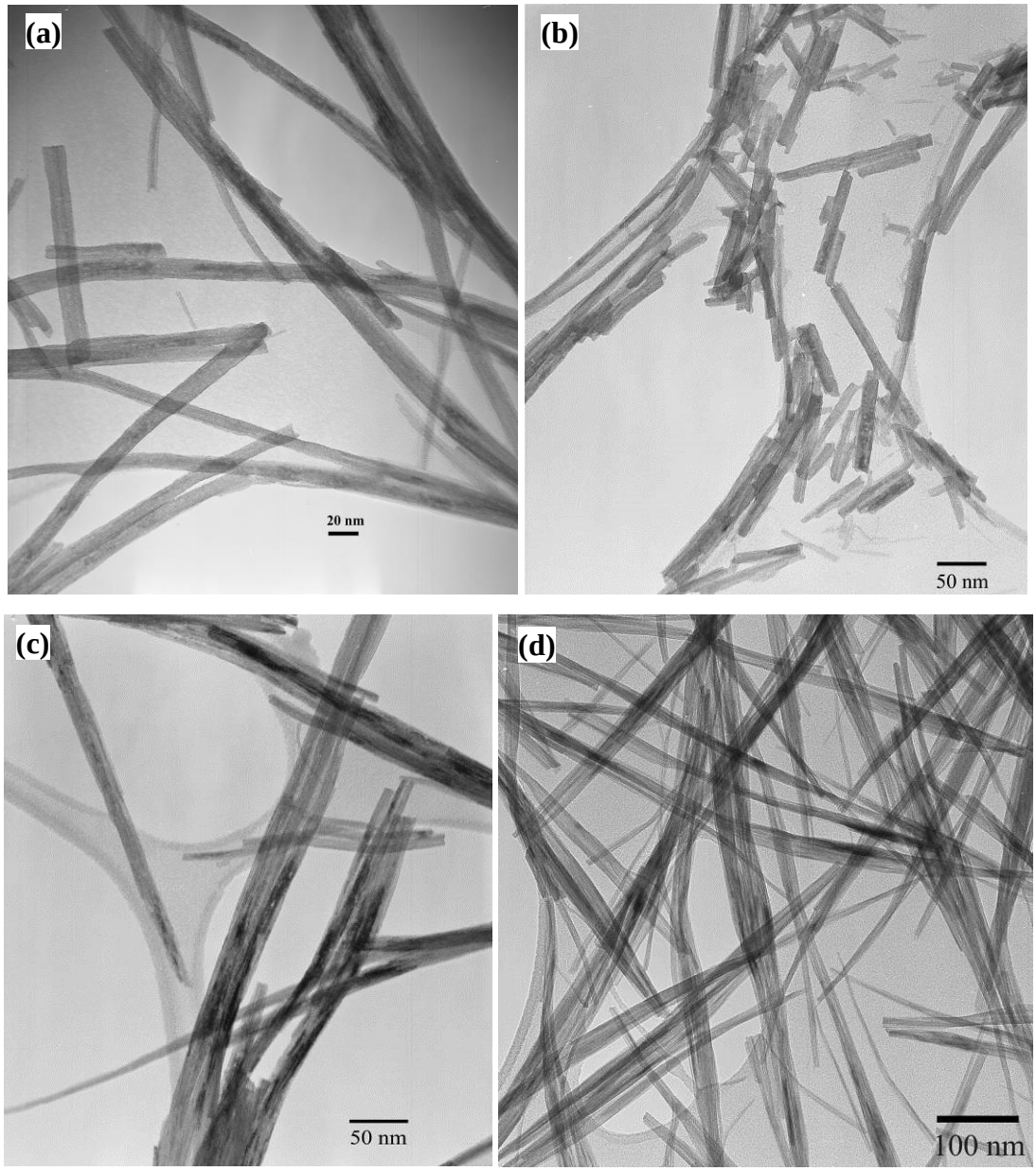

Figure 5-18 TEM images of WO_x nanowires synthesised from different parameters (a) 0.002 M, 2 h, sample A; (b) 0.004 M, 2 h, sample L; (c) 0.003 M, 3 h, sample G; and (d) 0.003 M, 6 h, sample J

The nanowire bundles shown in Figure 5-18a were produced after 2 h reaction at 0.002 M precursor concentration, though some of them exhibiting length less than 100 nm are at the very initial stage of their growth, the majority of them is very long with high aspect ratio. After the same period of reaction time in the products with 0.004 M (Figure 5-18b), the proportion of short nanowires less than 100 nm is much higher than that

from 0.002 M concentration, which confirms the length descendant with increased concentration. By comparing Figure 5-18c with d, the nanowires produced after 6 h at 0.003 M exhibit very huge length at least over 1 μm (Figure 5-18d), while shorter length is possessed by nanowires from 3 h reaction with same WCl_6 concentration (Figure 5-18c), this is consistent with the previous SEM observation, and reveals that nanowires from 6 h reaction is longer than nanowires from 3 h reaction though shorter than that from 5 h reaction.

After a thorough study about the morphology of nanowires by electron microscopies, it is concluded that, with a higher precursor concentration, the resultant bundles are larger in diameter, shorter and straighter along their axis. When the reaction time is increased, the bundles become larger and longer at the beginning, while a reduction in length follows as the diameter remains unchanged. This is most likely due to the breakage of growing bundles at a prolonged reaction time.

5.3.2.2 Ethanol solvent

In order to study the influence of different solvent on resulted nanowires, ethanol has been used as solvent. Based on the previous results and above discussion, further investigation has been carried out based on 0.002 M WCl_6 concentration, dissolved in ethanol, 5 h has been chosen as a starting reaction time when using ethanol as the solvent.

SEM images have showed the WO_x nanowires based on the ethanol solvent, with a reaction time of 5, 7, 8 and 9 h respectively.

The products from ethanol solvent after 5 h reaction is shown in Figure 5-19, which have exhibit three different morphologies, besides the nanowire bundles which were also widely observed in previous samples resulted from cyclohexanol solvent, some 2D networked wires were presented, as well as 3D flower like structures with diameter size around 1 μm. It is also noted that all 3 different types of structure consists of WO_x nanowires with length no more than 500 nm, particularly short nanowires formed the flower shape. In addition, the nanowire bundles are very thin in diameter.

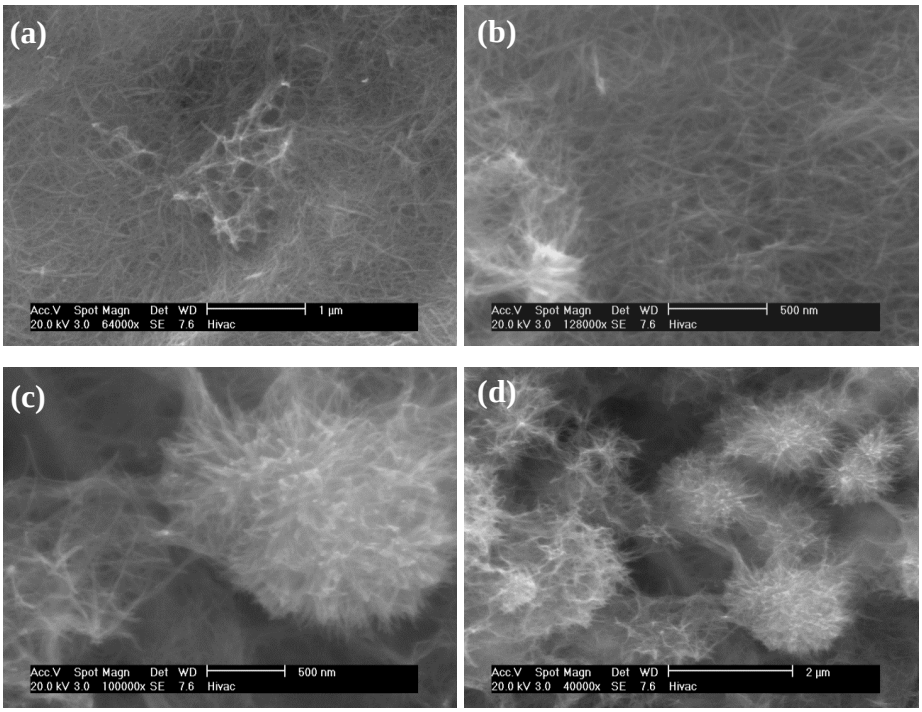

Figure 5-19 SEM images for WO_x nanowires from the ethanol solvent after 5 h reaction

After 7 h reaction, the nanowires grow much longer, as shown in Figure 5-20, the nanowires are dramatically longer than product from 5 h, with some of them longer than 2 µm. Nanowires from 8 h reaction presented very long and thin feature, with average length surpassed 3 µm, judging from the SEM images (Figure 5-21). Nanowires also demonstrate a curled feature compared with those from the cyclohexanol solvent, which might be attributed to the thinner diameter.

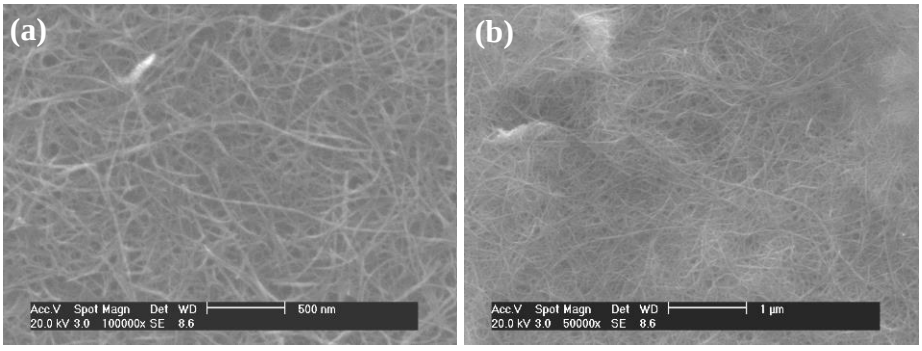

Figure 5-20 SEM images for WO_x nanowires from the ethanol solvent after 7 h reaction

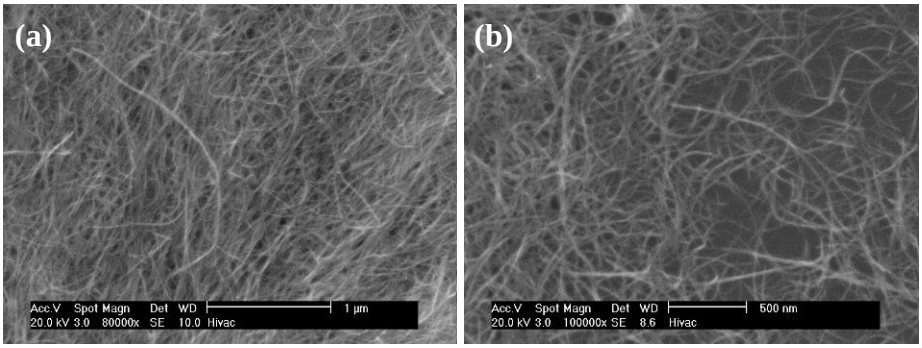

Figure 5-21 SEM images for WO_x nanowires from the ethanol solvent after 8 h reaction

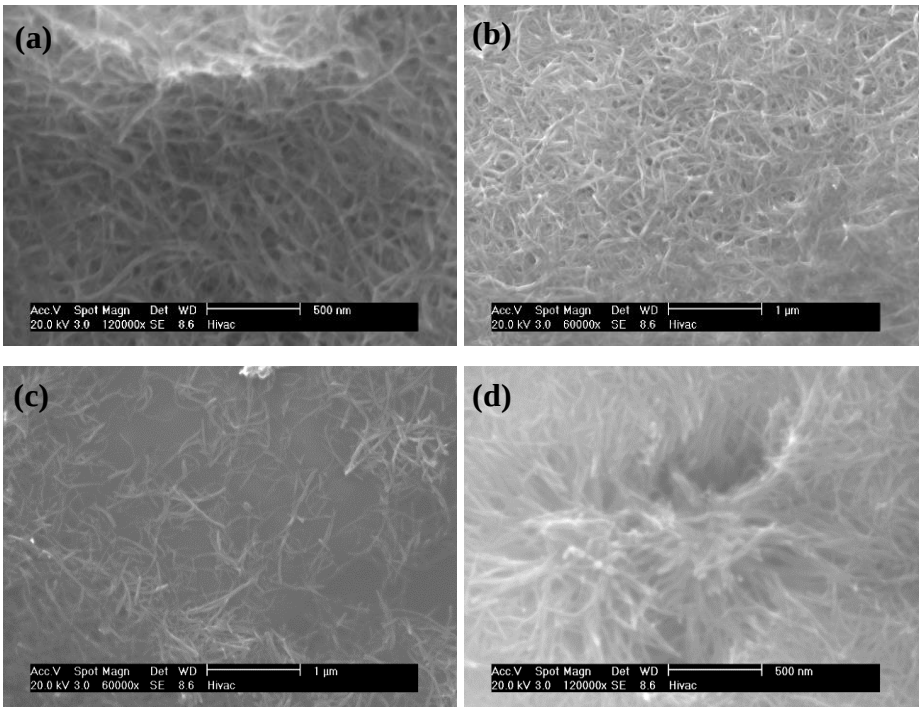

Figure 5-22 SEM images for WO_x nanowires from the ethanol solvent after 9 h reaction

For experiments starting from the ethanol solvent, it seems the breakage of nanowires happened too. After a 9 h reaction, the resulted nanowires are of length less than 1 μm, not straight in axis direction, similar to all other nanowires from the ethanol solvent, the SEM images look quite blurry, which probably resulted from some amorphous phase on the surface. Compared with nanowires from 8 h, it is believed that the nanowires broke into smaller pieces during 8 h and 9 h reactions. Thus it could be summarised that, up to 8 h, the length of nanowires produced from WCl_6 precursor and ethanol solvent has increased with increased reaction time, however a reduction of length occurred afterwards. This is in consistent with the length evolution phenomenon for nanowires from the cyclohexanol solvent. No obvious change could be observed for the diameter

evolution of resulted nanowires with different reaction time, probably due to the very thin bundle diameters.

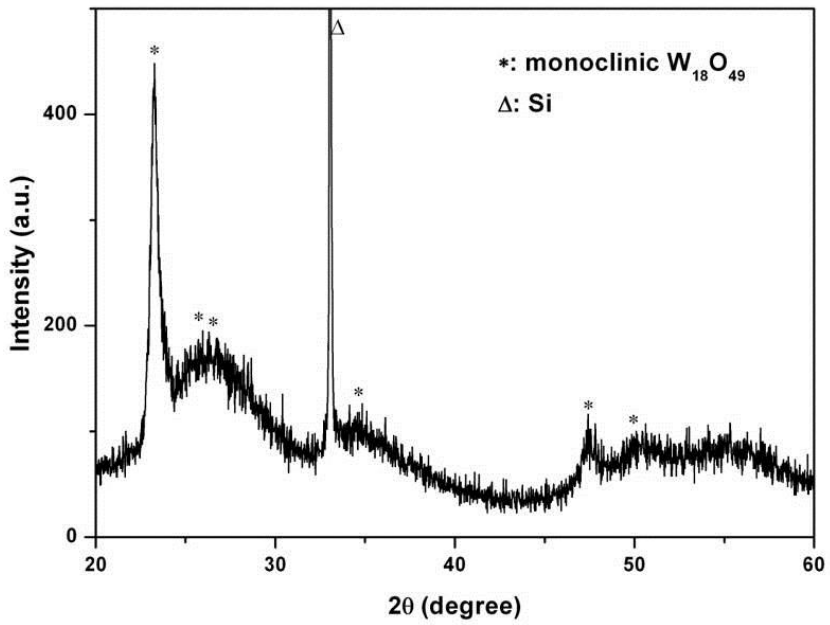

Figure 5-23 XRD patterns of WO_x nanowires using ethanol as the solvent

The XRD pattern for nanowires obtained from using ethanol the solvent is shown in Figure 5-23, similar to the WO_x nanowires from the cyclohexanol solvent, the main peaks also match well with monoclinic $W_{18}O_{49}$. Besides the highest intensity peak assigned to Si wafer which is used as the substrate for the XRD sample, the (010) plane at around 23.4 degree has the highest intensity than that of other planes of the nanowires. This indicates that these nanowires also adopted the growth direction of [010]. Other peaks besides (010) are not sharp at all, probably due to the extremely thin diameter of the nanowires, while the noisy background might be related to the unclean surface of nanowire bundles.

Compared with results from the cyclohexanol solvent, the nanowires from ethanol exhibit a longer and thinner morphology, but not very straight along the axis and have an amorphous layer on the surface. Most importantly, a longer reaction time is required, which is similar to previous works, i.e. with concentration of WCl_6 increased from 0.007 M to 0.014 M, nanowires and nanorods were achieved respectively after 10 h reaction [32].

It is noted that the boiling point of cyclohexanol [$(CH_2)_5CHOH$] is 160.84°C, whilst that of ethanol (C_2H_5OH) is only 78.37°C, which would result in much higher vapour

pressure at the same reaction temperature, 200°C, than the same volume of cyclohexanol. The high vapour pressure might have an influence on the agglomeration of nanowires, thus result in different bundle diameters and straightness. Previous studies have also revealed that the morphology as well as crystalline phase of WO_x depends strongly on the solvent composition [32, 33], and similar conclusion has been drawn for other nanostructure derived hydrothermally [171]. Different WO_x were resulted by using a gas mixture of different oxygen potentials in other studies [172], according to solvents with different oxygen percentages in hydrothermal experiments. Thus, the morphology difference between nanowires from ethanol and cyclohexanol solvents might be attributed to both the huge boiling point difference and the oxygen percentage difference of the two solvents.

5.3.2.3 Mixed solvent

Though the nanowires from solvent ethanol exhibit a very long and thin feature, the required reaction time is rather long, and the surface is not very clean, covered by an amorphous layer. It is interesting to try a mixed solvent, expecting to achieve an optimal status for a better product than using single solvent. A mixed solvent of ethanol and cyclohexanol at volume ratio of 1:2 has been used in the test, with reaction time fixed at 5.5 h.

Very uniform long and ultra-thin nanowires have been achieved, as confirmed by SEM and TEM images shown in Figure 5-24. Compared with nanowires from cyclohexanol and ethanol respectively, the nanowires from the mixed solvent exhibit combined advantages: longer and thinner than nanowires from the cyclohexanol solvent, whilst much straighter in the axis direction and cleaner on the surface than those from ethanol.

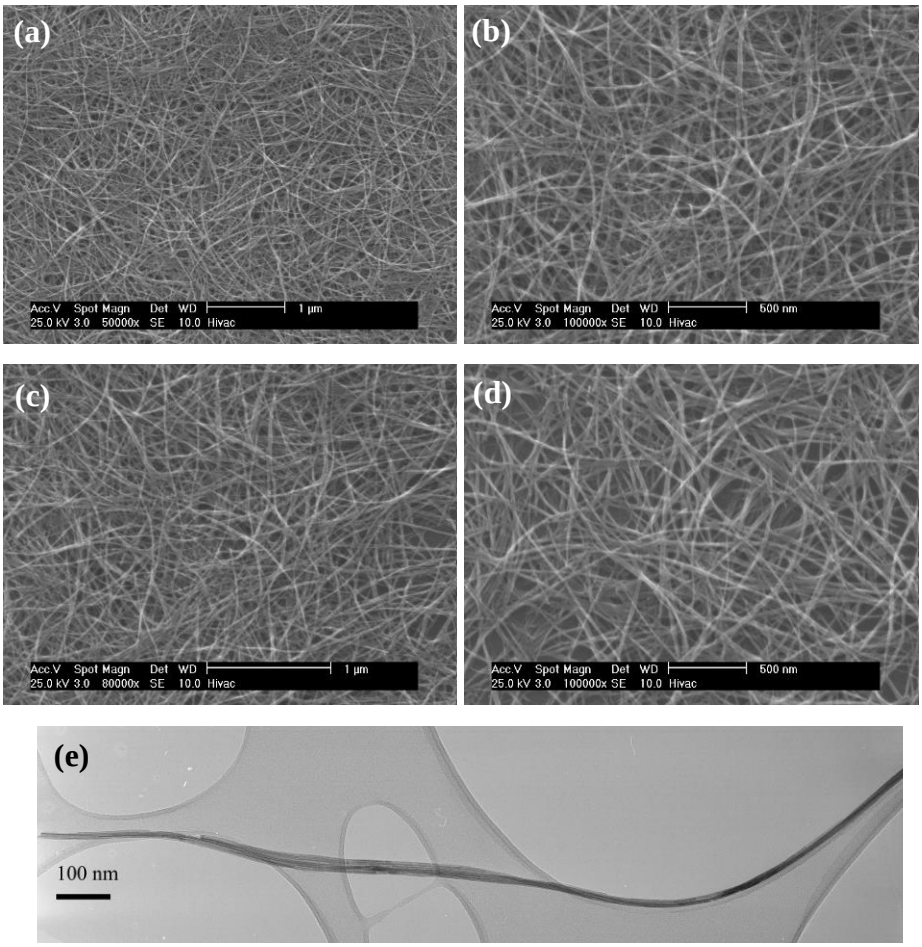

Figure 5-24 (a-d) SEM images and (e) TEM image of WO_x nanowires from the mixed solvent

To confirm the encouraging results, Brunauer-Emmett-Teller (BET) [173] gas-sorption measurement was carried out for the resulting nanowires from experiment U (mixed ethanol and cyclohexanol solvent) to investigate their specific surface areas and their porous nature. As shown in Figure 5-25 a, the N_2 adsorption-desorption isotherms for the nanowire bundles show the hysteresis at a relative pressure P/P_0 up to around 0.9, exhibiting a type IV curve that has been reported in mesoporous tungsten oxide thin films [174, 175]. The BET specific area of the sample calculated from the absolute adsorption is 275 m^2/g, which is much higher than 152 m^2/g for nanowires from cyclohexanol solvent [33, 41]. Barret-Joyner-Halenda (BJH) [142] analysis for the pore size distribution reveals an apex centred at about 2.2 nm, as shown in Figure 5-25b. A much narrower and more uniform size distribution has been achieved by the mixed ethanol and cyclohexanol solvent, compared to previous results from pure cyclohexanol solvent [176]. The total pore volume is calculated to be 1.063, significantly improved compared to 0.21-0.51, the value from nanowires synthesised using cyclohexanol.

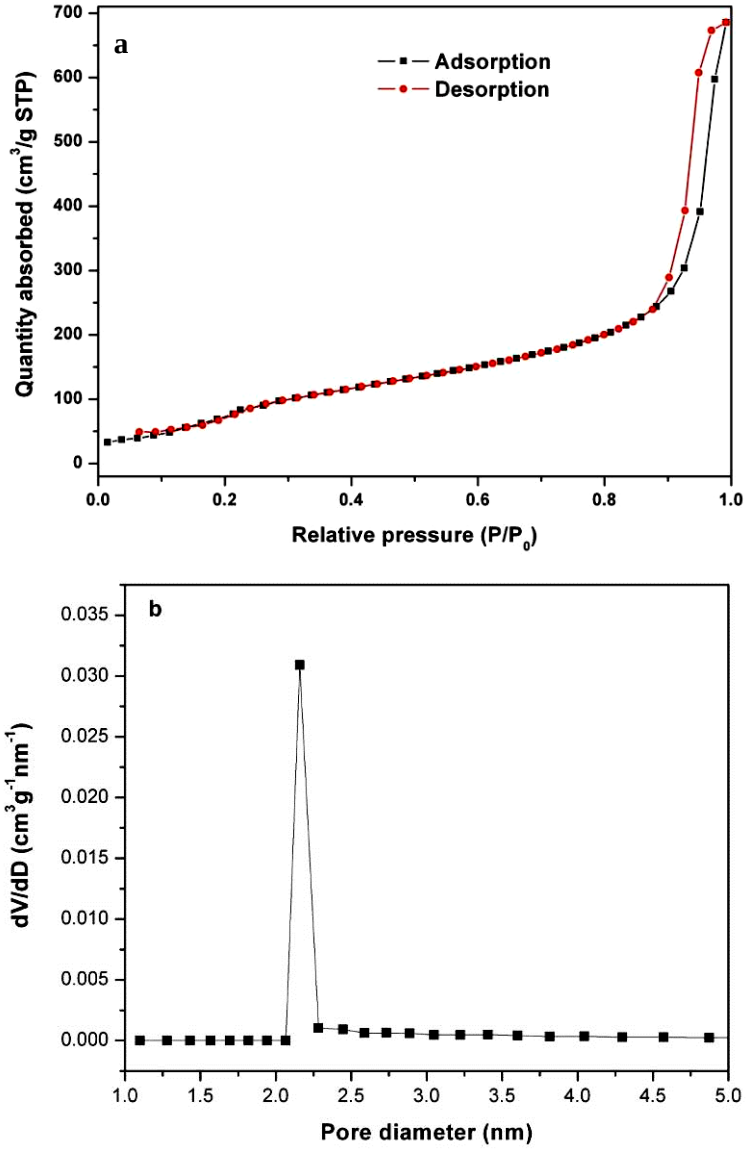

Figure 5-25 (a) N_2 sorption isotherms (black square: adsorption; red circle: desorption) and (b) Pore size distribution curves of WO_x nanowires synthesised by using a mixed solvent

The specific surface area value for nanowires from mixed ethanol and cyclohexanol solvent has dramatically surpassed all the reported value, almost twice of 152 m^2/g for $W_{18}O_{49}$ made of pure cyclohexanol solvent from our previous report [33, 41], nearly doubled of 143 m^2/g for the mesoporous WO_3 thin films [174] and more than doubled of 125 m^2/g for the mesoporous WO_3 [177], needless to say 10 times higher than 25 m^2/g for high surface area nano monoclinic WO_3 nanoparticles and hundreds times larger than the commercial WO_x particle [178]. A comparison of specific surface area between different tungsten oxide nanostructures has been listed in Table 5-3. The much higher specific surface area of present nanowires is resulted from the ultra-thin feature

of the individual nanowires, the way they are packed within the bundles, and the size and distribution of pores between the individual nanowires. Particularly, the improvement over other solvents lies in the higher aspect ratios and the higher pore distribution.

Table 5-3 Specific surface area comparison of WO_x nanostructures

	Specific surface area (m^2/g)	Total pore volume (cc/g)
Ultra-thin WO_x nanowires by mixed solvent*	275	1.063
$W_{18}O_{49}$ nanowire by cyclohexanol [33, 41]	106-152	0.21-0.51
WO_x thin film [174]	143	
Mesoporous WO_3	125	
Monoclinic WO_3 nanoparticles [178]	25	
Commercial WO_x particles [178]	1.7	

*: mixed ethanol and cyclohexanol solvent at a volume ratio 1:2

5.3.3 Conclusion

Ultra-fine WO_x nanowires have been synthesised by a solvothermal method. The influences of concentration of precursor (from 0.002 to 0.004 M) and reaction time (2 - 6 h) on the morphology of products have been systematically studied. The results have revealed the presence of the $W_{18}O_{49}$ phase in most of nanowire samples and the morphological evolution arising from these parameters. With a higher precursor concentration, the resultant bundles are larger in diameter, shorter and straighter along their axis. When the reaction time is increased, the bundles become larger and longer at the beginning, while a reduction in length follows as the diameter remains unchanged. This is most likely due to the breakage of the growing bundles at a prolonged reaction time. Furthermore, the dependence of morphology on different solvents, cyclohexanol, ethanol, as well as a mixture of both, has also been investigated in this study. Longer reaction time is required for nanowires produced from ethanol solvent. Nanowires from the mixed solvent exhibited combined advantages of each individual solvent. Long, thin

and clean nanowires have been achieved. At similar reaction time, nanowires produced using the mixed solvent were recorded a specific surface area as high as 275 m^2/g, almost twice of that obtained from using cyclohexanol alone.

5.4 Patterned growth of WO_x nanorods from Au-coated W foil

5.4.1 Introduction

Despite intensive studies on the synthesis of 1D nanostructured tungsten oxide, as discussed in the previous section, an efficient and simple way to produce patterned WO_x nanorods remains a challenge for device construction and demands further investigation. In this section, a simple growth to achieve patterned WO_x nanorods using a CVD technique will be explored.

5.4.2 Experimental

10×10 mm squared W foils were subjected to two different surface treatments in order to create the desired surface patterns: Au coating (substrate A) and blade engraving (substrate B). The details for spin coating of patterned Au-block copolymer composites and the plasma etching were described in Chapter **2** [137]. Briefly, the Au patterns were created on the surface of a well-polished W foil after the removal of the copolymer (PS-b-P4VP) [137]. In addition to the two types of pattern pre-treatment, a third type of W foil was treated with acid (immersed into 1 M HCl for 1 min, substrate C), to study the influence of W substrate. The pre-treated W foil was then placed in the centre of a quartz tube located in a horizontal tube furnace. After flushing with high purity Ar for 30 min, the furnace was raised to target temperature, 600-750°C as listed in Table 5-4, and high purity Ar was then bubbled through a wash bottle at a flow rate of 50 ml/min. The reaction lasted for 5-40 min, for the creation of the WO_x nanorod templates.

Table 5-4 summarises the W substrates used in the synthesis, under different growth conditions such as time, temperatures.

Table 5-4 Summary of experimental parameters for oxidation reactions

Starting material	Oxidation temperature (°C)	Oxidation time (min)
A	600	5
		40
B	600	5
		15
C	600	30
	650	30
	700	30
	750	30

The starting materials are substrate A: Au coated W foil; substrate B: blade engraved W foil; substrate C: acid etched W foil respectively.

5.4.3 Results and discussion

WO_x nanorods from Au-coated W foil

The surface morphology of the Au coated W substrate prior to oxidation was examined using SEM and AFM, as shown in Figure 5-26. The W substrate is covered by an Au coating which consists of numerous pores and vesicles with sizes ranging from nanometer up to more than 10 μm, which is adjustable. The thickness of the Au coating is estimated to be 15-20 nm, and the Au region and the W substrate are marked in the images (Figure 5-26a-c). Higher magnification SEM image in Figure 5-26c shows the particulate feature of the Au coating. Figure 5-26d displays an AFM image which displays a much uniform example of the nano-sized vesicles (black). Actually, besides the nanoporous film structure, the Au coating could be templated into 0D, 1D, 2D and complex 3D periodic nanostructures via structural control at different dimensions [179], which offers variable possibilities for the patterned growth of WO_x.

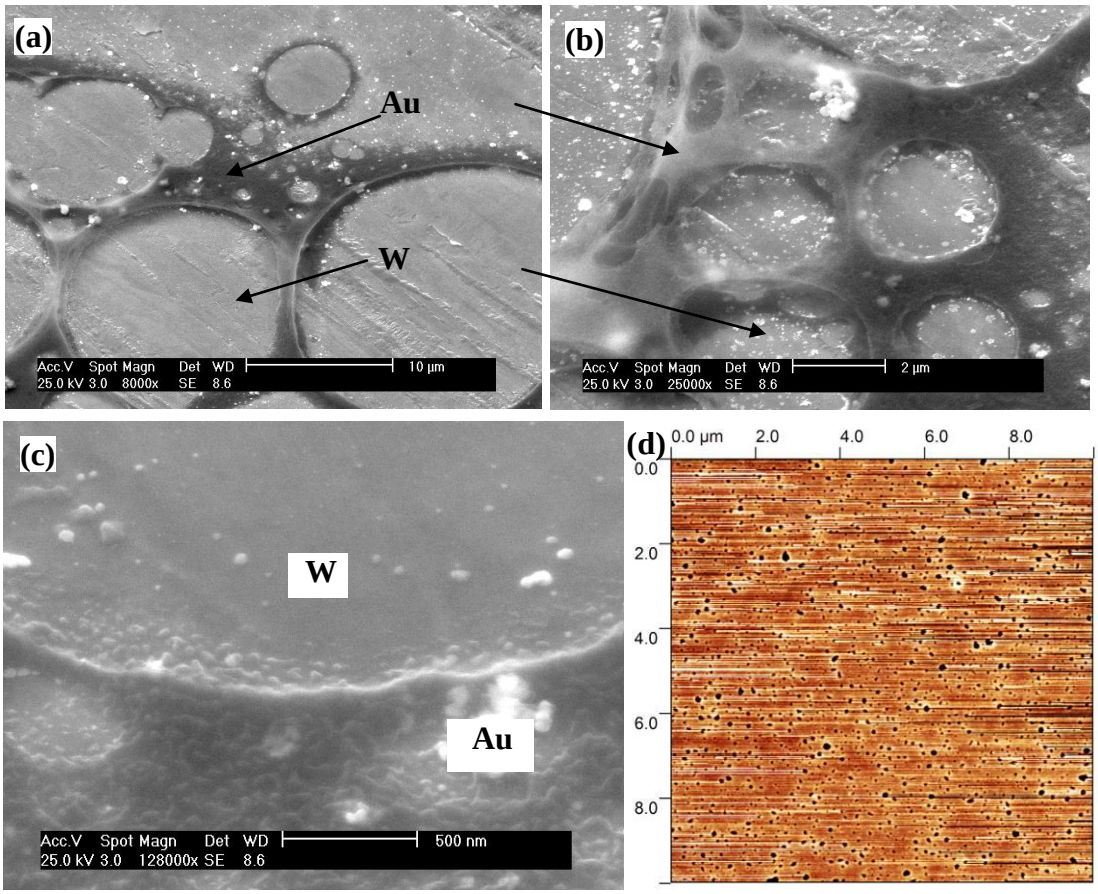

Figure 5-26 SEM (a, b and c) and AFM (d) images of the Au coated W foil substrate (substrate A)

For substrate A with porous Au film, after the oxidation stage by reaction of W and H_2O vapour for varied periods of time of 5 min and 40 min respectively, WO_x nanorods of different lengths and diameters were formed, as shown in Figure 5-27 and Figure 5-28. SEM images for sample after 5 min oxidation from substrate A show a relatively early stage of the oxidation and growth. Figure 5-27a and Figure 5-27b clearly show that the nanorods are only grown from the uncoated W areas, and there is no growth on the Au coated regions. This is exactly what we have expected and, based on this, we will try to realise the patterned formation of different 1D nanostructures. Further observation confirmed that the nanorods typically exhibited a diameter of ca. 20 nm and lengths of up to 300 nm (Figure 5-27c). Figure 5-27c also shows that some individual WO_x nanorods grew out of extremely tiny holes of nanoscale. Therefore, further development of advanced control of the patterns and holes of the Au coating could lead to a more precise nanorod growth. An area EDX scanning has been taken for the 5 min sample, as shown in Figure 5-27e. The EDX spectrum has confirmed that the nanorods were

composed of only O, and W. The much higher intensity of W peak than O peak attributes to the W substrate and much heavier W atom than O.

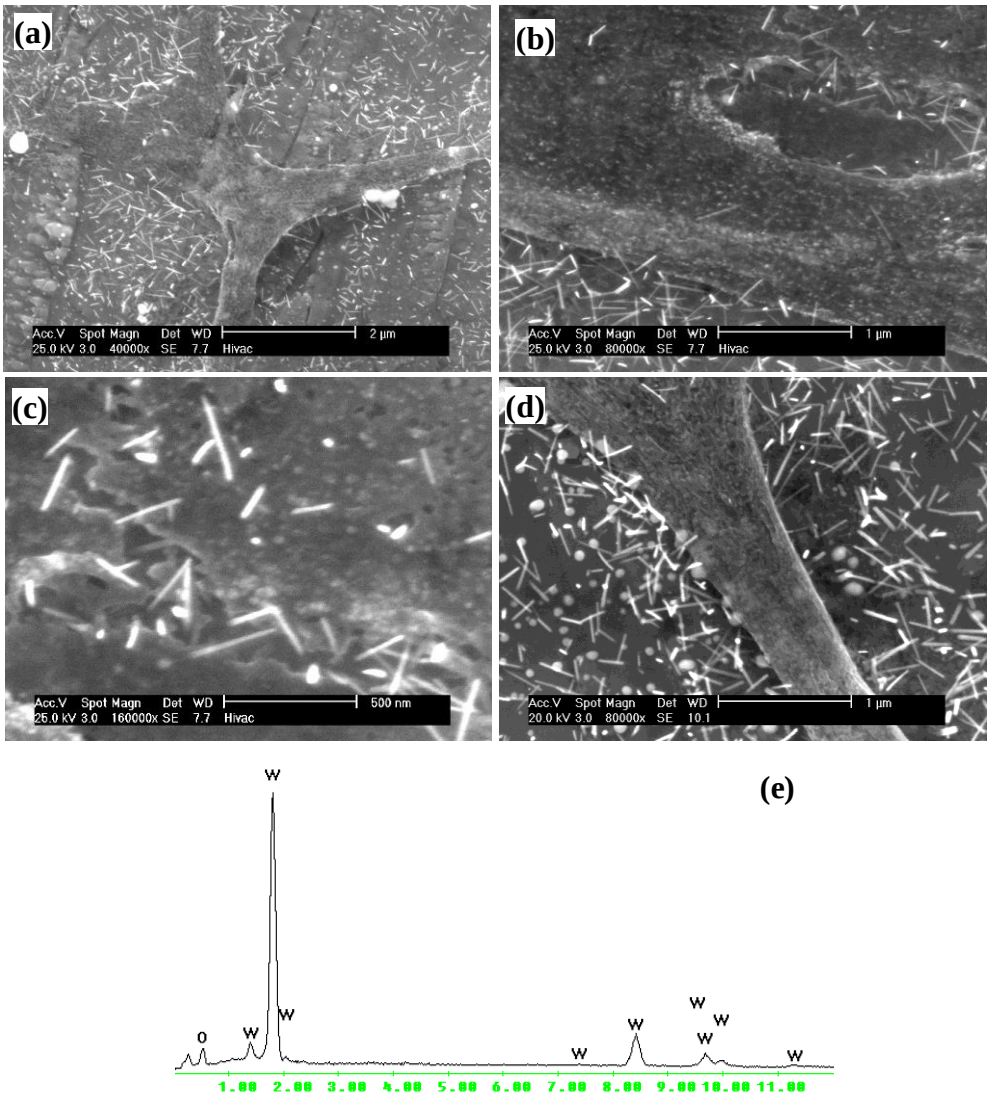

Figure 5-27 WO_x nanorods oxidised at 600°C from substrate A for 5 min (a, b and c), nanorods after nitirdation at 650°C for 6 h (d), and EDX spectrum from overall area scan (e)

After oxidation for 40 min, nanorods with lengths up to several microns were grown from the bare W substrate area without Au coating (Figure 5-28). The original nanoporous pattern of the Au coating was intact since the coated areas were free of WO_x nanorods (dark area in Figure 5-28a and Figure 5-28b), although some long rods overlapped and partially covered the coated area. Higher magnification SEM exhibits that the individual nanorod possesses a uniform diameter (ca. 30 nm) throughout their lengths, ranging from a few hundreds of nm to a few µm (Figure 5-28c-f). From a localized view, these nanorods appear to be perpendicular to the substrate and parallel to

each other (Figure 5-28d), but overall they are randomly oriented. The EDX spectrum for WO_x grown from the W foil after 40 min confirmed that the nanorods consist of only O and W, as shown in the inset of Figure 5-28g. Much longer tungsten oxide nanorods lead to relatively higher oxygen peak compared to that from 5 min sample.

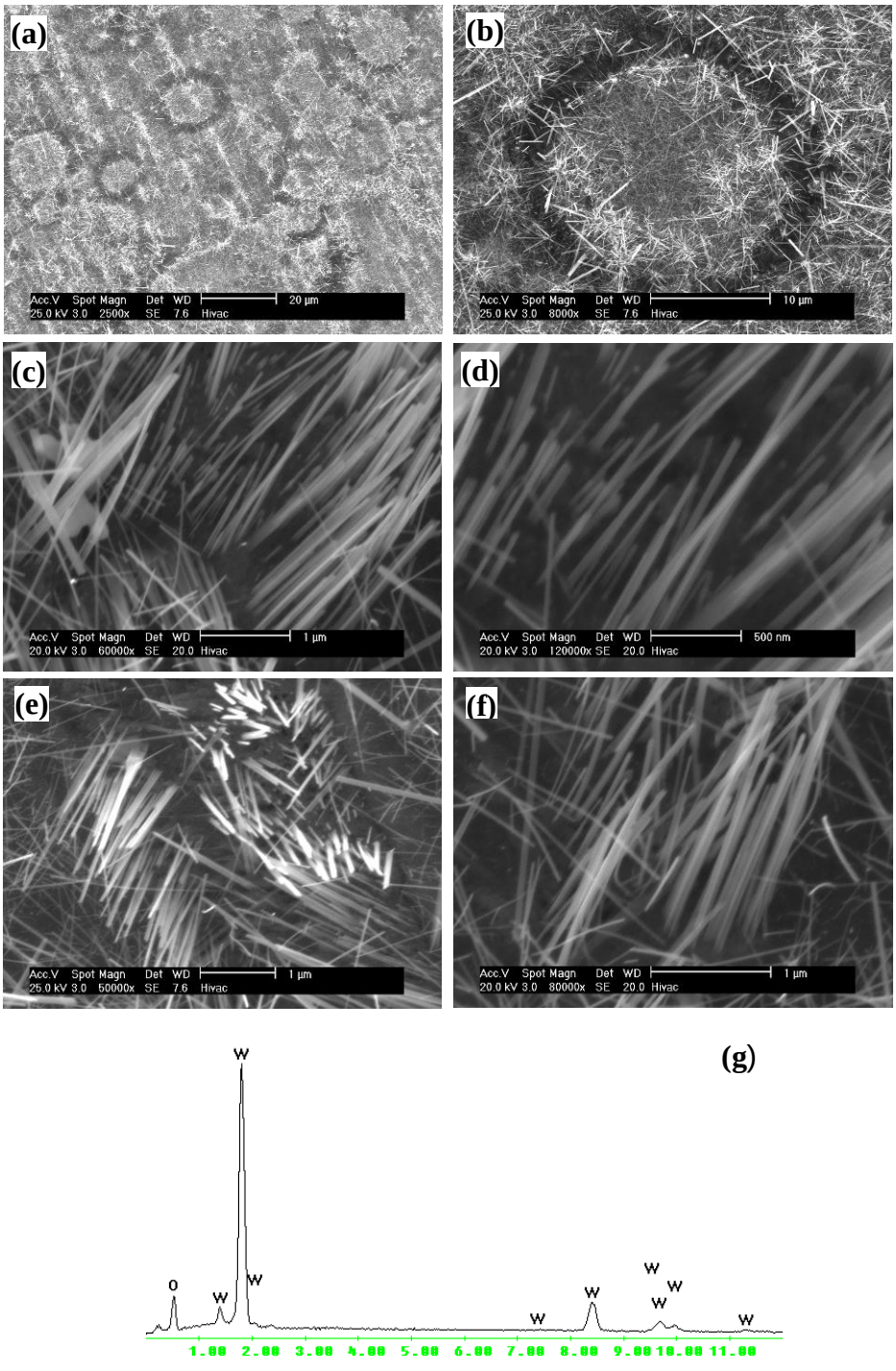

Figure 5-28 WO_x nanorods (a, b, c and d) grew from substrate A at 600°C for 40 min, WN_x nanorods (e and f) followed by nitridation in NH_3 at 650°C for 12 h, and EDX spectrum from overall area scan (g)

As shown in Figure 5-27 and Figure 5-28, during the oxidation process, WO_x nanorods only formed on the bare W area. This indicates that the bare W area would be favourable for the WO_x growth whilst the coated area hindered their growth. Unlike its renowned catalytic function, the Au particles in this case stopped the growth of WO_x. This is because the bare W area was directly exposed to oxygen in the experimental atmosphere and was easily oxidised, however the Au coating prevents oxygen from direct contact with the W underneath, which made the oxidation very difficult for the coated area.

WO_x nanorods from blade engraved W foil

To compare the influence of substrate, as-received W foil was also used to prepare WO_x nanorod following the same process, nothing but only a WO_x layer formed on the substrate.

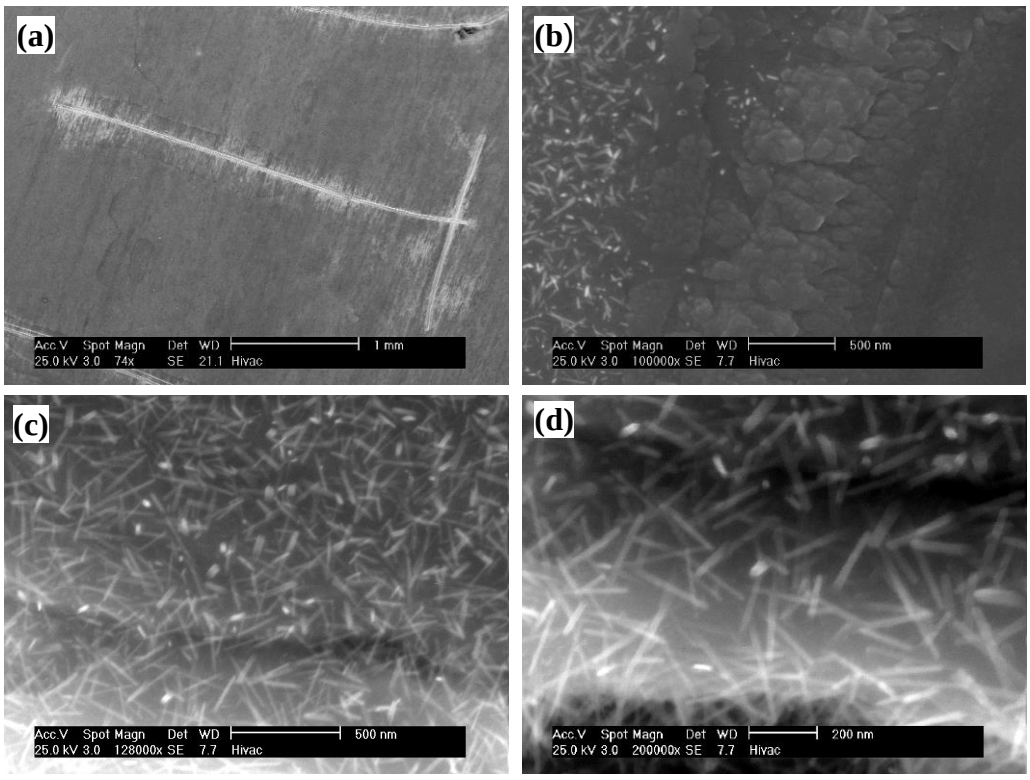

Figure 5-29 WO_x nanorods (a-d) after oxidation at 600°C for 5 min

Figure 5-29 shows the WO_x nanorods resulted from substrate B, which corresponded to the blade engraved substrate. A letter T is observed in Figure 5-29a, in which the bright area was corresponding to WO_x nanorods whilst the dark area was free of nanorods. It showed that nothing formed in areas far away from the marks (as received W area),

whilst more and more WO_x were found close to the centre of the mark. Detailed observation showed that the bright (nanorods area) and the dark (plain W) area was connected by an area with polycrystalline layers (Figure 5-29b), which reveals the early stage of nanorods formation. After 5 min oxidation, the produced nanorods exhibited a diameter of around 20 nm and length up to 200 nm (Figure 5-29c).

WO_x nanorods from acid etched W foil

For acid treated W foil (immersed into 1 M HCl for 1 min), substrate C, the effects of the annealing temperature on the product morphology were studied. After annealing for 30 min, there was no nanorod observed at 600°C, but a polycrystalline layers has formed on the W substrate (Figure 5-30a and Figure 5-30b); some very thick rods have protruded over this polycrystalline layer when temperature being increased to 650°C (Figure 5-30c) and Figure 5-30d). Dense, short and thick rods were visualised for samples processed at 700°C (Figure 5-30e and Figure 5-30f), which became longer and thinner at 750°C (Figure 5-30g and Figure 5-30h). For samples from 700°C, there was a layer of rods grown out of the substrate, with diameters of around 300 nm, and the cross section exhibit a polygonal feature, with length unknown as only a few of them protruding out of the layer by several hundreds of nanometer (Figure 5-30e and Figure 5-30f). At higher temperature of 750°C, nanorods with diameters ranging from 50 nm to 300 nm were observed protruding out of the substrate by up to 5 μm, and the thicker ones of which also exhibited a polygonal cross section (Figure 5-30g and Figure 5-30h).

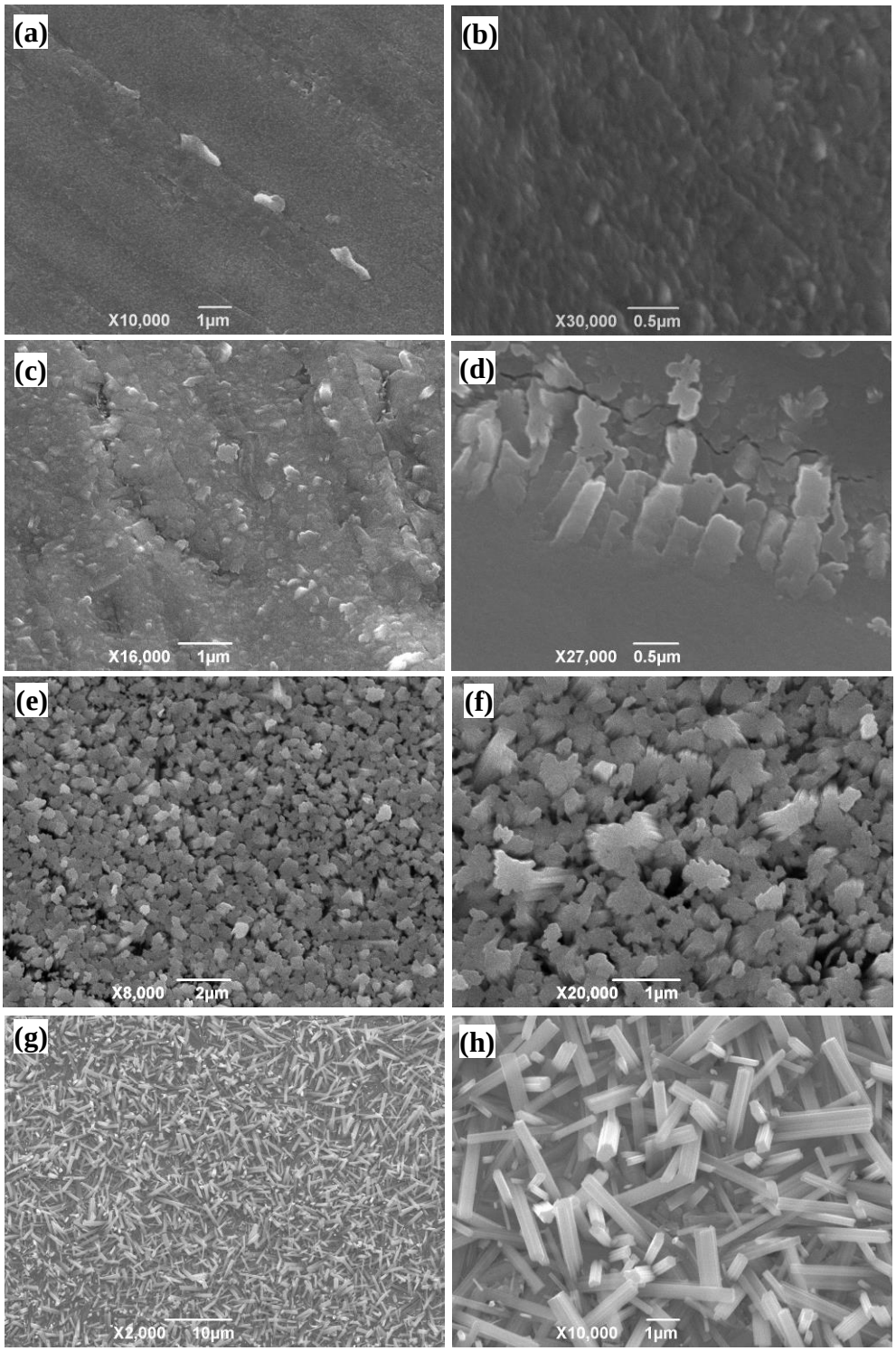

Figure 5-30 SEM images of WO_x nanorods from substrate C (acid etched W foil): (a) and (b), WO_x rods grown on W foil at 600°C for 30 min; (c) and (d), WO_x nanorods grown on W foil at 650°C for 30 min; (e) and (f), WO_x nanorods grown on W foil at 700°C for 30 min; (g) and (h), WO_x nanorods grown on W foil at 750°C for 30 min

XRD profiles were acquired to assess the crystalline features of samples from different stages. Figure 5-31 shows XRD pattern of original substrate A and WO_X nanorods on

different substrates, all patterns showed huge peaks of W (JCPDS No.1-1203) at 2θ angles at 40.416 (110), 58.357 (200) and 73.3 (211) respectively. On substrate A (pattern c) and WO_x nanorods from substrate A (pattern a), there are extra peaks with star label, which are due to Au coating (JCPDS No. 1-071-4616) at 38.1 (111), 44.4 (200), 64.5 (220) and 77.5 (311), though only the peak at 38.1 (111) was strong enough to be observed in pattern c. In patterns a and b, peaks labelled with '⊥' should be assigned to tungsten oxide, mainly $W_{19}O_{55}$ (JCPDS No. 45-0167).

Some minor peaks in pattern (a) correspond to WO_2 (JCPDS No. 1-071- 0614) at 25.99 (110), 37.1, 53.2-54 and 59.8 (130), labelled with circle. Other peaks in pattern b labelled with triangle match well with $W_{18}O_{49}$ (JCPDS No. 71-2450).

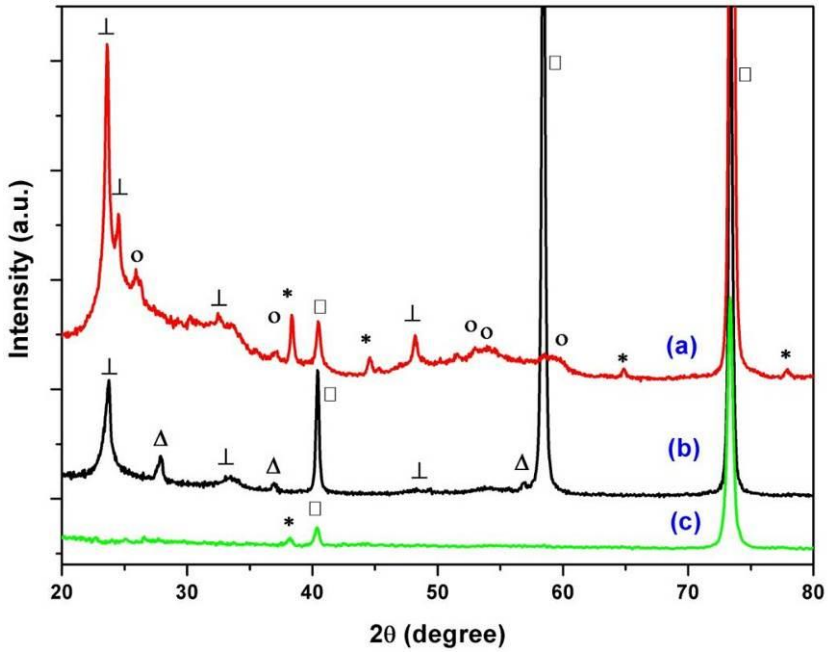

Figure 5-31 XRD profiles of WO_x nanorods on substrate A (a) and substrate B (b), and the original substrate A before growth (c)

Raman spectrum of WO_x nanorods shown in Figure 5-32 presents a quite complicated feature, which is typical for nanorods produced in this work. Raman technique has been widely used to study WO_3, with the bands at around 717 cm^{-1} and 807 cm^{-1} being assigned to the W-O-W stretching vibrations, bands at 273 cm^{-1} and 326 cm^{-1} assigned to W-O-W bending vibrations [180, 181], and bands below 200 cm^{-1} generally ascribed to lattice vibrations. The current spectrum a in Figure 5-32 is quite similar to the results recorded by Frey and co-works during an in-situ Raman investigation from WO_3 to

$WO_{2.9}$ and WO_2 [180], but not identical to a combination of the $WO_{2.9}$ and WO_2 Raman spectra.

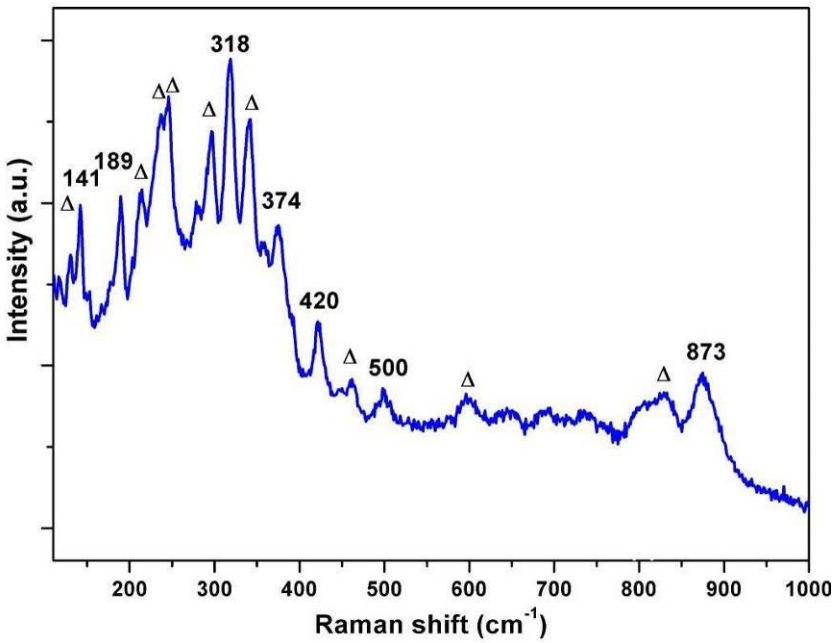

Figure 5-32 Raman spectra of WO_x nanorods from substrate C

The broad peak at around 800 cm^{-1} should be a combination of 795 to 805, 825, 840 cm^{-1}, and even 873 cm^{-1}, and could be assigned to the W-O-W stretching mode shifted to higher energies compared to WO_3, as a result of the decreased W-O-W caused by the edge-sharing octahedral in suboxides. The peak at 873 cm^{-1} has been previously associated with the stretching mode of a 0.178 nm W-O bond [181]. The two bands below 200 cm^{-1} at 141 and 189 cm^{-1} should be ascribed to lattice vibrations, with a slight shift compared to results presented in literatures [182, 183].

The abundant bands (213, 235, 245, 278, 296, 318, 342 and 374 cm^{-1}) at 200-400 cm^{-1} region are normally assigned to W-O-W bending vibrations [180]; while only one peak appears at 275 cm^{-1} for WO_3. This could be explained by several distinct W-O-W bond lengths in WO_x, due to the different amounts of oxygen vacancies arising from the co-existence of at least $W_{19}O_{55}$ and WO_2 as confirmed by XRD. Very similar to the spectrum obtained previously from needle-like precursor reduced for 20 min [180], which is believed to almost coincide with the spectrum of crystal shear structure of WO_2, several peaks in the central 400-700 cm^{-1} region at 422, 462, 500, 602, 650 and 695 cm^{-1} were slightly shifted when compared with 425, 511, 600, 620, and 650 cm^{-1} reported [180]. Thus, the feature of bending modes in the lower wavenumber region and

broad peaks in the higher wavenumber area could be arisen from a combination of different WO_x compositions and crystal shear structures [180].

5.4.4 Conclusion

In summary, selectively patterned WO_x nanorods were generated from a reverse-patterned W foil with Au coating by a simple W-water vapour reaction. The influence of different substrate, reaction time and temperature have been studied, the knowledge of which will help to achieve nanorods with desired diameter, length and pattern. This result represents a simple, innovative and efficient process for reverse-patterned growth of new nanomaterials.

5.5 Patterned growth of the tungsten nitride nanorods from WO_x nanorods template

5.5.1 Introduction

As an analogue to WO_x nanomaterials, nanostructured WN_x are very useful as a photocatalyst for water decomposition [35], effective barriers for microelectronics [36], electrodes in semiconductor devices [37], cathode catalyst for fuel cells [38] and catalyst for NO dissociation etc. [39], owing to their chemical stability [184], high melting point (>2000K), low electrical resistivity, exceptional hardness (>10 GPa) [185], and a relatively low bandgap (2.2 ev) [35]. Though intensive studies have focused on the production of 1D WO_x nanowires/nanorods using a variety of different approaches [29-34], in contrast, there are relatively less studies on the preparation of 1D WN_x, although thin films of tungsten nitride are widely investigated [166, 186-188], or their nanoparticles [189-191]. For thin films of WN_x, their generation can be realised by reactive sputtering [186], chemical vapour deposition [166], ion-beam assisted deposition [188] and atomic layer deposition [36, 187], of which atomic layer deposition has been considered as one of the most efficient methods, due to its precise control over film thickness.

The unique catalytic behaviour of group 6 nitride was usually hindered by the relatively low specific surface areas. Attempts to prepare nitride catalysts with high surface areas normally utilise tungsten containing precursor, followed by thermal nitridation in an

ammonia atmosphere. By pyrolysis of $W(N^tBu)_2(Ph_2pz)_2$ at 800°C under N_2 atmosphere, ultra-fine β-W_2N with sizes of 2-3 nm were created [189], whilst larger β-W_2N nanoparticles (5-40 nm) were produced by applying a direct current arc-discharge method using W and N_2 [190]. Mesostructured β-W_2N nanocrystals with a high surface area of 89 m^2/g have been synthesised from H_2WO_4 via a temperature programmed reaction with NH_3 at 700°C, reported by Bai and co-workers [191].

Very recently, new techniques have been developed to synthesise 1D tungsten nitride nanorods/nanowires of large aspect ratios [35, 40, 41], using WO_x as the precursor followed by a simple nitridation in NH_3. However, the growth and control the alignment of these 1D nanomaterials remain a challenge and request further investigations.

As a further extension of last section, in this part patterned WN_x nanorods have been achieved through nitridation of patterned WO_x nanorods prepared in previous section. Interesting microstructure of tungsten nitride has been revealed and the possible growth mechanism has also been discussed accordingly at the end.

5.5.2 Experimental

In last section (Section **5.4)**, WO_x nanorods has grown on W foils (thickness 0.05 mm, sigma-Aldrich) subjected to different surface treatments: Au coating (substrate A) and blade engraving (substrate B), and acid etching (substrate C). Moving this investigation a step further, a subsequent reaction at 650°C with NH_3 replaced Ar at a flow rate of 100 ml/min (without bubbling through the wash bottle) for 6-12 h, the oxide-nitride conversion was completed and the WN_x resulted.

Table 5-5 summarises the WO_x nanorods template chosen for nitridation, the substrate and oxidation parameters used and the nitriding conditions such as time, temperatures.

Table 5-5 Summary of experimental parameters for oxidation and nitriding reactions

Starting material	Oxidation experiments		Followed nitriding experiments	
	Oxidation temperature (°C)	Oxidation time (min)	Nitriding temperature (°C)	Nitriding time (hour)
A	600	5	650	6
	600	40	650	6
			650	12
			650	18
B	600	5	650	6
			650	12
C	750	30	650	12

The starting materials are substrate A: Au-coated W foil; substrate B: Scratched W foil; and substrate C: acid etched W foil, respectively.

5.5.3 Results and discussion

It is expected that a simple oxide-to-nitride conversion would occur by N replacing the O in WO_x nanorods, thus the resulted WN_x nanorods would inherit the size and shape of WO_x nanorods, and the patterns on the substrate.

Figure 5-33 shows tungsten nitride nanorods after nitridation at 650°C for 6 h, based on oxidation at 600°C from substrate A for 5 min. The nanorods maintained an identical patterned feature following the oxide-to-nitride conversion, and Au-coated areas were still free of nanorods. With similar diameter and length, no changes in the morphology of nanorods before and after the oxide-to-nitride conversion were observed by SEM, as compared to Figure 5-27.

.

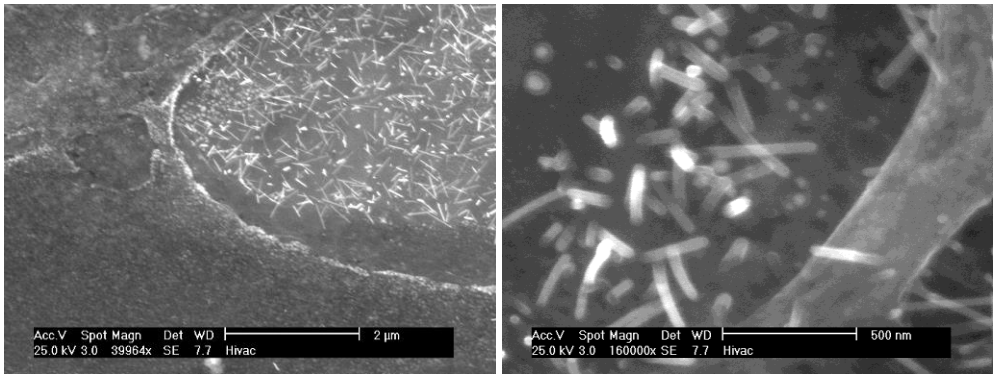

Figure 5-33 SEM images for tungsten nitride nanorods after nitridation at 650°C for 6 h, based on oxidation at 600°C from substrate A for 5 min

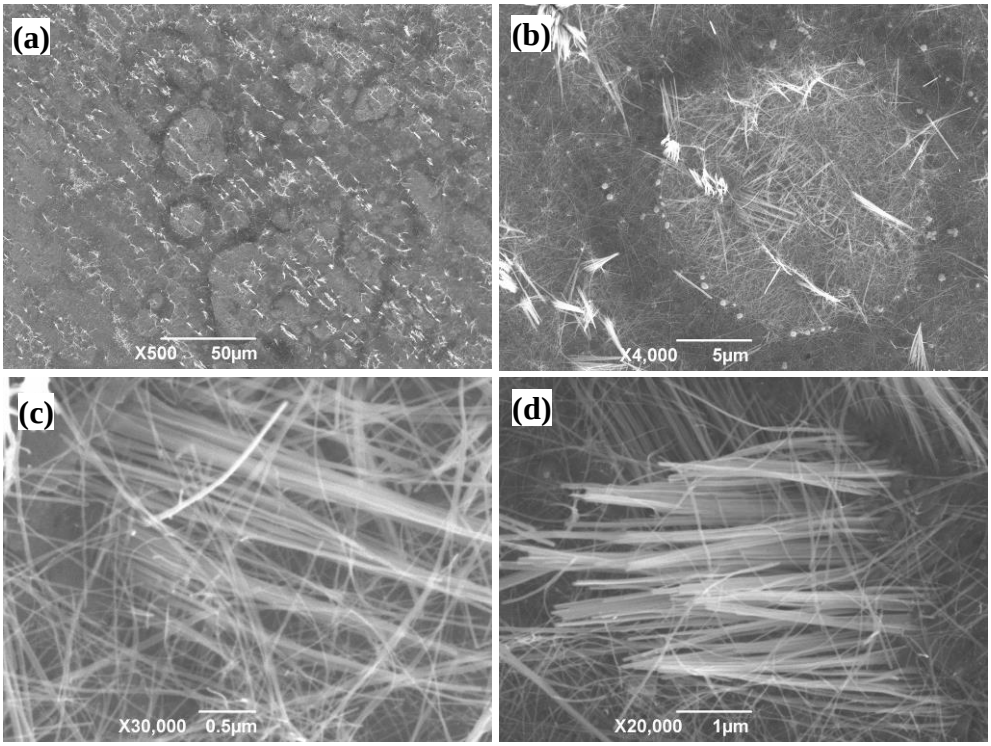

Figure 5-34 SEM images for tungsten nitride nanorods after nitridation at 650°C for 12 h, based on oxidation at 600°C from substrate A for 40 min

Similar phenomena have been observed for tungsten nitride nanorods converted by 12 h nitridation from nanorods from substrate A for 40 min oxidation, as shown in Figure 5-34 and Figure 5-28 respectively. With the original nanoporous pattern of the Au coating inherited, the tungsten nitride nanorods show a similar pattern as to the tungsten oxide nanorods. The coated areas, free of WO_x nanorods (dark area in Figure 5-28a and Figure 5-28b), is also free of WN_x nanorods (Figure 5-34a and b). The tungsten nitride nanorods also present a uniform diameter through their length which is up to several µm, and a localized parallel feature is exhibited (Figure 5-34c and d).

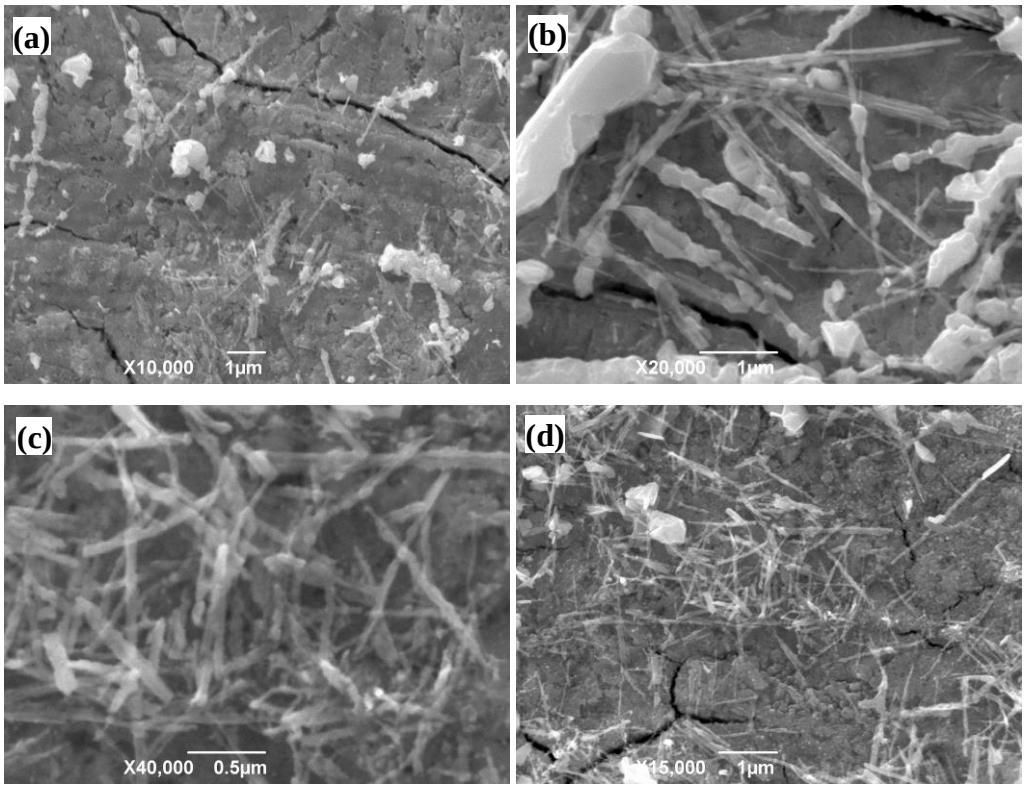

Figure 5-35 SEM images for tungsten nitride nanorods after nitridation at 650°C for 18 h, based on oxidation at 600°C from substrate A for 40 min

However, after longer nitridation time, these tungsten nitride nanorods would break from the bottom and fall down lying on the substrate, as shown in Figure 5-35. Some knots have formed through its axis direction which makes the diameter bigger and not uniform anymore, compared to nanorods after 12 h reaction (Figure 5-34). Some very big particles are observed lying on the substrate. The morphology evolution might partially be attributed to the brittle characteristics of the tungsten nitride, and will be discussed further later.

Figure 5-36 shows the tungsten nitride nanorod in the bright area maintained the feature of original oxide nanorods, as shown in Figure 5-29, and possessed a diameter of around 20 nm and length up to 200 nm, with no morphology difference being detected by SEM. The nanorods grew around the T-shaped engrave, whilst away from this mark no growth is observed, thus the patterned growth is maintained, as shown in Figure 5-29.

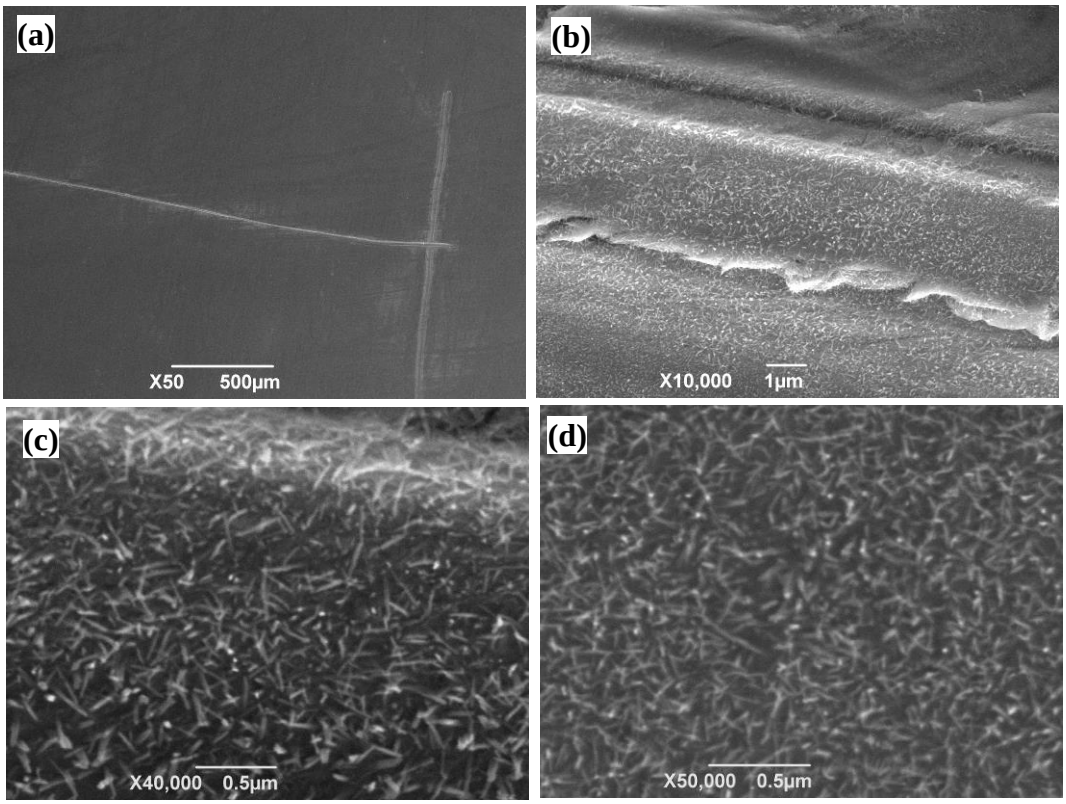

Figure 5-36 SEM images for WN_x nanorods after nitriding at 650°C for 6 h from substrate B based upon WO_x nanowires formed from oxidation at 600°C for 5 min

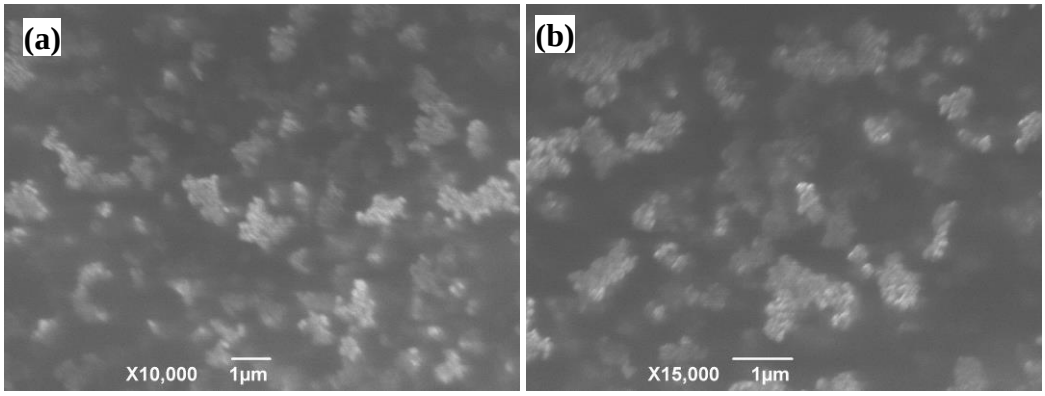

Figure 5-37 SEM images for WN_x nanostructures after nitriding at 650°C for 12 h from substrate B based upon WO_x nanowires formed from oxidation at 600°C for 5 min

In addition to the 6 h nitridation for substrate B (Figure 5-36), a much longer nitridation time of 12 h has also been applied, and the results are shown in Figure 5-37. Surprisingly, no nanorods but very tiny nanoparticles were observed on the substrate. These particles distribute on the substrate as isolated regiments, rather than a uniform layer, which indicated they were converted from the previous nanorods rather than growing from the substrate directly.

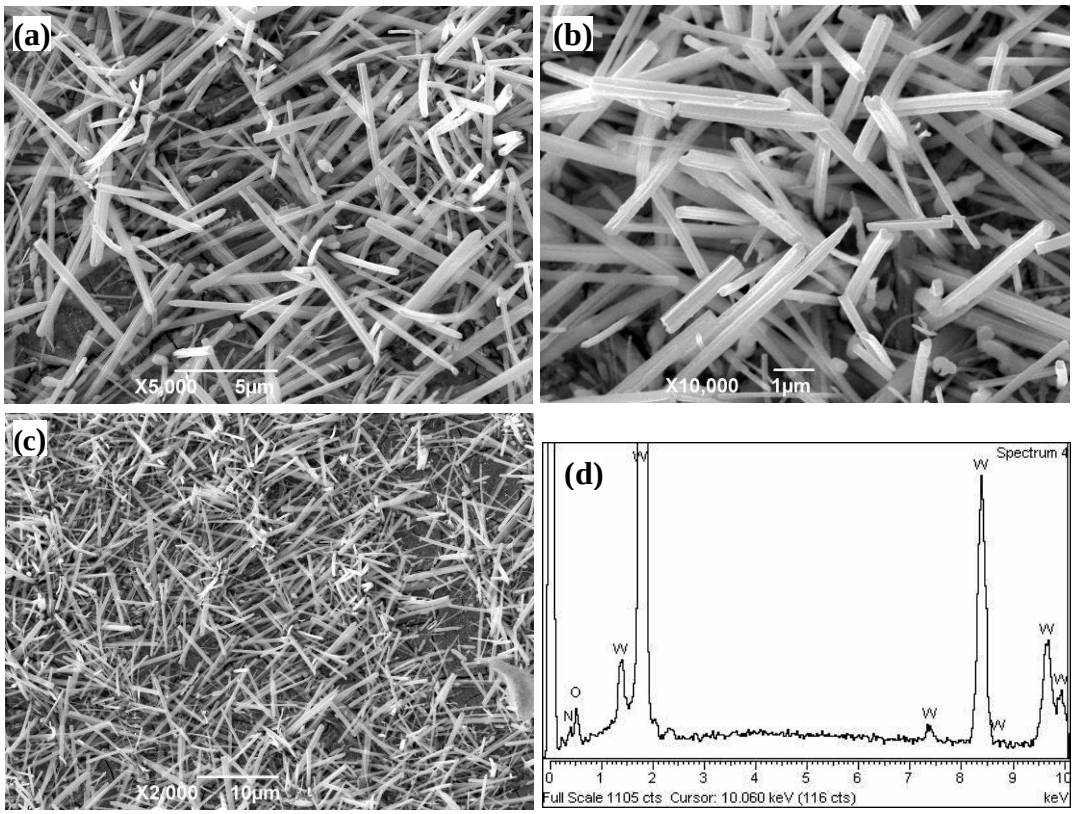

Figure 5-38 SEM images for WN_x nanorods after nitriding at 650°C for 12 h from substrate C based upon WO_x nanorods formed from oxidation at 750°C for 30 min

Though the overall distribution and appearance of the tungsten nitride on substrate C (Figure 5-38) have also inherited the distribution feature of WO_x nanorods (Figure 5-30g and h), it is noteworthy that compared with the WO_x nanorods in Figure 5-30g and Figure 5-30h, the nitride nanorods in Figure 5-38a to c seemed to be longer (up to 10 μm) and thinner (300 nm). The difference in length could be explained by the further growth during the process of rising temperature prior to nitridation; however the thinner diameter might relate to recrystallization during the nitriding process, and will be discussed further.

The EDX spectrum for WN_x grown from the W foil confirmed that the nanorods were composed of only O, N and W, as shown in the inset of Figure 5-38d, which is from an area element analysis for Figure 5-38c. The elemental analyses have confirmed that the resulting nanorods are not pure tungsten nitride (WN_x) but tungsten oxynitride (WO_xN_y), containing oxygen. O is reported to contribute to prevent the N desorption and help stabilize the tungsten nitride structure [192]. This is probably because the W possesses a stronger affinity to O than to N, and thermodynamically, the formation of WO_x (-842.9

kJ/mol for WO_3 and -589.7 kJ/mol for WO_2) is energetically favoured over the formation of tungsten nitrides (-22 kJ/mol for W_2N and -15 kJ/mol for WN) [193].

Figure 5-39 exhibits the three different stages of the XRD profiles during nanorods conversion on substrate A. All profiles show obvious W peaks (JCPDS No.1-1203) at 2-theta angles at 40.416 (110), 58.357 (200), and 73.3 (211), respectively. The peaks at 2-theta angles at 37.5, 43.8, 63.5 and 76.3 are corresponding to (111), (200), (220) and (311) planes of three possible cubic forms of tungsten nitride, W_2N (JCPDS No. 25-1257), WN (JCPDS No. 03-065-2898) or $W_{0.62}(N_{0.62}O_{0.38})$ (JCPDS No. 01-089-4762), which have almost identical cubic lattice structures with only small variations in their 'a' values, e. g. 4.126, 4.13 and 4.138 Å, respectively. Therefore, it is very difficult to precisely assign the XRD profiles to one or more particular nitride or tungsten oxynitride forms. However, the detection of oxygen content in these nanostructures by EDX analysis has indicated that these structures should be tungsten oxynitride rather than pure tungsten nitride, leaving only $W_{0.62}(N_{0.62}O_{0.38})$ (JCPDS No. 01-089-4762) being the closest match for the nitride products which has a content of 6.7 wt% N and 5.03 wt% O.

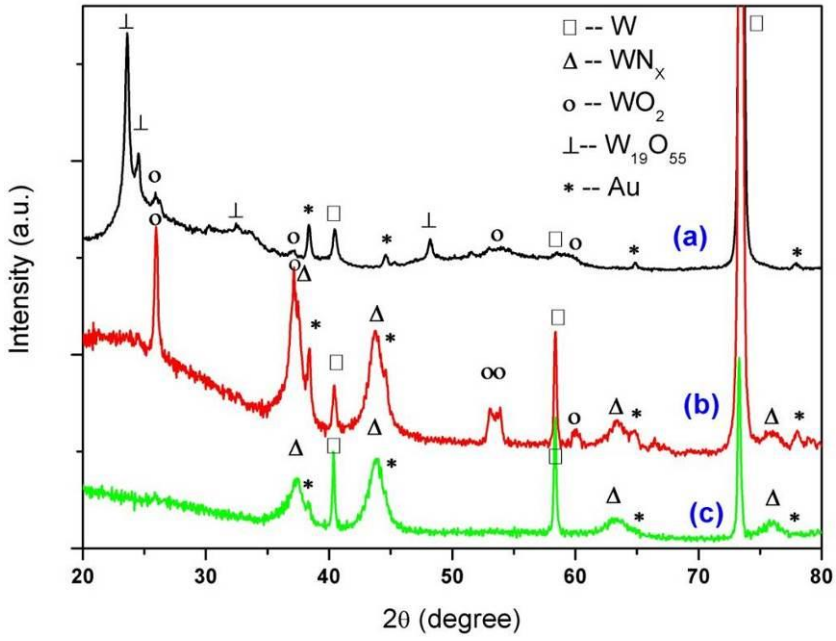

Figure 5-39 XRD profiles of nanorods on substrate A. (a): WO_x grew for 40 min, (b): nitriding of (a) in NH_3 for 6 h, (c): nitriding of (a) in NH_3 for 12 h.

It is noteworthy that in previous studies of various WN_x thin films or nanostructures, a certain amount of O content has been detected from almost all the final materials by

XPS and/or elemental analyses [40, 41, 166, 186], though some of which have been assigned as pure WN_x based only on XRD patterns [166, 186], In reality, XRD alone would not be able to see the differences between pure tungsten nitride and tungsten oxynitride.

After nitridation, the XRD results in patterns b and c display clearly the differences: shoulders of the $W_{0.62}(N_{0.62}O_{0.38})$ peaks at 38.1 and 44.4 as well as the two other peaks labelled with star at 64.5 and 77.5 should be assigned to the Au coating (PDF-01-071-4616), of which every peak presents separately in pattern (a). Furthermore, WO_2 (JCPDS No. 1-071-0614) peaks were indexed in (a) and (b), with circle labelled at 25.99 (110), 37.1, 53.2-54 and 59.8 (130). There still several peaks with '⊥' label remain in pattern (a), which matched well with the monoclinic $W_{19}O_{55}$ (JCPDS No. 45-0167). It is believed that the WO_2 peak in Figure 5-39 (a) is associated with the WO_x layer formed on the surface of the W substrate. The WO_2 intensity in Figure 5-39b is much higher compared to that of Figure 5-39a; whilst the strong peaks for $W_{19}O_{55}$ in pattern (a) disappeared. This result indicates that during the nitridation, the reduction of tungsten suboxide to WO_2 took place first, leaving the O vacancies for N to fill until almost all the O in the WO_2 being replaced by N, leading to the final product as pure $W_{0.62}(N_{0.62}O_{0.38})$ (Figure 5-39c). The XRD patterns of nanorods on other substrates showed similar peaks except the absence of Au signals.

Raman spectra of WO_xN_y nanorods were shown from Figure 5-40 to Figure 5-42. Figure 5-40 has shown Raman spectra for both WO_x nanorods and WO_xN_y nanorodsfrom substrate C (SEM images shown in Figure 5-30g to h and Figure 5-38a to c respectively). In comparison with Raman spectrum of WO_x nanorods shown in Figure 5-40b, Raman spectrum of WO_xN_y nanorods presented in Figure 5-40a showed predominant bands at 129, 183, 263, 323, 707 and 804 cm^{-1}, which shifted significant to lower wavenumbers compared to those of WO_3 nanorods [183], which indicated an increase in the bond lengths.

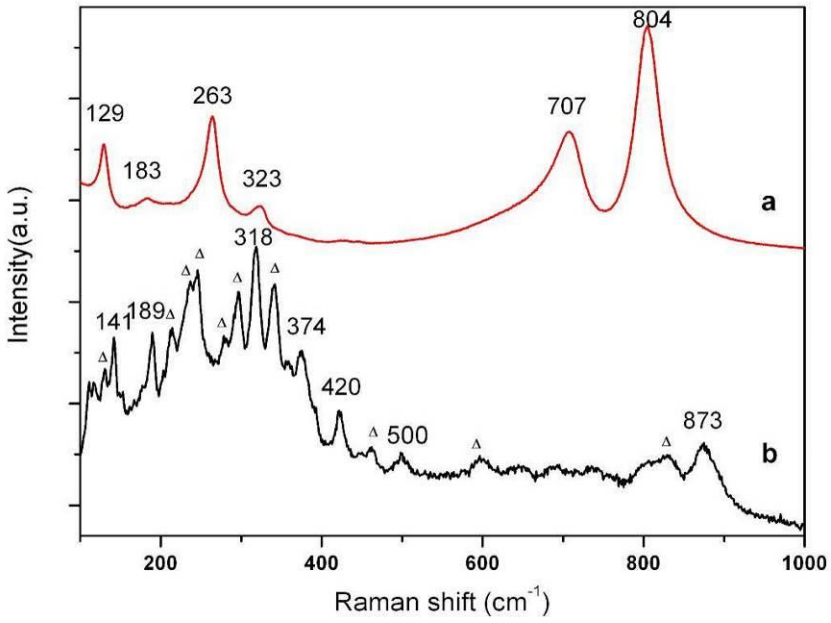

Figure 5-40 Raman spectra of (a) WO_xN_y nanorods from substrate C after nitridation for 12 h based on (b) WO_x nanorods on substrate C after oxidation at 750 for 30 min

Raman spectrum for the thinner and shorter WO_xN_y nanorod from blade engraved substrate B is shown in Figure 5-41. Very similar to Figure 5-40a, peaks are exhibited at 130, 183, 266, 323, 710 and 805 cm^{-1}, some of them have an extremely slight shift to higher wavenumbers while some appear at same wavenumbers. The similarity of Raman spectrum has implied the resemblance of structures in both nanorods from substrate B and C.

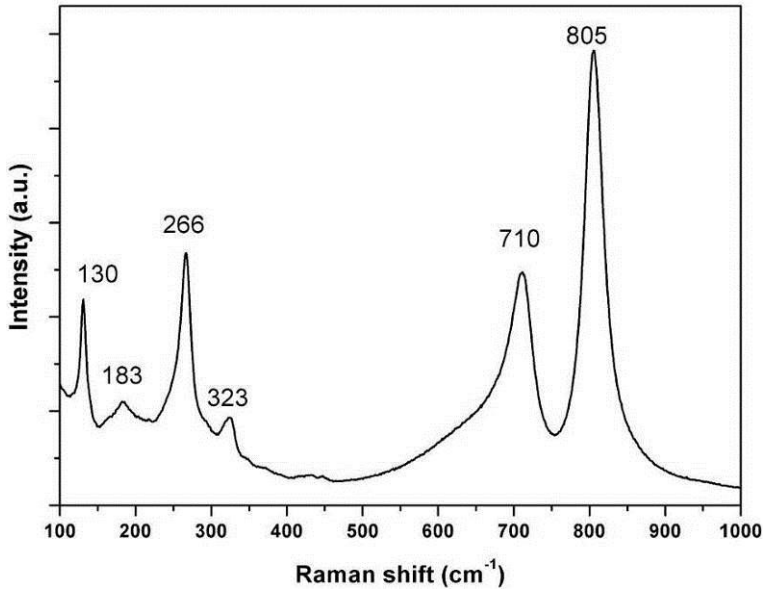

Figure 5-41 Raman spectra of WO_xN_y nanorods on substrate B after nitridation for 6 h

Figure 5-42 shows Raman spectrum for thin nanorods (from substrate A, SEM images shown in Figure 5-34), bands appeared at 126, 183, 253, 318 plus broad bands at 694, 799 and 807 cm^{-1}. The peak at 318 cm^{-1} consists of 4 tiny peaks at 307, 313, 318 and 322 cm^{-1}; whist the bands at 799 and 807 cm^{-1} almost merged into one peak. Compared with Figure 5-40a and Figure 5-41, several bands of the WO_xN_y nanorods on substrate A have shifted to lower wavenumbers. The multiply tiny shoulders for this spectrum for example the 318 peak cm^{-1}, might result from the coated substrate; whereas in substrate B and C, a more simple and clean substrate have led to a more clean and tiny spectrum for nanorods as shown in Figure 5-40a and Figure 5-41. In conclusion, these Raman results for WO_xN_y nanorods are similar to the only one literature found on WN_x with slight shift [35].

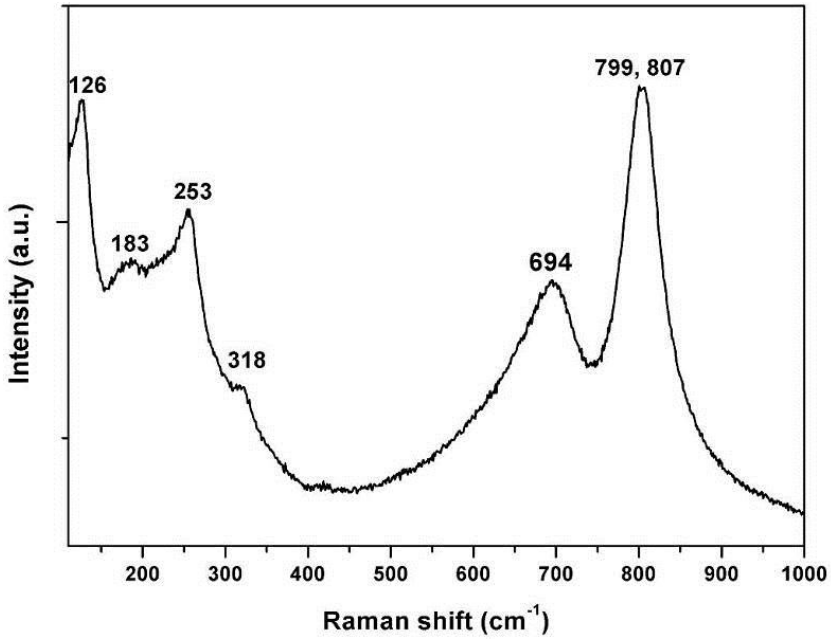

Figure 5-42 Raman spectrum of WO_xN_y nanorods on substrate A after nitridation for 12 h

TEM and HRTEM examination was also used to analyse the structural and compositional features of the nanorods. In our SEM study, there was no obvious change detected after the nitridation, but the TEM results revealed significant differences at the microstructural level. After ammoniating, the uniform crystalline WO_x nanorod became less uniform and exhibited a bamboo-like appearance at low magnification. The TEM images of different nitridation stages of nanorods upon 40 min oxidation of substrate A (Au coated W foil) were showed in Figure 5-43a shows a partically converted WO_x nanorod consisting of a clear bright shell and a dense dark core along its axial direction,

which occurred at the very early stage of the nitriding. The nanorods shown in Figure 5-43b and Figure 5-43c represent the completion of the nitriding process, with uniform contrast through the radial direction at low magnification. At high magnification, the detailed characteristics of some cavities or pores were observed (Figure 5-43c). Further HRTEM study confirmed that these porous-like structures in Figure 5-43c were arisen from the numerous multi-contrast areas within the nanorod, as shown in Figure 5-43d. An SAED pattern (inset in Figure 5-43c) reveals the single cubic crystalline structure of the nanorod, in consistent with the corresponding HRTEM results shown in Figure 5-43d.

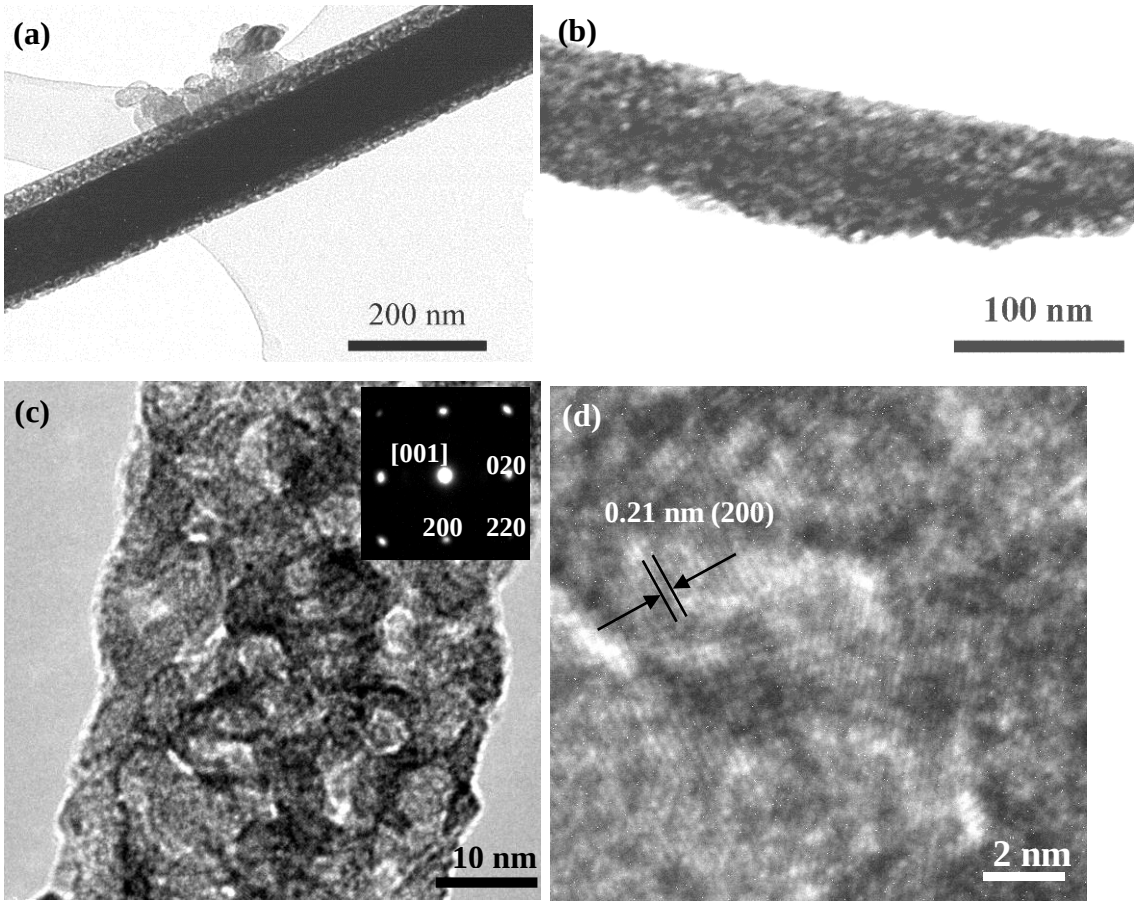

Figure 5-43 TEM and HRTEM images of WO_xN_y nanorods, (a) showing a partially reacted WO_xN_y nanorods from 6 h nitriding upon oxidation of substrate A for 40 min; (b) and (c) showing the completely reacted WN_x nanorods, from 12 h nitriding upon oxidation of substrate A for 40 min, and (d) showing the HRTEM image of (c)

Similar structures have previously been reported when converting the ultra-thin WO_x nanowires bundles into an ultrathin tungsten oxynitride nanowire [$W_{0.62}(N_{0.62}O_{0.38})$] [41]. It is believed that during nitridation process, crystalline re-arrangement have

occurred involving neighbouring oxide nanowires via inter-diffusion (mass transport). The inter-linked nanowires in the bundle recrystallized in appropriate sites upon heating to form a single-crystalline nitride nanowire with bamboo-like structure and larger diameter. However in our case, due to the largely incontinuous connection feature of the WO_x nanorods, it is unlikely for the inter-diffusion to occur as occurred to the aligned bundles. Another study regarding β-W_2N nanocrystals derived from tungstate-based inorganic–organic hybrid nanobelts also exhibited some resemblance to the current images [194], but the scrolled contrast suggested that their nanoplates composed of aggregates of multicrystalline nanoparticles, as showed in their SAED patterns. In this context, the WO_xN_y nanorod is believed to form directly from a single WO_x nanorod, based on our SAED and HRTEM results which both confirmed its single crystalline feature. However, the HRTEM further showed that the crystal re-arrangement indeed occurred during the compensation of N for O vacancies and the replacement of O by N. The recrystallization have some preferred favourite sites or orientations, and this might lead to the numerous domain orientations within the nanorod. The multicontrast areas also imply the exisitence of ultrafine pores/cavities or defects within the nanorod. Providing that the density of $W_{0.62}(N_{0.62}O_{0.38})$ is similar to the value of W_2N, 17.8 g/cm^3 [195], it is much higher than that of WO_x (7.16 g/cm^3 for WO_3 and 12.1 g/cm^3 for WO_2 with *d* spacing of 0.318 nm). The *d* spacing of the close-packed plane (111) for fcc $W_{0.62}(N_{0.62}O_{0.38})$ is 0.239 nm, much lower than that of 0.3787 nm for the close-packed plane (010) of monoclinic $W_{19}O_{55}$. Therefore it is not surprising that after conversion and recrystallisation, many tiny cavities within the rod would be left owing to lattice shrinkage. These cavities would be filled by lattice expansion if the nitride were oxidised again, according to a recently report [196]. Tungsten oxynitride nanorods from substrate C were observed longer and thinner. For the same reason during recrystallisation, the whole volume would shrink when the nanorods were reduced from $W_{19}O_{55}$ to WO_2 and eventually to $W_{0.62}(N_{0.62}O_{0.38})$, as shown in Figure 5-30.

Based on discussions above, a possible growth mechanism for the conversion of WO_x to $W_{0.62}(N_{0.62}O_{0.38})$ nanorod is proposed as follows (Figure 5-44). At first, the compensation of N and replacement of O by N take place simultanously at preferred sites on the nanorod surface. Accompanied by recrystallization, these sites will then be converted to WO_xN_y, leaving behind ultra-fine cavities due to lattice shrinkage (Figure

5-44b). After the initial nitriding, N has to diffuse through the surface layer with max spacing of 0.239 nm [*d (111)* for fcc tungsten nitride]. It will be difficult for the N (diameter of 0.15 nm) to diffuse through this outer barrier but relatively easier to penetrate through the tiny cavities. These diffusion chanels will be blocked after the size of the newly grown tungsten oxynitride reached a few nanometer, and freshly formed spaces need to be explored as new diffusion path for N, hence various domain orientations uniformly distributed throughout the nanorods at the end (Figure 5-43c and Figure 5-44c). The mechnism shows that nitriding reaction starts from the surface and progresses inwards to the core via a slow diffusion-controlled process (Figure 5-43a, Figure 5-43b and Figure 5-44b). The incontinous intra-diffusion of N through nitride frameworks and volume shrinkage during the oxide-to-nitride conversion lead to cavities everywhere (Figure 5-43c and d, Figure 5-44c).

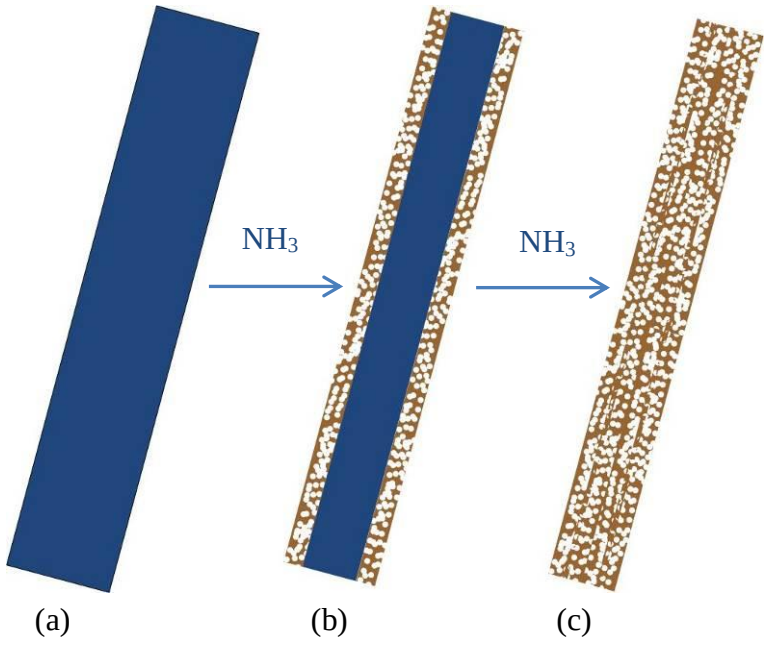

Figure 5-44 Sketch for conversion mechanism from WO_x to WO_xN_y rod: (a) WO_x nanorods from W-water vapour reaction; (b) partially reacted WO_xN_y nanorods from WO_x template and (c) completely reacted WO_xN_y nanorods

Further to SEM images shown in Figure 5-35, after 18 h nitridation in NH_3, tungsten nitride nanorods break from the bottom and lied on the substrate. TEM images have been taken for those nanorods and are shown in Figure 5-45. The nanorods with knots through the axil structure were also observed under TEM (Figure 5-45a). Figure 5-45b has shown the shape of nanorods, but seems to consist of sub structures with nanosize,

might be an agglomeration of nanoparticles; while Figure 5-45c clearly presents the agglomerate of nanoparticles which still maintained the shape of nanorod. These 3 different kinds of structure all present in one sample, reveal a possible morphology evolution process, in the order of Figure 5-45a to c.

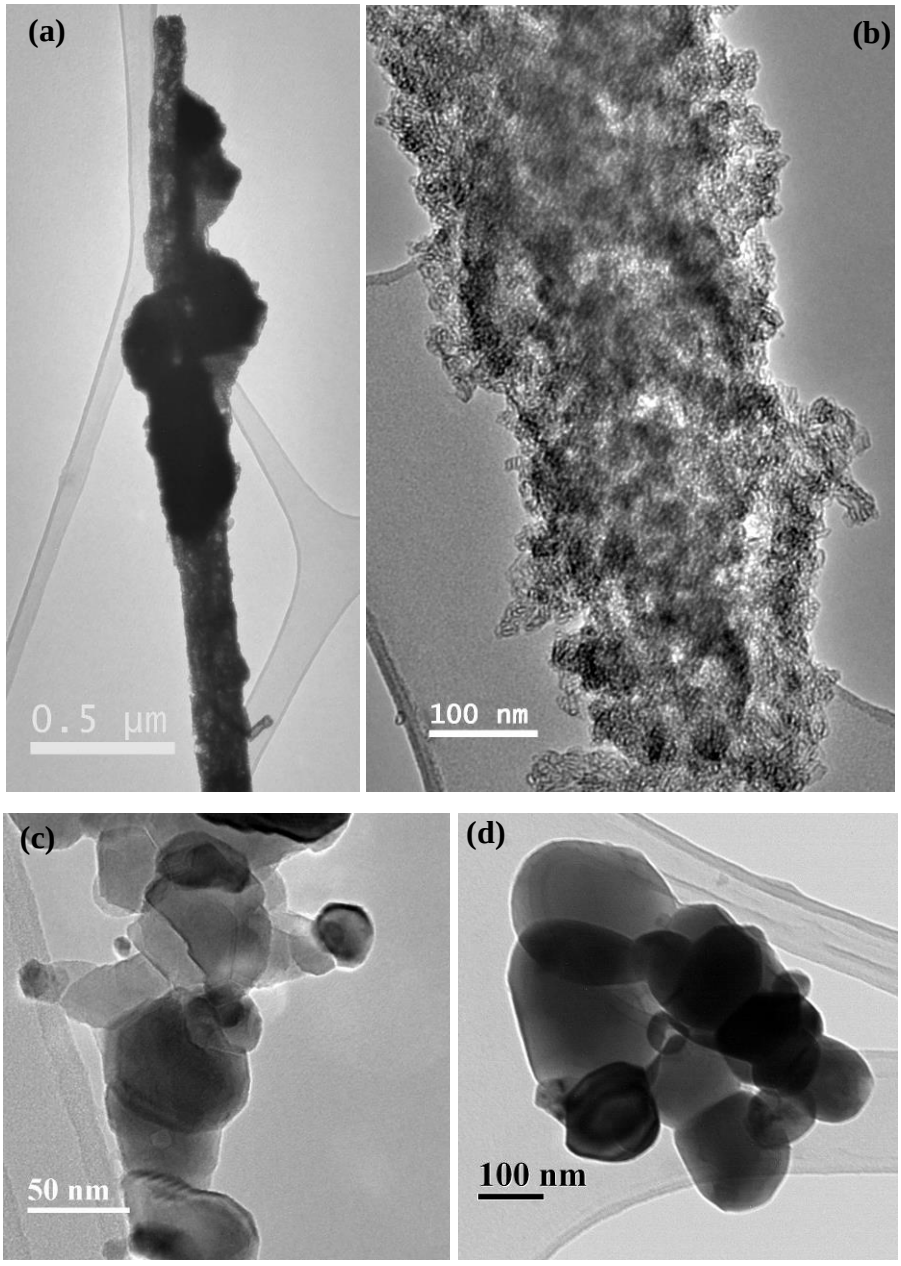

Figure 5-45 TEM images for WO_xN_y nanostructures (a, b and c) from 18 h nitriding upon oxidation of substrate A for 40 min (d) from 12 h nitriding upon oxidation of substrate B for 5 min

The different evolution stages of the nanorods might attribute to different diameter sizes. The nanorod shape structure shown in Figure 5-45b is quite similar to the nanoplates

reported in a previous study, as discussed above, and the nanoplates are proved to consist of aggregates of multicrystalline nanoparticles [194].

In addition, Figure 5-45d confirms the nanostructures observed in SEM images shown in Figure 5-37. This final stage of the nanoparticles formation took place for all nanorods on substrate B after 12 h, compared to only some of them reached this stage even after 18 h nitridation for long nanorods from substrate A. This is not difficult to understand, since it takes more time for longer nanorods to be fully nitride and converted to particles.

Based on the formation mechanism discussion for nanorods, further discussion for the conversion into nanoparticles is possible. After a certain reaction time, the nitridation of WO_x nanorods to tungsten oxynitride [$W_{0.62}(N_{0.62}O_{0.38})$] nanorods is finished. However the ammonia atmosphere in high temperature would continue the nitridation process, the O in tungsten oxynitride would also be replaced by N, and this time, the porous structure would provide more channels for N to penetrate through, the density of resulted product would be further improved and thus more space would be left, which finally make these bridging parts in tungsten oxynitride porous nanorod disappear and nanoparticles would form at last. During this process, there is a stage that not all particles become separated, thus the original shape of the nanorods would be preserved, correspond to Figure 5-45b. Figure 5-45c and d present the final stage of nanoparticles formation clearly, confirming the above discussion.

5.5.4 Conclusion

In summary, selectively patterned tungsten (oxy)nitride nanorods were generated from a WO_x nanorod precursor which was grown on a reverse-patterned W foil with Au coating by a simple W-water vapour reaction. The pattern was introduced by self-assembling hybrid materials based on copolymers followed by plasma etching. By adjusting the reaction time and temperature, the nanorod diameters, lengths and chemical compositions can be tailored. The evolution mechanism of tungsten oxynitride nanorods has been proposed, which will help future production of similar nanostructures. This result represents a simple, innovative and efficient process for reverse-patterned growth of new nanomaterials.

5.6 Summary

In this chapter, 0D and 1D WO_x nanomaterials have been produced by different methods, including 0D nanoparticles from decomposition of APT over melting point of tungsten oxide, ultrathin 1D nanowires from solvothermal synthesis starting with WCl_6 precursor and cyclohexanol or ethanol solvent, and 1D nanorods from a CVD process by reaction of water vapour and tungsten foil. In addition, 1D tungsten oxynitride nanorods have also been generated successfully, based on the 1D tungsten oxide nanorods. The main findings are summarised as below:

1. Very fine monoclinic tungsten oxide nanoparticles within 100 nm are produced by an APT decomposition, which could provide an high quality precursor for IF-WS_2 synthesis. Key parameters such as Ar flow rate, length of quartz tube, reaction time and reaction temperatures are investigated and optimised.

   Ultra-fine WO_x nanowires have been synthesised by a solvothermal method. Parameters to achieve nanowires with desired aspect ratios, diameters and lengths have been obtained. Using a mix solvent, we have obtained nanowires with a record high specific surface area of 275 m^2/g, nearly twice of the highest value reported so far, 152 m^2/g, for nanowires from solvent cyclohexanol alone.

2. Patterned tungsten (oxy)nitride nanorods were generated from a WO_x nanorod precursor which was grown on a reverse-pattern W foil with Au coating by a simple W-water vapour reaction, for the first time. The diameters, lengths and chemical compositions of nanorods can be tailored through different reaction temperatures, time and substrate treatments. A structural evolution mechanism has been proposed to explain the interesting nanoporous microstructure feature of the tungsten oxynitride nanorods. This work represents a simple, innovative and efficient process for reverse-patterned growth of new nanomaterials

Chapter 6 Synthesis of pure and composite IF-WS_2 nanoparticles using the rotary process

6.1 Introduction

This chapter introduces the synthesis of WS_2 nanomaterials. Based on the current rotary system, different preparation methods starting with different precursors have been investigated first, of which the gas-solid reaction starting with WO_3 nanoparticles precursor was proved the most efficient technique. Furthermore, systematic studies have been carried out to investigate the influence of temperature, reaction time, precursor types and reaction gases etc. on the synthesis of WS_2 nanomaterials, to optimise the parameters for WS_2 manufacturing. Furthermore, a new binary phased composite nanoparticle with an IF-WS_2 core and carbon shell was produced, for the first time, using our rotary reactor.

6.2 WS_2 synthesis by different methods

In the last chapter, WO_x nanomaterials, as an important precursor for WS_2 nanomaterials, have been synthesised by different methods, including the decomposition of APT, CVD and hydrothermal. In this part, the study will be focused on the IF-WS_2 synthesis via different processes, such as WO_3 and S mixture reacting with H_2, APT as precursor and H_2S as reaction gas, as well as WO_3 reacting with H_2S.

6.2.1 WO_3 and S mixture as precursor

For the initial trial, a composite powder of WO_3 and S at mole ratio of a 1:10 was used as the precursor and reacted under H_2 atmosphere at 800°C, following the procedure described in Chapter **3**. The products were collected from the quartz tube and analysed using XRD and SEM.

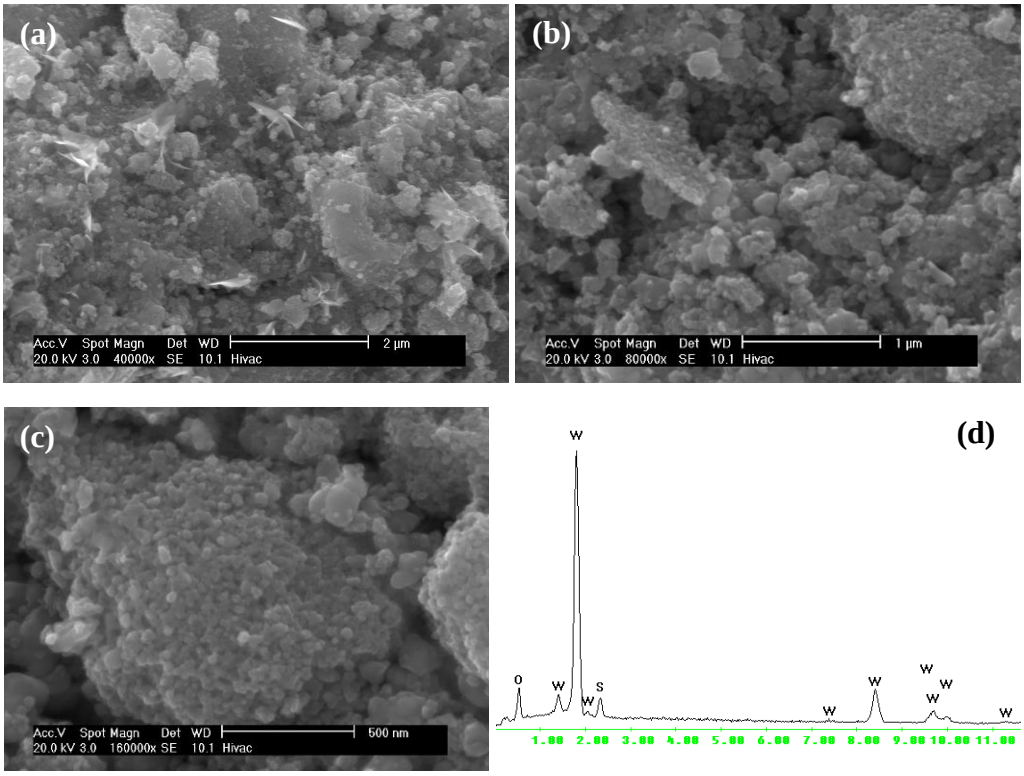

Figure 6-1 SEM images and EDX spectrum for products from experiment S1

SEM images of products from experiment S1 were shown in Figure 6-1. Very small nanoparticles and agglomerates were observed, with some nanoplatelets. The EDX spectrum shows that although WS_2 has formed, WO_x still dominates the products.

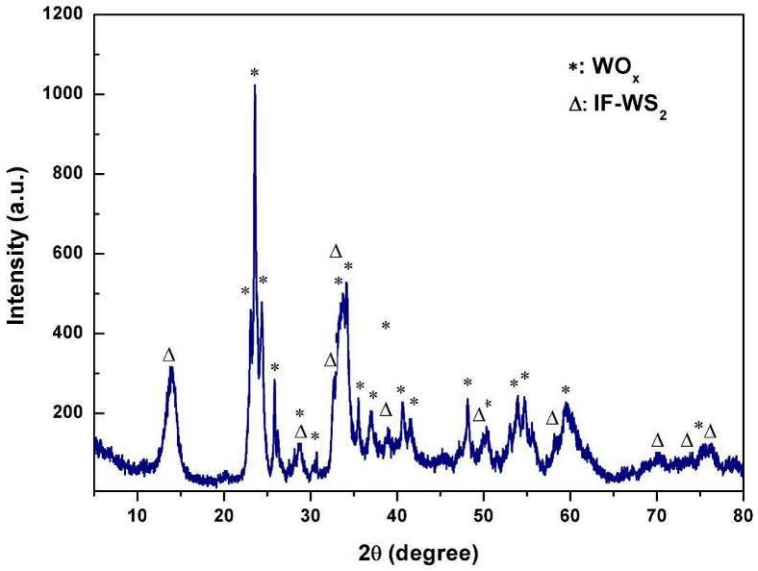

Figure 6-2 XRD pattern for WS_2 from S1 (reaction of WO_3, S and H_2)

An XRD result is shown in Figure 6-2. The peaks labelled with triangle matched well with WS_2 (JCPDS No. 84-1398), appearing at 14.364 (002), 28.959 (004), 32.769 (100),

33.587 (101), 35.943 (102), 39.599 (103), 44.055 (006), 44.289 (104), 49.798 (105), 55.977 (106), 57.495 (110), 60.010 (008), 60.573 (112), 62.746 (107) and etc. All the other peaks labelled with star could be assigned to $W_{18}O_{49}$ and $W_{20}O_{58}$. The highest WS_2 peak is at 2-theta 14.3° corresponding to (002), of which the layers are perpendicular to the radius direction of the particles. The relatively low intensity of (002) plane for WS_2 reveals that only a few WS_2 layers has formed from the outside and leaving behind a WO_x core which has been reduced from WO_3 to $W_{18}O_{49}$ and $W_{20}O_{58}$. The presence of $W_{18}O_{49}$ and $W_{20}O_{58}$ is in consistent with previous studies [18, 53, 89, 90], in which partially reduced $W_{20}O_{58}$ and thoroughly reduced $W_{18}O_{49}$ were reported during the process of oxide-to-sulphide conversion from WO_3 to IF- WS_2. There is no detectable S left in the products, according to the XRD.

Thus, it seems that there was not enough S to react with the reduced WO_x core, though a molar ratio of 10:1 had been chosen for S and W. This is because the S cannot stay long enough in the hot zone. As soon as the mixing powders reached the high temperature area, the S would sublime and the resulting S vapour was blown out of the high temperature area in a short time, though the gas flow rate was chosen as 80 ml/min according to an optimised flow rate in reference [197]. Therefore, no more WS_2 layer could form any more after all the S vapour left the hot zone.

There are some other work using WO_3 to react with S under H_2 to produce IF-WS_2 [197], also using a high molar ratio of S: WO_3 = 10:1, however the IF-WS_2 was produced with a yield of less than 0.1 g per batch. It is obvious that this method could not be scaled up, as the product quality depends upon the quantity of WO_3 nanoparticles used which cannot exceed 0.1 g per batch using traditional tube furnaces. To stop the S loss, other batch process has also been reported for the synthesis of WS_2 and MoS_2 [198], using solid $NaBH_4$ or $LiAlH_4$ as the H_2 releasing agent in a sealed ampoules, which is not suitable for continuous production neither.

In this thesis, evapouration continuous S feeding system was tested to investigate the loss of S during the reaction. In this experiment, a WO_3 and S mixed powder at a molar ratio of 1:10 was fed directly into the hot zone gradually using a syringe, when the temperature reached 600°C, rather than being pre-placed at the inlet end of quartz tube. Other parameters remain the same to previous investigations, H_2 (80 ml/min) and Ar (30 ml/min). The powder was kept feeding for 30 min and the reaction was lasted for

1.5 h at 800°C. The products were then collected from different areas of the quartz tube and prepared for XRD and SEM characterisation.

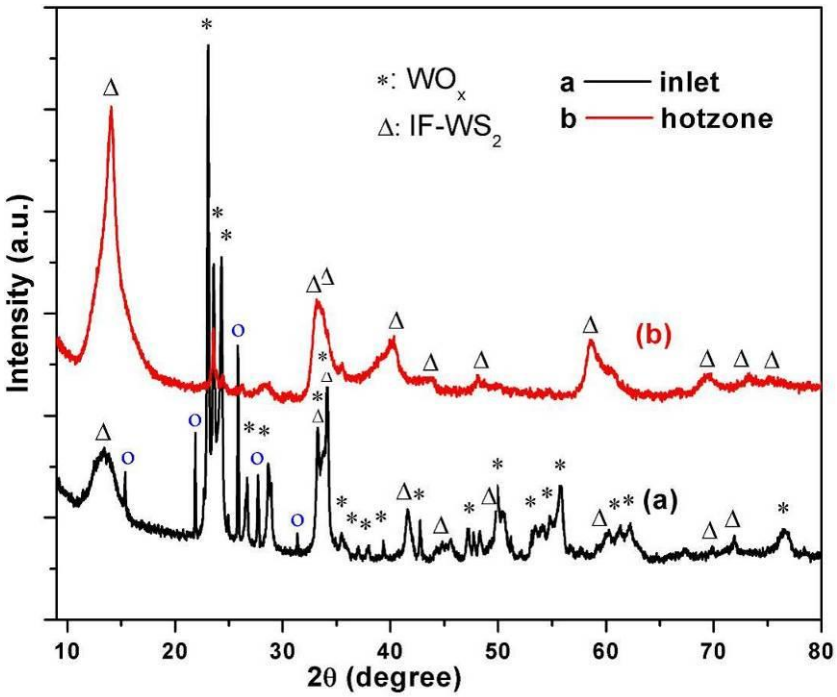

Figure 6-3 XRD patterns of products from experiment S2, (a): the products collected from inlet zone; (b): the product central hot zone

The XRD patterns of powders collected from both inlet and hot zone are shown in Figure 6-3. In both patterns, the peaks labelled with triangle matched well with WS_2 (JCPDS No. 84-1398), while all the other peaks labelled with star could be assigned to $W_{18}O_{49}$ and $W_{20}O_{58}$. For powders collected from the inlet zone (small leading tube in Figure 4-41), the (002) peak intensity for IF-WS_2 is very week, suggesting that only a few WS_2 layers was formed and the majority was WO_x, and S peaks were detected. Particles collected from the hot zone exhibit a high intensity of WS_2 peaks and very minor WO_x peaks, indicating that most of the oxide particles have been converted into IF-WS_2 in this zone, although some WO_x residue cores were occasionally visible.

The SEM images of blue powders collected from the small leading tube (Figure 4-41) are shown in Figure 6-4. Both very small particles and big aggregates were observed. There were also some very bright pieces, as shown in Figure 6-4c, which should be S residue, as also confirmed by XRD results (Figure 6-3a). Because the temperature in the inlet zone was relatively low, S could not completely react with the reduced WO_x in this zone.

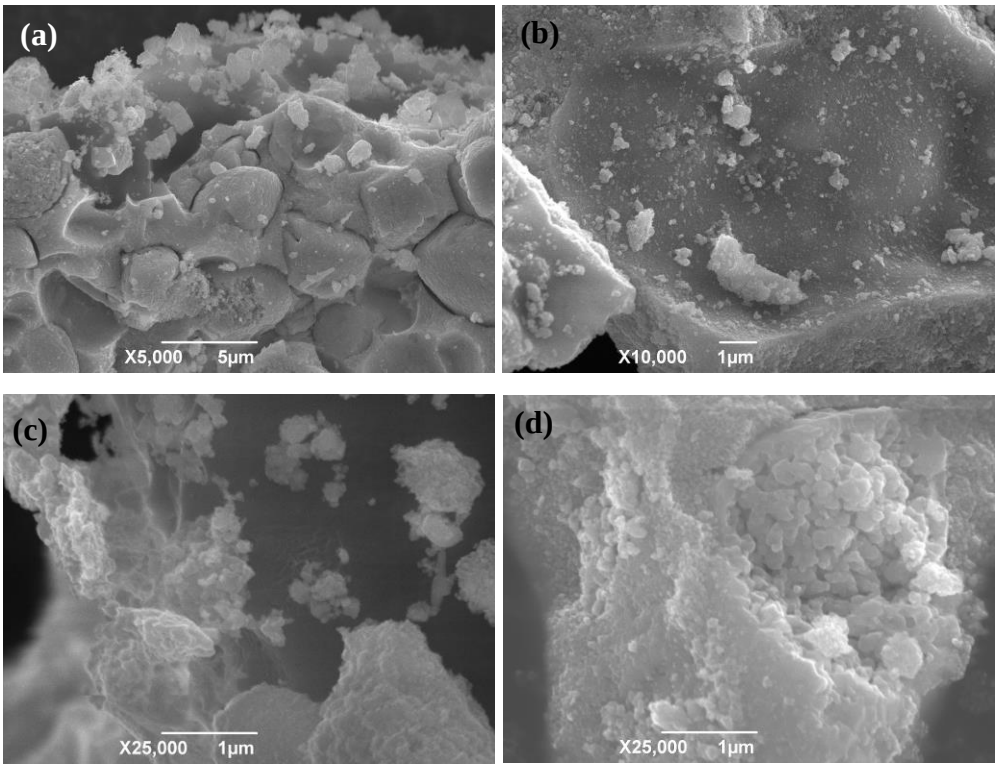

Figure 6-4 SEM for products collected from the inlet zone of experiments S2

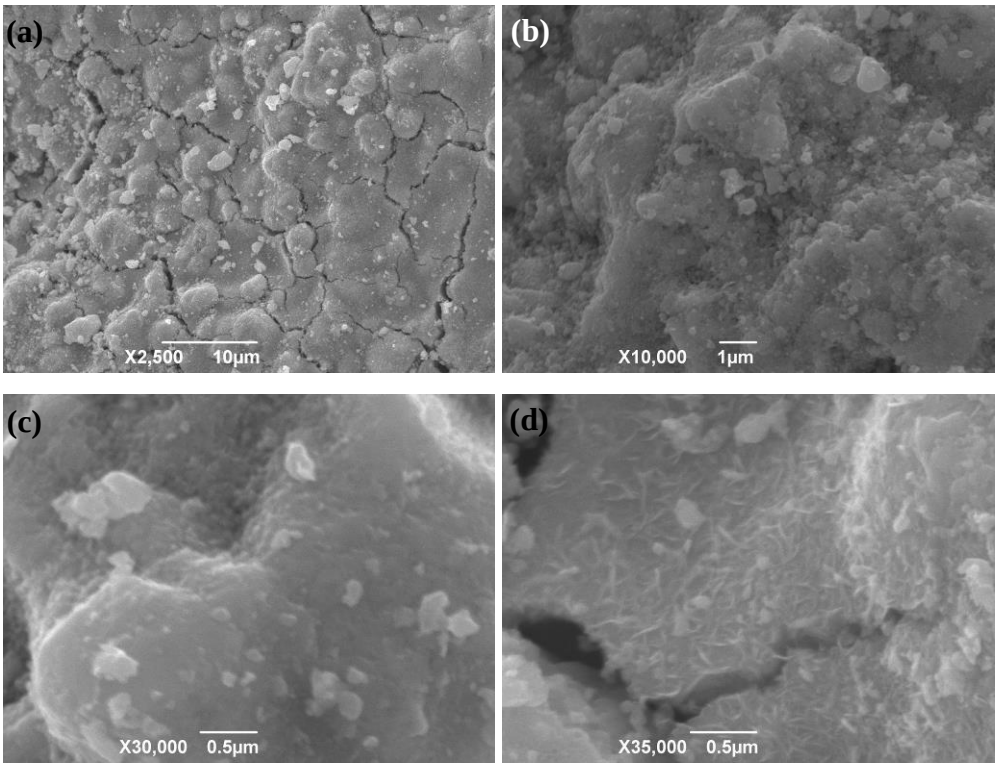

Figure 6-5 SEM images of samples collected from the hot-zone of experiments S2

SEM images for particles from the hot zone are shown in Figure 6-5. Some big agglomerates are visible, and they are composed of nanoparticles. As shown in Figure 6-5d, nanorods or nanoplatelets co-existed with nanoparticles.

Starting from WO_3 and S precursor reacting with H_2 gas has the potential for scaling up the manufacturing process, based on the current continuous feeding system. The S could be introduced from the feeding system all the time until the end of reaction. Refinement and optimisation of the process parameters could lead to high quality IF nanoparticles. However, it is worthy to note that the S vapour deposited onto the inner wall of the quartz tube and the gas pipes wherever the temperature dropped below its boiling point. Thus, the gas pipe was found blocked at the end of the experiment and would have to stop the experiment if the reaction were kept any longer. This is another practical issue, in addition to the large amounts of S consumption which would make this process less cost effective.

6.2.2 APT as precursor and H_2S as reaction gas

Since WO_3 nanoparticles were fabricated by the decomposition of APT, as described in the last chapter, and WO_3 nanoparticles have been proved to be very valuable precursor for WS_2 nanomaterials in previous two steps studies [1, 17-19], i.e. first decomposition of APT to form WO_3 then via sulphidisation to create WS_2, it is thus possible to combine the two steps together in our present set-up, to produce IFs in one go. This would be an advantage in terms of energy saving and process efficiency.

6.2.2.1 Experimental

During the first trail (named AHS1 after APT and H_2S), 6 g APT were placed into the centre of the quartz tube for the experiment, Ar flow at rate of 50 ml/min were flushed for 30 min before the furnace was switched on, H_2S flow was started from 550°C till the end of the process, at a rate of 12 ml/min. The whole reaction lasted for 2 h at 800°C, at a fixed Ar flow rate of 50 ml/min. After the reaction, the products were collected from different areas and characterised with both SEM and XRD. Two types of SEM sample were prepared: the as-produced particles directly on carbon film stickers and ultrasonicated deposited on a Si wafer.

6.2.2.2 Results and discussion

SEM images of the as-received APT particles are shown in Figure 6-6, they are crystals of several tens of μm in size, with nano-sized particles attached on the surface of these big crystals. Under high magnification, cracks and sub μm sized particles could be observed at the corners of damaged crystals.

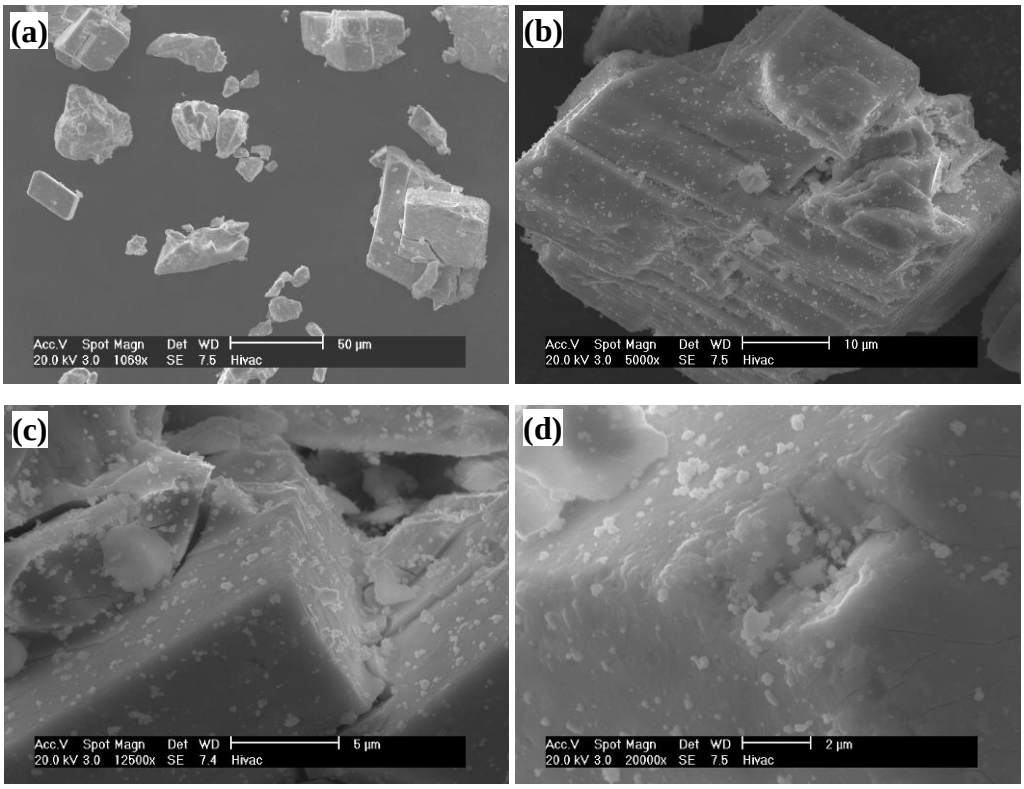

Figure 6-6 SEM images of as received APT particles

After reaction with H_2S at high temperatures, the particles collected from the hot zone are shown in Figure 6-7. These particles appear to maintain their original shapes of the APT particles, but high magnification study revealed that these 'crystals' were actually made of nanoparticles (Figure 6-7c), although nanoplates were also observed (Figure 6-7d). To further confirm this, an ultrasonic bath was applied for 1 h trying to split the aggolamorates. Indeed, the big agglomerates were fallen appart into small parts (Figure 6-7e and f), however these nanosized parts were proved to be dominated by nano platelets, with some nanoparticles co-exist.

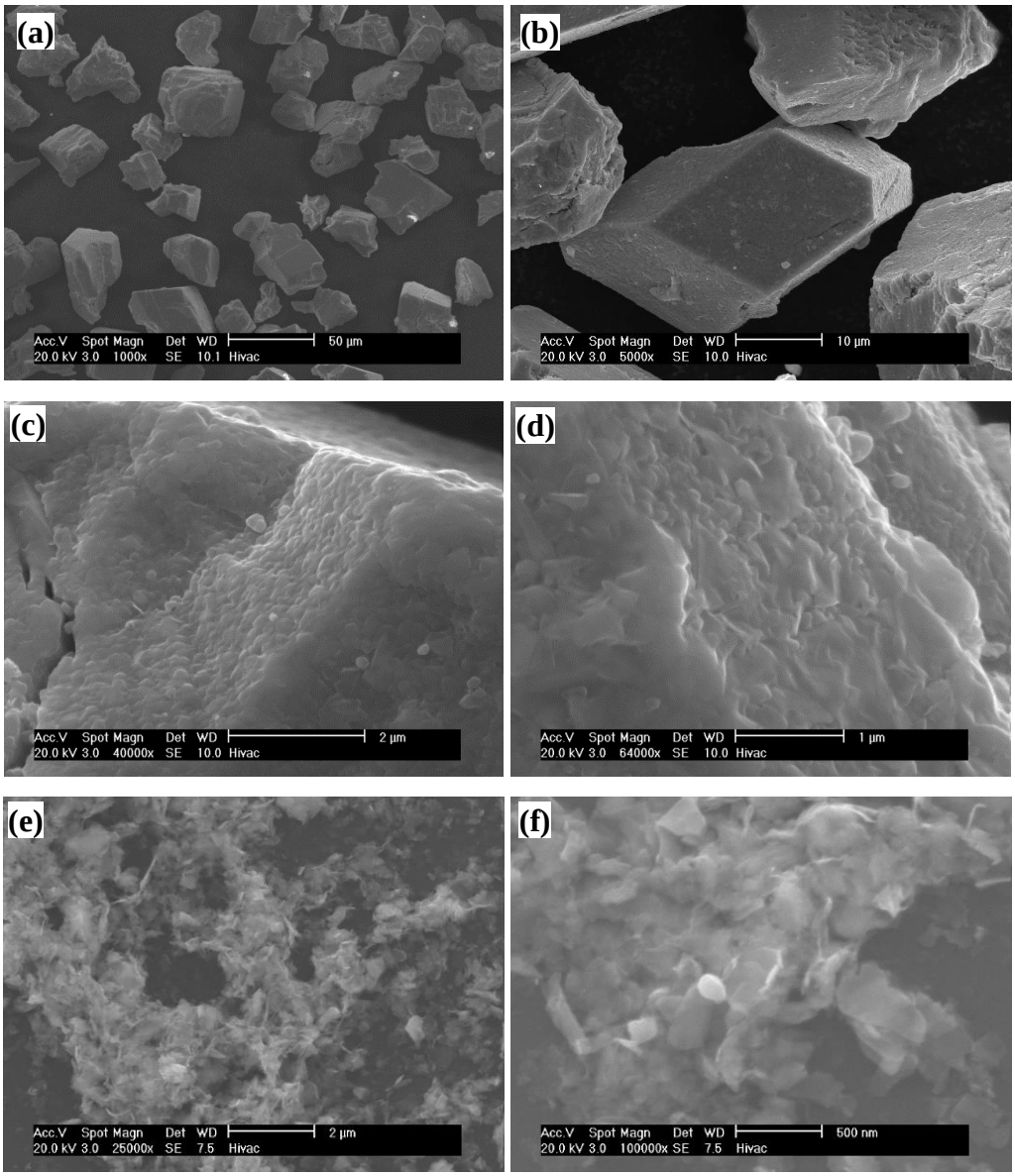

Figure 6-7 SEM images for products from AHS1

XRD profiles of particles collected from both the hot zone and the outlet zone are shown in Figure 6-8. In both profiles, the WS_2 (JCPDS No. 84-1398) peaks, labelled with triangles, appear at 2θ angles at 14.364 (002), 28.959 (004), 32.769 (100), 33.587 (101), 35.943 (102), 39.599 (103), 44.055 (006), 44.289 (104), 49.798 (105), 55.977 (106), 57.495 (110), 60.010 (008), 60.573 (112), 62.746 (107), 69.169 (201), 70.080 (108), and etc. In the pattern of the hot zone products, very high intensity WS_2 peaks are visible, with very weak WO_x peaks labelled with stars. The XRD pattern for products from the outlet zone shows the existence of WS_2 and tungsten suboxide (WO_x) which exhibits relatively high intensity, as these particles from the outlet stayed in the high temperature zone for a short time and failed to convert to WS_2 completely.

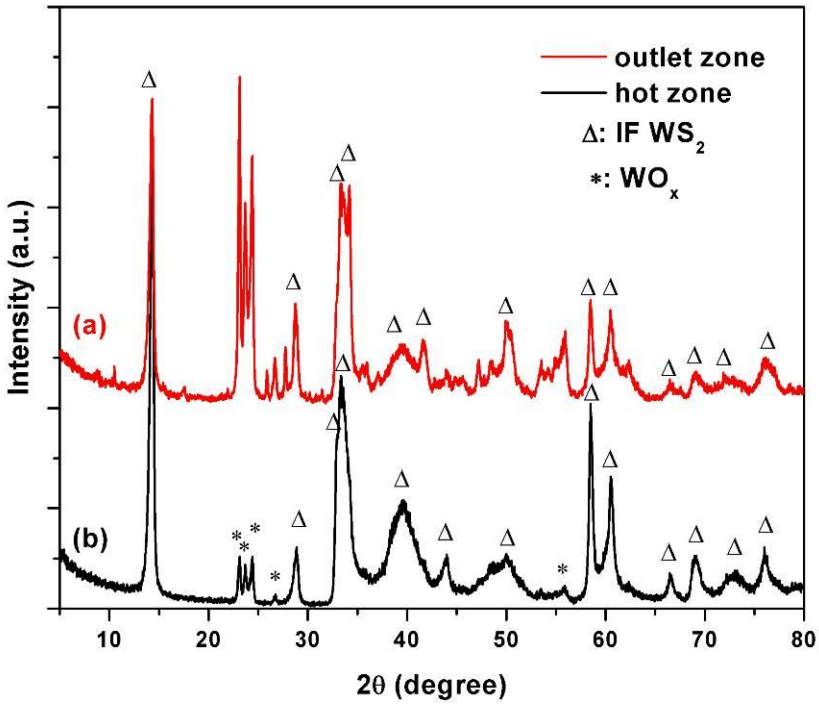

Figure 6-8 XRD pattern for samples collected from different areas in experiment AHS1

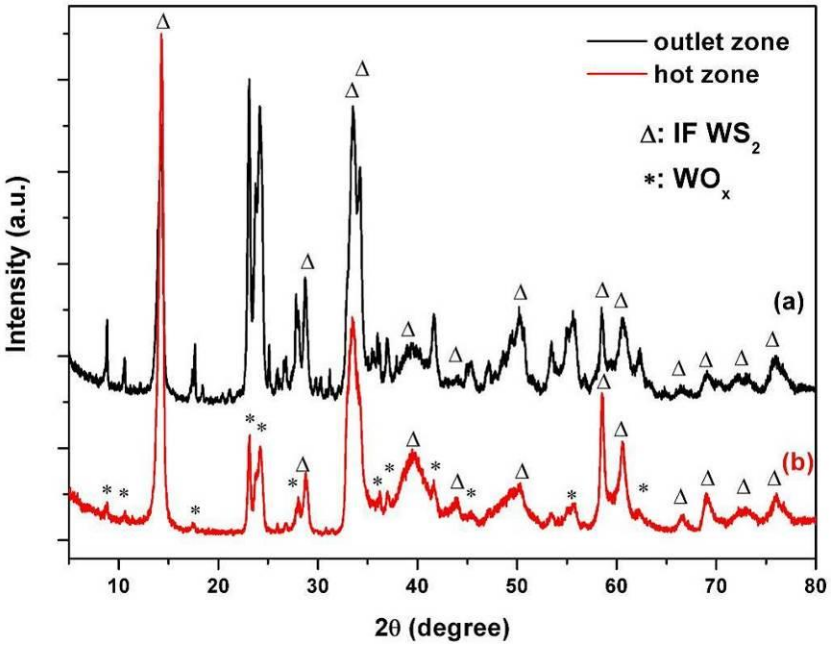

Figure 6-9 XRD patterns of samples collected from different areas in experiments AHS2

As the big agglomerates would split into small pieces under ultrasonic treatment, we then treated the APT particles prior to experiments. In this experiment (AHS2), using treated APT and H_2S, whilst kept all other experimental parameters identical to the initial experiment, the XRD patterns of products from the hot zone and the outlet zone are quite similar to those shown in Figure 6-8, as displayed in Figure 6-9. The hot zone products show very high intensity WS_2 peaks, with minor peaks of WO_x. As very strong

peaks (unlabelled peaks in the pattern (a) represent a high portion of WO_x in the final products owing to a shorter reaction time in the hot zone, this phenomenon could be improved by forcing the particles backwards into the hot zone, which can be easily realised by changing the inclination angle of the working quartz tube.

The hot zone WS_2 particles, as shown in Figure 6-10, appear to be different from those obtained from experiment AHS1. On average, the agglomerates are smaller (Figure 6-10a), although some bigger aggregates which kept the original APT crystal shape were observed, as shown in Figure 6-10a and b. Higher magnification study shown in Figure 6-10c and d revealed the nanostructural feature within the agglomerates, and they were composed of both IF-WS_2 nanoparticles and nano-platelets, roughly at the same amounts.

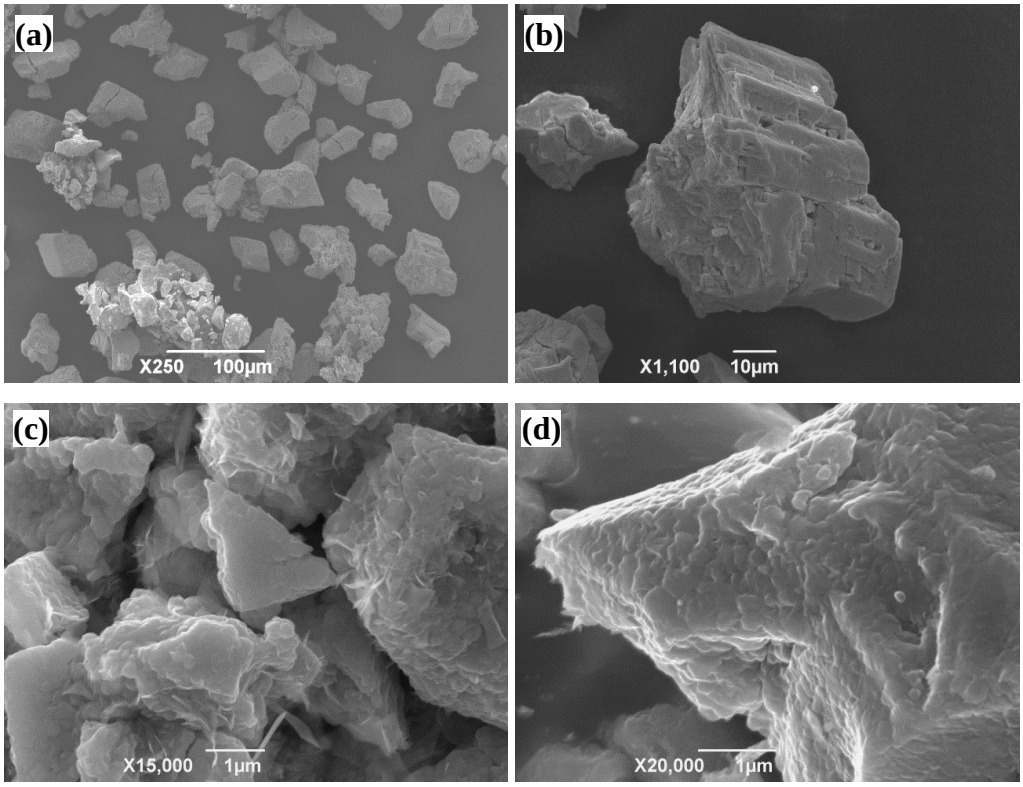

Figure 6-10 SEM images of samples from experiments AHS2

As discussed in Chapter **5**, the temperature needed to be above the melting point of tungsten oxide, which is 1200°C for nanoparticles and 1350°C for micro particles [20, 29], for the tungsten oxide vapour to be brought to and deposit in the low temperature area to achieve uniform tungsten oxide nanoparticles, which would then play the role as template in subsequent sulphidisation to form WS_2 nanoparticles. Owing to the temperature limitation, the experiments based on APT reacting with H_2S directly have

been proved unsuitable for the production of IF-WS_2 using current furnace. However, it is still possible that this method could work if a very long furnace with temperature up to 1400°C were available. Ideally, two furnaces with different temperature controllers, one produces vapour for uniform WO_3 nanoparticles growth at 1400°C and the other allows them to react with H_2S at 800°C, to complete the WS_2 nanoparticle formation. This could be future projects.

6.2.3 WO_3 and H_2S synthesis of WS_2 nanomaterials

The main emphasis was focused on the classic gas-solid reaction using WO_3 as the precursor and H_2S as the reaction gas, using current furnace, for IF-WS_2 synthesis.

6.2.3.1 Experimental

In the experiment, 6 g WO_3 nanoparticles were placed into the working tube from the inlet end, H_2S at the flow rate of 12 ml/min from 550°C, and the reaction lasted for 90 min at 800°C before furnace was turned off and the H_2S feeding was stopped. During the whole process, the majority of particles were kept within the hot zone. XRD, SEM and TEM were used to analyse the composition and morphology of the resulting products. The as-received WO_3 precursors have also been characterised by SEM and XRD respectively for easy comparison.

6.2.3.2 Results and discussion on IF-WS_2 nanoparticles

The SEM images of WO_3 precursor have been displayed in Figure 4-26 in Chapter **4**; and the average particles size was about 59.8 nm, calculated according to Derby-Scherrer Equation by using the FWHM of XRD peaks including 2θ angles at 26.7, 47.2 and 48.3. Figure 6-11 shows the XRD pattern of WO_3 nanoparticles, which matches very well with the monoclinic WO_3 (JCPDS No. 43-1035).

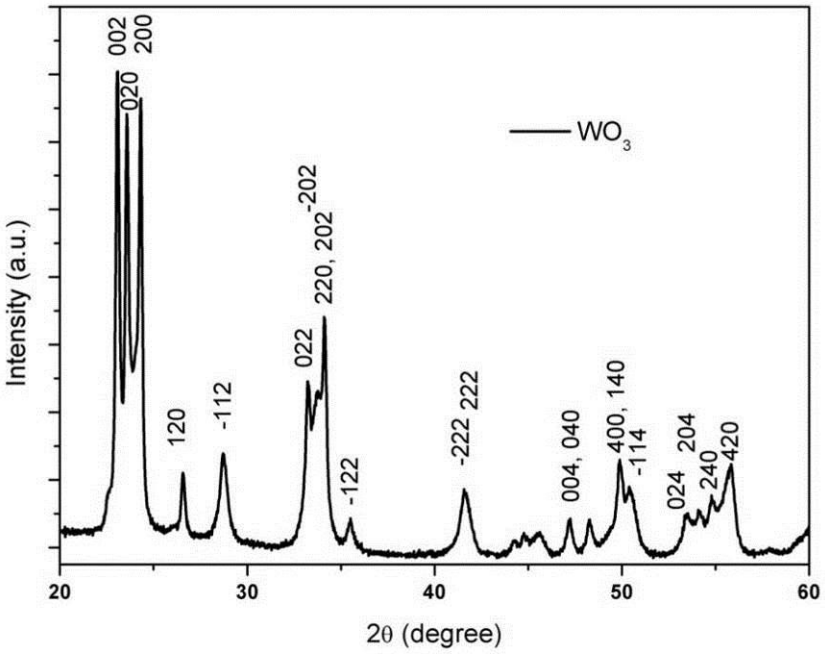

Figure 6-11 XRD pattern of the WO_3 precursor

Figure 6-12 shows the XRD pattern of resulting products. All the peaks labelled with triangle match very well with WS_2 (JCPDS No. 84-1398), confirming that the majority of the products are IF-WS_2 nanoparticles. Occasionally, WO_x residue remained in the core of some IFs, as elucidated by the WO_x peaks at 23-25 degree in the profile, labelled by stars.

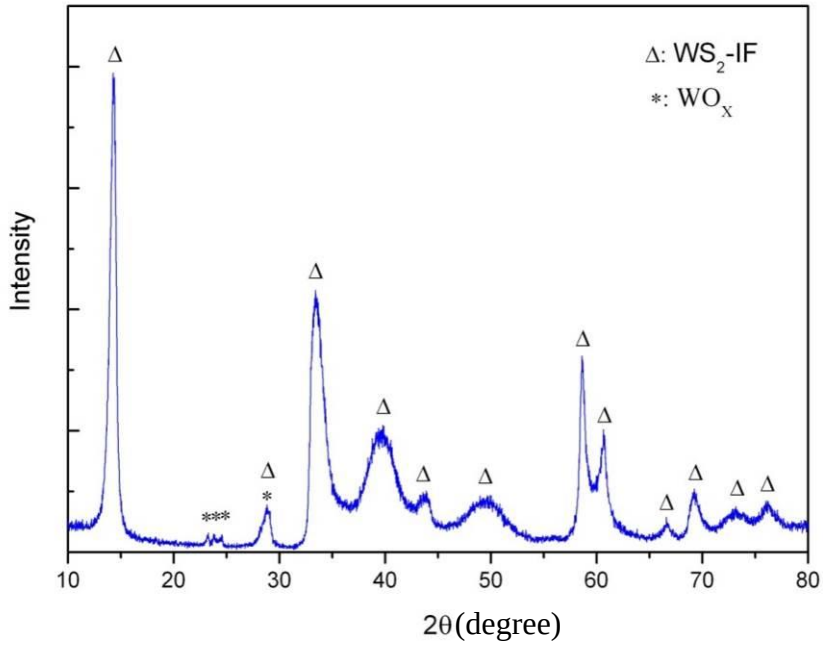

Figure 6-12 XRD profile of the WS_2 synthesised using the rotary process

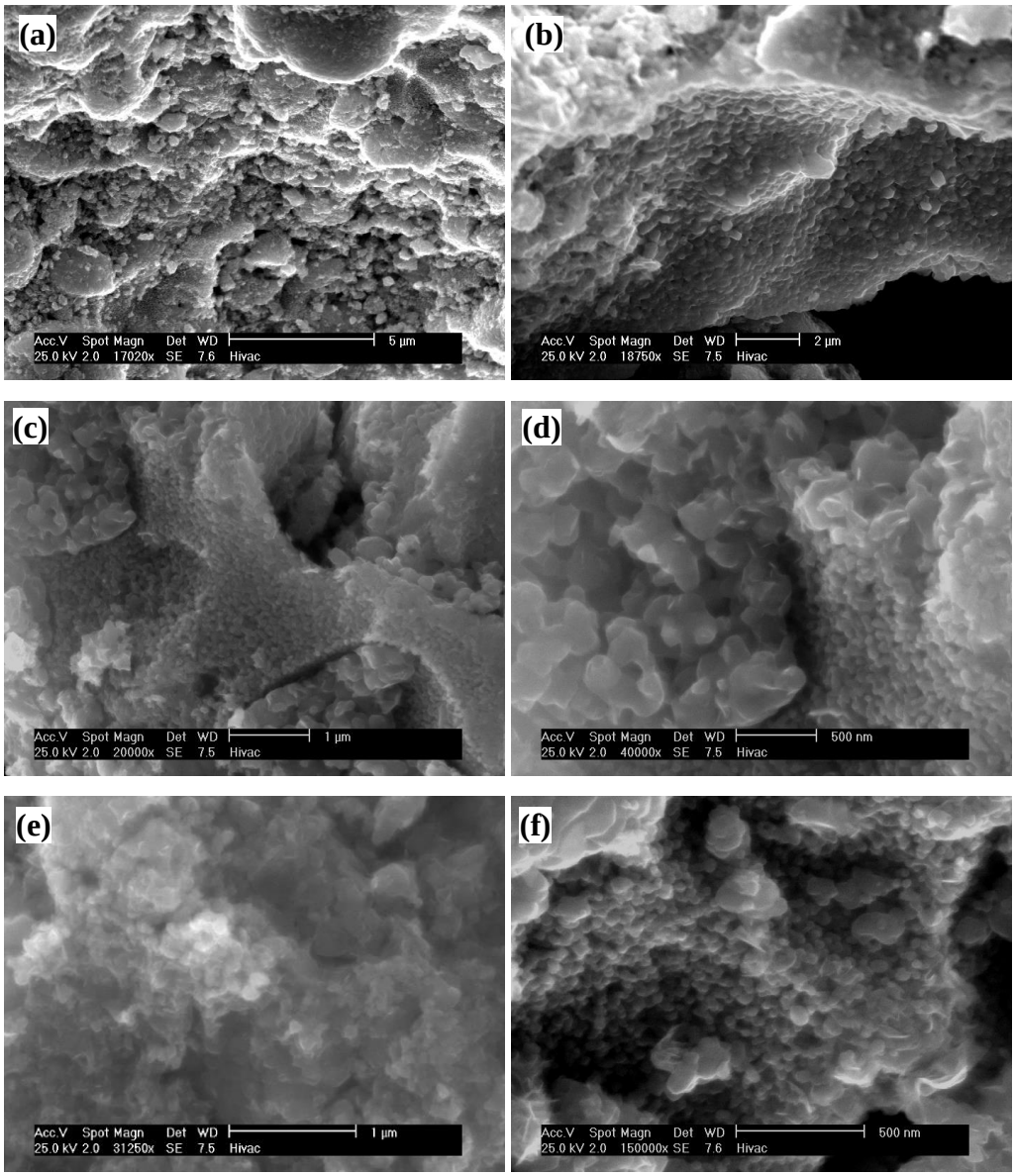

Figure 6-13 SEM images of IF-WS_2 synthesised using the rotary process

Figure 6-13 shows the images of resulting samples at different magnifications. The nanoparticles domination could be observed, with big agglomerates (Figure 6-13a and b). The nanoparticles exhibited different sizes (Figure 6-13c and d): the tiny ones having diameters <50 nm which are the same to the WO_3 precursor; whilst the big ones having diameters of 100-200 nm seemingly being merged from 2 or more nanoparticles. From Figure 6-13e, the presence of nanosheets or nanoplates amongst nanoparticles could also be observed from Figure 6-13d and f. This promising result led to further examination by using TEM, and the result is shown in Figure 6-14.

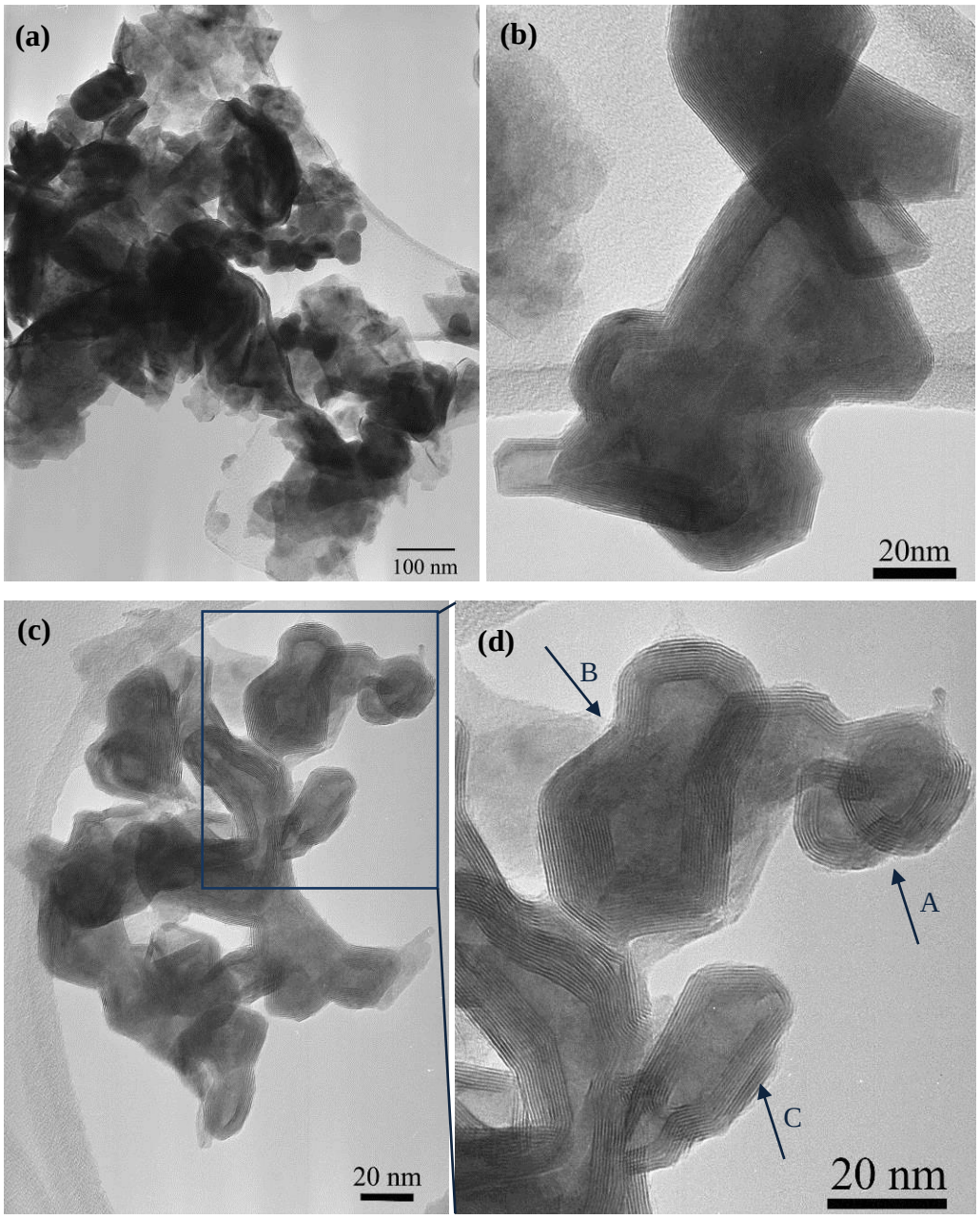

Figure 6-14 TEM images of the WS_2 synthesised using the rotary process (a, b and c, d is a zoomed in image of framed area in c)

Indeed, the TEM observations have confirmed that the sample contained both nanoparticles and nanosheets/nanoplatelets, as shown in Figure 6-14a. Figure 6-14b-d further reveals that the WS_2 exhibited the multi-layered, hollow core characteristics, and they are the dominant phase, which is in line with the SEM result. Some particles followed the principle shape of their oxide precursor, exhibited a perfectly spherical, seamless, and close-caged structure (as pointed by arrow A); whilst some displayed a peanut-like structure (pointed by arrow B) or a long elliptical shape (labelled by arrow C), possibly formed from several adjacent WO_3 nanoparticles that fused together during

the heating. The continuous contour of WS_2 layers suggests that these particles must have fused together first, then the oxide-to-sulphide conversion occurred. This observation has also explained the different particle sizes observed under SEM, as shown in Figure 6-13c and d. The products, regardless their different shapes, possess a hollow core and a generally equal *d* spacing of 0.62 nm which corresponding to the (002) plane distance for IF-WS_2.

6.2.3.3 Characterisation of bulk 2H-WS_2 and comparison with IF-WS_2

For a full understanding of the structure characteristics of IF-WS_2 nanostructures, 2H-WS_2 particles bought from Sigma Aldrich have also been characterised for comparison.

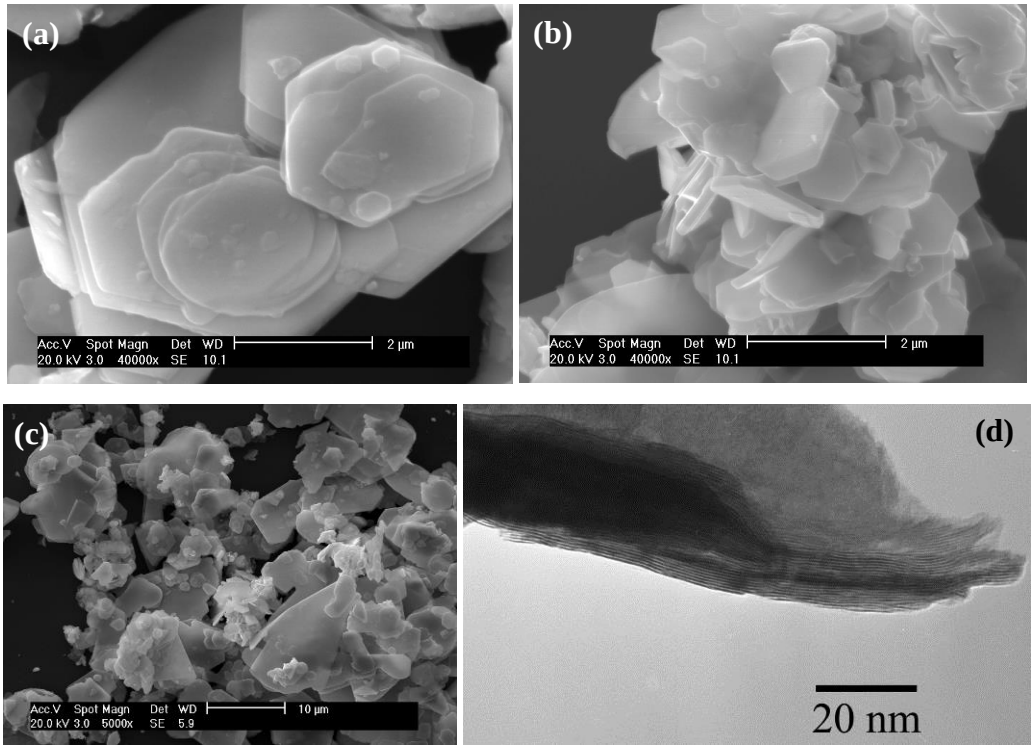

Figure 6-15 SEM (a, b and c) and TEM (d) images of commercial 2H-WS_2 particles

Unlike the semi-spherical IF-WS_2 nanoparticles, 2H-WS_2, as shown in Figure 6-15, showed a very clear platelet feature. The existing dangling bonds at the exposed prismatic edges made the rims of these platelets chemically reactive [7, 71]. The majority of these hexagonal plates are about 1 µm in size and 200 nm in thickness. TEM result showed their laminar layer structure (which one),with a *d* spacing of slightly smaller than 0.62 nm for the (002) plane. These structuctural chacterisations demonstrate that the 2H platelets are different from current closed nanocage structure of IF-WS_2 nanoparticles.

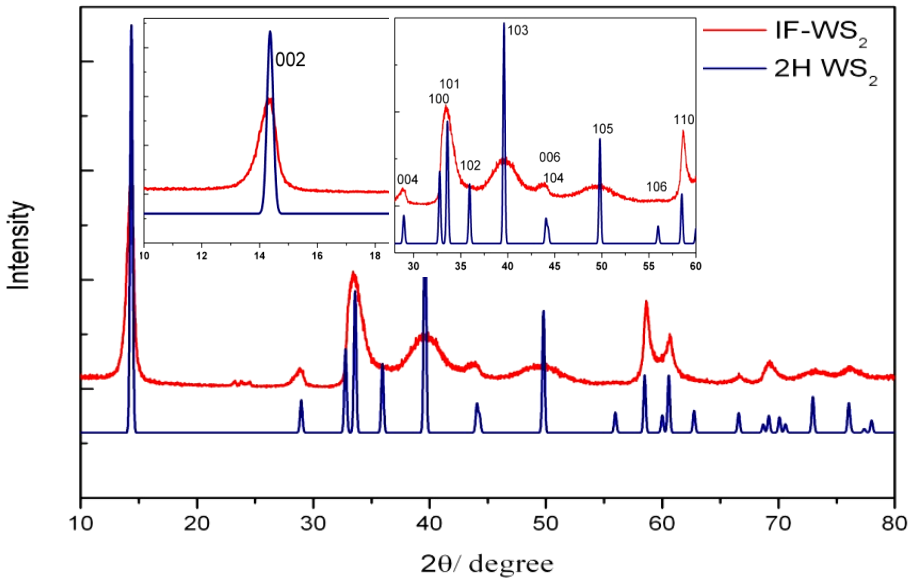

Figure 6-16 XRD profiles of commercial 2H-WS_2 and currently synthesised IF-WS_2

A comparison of the XRD profiles of both WS_2 samples is shown in Figure 6-16. Both patterns showed peaks of very similar position. The peaks of IF-WS_2 were assigned according to 2H-WS_2 (JCPDS No. 84-1398), as no standard XRD pattern is available for IF-WS_2 [18], and typically peaks appeared at 2θ angles at 14.364 (002), 28.959 (004), 32.769 (100), 33.587 (101), 35.943 (102), 39.599 (103), 44.055 (006), 44.289 (104), 49.798 (105), 55.977 (106), 57.495 (110), 60.010 (008), 60.573 (112), 62.746 (107), 69.169 (201), 70.080 (108), 72.957 (203), and 76.040 (116). For the 2H-WS_2, all the peaks detected are very sharp, which indicates a well-crystallized, standard 2H structure, with (002) as the strongest peak, followed by (103) as the second strongest. Compared with 2H-WS_2, the (002) peak of IF-WS_2 is left-shifted, indicating a lattice expansion of (002) layers, due to strains in the curved closed-cage layers [3], and the (103) and (105) peaks are broadened, attributing to ultra-low dimensions. Along with (002) remaining as the strongest peak, two peaks representing (100) and (101) have merged into one peak exhibiting the second highest intensity; also (006) and (104) peaks merged at around 44.1 degree. The peak for (102) at around 35.9 degree was not detected in the IF-WS_2 profile. The small peaks appeared at 23-25 degree in the IF-WS_2 pattern are assigned to WO_x, which must exist as the residue core of some IF-WS_2 particles that have yet to be totally converted.

In conclusion, characterisations of the products synthesised using the rotary process starting from WO_3 precursor and H_2S reaction gas have confirmed that IF-WS_2 are the dominant phase in the product with high quality. This shows the great potential for the

production of IF-WS_2 at large quantity and high quality, using our developed rotary process. Further detailed investigation will be carried out for quantity assessment and for quality improvement.

6.3 Investigation of IF-WS_2 synthesis

Based on the positive results from the initial trial, to optimise the parameters towards the synthesis of the IF-WS_2, a series of systematic studies was carried out. Different experiments using different parameters, gases, reaction time and temperatures were carried out to optimize the parameters for IF-WS_2 production. Some typical examples have been presented in the following section.

6.3.1 IF-WS_2 synthesis at different reaction time

In this part, some experiments have been conducted with the same rotary speed and temperatures, but different reaction time, in order to investigate the effect of reaction time on the final products of WS_2.

Table 6-1 summarises the parameters used for a series of experiments at a fixed rotation speed of 140 rpm, with reaction time varying from 10-170 min.

Table 6-1 Example parameters used for the synthesis of IF-WS_2 at varying reaction time

	WO_3 Precursor (g)	Gas feed rate (H_2S:Ar) (ml/min)	Reaction time (min)	Reaction temperature (°C)
A	6	12:100	10	800
B	6	12:100	50	800
C	6	12:100	80	800
D	6	12:100	110	800
E	6	12:100	140	800
F	6	12:100	170	800
G	6	12:100	80	900

XRD results of these experiments are shown in Figure 6-17. All these profiles exhibit similar features as discussed in detail in Section **6.2.3**. For experiment carried out for only 10 min (experiment A, Figure 6-17a), there only a very minor peak appeared at *ca*. 14.3 degree, presumably being the (002) plane of WS_2, whilst the peaks at 23-25 dominated which should be assigned to WO_3. All other protruding peaks of the black profile from other patterns should also be assigned to WO_3. This implies that the tungsten oxide was just about to be reduced, and only the outer layer finished the oxide-to-sulphide conversion while the inner core was intact. It is also inferred that the reducing of WO_3 to suboxide and the sulphidisation of these suboxides took place simultaneously during the process. For experiment B which lasted for 50 min (Figure 6-17b), the intensity of the (002) peak for WS_2 become considerably high, so are other peaks for WS_2. The peaks around 23-25 degree for tungsten oxide are decreased, demonstrating the fact that the oxide particles have mostly converted to IF-WS_2 and much less suboxide left in the core. Similarly, lower WO_x peaks at around 23-25 degree and higher IF-WS_2 peaks were presented for results of 80 min (Figure 6-17c), compared to that of 50 min, indicating very few oxides in the core and much more IF-WS_2 layers formed outside after longer reaction time.

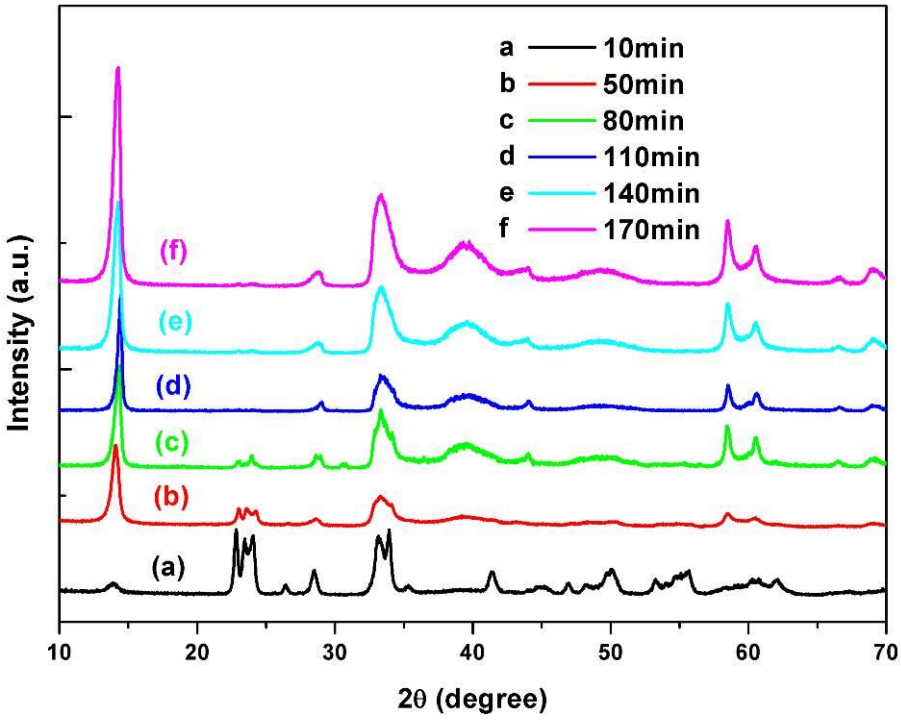

Figure 6-17 XRD profiles of samples from experiments A-F, demonstrating the effect of different reaction time at 800°C from 10 min to 170 min

For experiments carried out for 110, 140 and 170 min (profiles in Figure 6-17d, e and f), much higher intensities of WS_2 peaks are observed with increased reaction time, which means more and more seamless WS_2 layers have formed. Very minor WO_x peaks were also detected for samples obtained from 140, 170 min reaction, this should be attributed to those particles failed to stay in the hot zone long enough, which is somehow normal in a rotary process as some particles especially the heavier ones (agglomerates) would reach the end very quickly therefore failed to complete the conversion. It is worth to note that after 110 min reaction, there almost no peak is detected for any tungsten oxide, suggesting that around 2 h reaction time is enough for a thorough sulphidisation.

6.3.2 WS_2 synthesis at different temperatures

Of the above experiments, batches C and G used similar parameters, except for the temperature which was 900°C for batch G but 800°C for batch C. The XRD patterns and SEM images of both experiments are shown below.

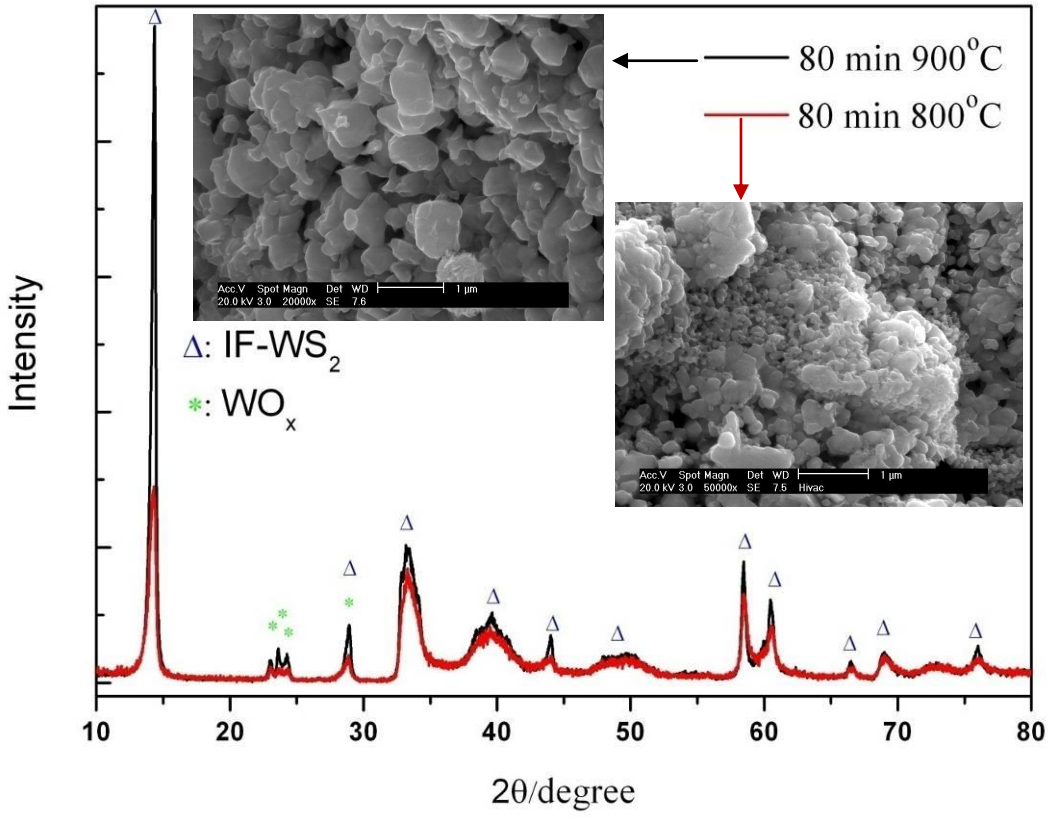

Figure 6-18 XRD profiles of samples from batches C and G and their SEM images

In the XRD pattern (Figure 6-18), the intensity of WS_2 in batch G (900°C) is much higher than that in batch C (800°C), indicating more WS_2 layers could be formed in the

sample from batch G, within the same reaction time of 80 min. As discussed above, some oxide peaks appear inevitably for both XRD profiles, indicating the presence of tungsten suboxide residue in the sample.

SEM images for samples from batches C and G are shown in Figure 6-19 and Figure 6-20 respectively. 2H-WS_2 flakes presented in both samples, however there were much more 2H-WS_2 formed in batch G, possibly due to the higher temperature which made agglomeration severer.

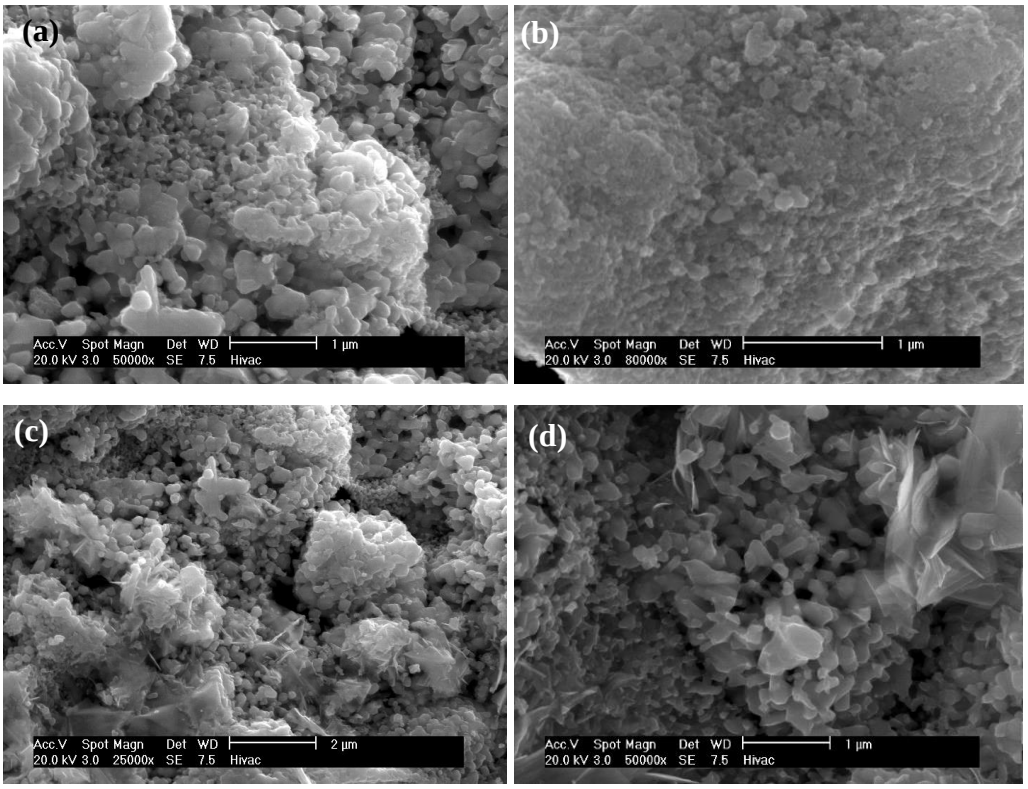

Figure 6-19 SEM pictures of samples from batch C

In addition to the 2H-WS_2 flakes, the IF-WS_2 particles are considerably bigger in batch G, and some of which exhibited a diameter of 300-500 nm, against that of 100-200 nm in experiment C. This observation accounted for the extremely high relative intensity of the (002) peak for samples in experiment G. Because a very big particle contains more regular, flat (002) layers than those of curved and bended (002) layers in an IF-WS_2, thus the intensity of (002) at around 14.3 degree and the intensity ratio with other planes is much higher than those small particles in experiment C, as presented in Figure 6-18.

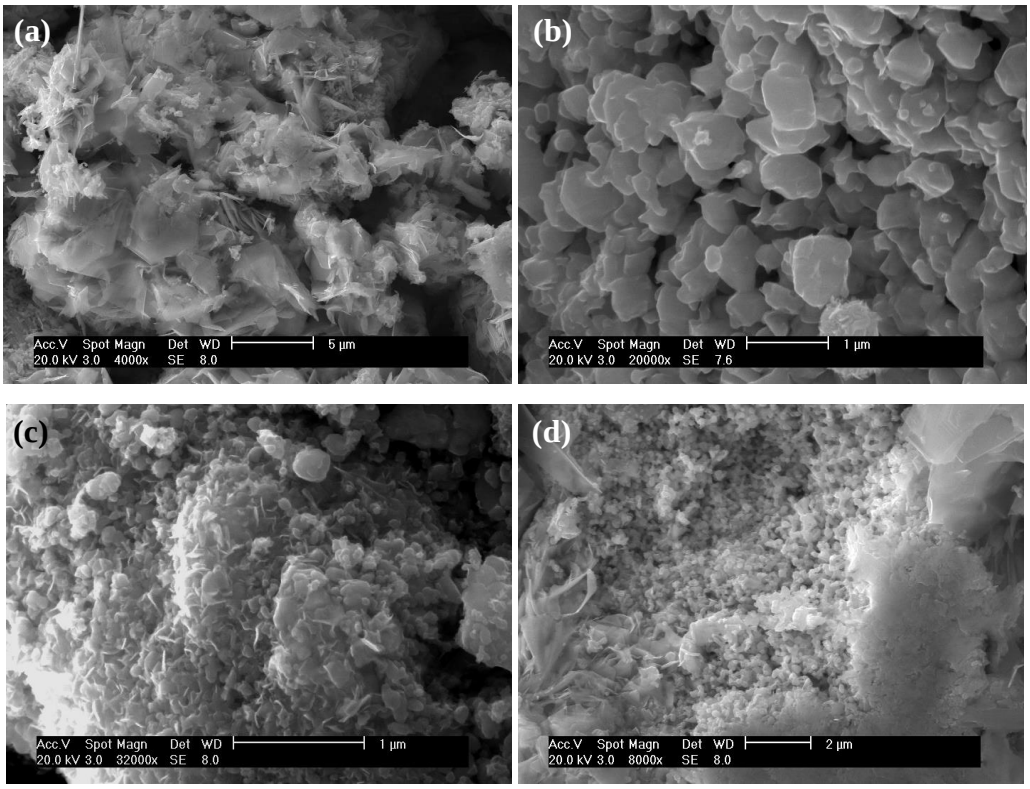

Figure 6-20 SEM pictures of samples from batch G

Actually, when compared with other experiments from A-G, the quality of products from batch G is the worst, and the temperature used (900°C) was the highest, regardless of different reaction time. Thus, temperature is probably one of the most significant parameters directly linked with agglomeration, at least over the tested time periods.

6.3.3 IF-WS_2 synthesis with the presence of H_2

After several experiments, H_2 was introduced to the reaction tube, to promote the WO_x and H_2S reaction. The experimental parameters were optimised after a series of experiments. H_2 was introduced at around 450°C at a flow rate of 8 ml/min, before the introduction of H_2S at 550°C, and the final gas ratio of H_2:H_2S:Ar during the reaction was maintained as 8:12:100, at 800°C and the reaction lasted for 90 min.

Figure 6-21 shows the occurrence of very few 2H-WS_2, (Figure 6-21a), and the majority of the product is IF-WS_2 of less than 100 nm in size (Figure 6-21b and c). Rod shaped WS_2 were also observed, in Figure 6-21d. Indeed, the formation of nanotubes of WS_2 was previously reported with the presence of H_2 in the reaction gas [6, 199, 200]. The XRD profile appeared identical to those without H_2. Overall, the results show a positive effect when H_2 were added to the reaction gas.

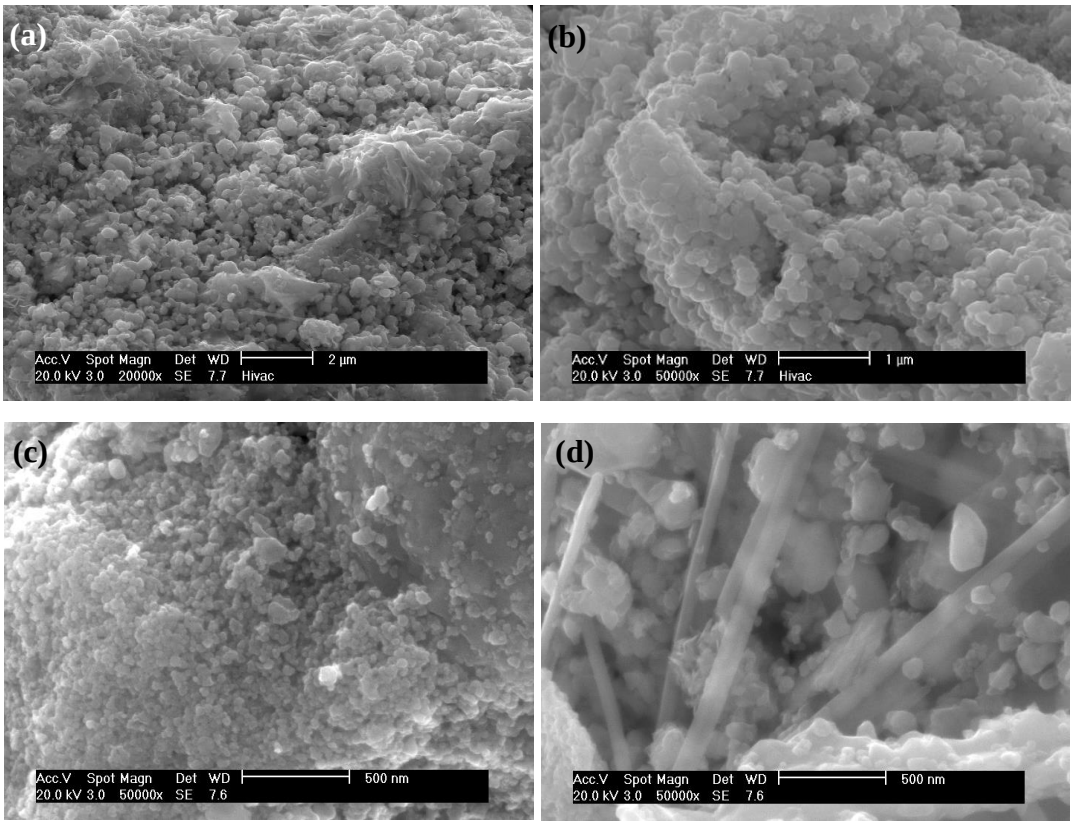

Figure 6-21 SEM images of samples involving H_2 in reaction

Many previous studies had indicated that, during the conversion from WO_3 to WS_2, the WO_3 was first reduced to tungsten suboxide such as $W_{20}O_{58,}$ $W_{18}O_{49}$ etc. gradually, then S started to replace the O in the reduced tungsten suboxide [18, 53, 89, 90]. Thus, the addition of H_2 into the reaction gases would accelerate the reduction of tungsten oxide, speeding up the process of subsequent sulphidisation, which led to the formation of WS_2 layers on the oxide surface. Since the early formation of an inert WS_2 layer would prohibit the diffusion and agglomeration of neighbouring nanoparticles, therefore H_2 helped prevent particles from agglomeration hence reduced the chance for the formation of 2H-WS_2.

6.3.4 Further refinement and modification

6.3.4.1 IF-WS_2 synthesis using a new baffled quartz tube

As initially demonstrated in Chapter **4**, the new baffled quartz tube could improve the batch yield from 5 to 15 g. We here continue to optimize the process parameters. Based on previous optimal parameters, changes were made to reflect the significant increase of

the amount of precursor from 6 to 18 g. For example, the gas rate of H_2 and H_2S, the reaction time and inclination angle etc. were finely adjusted.

Table 6-2 Experiments parameters for the IF-WS_2 synthesis using the new tube with baffles

	Powder put in (g)	Gas feed Rate (H_2: H_2S: Ar)	Reaction time (min)	Reaction temperature (°C)
B1	18	10:30:160	120	800
B2	18	20:30:100	120	800
B3	18	20:30:100 10:30:100	120	800

For the new baffled tube, it was found that a bigger inclination angle is required at the beginning of the experiment in order to move the particles towards the hot zone, otherwise they would only move around the cross sections perpendicular to the quartz tube axis. As soon as all the particles marching into the hot zone, the angle could be decreased to zero for better reaction.

In a typical experiment, B1, 18 g WO_3 nanoparticles were used with an initial inclination angle of 5 degree and H_2: H_2S: Ar ratio of 10:30:160 for the whole process. After the experiment, 15 g out of 18 g were collected from the hot zone, subject to characterisation.

The XRD patterns of products from three different areas (inlet, hot zone and outlet) are shown in Figure 6-22. For samples collected from the low temperature inlet area, the low WS_2 peaks and dominant WO_3 peaks detected suggest that there were very few WS_2 layers formed. Particles from the hot zone are dominated with WS_2 peaks, accompanied with minor oxide peaks at around 23-25 degree. For particles travelled to outlet before the end of experiment, which were difficult to move back into the hot zone, their XRD pattern shows quite high intensities for WS_2 peaks, although lower than those from the hot zone, whilst the oxide peaks are stronger. It is believed that these particles have stayed in hot zone for a considerably long time before reaching the other end, therefore many WS_2 layers must have already formed, and left behind a small portion of tungsten oxide core.

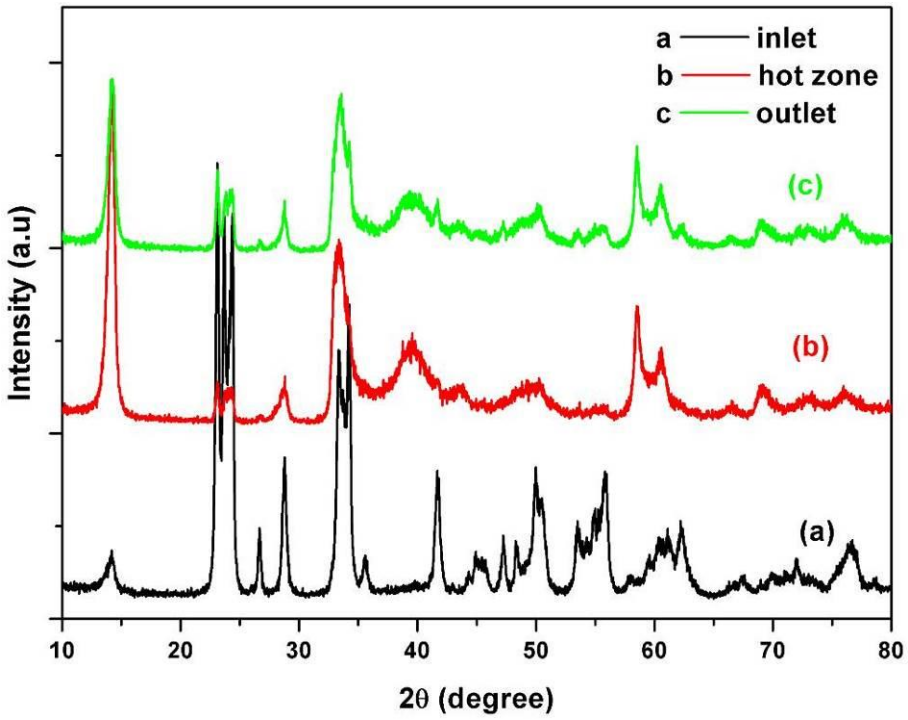

Figure 6-22 XRD patterns for particles from experiment B1

SEM images for particles collected from hot zone of B1 are shown in Figure 6-23. Many 2H-WS_2 nanoflakes are observed and many IF-WS_2 particles exhibit diameters around 200 nm. This should be resulted from the tripled amount of particles. As discussed in Chapter **4**, the transverse motion of particles varies with the filling degree of the working tube, and 3 times more of the filling degree would cause more serious agglomeration.

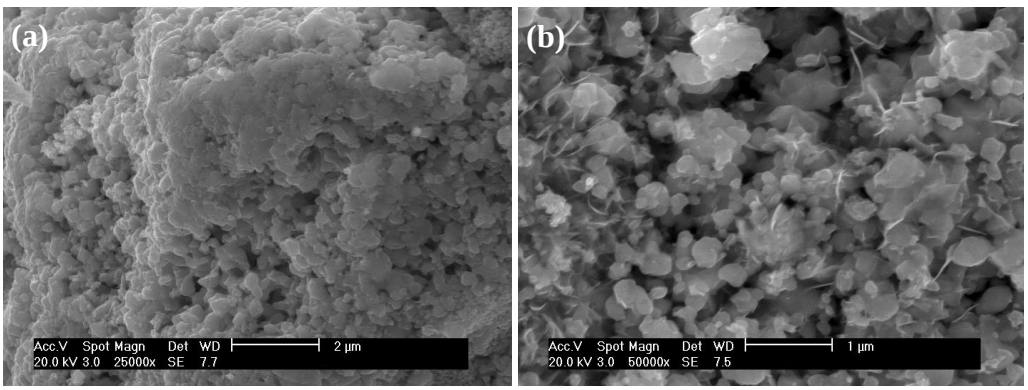

Figure 6-23 SEM pictures for particles from hot zone of experiment B1

Based on the previous experiments, more H_2 and H_2S were added to the reaction gas during B2, and the ratio of H_2:H_2S:Ar was adjusted to 20:30:100 ml/min, aiming to minimise the formation of 2H-WS_2 nanoflakes and achieve more complete sulphidisation. Figure 6-24 shows the XRD patterns of samples collected from the

central hot zone, and the strong WS_2 peaks accompanied by hardly visible tungsten oxide peaks indicated a thorough conversion from oxide to sulphide.

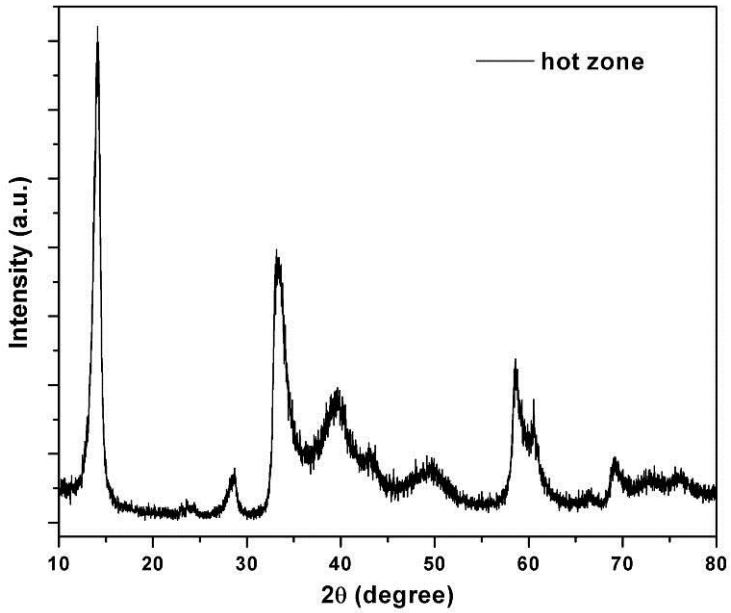

Figure 6-24 XRD pattern for sample collected from the hot zone from experiment B2

Corresponding SEM characterisation results of the hot zone sample are shown in Figure 6-25. The IF-WS_2 nanoparicles which dominate the products exhibited uniform and small diameters (Figure 6-25a), with a considerably big proportion of WS_2 INTs. The presence of the abundant INTs attributed to the addition of H_2 of 20 ml/min throughout the whole process. Accordingly, fewer INTs would form if less H_2 was involved. This is verified by experiment B3, with H_2 flow rate adjusted during the reaction, as detailed in Table 6-2. A 20 ml/min H_2 was introduced for the first 1 h, and then reduced to 10 ml/min for the second 1 h reaction to finish the process.

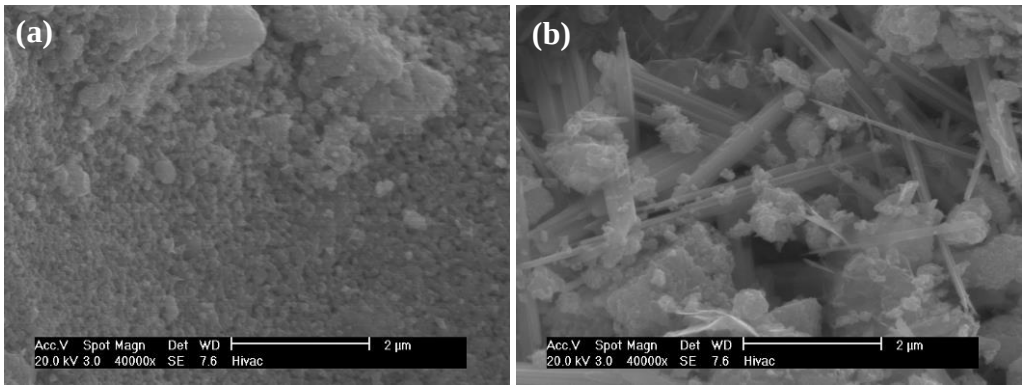

Figure 6-25 SEM pictures for particles collected from hot zone of experiment B2

Particles collected from different areas have been analysed for XRD and SEM, and the results for samples from the hot zone are shown in Figure 6-26 and Figure 6-27. The XRD pattern is very similar to B2, with remarkable WS_2 peaks and very tiny WO_x signal, which is again indicative of a complete sulphidisation. It is also shown from SEM images in Figure 6-27 that the amount of WS_2 INTs have been dramatically decreased, and they are much shorter, compared to those from B2. The dominant IF-WS_2 nanoparticles appear to be uniform, fine and spherical, with diameters < 100 nm (Figure 6-27b).

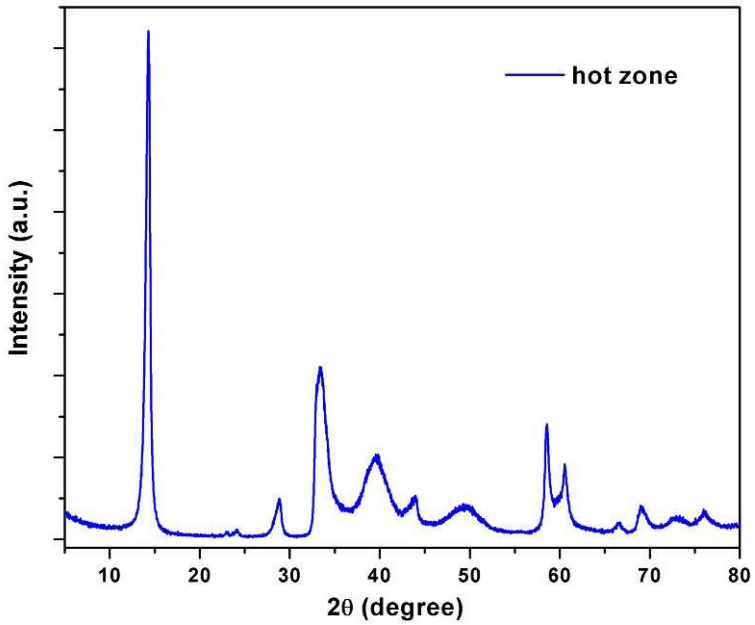

Figure 6-26 XRD pattern of samples collected from the hot zone of experiment B3

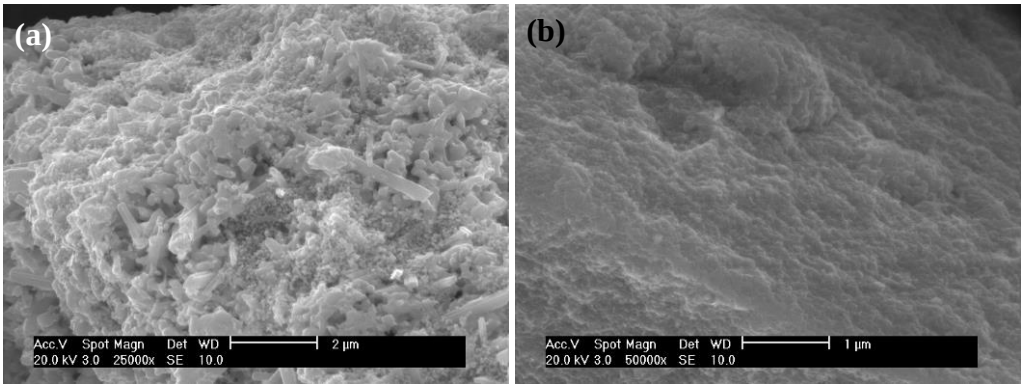

Figure 6-27 SEM images for samples collected from the hot zone of experiment B3, revealing the existence of a small amount of INTs and the fine and uniform feature of the IF-WS_2.

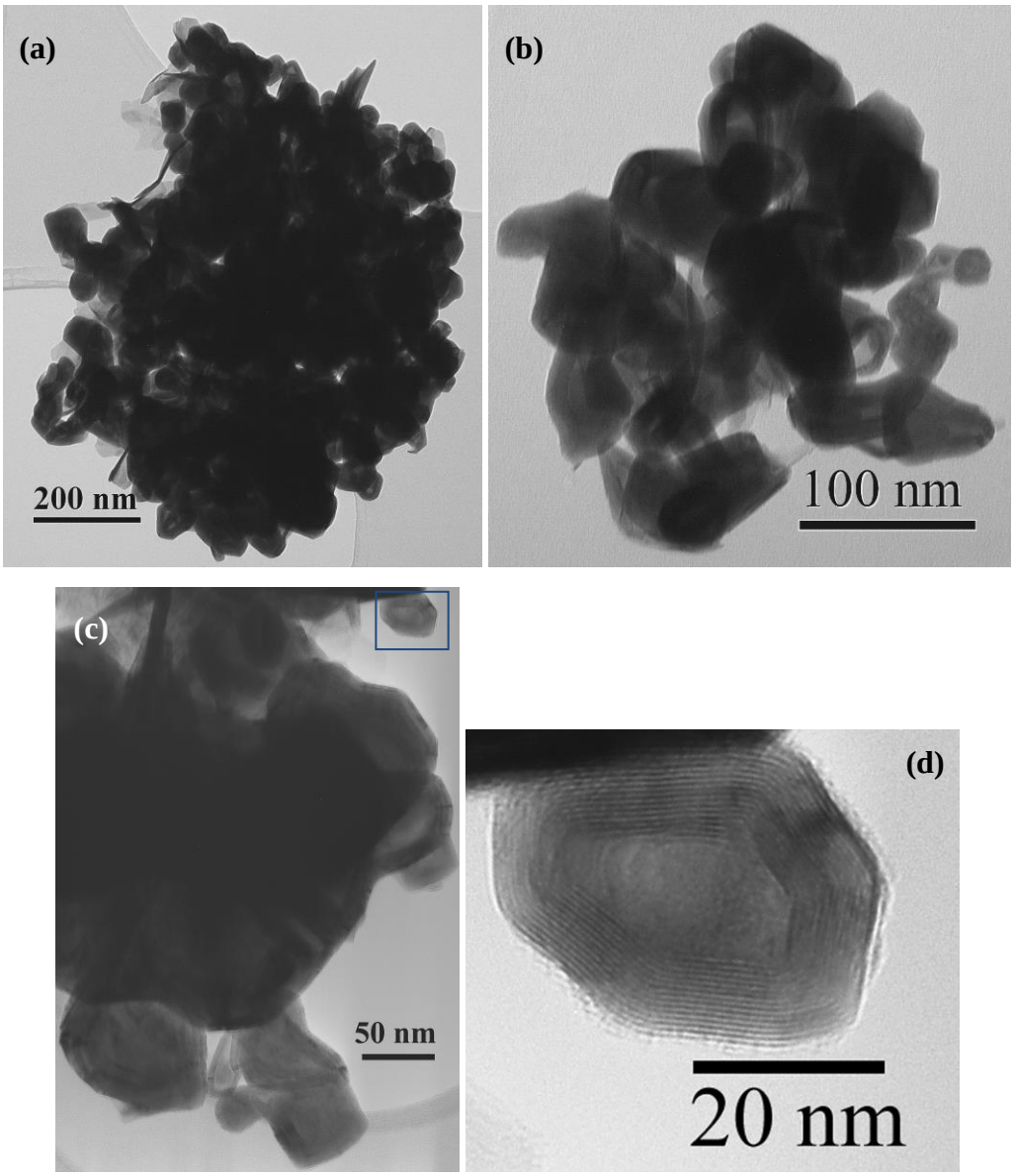

Figure 6-28 TEM images for samples collected from the hot zone of experiment B3

TEM characterisation was also carried out for samples collected from B3, and the results are shown in Figure 6-28, which further confirmed the dominant nature of the IF-WS_2, with sizes ranging from below 50 nm up to over 100 nm. Both Figure 6-28a and b also demonstrate that some particles coalesced by 2 or 3 nanoparticles, exhibiting a peanut shape or a curving channel shape. Those single particles are always < 50 nm. Figure 6-28c shows a higher resolution image of several well-crystallised particles, and further zoom in the top right corner of Figure 6-28c (framed area), as shown in Figure 6-28d, has revealed a typical IF-WS_2 particle with a hollow core and around 15 seamless layers.

In summary, the parameters for the production of IF-WS_2 using the new baffled quartz tube have been optimised. The XRD, SEM and TEM characterisations have confirmed the high quality of resulting nanoparticles. The applied baffles within the quartz reaction tube have enabled the yield improvement from 5 g to 15 g per batch, while successfully maintained the products quality.

6.3.4.2 IF-WS_2 synthesis using a continuous feeding system

Further investigation have been focused on the realisation of the rotary production of IF-WS_2 nanoparticles as a continuous process. Experiments have been carried out to explore the optimal parameters for the continuous rotary process, by applying a new gas blow-piston feeder system, as shown in Figure 4-38.

As the experiments take place based on both new Feeding system and Baffled tube, they are then named FBN, starting from FB1, till FB3.

First trial with gas blow-piston feeder

The feeder made of a 20 ml syringe containing around 50 g WO_3 particles to be introduced into the furnace by blowing of Ar. As usual, after the Ar purge and H_2 of 50 ml/min was first introduced at 550°C, WO_3 feeding and H_2S gas of 50 ml/min were started at 650°C. The temperature reached 800°C after around 30 min, and all particles in the syringe were used after another 30 min (i.e. 1 h after the initial feeding). The H_2:H_2S:Ar at a ratio of 50:50:100 was continued until H_2 being switched off after 1 h, and H_2S:Ar ration changed to 25:100 for another 1 h then only Ar being remained for cooling.

The samples collected from different areas were analysed with SEM and XRD, and the SEM images of the hot zone sample are shown in Figure 6-29. In the image, very uniform nanoparticles are seen, with few aggregates. Overall, a very promising size distribution has been achieved.

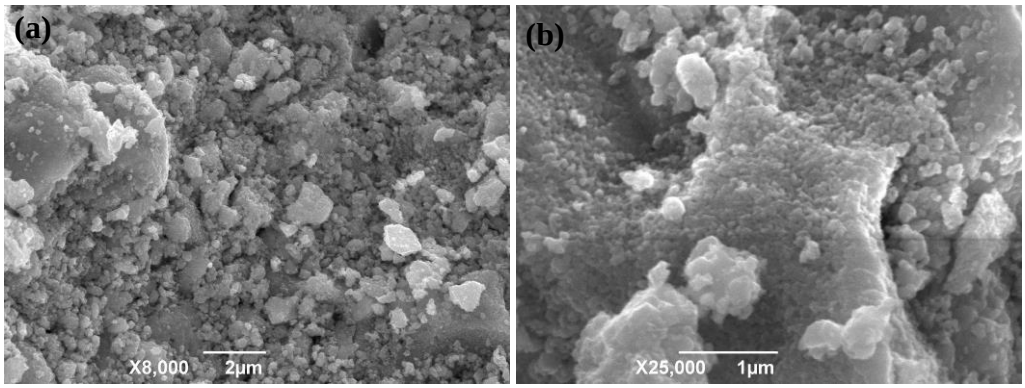

Figure 6-29 SEM images for samples collected from the hot zone from experiment FB1

The XRD pattern in Figure 6-30 shows a very different trend from all others results obtained in previous experiments, and the sample collected form the hot zone exhibited less intense peaks for the IF-WS_2 than those collected from the outlet zone, although much stronger than those from the inlet zone.

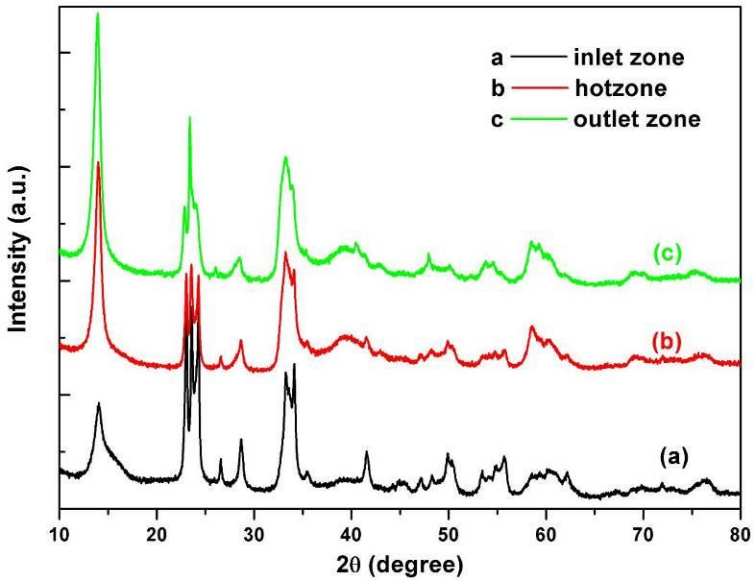

Figure 6-30 XRD profiles of samples collected from different areas from experiment FB1

We believe that the above problem lies in the v shape quartz connector which was designed to extend the outlet end of the shaft and to act as a pathway for both the precursor and gases. It is supposed to help both the precursor and gas to start mixing in this leading tube, however after the WO_3 feeding was stopped, H_2S and Ar were continued, through the same pathway, to ensure a complete sulphidisation. Thus, WO_3 left inside this long quartz connector would be brought into the reaction area, mixing with the well-converted IF-WS_2 which normally stayed in the hot zone, hence leading to the abnormal signals.

Separated gas and precursor feeding

In order to avoid the above technical issue, i.e. the excessive introduction of WO_3, the original v-shaped connector was replaced by a single long leading tube without the v nozzle, to act as the extend pathway for WO_x particles (as shown in Figure 4-41b), thus the path for WO_x and reaction gases was separated. The new design was tested in experiment FB2. During the test, the feeder was stopped after 1 h when the 20 ml syringe was empty; while the H_2S, H_2 and Ar gas mixture was kept for another 2 h, with the inclination angle being adjusted several times to allow for the most uniform reaction in the hot zone. At the end of the experiment, around 40 g WS_2 were collected, about 25 g from the hot zone and 15 g from the inlet and outlet zones. It is proved that the separation of gases path from precursor feeding channel, and the inclination angle adjustment, led to successful experiments. The XRD patterns of samples collected from experiment FB2 (Figure 6-31) demonstrate that a completely conversion of WO_x into WS_2 had taken place with no WO_x peaks for particles from the hot zone and extremely minor peaks of WO_x for samples the outlet zone.

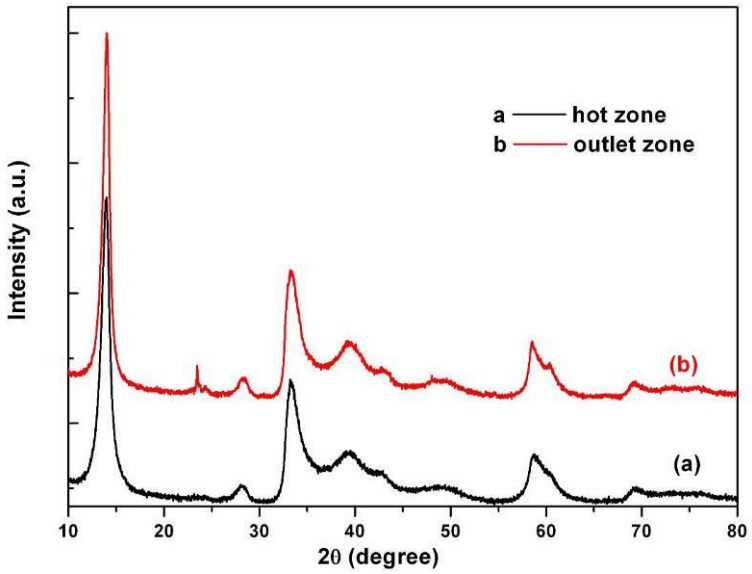

Figure 6-31 XRD profiles of samples collected from different reaction zones in experiment FB2

The SEM images in Figure 6-32 have revealed the morphology of particles collected from the hot zone in FB2, and they are quite uniform with sizes no more than 100 nm. The very bright pieces at the right bottom corner of Figure 6-32b could be residue S, owing to the excessive amount of H_2S gas used.

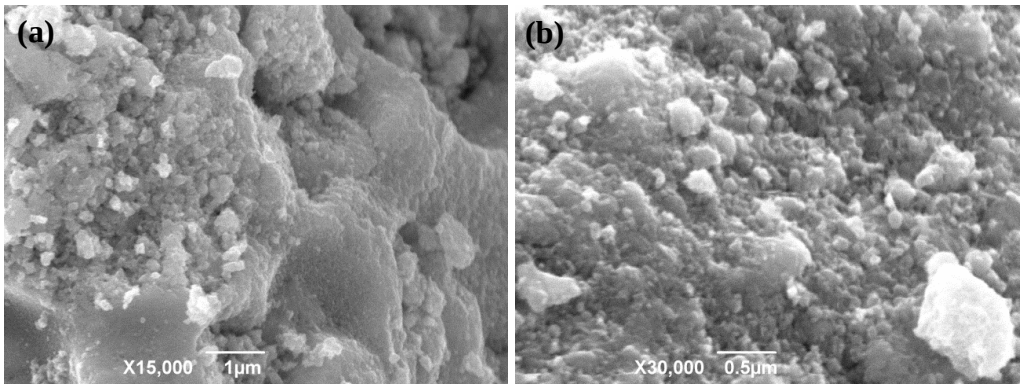

Figure 6-32 SEM images for particles collected from hot zone of experiment FB2

Double syringe feeding

The process has been further modified to simulate a real continuous one, by replacing of the empty syringe with a full one immediately, which was realised through the addition of a valve between the feeder and leading plastic tube to shaft, as shown in Figure 4-41a. The valve would be switched off to isolate the feeding system with the reaction working tube, while the empty syringe could be replaced safely.

All other experiment parameters remained no alternation to FB2, except for the longer feeding time. The time for the gas supply was doubled, i.e. being kept for another 4 h after precursor feeding stopped.

After experiment, with around 50 g samples was collected from the hot zone, 25 g from the inlet and outlet zone, and around 15 g remained in the thin leading tube. The XRD patterns are shown in Figure 6-33 and SEM images are shown in Figure 6-34 for samples from different zones.

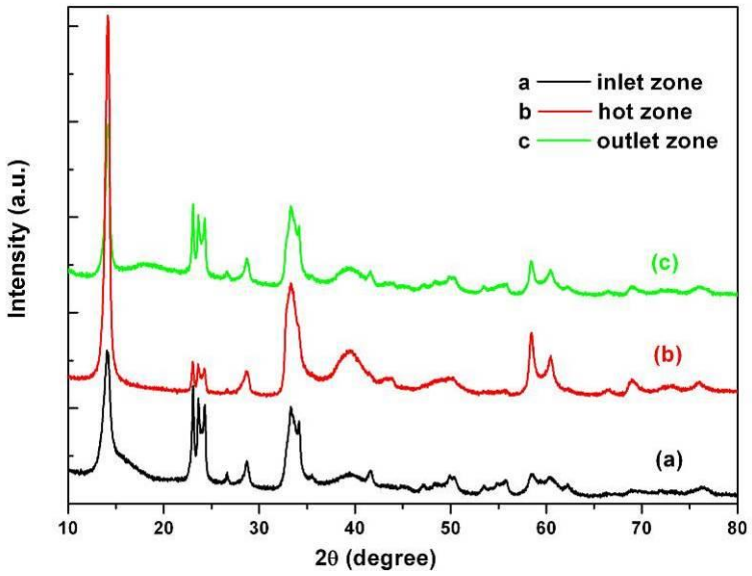

Figure 6-33 XRD profiles of samples collected from different areas of experiment FB3

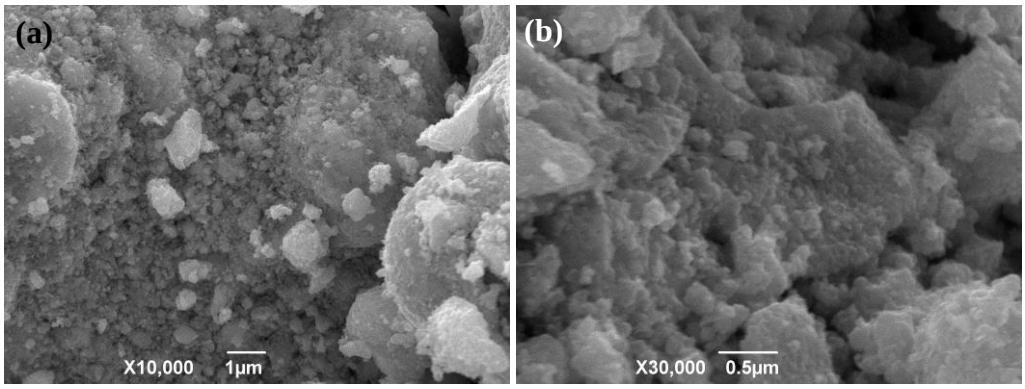

Figure 6-34 SEM images for particles collected from the hot zone from experiment FB3

The XRD patterns of particles from the hot zone area exhibit very strong WS_2 peaks, with (002) peak being much higher than other peaks, and minor WO_x peaks remaining. For particles collected from the inlet and outlet zone, the patterns revealed that they were mostly partially converted, forming a WS_2 shell and oxide core structure. Nanoparticles dominate the samples, as shown in the SEM images in Figure 6-34, although aggregates are observed, with very few nanoflakes. TEM images of nanoparticles collected from hot zone of FB3 were shown in Figure 6-35. Nanoparticles with size uniformly distributed around 50 nm were displayed in Figure 6-35a and c, though some nanoparticles appear in Figure 6-35b, exhibiting size from 20 nm to almost 100 nm, accompanied by some nano-sheets in the upper part of Figure 6-35b.

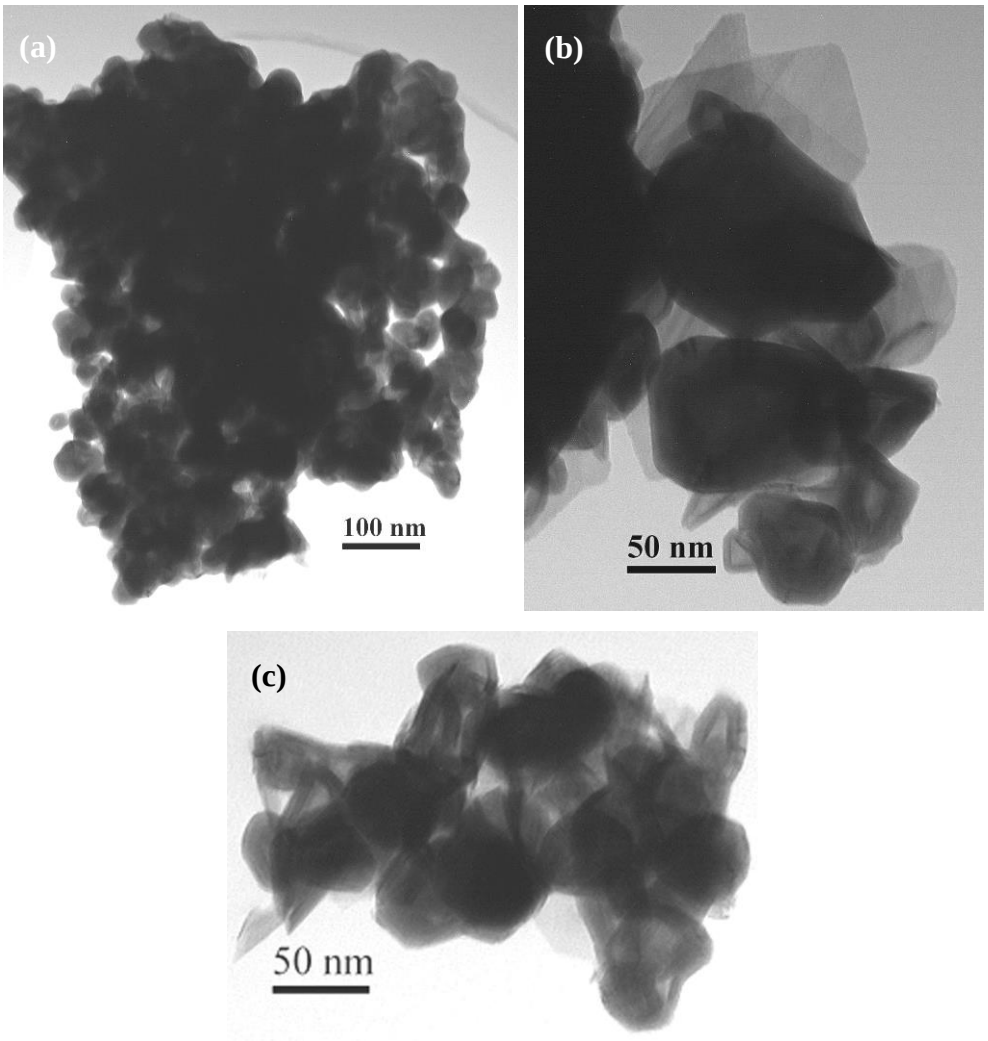

Figure 6-35 TEM images for particles collected from the hot zone from experiment FB3

To summarise, the continuous feeding system has been proved a success and has improved the yield of IF-WS_2 to several tens of grams per batch (depends on the number of loaded syringe container), without obvious compromising in quality.

Technically, the feeding of precursor could be continued by simply loading more syringe container, however longer reaction time would be required. In an industry environment, where a proper sample collection system is easily available and automated reaction would not be a limitation, this reactor is easily adaptable as a whole continuous rotary process for the scaling up production of IF-WS_2 nanoparticles.

6.4 Carbon coated IF-WS_2 composite nanoparticles

6.4.1 Introduction

In Chapter **2**, it has been discussed that IF-MS_2 nanoparticles (M=W, Mo) are thermally less stable than bulk 2H-MS_2 particles [7, 72], though possess various excellent properties [12, 15, 46, 54, 201]. Numerous research interests have been focused on exploring the new potential applications for IF-MS_2 nanomaterials according to these outstanding performances [16, 45, 65, 66, 75, 202]. To further explore their properties, the improvement of thermal stability for such IF-MS_2 becomes an interesting and significant challenge.

As a significant feature for nanoscience, the fabrication of heteronanostructures has always been an interesting subject, seeking for better performance over single phased nanomaterials. So far, a number of intriguing MS_2/C nanocomposites has been produced, including WS_2 coated single-walled and multi-walled CNTs [73, 203, 204], mixed phase $W_xM_yC_zS_2$ nanotubes [205], as well as IF-MoS_2 embedded CNTs, IF-WS_2 embedded CNTs and MoS_2 coated carbon particles [206] and MoS_2 coated CNTs [207].

The thermal stability has been studied for the WS_2-coated CNTs produced by Raymond and co-workers [73], and their results revealed that, compared to pure INTs, the WS_2-coated CNT exhibited better oxidation resistant in air, owing to the WS_2 coating, although the onset oxidation temperatures of both are still lower than pure WS_2 INT. Nevertheless, it confirms that WS_2 coating had played a role as an antioxidant for CNT, as the oxidation of WS_2 layers had delayed the oxidation of CNTs. Dielectric properties of these WS_2-coated CNT had also been studied [208], by means of energy-loss spectroscopic profiling. It was found that aiming for a change in its dielectric properties, that is, to have defined dielectric internal and external interfaces, a minimum width of WS_2 coating needs to be 5 monolayer.

These achievements have inspired us that what properties would be achieved if IF-WS_2 were coated with C? In this context, for curiosity, a binary phase of layered nanostructure, i.e. C-coated WS_2 will be studied using a CVD method, during our rotary process.

6.4.2 Experimental

Following previous IF-WS_2 production as described in Section **6.3** and Chapter **3**, I switched the H_2S gas to the supply of carbon source via the injection of 20 vol% styrene and 80 vol% acetone mixed solution at a rate of 1.2-2.4 ml/h for 10-40 min, via 100 ml/min Ar carrier gas.

Several experiments were carried out using different parameters, as summarised in Table 6-3. The resulting particles were then examined by TGA-DSC, Raman and TEM.

Table 6-3 Summarised parameters for carbon coating experiments

	Temperature (°C)	Injection rate (ml/h)	Reaction time (min)
CWS1	700	1.2	10
CWS2	800	1.2	20
CWS3	775	2.4	20
CWS4	775	2.4	40

6.4.3 Results and discussion

6.4.3.1 TEM characterisation

All the samples were examined by TEM. Products from CWS1 are shown in Figure 6-36. Hollow IF-WS_2 particles with size dominated around 50 nm are presented, with no C coating. However in Figure 6-36a, there is a layer of nanosheet on the right part of image (as in the framed area) surrounding the particles, possibly WS_2 or C sheet, as both possess similar morphologies at this magnification. In the left part of Figure 6-36c, there might be C connecting the two IF-WS_2 particles, as pointed by the arrow.

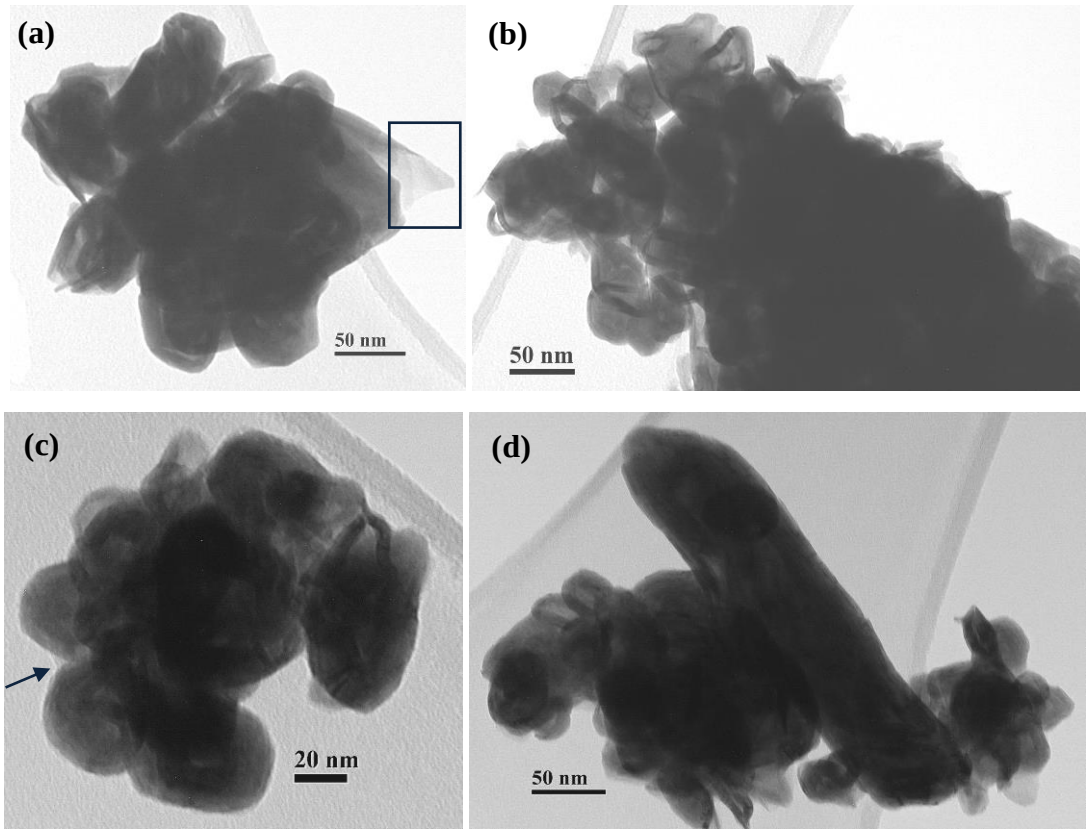

Figure 6-36 TEM images for products of CWS1 (at a 1.2 ml/h injection rate for 10 min at 700°C)

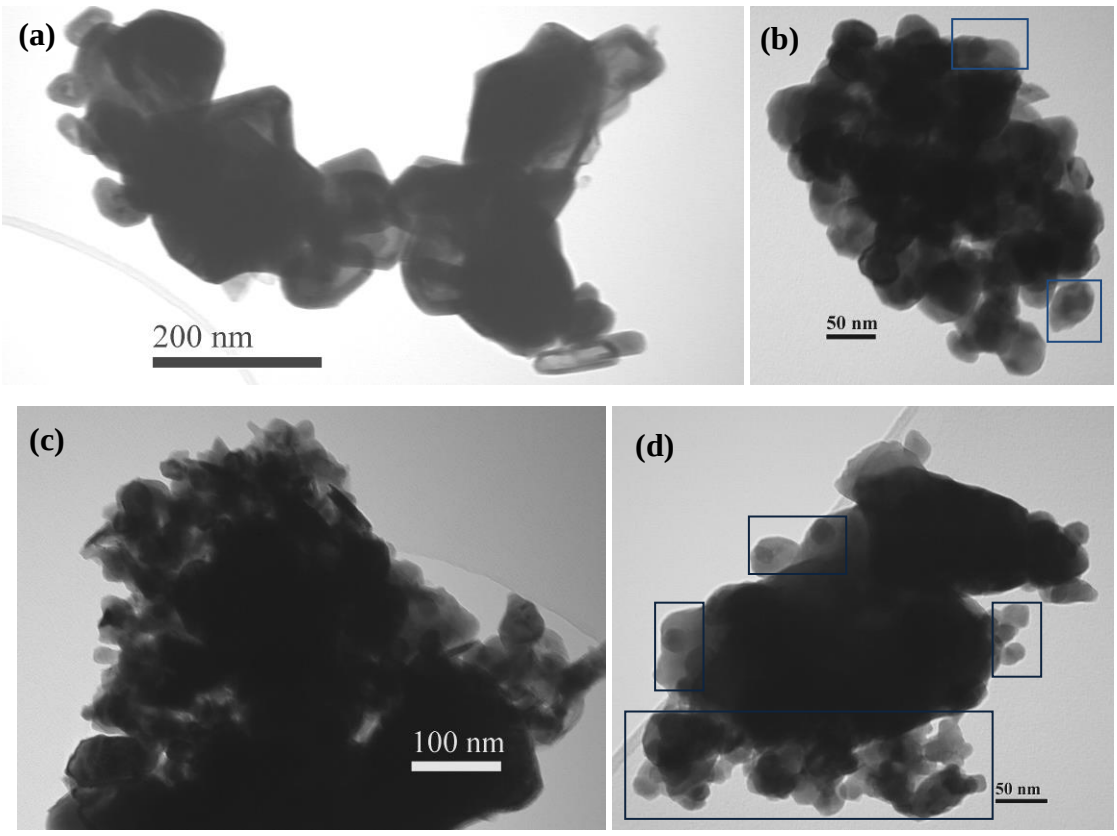

Figure 6-37 TEM images from CWS2 (at a 1.2 ml/h injection rate for 20 min at 800°C)

Figure 6-37 shows the TEM images of samples from experiment CWS2, which took place at 800°C. Figure 6-37a shows IF-WS_2 nanoparticles with a clear surface, but Figure 6-37b-d show an agglomeration containing both IF-WS_2 and C spheres. Even at this low magnification, it could still be deduced that the particles surrounding the outer edge of these agglomerates are C, rather than IF-WS_2. Especially in Figure 6-37b and d, the particles with 20-40 nm in diameter, with non-polygonal irregular shapes and non-uniform contrasts, are not IF-WS_2, should be C (as framed in Figure 6-37b and d).

The present of C particles from pyrolysis of hydrocarbon, mixture of styrene and acetone, at high temperature is not surprising. However, the critical temperature varies with different circumstances. In Jin's work [209], the pyrolysis of styrene led to very big C spheres from 900°C, no carbon spheres were resulted at temperature up to 800°C.

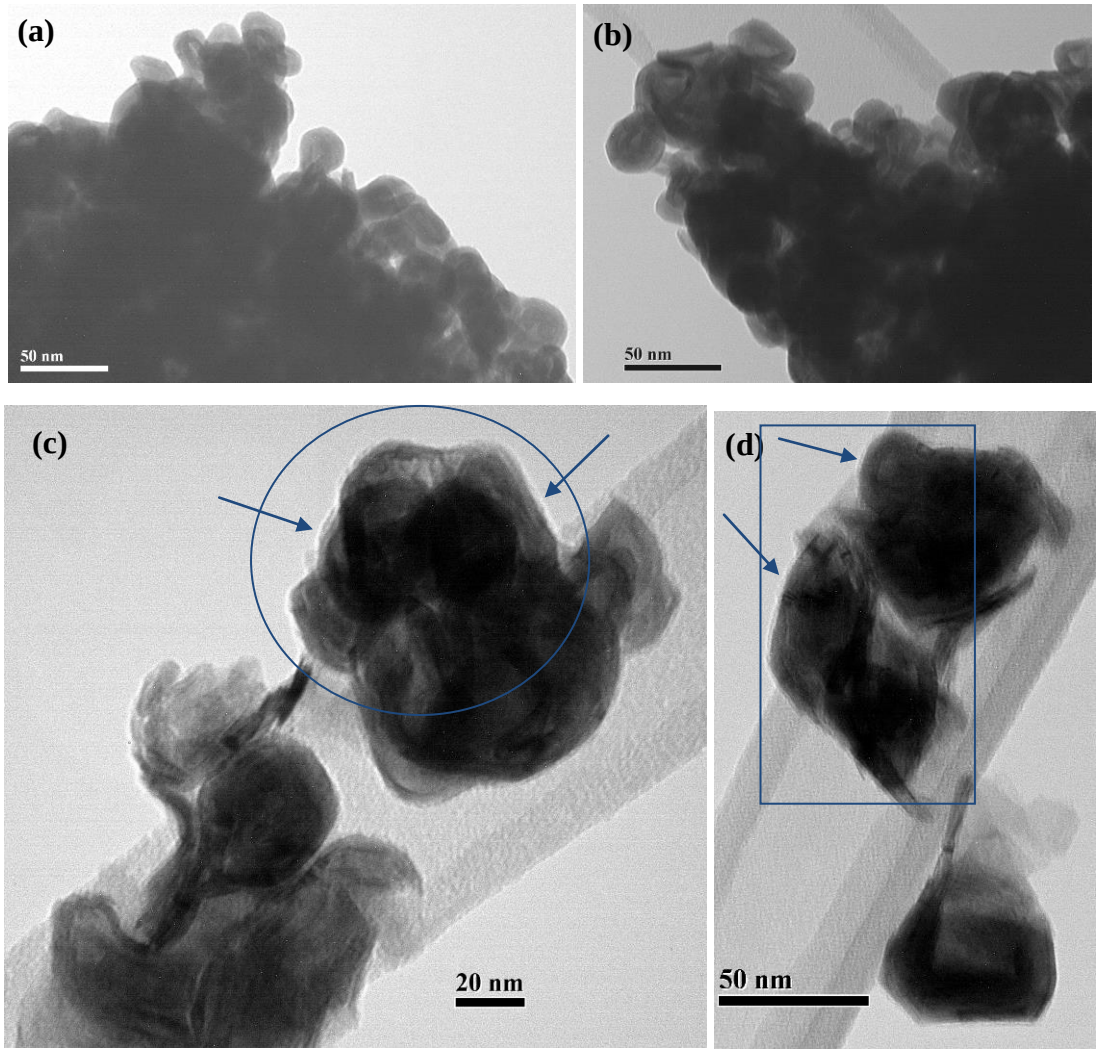

Figure 6-38 TEM images from CWS3 (2.4 ml/h injection rate for 20 min at 775°C)

Thus, the CVD temperature has been decreased for further experiments, to avoid the formation of C spheres. More experiments have been carried out at 775°C, with an injection rate doubled from 1.2 ml/h to 2.4 ml/h. The first experiment was lasted for 20 min, and the TEM results are shown in Figure 6-38. It is found that high quality IF-WS_2 were produced, Figure 6-38a and b, with no obvious layers on top of the surface. However in Figure 6-38c and d, a very thin layer was observed on the top of IF-WS_2, labelled in the frame. The layers are particularly bright, arrowed.

To get a thicker layer of coating on top of the IF-WS_2, the CVD reaction time was lengthened to 40 min, and the TEM results are shown in Figure 6-39. A layer was clearly shown coating the IF-WS_2 particles. The framed area in Figure 6-39a is zoomed in and further displayed in Figure 6-39b, which confirms that the thickness of the coating is about 3 nm, uniformly covering these IF-WS_2 nanoparticles.

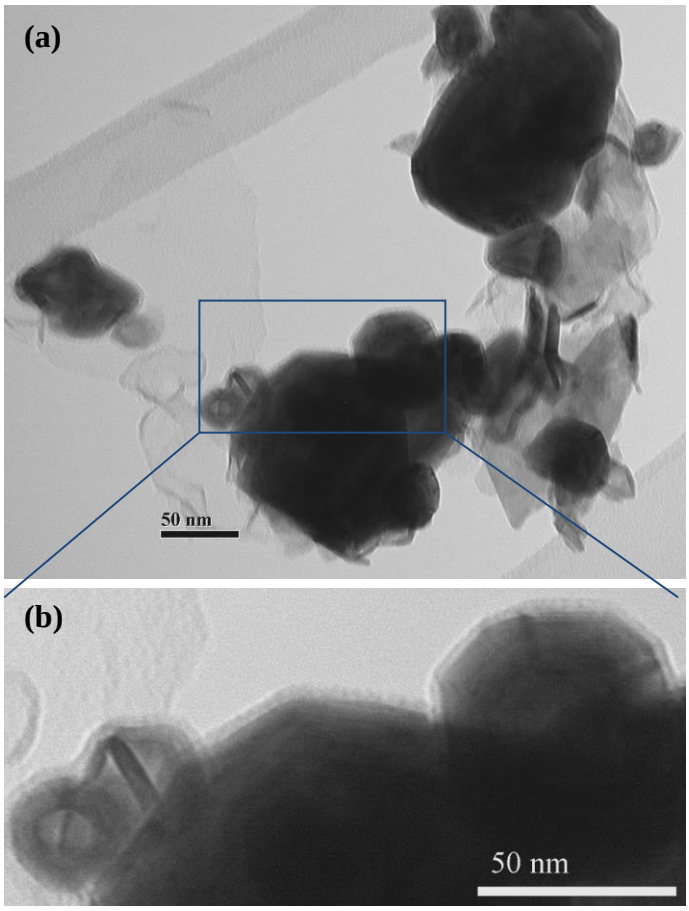

Figure 6-39 TEM images of C coated IF-WS_2 from experiment CWS4 (at a 2.4 ml/h injection rate for 40 min at 775°C)

HRTEM was used to further study the structural feature of the C coating, and the results are shown in Figure 6-40. The images demonstrate well-crystallined IF-WS_2 of 15

layers were coated by a fairly concentric C shell of 2-3 nm in thickness (Figure 6-40a-d), and the layers are separated by ca. 0.33-0.36 nm, which is very close to that of graphite. Occasionally the C shell was over 5 nm thick, as shown in Figure 6-40(d), which must have stayed in the hot zone for a longer time. The HRTEM has also confirmed the uniform C coating on the IF-WS_2, although sometimes several IF-WS_2 particles are enveloped within the same shell (Figure 6-40a and d). Unlike the two separated particles covered together by carbon coated as shown in the frame area of Figure 6-40a, some particles became aggregates after being coated separately (Figure 6-40b, as indicated by visible carbon coating around the particles in the arrow pointed areas.

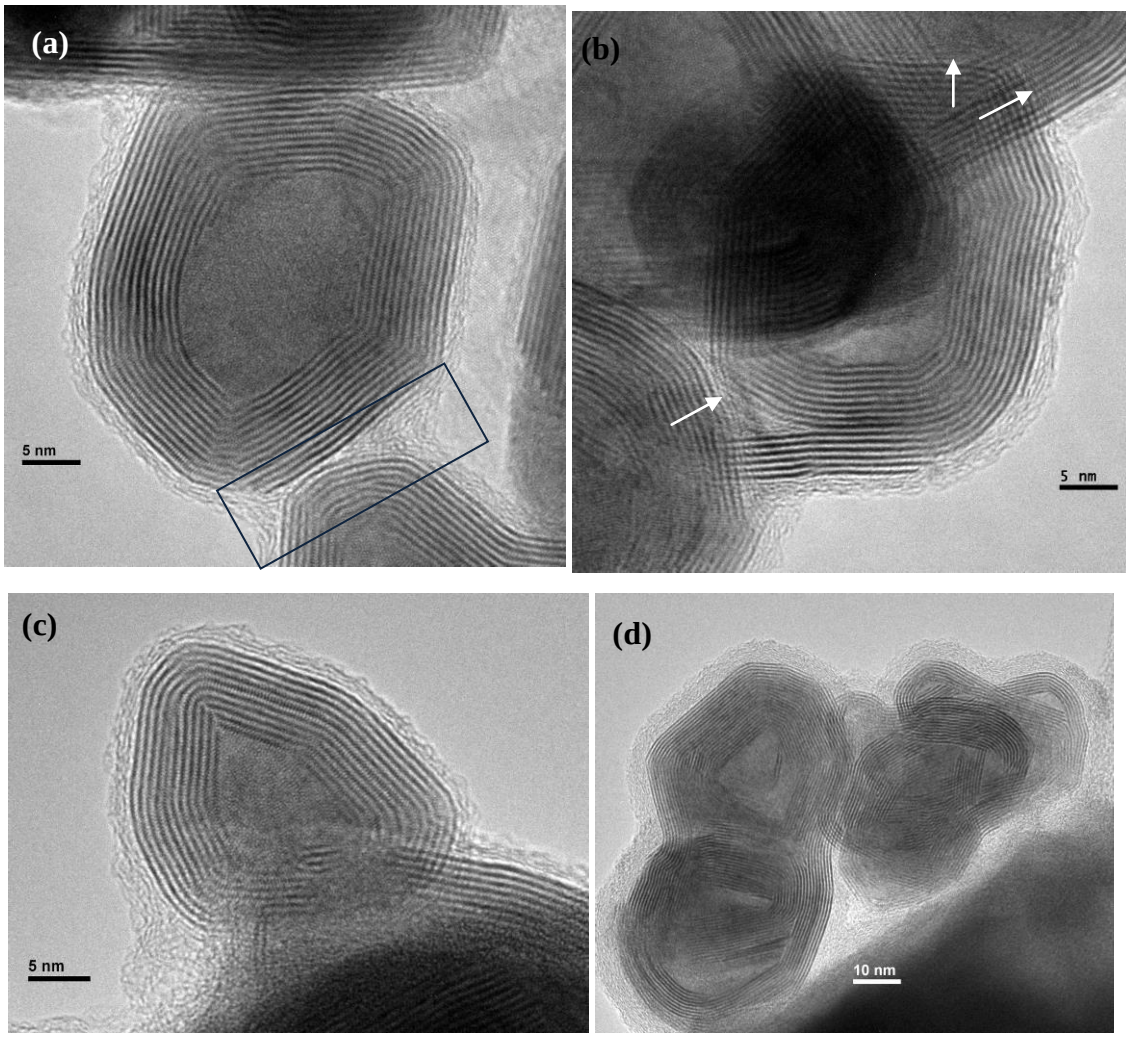

Figure 6-40 HRTEM for carbon coated IF-WS_2 particles (experiment CWS4)

In comparison with experiment CWS3, only the injection time has been changed for CWS4, and a much thicker and uniform C layer has formed. This result shows that the

thickness of the C shell could be tailored accordingly, by simply varying the injection time or/and injection rates.

6.4.3.2 Thermal stability

To examine thermal properties of carbon coated particles, TGA-DSC analysis was applied in air for both pristine IF-WS_2 and C-coated WS_2 from each experiment, respectively. Figure 6-41 presents TGA-DSC curves of the pristine IF-WS_2, and the weight loss begins at 350°C, also accompanied by an onset of the exothermal peak which peaked at 436°C. This weight loss was attributed to the oxidation of IF-WS_2 to WO_3, almost no further weight loss is observed after 550°C. The total weight loss in the whole process is around 6.3%. The precise weight left after oxidation of IF-WS_2 is 93.68%, this is in very good agreement with the theoretical value 93.55%, i.e. the weight percentage of WO_3 compared to the same mole amount of WS_2 (calculated by (184+16×3)/(184+32×2)=232/248=93.55%).

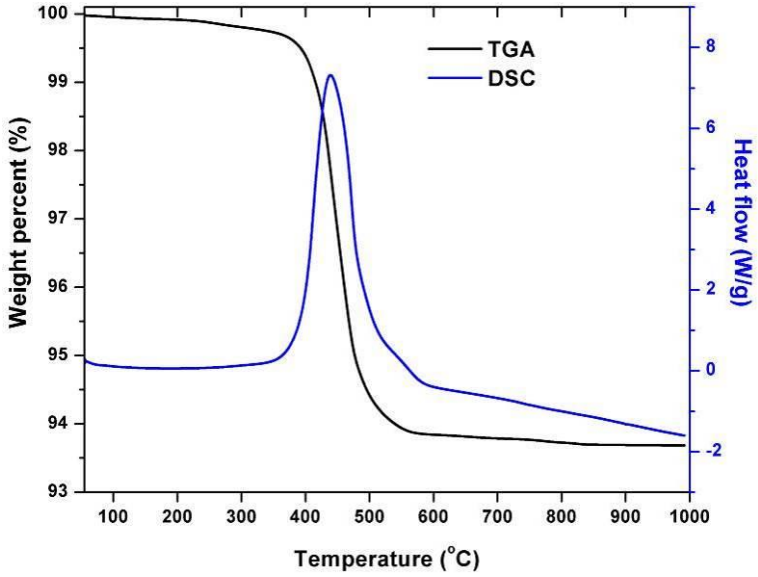

Figure 6-41 TGA-DSC curves for pristine WS_2

TGA and DSC curves from experiment CWS1 and CWS2 are presented in Figure 6-42 and Figure 6-43, respectively. For experiment CWS1 (700°C 10 min), although no obvious C layer could be observed under TEM, the TGA-DSC curves shows different signals from the pristine IF-WS_2. Besides the main weight loss starting at 350°C, there is a tiny weight decrease at around 220°C, which corresponds to a tiny peak at 229°C in the DSC curve. This peak should be resulted from the residue S, as the auto ignition temperature of which is around 232°C. Different from the previous weight loss slope, it

changes at around 460°C, associated with a shoulder in the DSC curve which begins at around 460°C after the exothermal peak for the oxidation of IF-WS_2 at around 436°C. This weight loss and exothermal peak shoulder are attributed to the oxidation of C.

Beside this tiny peak from S, the CWS2 sample also started the major weight loss at around 350°C, followed by a slope change at around 460°C, associated with the DSC curve exhibiting an exothermal peak at 437°C, accompanied by a shoulder from 460°C. Consistent with others, there was no further weight loss above 550°C.

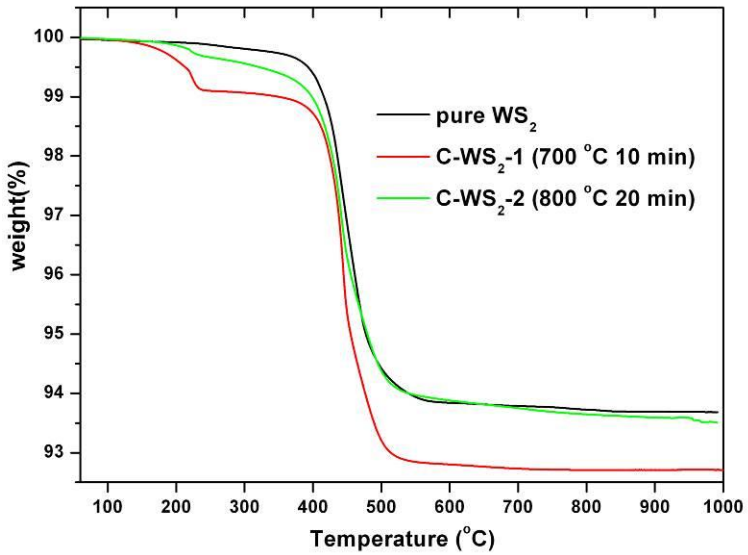

Figure 6-42 TGA profiles for pristine IF-WS_2, C-coated IF-WS_2 from CWS1 (C-WS_2 -1, at 700°C for 10 min) and CWS2 (C-WS_2 -2 at 800°C for 20 min)

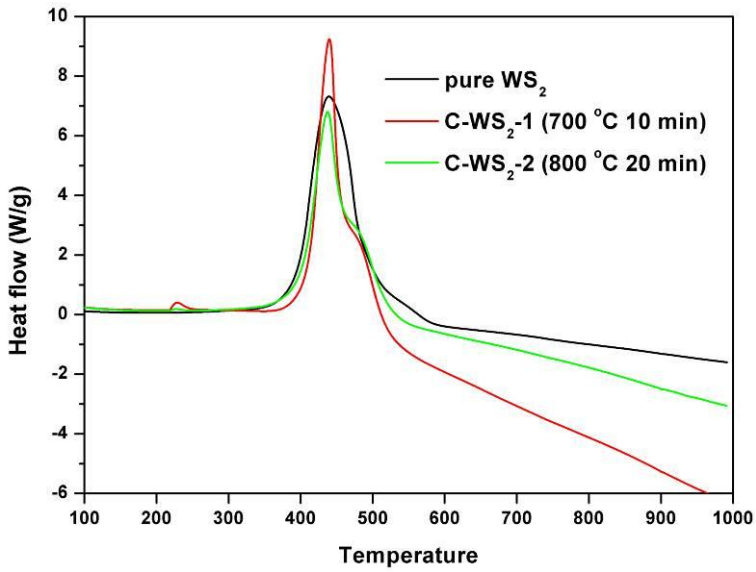

Figure 6-43 The DSC profiles for pristine IF-WS_2, C-coated IF-WS_2 from CWS1 (C-WS_2 -1, at 700°C for 10 min) and CWS2 (C-WS_2 -2 at 800°C for 20 min)

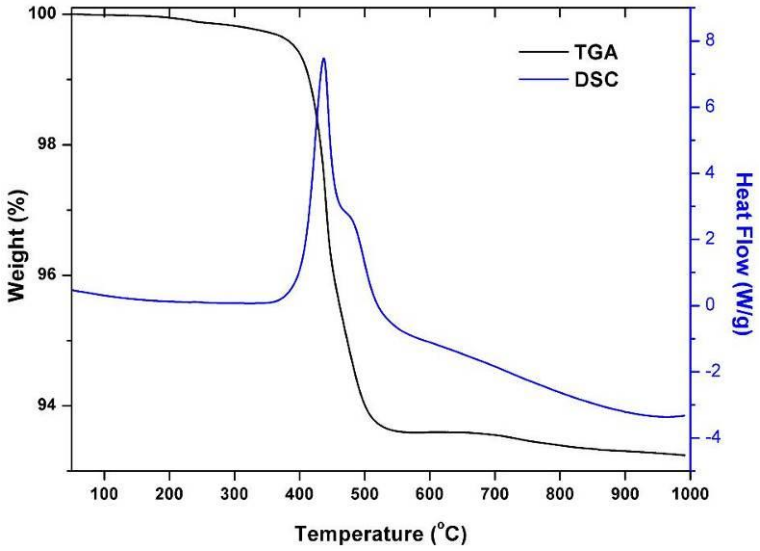

Figure 6-44 TGA-DSC of carbon coated WS_2 from CWS3

When the deposition temperature was decreased to 775°C, a longer time allows for S to escape, therefore no S signal was observed in the TGA-DSC curves for CWS3, as shown in Figure 6-44. Furthermore, the result from CWS3 is quite consistent with previous experiments, and the DSC shoulder at 464°C is very distinct. From TEM observation, it is found that some of the IF-WS_2 nanoparticles have been coated. Thus, it is inferred that this shoulder in the DSC curve is the onset of oxidation of C. The IF-WS_2 enveloped within the C start to be oxidised as soon as the C shell was gone. Thus, the oxidation of both leads to this peak appearing to be more apparent.

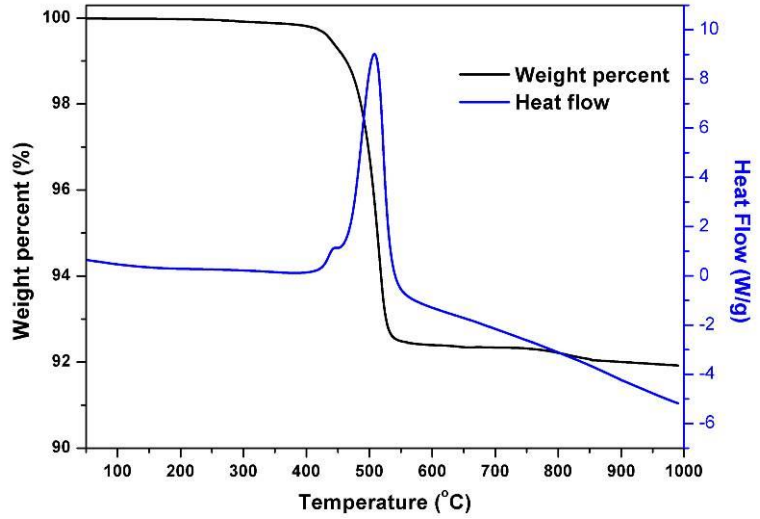

Figure 6-45 TGA-DSC curves for carbon coated IF-WS_2 (CWS4)

For IF-WS_2 coated well with C, experiment CWS4, the TGA- DSC curve is presented in Figure 6-45. The major exothermal peak appears at 507°C, with a very minor peak at 437°C. Correspondingly, the weight loss starts at around 350°C, and then a slope changes at around 460°C. The minor exothermal peak, i.e. the first weight loss, is due to the oxidation of occasionally not fully coated IF-WS_2, which is expected because of the long working tube.

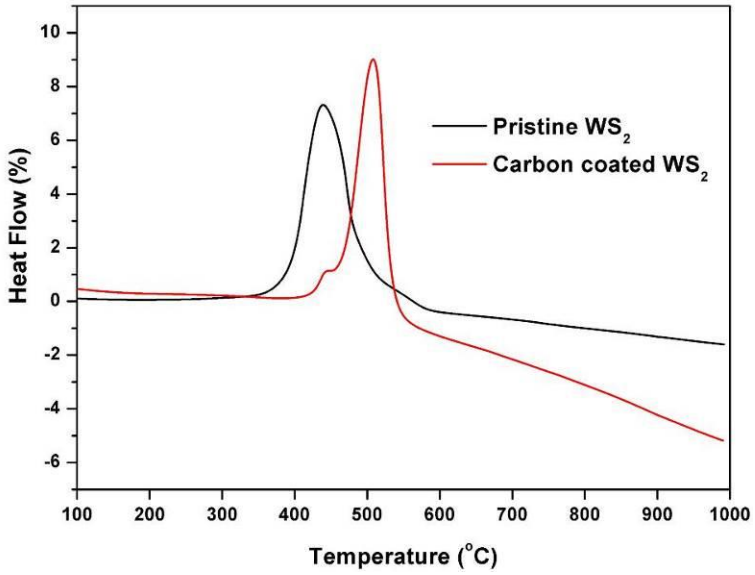

Figure 6-46 Comparison of DSC curves for pristine WS_2 and carbon coated WS_2 from CWS4

By comparing with the TGA-DSC behaviour of pristine IF-WS_2, the DSC of C-coated IF-WS_2 shows a right shift of major exothermal peak from 436°C to 507°C, by almost 70°C (Figure 6-46). The TGA results show that the C-coated IF-WS_2 has the same residue weight percentage than that of the pure IF-WS_2 at a temperature around 70°C higher (Figure 6-47). This oxidation temperature of C-coated IF-WS_2 nanoparticles has been improved by around 70°C.

This oxidation sequence could be explained as follows. When heated in air, the few not fully coated IF-WS_2 started to be oxidised at around 350°C, as usual, reaching the exothermal peak at 437°C. The oxidation of the C shell for other IF-WS_2 began at 460°C. As soon as the C layers were gone, the IF-WS_2 oxidation to WO_3 was followed without delay, since the temperature was already dramatically surpassed their onset oxidation point. Thus, on an overview for the whole sample, the oxidation of C shell and IF-WS_2 core took place both consequently and simultaneously, leading to no slope in the weight loss curve and no shoulder for the exothermal peak at around 507°C.

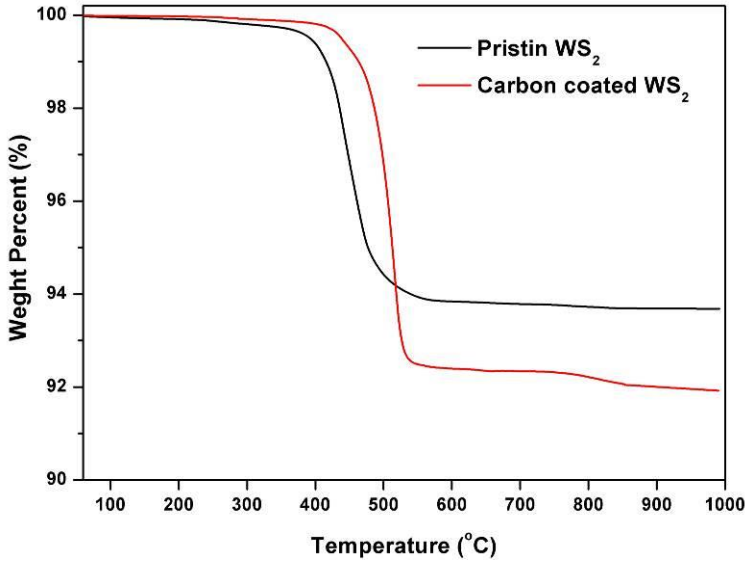

Figure 6-47 A comparison of the TGA curves between the pristine IF-WS_2 and C-coated IF-WS_2

It is not difficult to work out how much carbon is coated on the surface, based on the fact that regardless whether the particles are coated or not, WO_3 should be the only survival product after being heated to 1000°C in air, i.e. fully oxidised. In the situation of CWS4, the residue weight was 91.92%. Assume no WO_3 in the core of pristine IF-WS_2, this amount of WO_3 can be converted back to equivalent molar amount of IF-WS_2 of 98.25%, i.e. 91.92%/(232/248)= 91.76%/93.55%= 98.25 wt%, thus the proportion of C in the C-coated IF-WS_2 was about 1-98.25%=1.75 wt%.

Thus, the improved thermal stability is contributed by the oxidation of around 1.75 wt% of C shell (to CO_2) and 98.25% of IF-WS_2 to WO_3 during the TGA analysis. Similarly, samples from CWS3 consisted of 0.33 wt% of C and 99.67 wt% of IF-WS_2, based on 93.24 wt% of remaining after 1000°C oxidation, hence a small thermal stability improvement.

6.4.3.3 Raman spectrum

Figure 6-48 shows the Raman spectrum for samples produced from each experiment. The two peaks at 349 cm^{-1} and 419 cm^{-1} exhibiting the highest intensity in all the spectra are assigned to the E_{2g} and A_{1g} modes of IF-WS_2 [210]. Compared with previous Raman spectra for WS_2 [210, 211], it could be concluded that, besides the peak at 805 cm^{-1} and 128 cm^{-1}, 259 cm^{-1} which correspond to WO_x [180, 181], all other peaks below 1000 cm^{-1} match well with WS_2 [210].

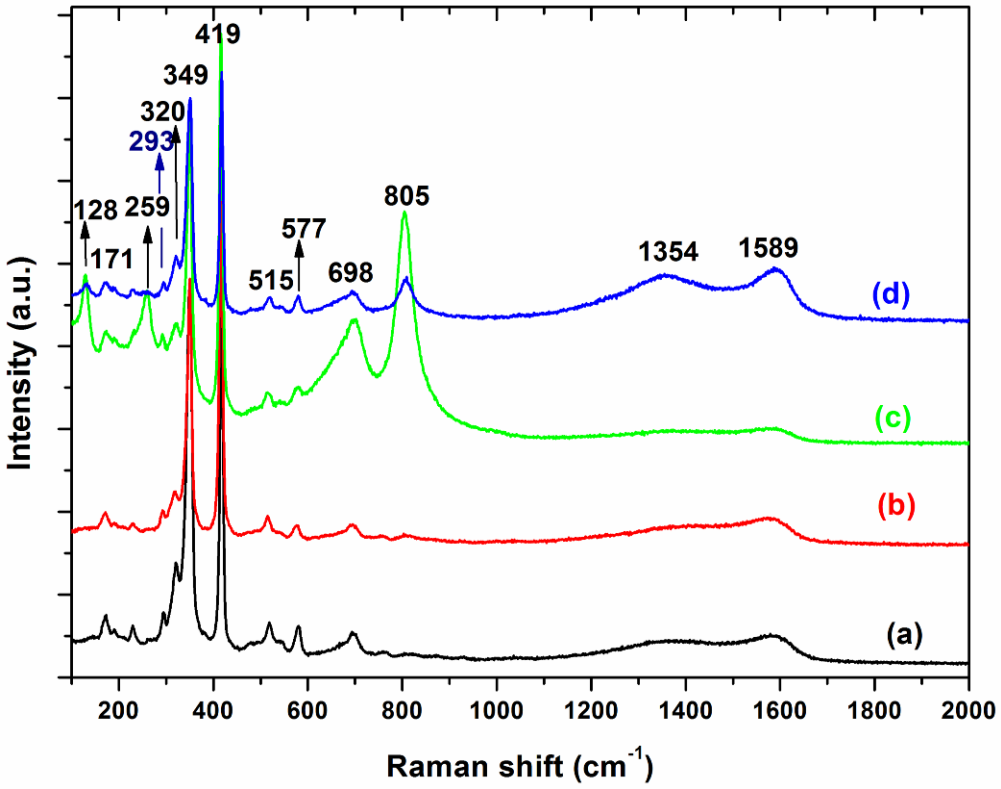

Figure 6-48 Raman spectra of different C-coated IF-WS_2 samples, (a) from CWS1, (b) from CWS2, (c) from CWS3 and (d) from CWS4

The spectra after 1000 cm^{-1} also showed two Raman shifts at 1353 cm^{-1} and 1588 cm^{-1} for C, assigned to the first order D band and first order G band. These C peaks are very weak in spectrum (a) to (c), with only 1589 cm^{-1} visible in (b) and (c), however become distinctive in spectrum (d), samples from CWS4.

The above Raman spectra have also revealed that samples from CWS1 to CWS3 (spectra (a) to (c) in Figure 6-48) have a very few layer of C on the IF-WS_2 surface; meanwhile sample CWS1 and CWS2 (spectra (a) and (b) in Figure 6-48) have completely sulphidised, and a tiny amount of oxide core exists in the IF-WS_2 for sample CWS3 as indicated by spectrum (c) in Figure 6-48. The strong C peaks from CWS4 (spectrum (d) in Figure 6-48) is consistent with the much high C content estimated earlier.

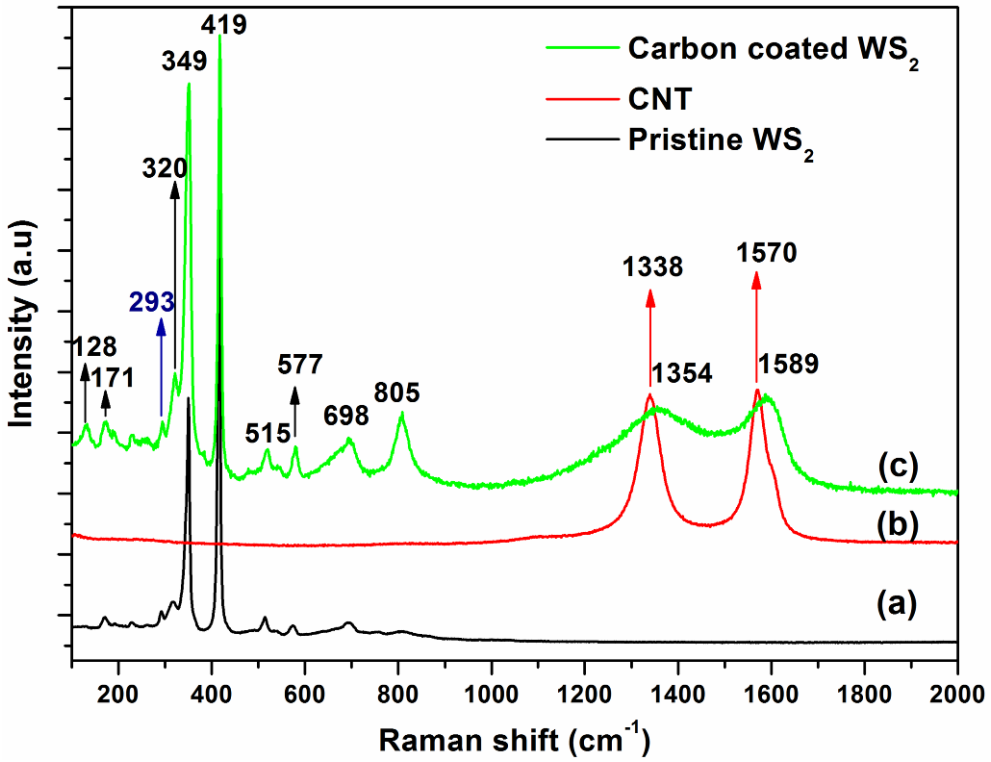

Figure 6-49 Raman spectra of C-coated IF-WS_2 (a), carbon nanotubes (b) and the pristine IF-WS_2 (c)

Figure 6-49 shows a comparison of the Raman spectra of C-coated IF-WS_2 from CWS_4 with pure CNTs and IF-WS_2. The spectrum (a) for pristine IF-WS_2 shows almost identical spectrum to literatures [210], even the smallest detail, and very similar to spectra shown in Figure 6-48. Spectrum (b) for the typical CNTs shows Raman shifts at *ca*.1338 cm^{-1} and 1570 cm^{-1} for the D band and G band respectively, with a shoulder for D` band at around 1604 cm^{-1} [212]. The first half of spectrum (c) for C-coated IF-WS_2 shows the same patterns as to the pristine IF-WS_2 particles, although minor WO_3 peaks appeared at 128 cm^{-1} and 805 cm^{-1}. The second half of spectrum (c), as discussed above, displays significant C peaks at 1353 cm^{-1} and 1588 cm^{-1}, which are close analogies of the D band and G band for graphite [213]. However the D` band, which is supposed to appear near 1620 $cm^{-1}$ could not be distinguished from G band peak at 1588 $cm^{-1}$. In comparison with spectrum (b) for CNTs, besides the invisible D` band, there is a right shift of around 18 cm^{-1} from 1338 cm^{-1} to 1353 cm^{-1} and 1570 cm^{-1} to 1588 cm^{-1} respectively.

Further comparing the spectrum of C in this context with previous Raman studies for graphite [214, 215], CNTs [212] and carbon nano-spheres [209] or carbon onions [216, 217], we have found that the current spectra for C-coated IF-WS_2 resemble the C nano-

spheres produced by Jin and co-worker [209], where peaks at 1355 and 1588 cm^{-1} are reported and an intensity ratio of the D- and G-bands I_D/I_G was calculated as 1.05. Indeed, the HRTEM images of these solid carbon spheres are also similar to the C shells outside the IF-WS_2. This similarity could be resulted from the similar CVD process, although a mixed hydrocarbon solution consisting of 20 vol% styrene and 80 vol% acetone was used in this work, in contrast to the pure styrene applied for their C sphere production [209].

6.4.4 Conclusion

In this section, C-coated IF-WS_2 has been produced, in large quantity, through a simple CVD process in our rotary furnace, which could potentially adopted for continuous production. TEM and Raman characterisations have confirmed the success of the coating process. The C layer shows great resemblance to pure C nano-spheres reported earlier. TGA-DSC analysis has further revealed the significant improvement in the thermal stability of the C-coated IF-WS_2, by ca. 70°C, against the pristine IF-WS_2. The thickness of C coating and thus the thermal performance and other related properties, could be further tailored by using variable injection rates and reaction time.

6.5 Summary

Based on the built rotary system, the large scale manufacture of IF-WS_2 nanoparticles has been realised. Several synthesis methods have been studied and the process starting with WO_3 precursor and H_2S reaction gas has been proved as the most successful technique. Systematic studies have been carried out to optimise the parameters for IF-WS_2 nanoparticles synthesis, including precursor types, reaction temperature, reaction time and reaction gases, in addition to refine the experimental set-up by modifying the quartz tube and feeding system. The IF-WS_2 nanoparticles could be produced in large scale through the effective and continuous rotary process.

Furthermore, the continuous CVD production of C-coated IF-WS_2 core shell structured nanocomposites particles has been reported for the first time on the same rotary furnace. A C shell ranging from 0.33-1.75 wt% has been produced on top of IF-WS_2 core. Importantly, the thermal stability of the composite core-shell nanoparticle has been improved by about 70°C. This new material could find application where thermal stability is critical.

Chapter 7 Nylon 12 reinforced with IF-WS_2 nanomaterials

7.1 Introduction

In the past two decades, attention has been focused on improving the properties of traditional polymer by adding nanofillers. Notwithstanding the successful enhancement of stiffness, lower toughness and deteriorated ductility have been reported for most polymers reinforced with nanofillers. However there are still several studies reported improved toughness by incorporation of nanofillers into polymer matrix [218-223]. In these studies, the improvement of toughness is normally attributed to different mechanisms, including interaction between particles and polymer matrix, crack deflection and local plastic deformation of the polymer surrounding the particles following debonding, the degree of mobility of polymer chain, and alteration of crystalline structure and morphology of polymer matrix resulted from the addition of nanoparticles etc. [218-223].

With a very low concentration of IF-WS_2 in epoxy resin matrix, there is a remarkable simultaneous increase of both shear and peel strength at very low concentration. The enhancement of toughness is attributed to a C-S bond formed between IF-WS_2 nanoparticles and epoxy resin, evidenced by the detection of R-SO_3 or R-SO_3H band at 1246 cm^{-1} in the FTIR spectrum [125].

Recently, the addition of a small amount of graphene into polyamide 12 (PA12, also named nylon 12) matrix has been reported to improve the toughness of nylon 12 composite significantly [224], probably attributed to the higher amount of γ-form nylon 12 resulted from the loading of graphene in nanocomposites. Numerous studies have also reported that the impregnation of low weight percentage of IF-WS_2 nanoparticles into polymer matrix have resulted in significantly improved thermal, rheological and mechanical properties, compared to their neat polymers [45, 124, 125, 127, 134].

The purpose of this work was to prepare nylon 12 nanocomposites reinforced with IF-WS_2, and to study the influence of the addition of well-dispersed IF-WS_2 on the thermal, morphological, and mechanical properties of nylon 12 matrix.

7.2 Experimental

The IF-WS_2 nanoparticles were first dispersed in ethanol for 1 h by ultrasonic probe, then mixed with the nylon 12 powders under intensive stir at 80°C till all ethanol vaporized. After being dried in an oven at 120°C for 12 h, the well-mixed composite powders were then filled and pressed into a mould at 220°C for 2 h to melt and produce the tensile and bending test samples. The concentrations of IF-WS_2 in the nanocomposites were ranged from 0, 0.1 wt%, 0.25 wt%, 0.5 wt%, 2 wt% to 4 wt%.

Mechanical properties of the resulted composites were evaluated by tensile and flexural testing. Tensile samples were finished and tested according to ASTM D638 standard, and three-point flexural testing was conducted in accordance with ISO178 [143], using a Lloyd Instrument EZ20 on a 10 KN load cell and 1 KN, at a loading speed of 0.5 mm/min and 2 mm/min, respectively. 3 samples were tested for each type of composite sample. SEM, TEM observations and Micro-CT technique were used to evaluate the dispersion of IF-WS_2 nanoparticles in nylon 12 matrix.

7.3 Results and Discussion

7.3.1 Dispersion of IF-WS_2 nanoparticles in the nylon 12 matrix

Dispersion of nanoparticles is one main impediment in the development of high performance of polymer nanocomposites. The properties of polymer nanocomposites highly depend on how uniform the nanoparticles are distributed over the polymer matrix.

The SEM images of the mixed nylon 12 with 0.1 wt% IF-WS_2 composites particles were presented in Figure 7-1, which show a very efficient mixing, with bright WS_2 nanoparticles located separately on the nylon 12 particles surface. The inset EDX spectrum in Figure 7-1b has confirmed that the bright dots consisted of W and S indeed, attributed to IF-WS_2 nanoparticles, under back scattered electron mode, due to the density difference of WS_2 and nylon 12 particles.

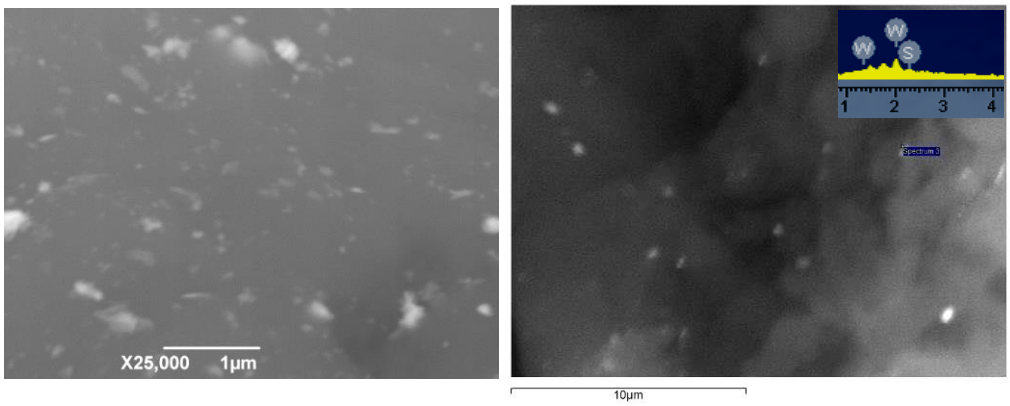

Figure 7-1 Back scattering SEM images revealing for the distribution of 0.1 wt% IF-WS_2 in the nylon 12 matrix

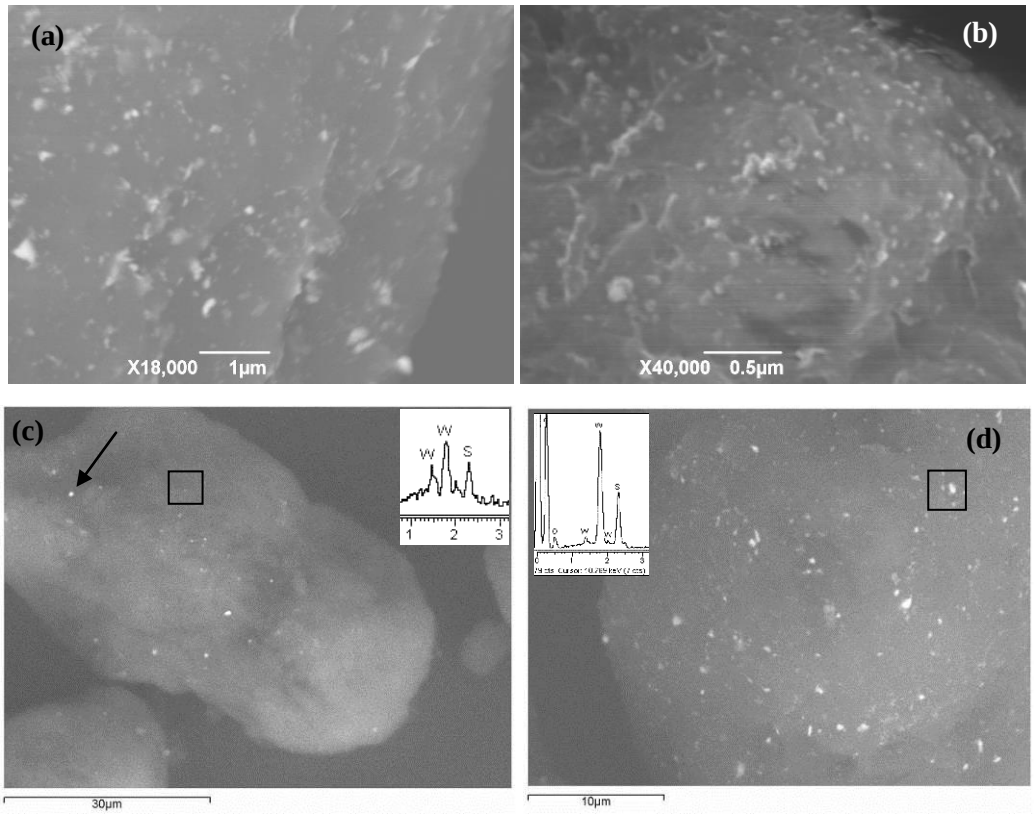

Figure 7-2 Back scattering SEM images showing the distribution of IF-WS_2 in nylon 12. 0.5 wt% (a, b and c) and 2 wt% (d)

Images for composites powder with 0.5 wt% IF-WS_2 are displayed in Figure 7-2. The nanoparticles are found uniformly distributed on the nylon 12 particle surface, and the nylon 12 particles exhibit a size of around 60 μm, as shown in Figure 7-2c, with bright dots over the surface, confirmed as WS_2 particles by the EDX spectrum (Figure 7-2c) which was taken from the particle arrowed. Actually, those very bright ones shown in Figure 7-2c and d, from which the EDX was applied to, might be small aggregates of

several particles; whilst the majority of the white dots should consist of single particles and thus not that bright in BSE mode, such as the particle within the framed area.

For comparison, a thicker distribution of particles was observed in Figure 7-2d for composite powders with 2 wt% IF-WS_2 loading, where even the EDX (Figure 7-2d top left inset) shows a very high intensity signal for IF-WS_2 particles framed.

TEM images showing the distribution of WS_2 in IF-WS_2/nylon 12 nanocomposites are displayed from Figure 7-3 to Figure 7-6. Images from composites with 0.1 wt% IF-WS_2 nanoparticles are shown in Figure 7-3. IF-WS_2 nanoparticles are represented by the dark particles in the matrix with much lower contrast, attributed to the huge difference in density. Figure 7-3 represents a very good dispersion of the nanoparticles, with most of them separated from each other in the polymer matrix. Occasionally, two or three particles were agglomerated together. Nanotubes were also observed within the matrix, which evidenced that WS_2 INTs were produced as a by-product during the nanoparticles manufacturing.

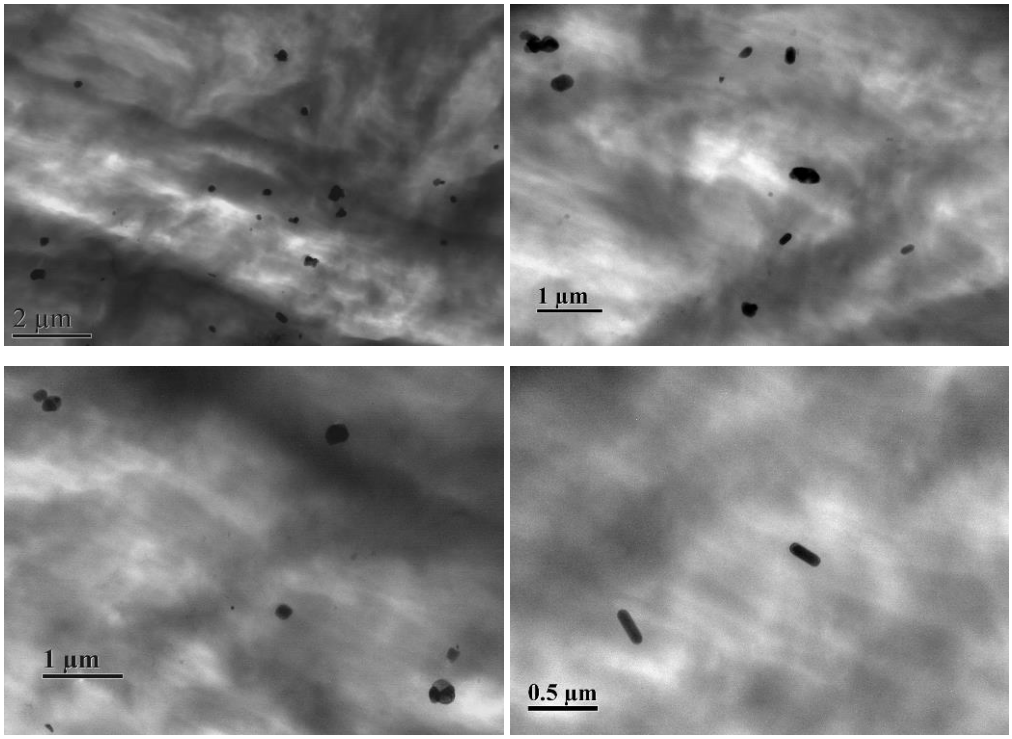

Figure 7-3 TEM images of 0.1 wt% IF-WS_2 reinforced nylon 12 composites

With 0.5 wt% of IF-WS_2 particles loaded to the polyamide matrix, a uniform distribution of IF-WS_2 nanoparticles is observed, in Figure 7-4. The nanoparticles are well-dispersed and the majority of them are isolated from each other. It is also could be

judged only from the image that a much higher amount of particles are impregnated within the matrix in Figure 7-4 compared to that in Figure 7-3, reflecting the differences of the 0.5 wt% addition in contrast to 0.1 wt%.

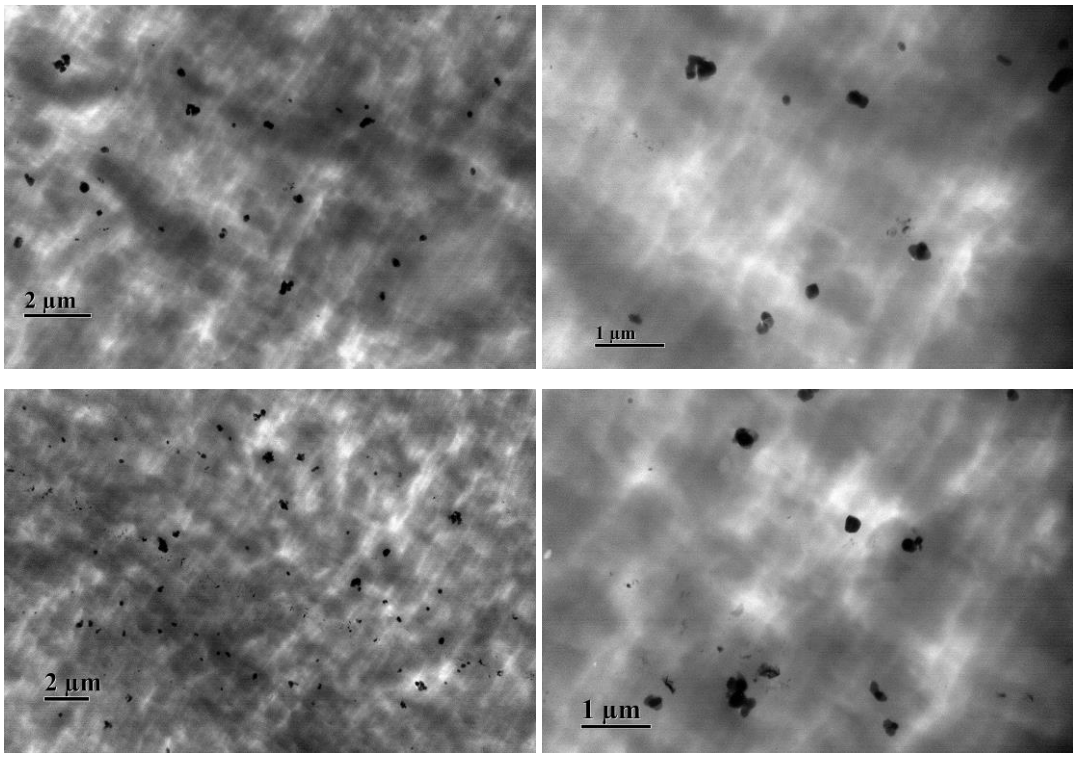

Figure 7-4 TEM images of 0.5 wt% IF-WS_2 reinforced nylon 12 composites

At a much higher concentration of 2 wt% IF-WS_2 nanoparticles being impregnated into the nylon 12 matrix, the dispersion of IF-WS_2 is still very good, as shown in Figure 7-5, though 3-particle agglomerations occured more often.

For comparison, sample prepared using half power/amplitude during the ultrasonic dispersion of IF-WS_2 nanoparticles in ethanol solvent was also characterised by TEM, and the results are shown in Figure 7-6. Depends on the different treatments, aggregates exhibit different sizes ranging from 200 nm by around 10 particles (as shown Figure 7-6b) to >500 nm bigger ones consisting of several tens of particles, as shown in Figure 7-6d.

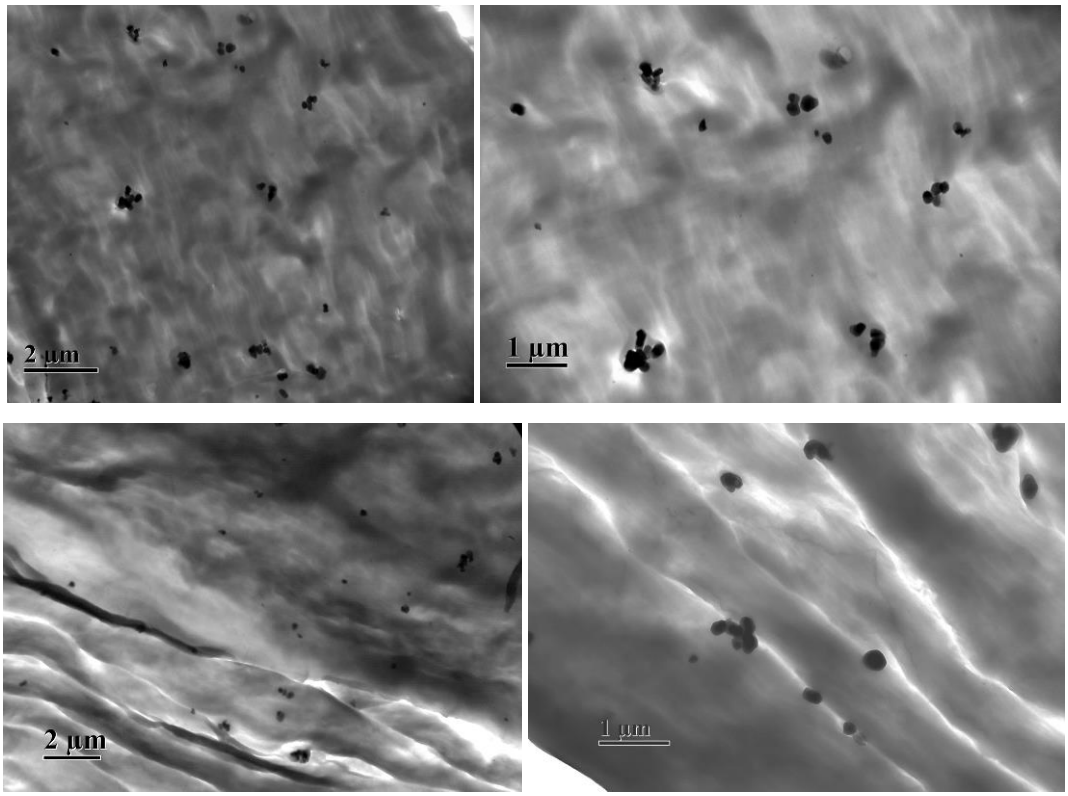

Figure 7-5 TEM images of 2 wt% IFWS_2 reinforced nylon 12 composites

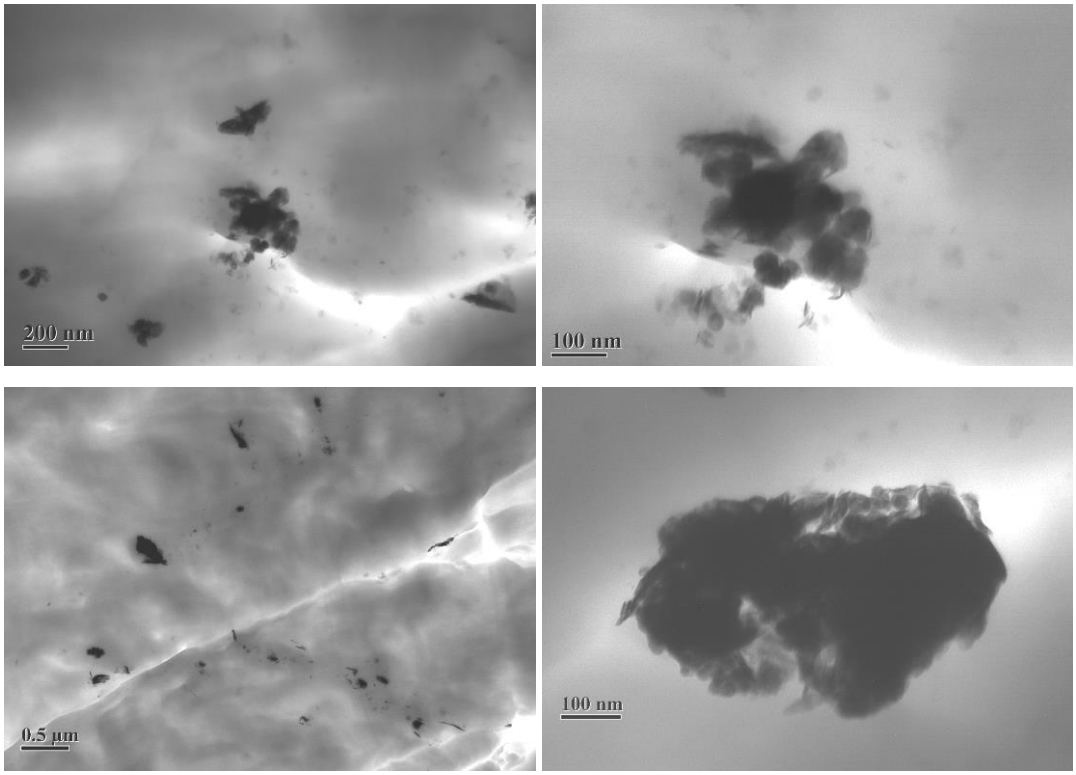

Figure 7-6 TEM images of 2 wt% IF-WS_2 reinforced nylon 12 composites

Micro-CT was applied to evaluate the porosity of the composites, and the results are shown in Figure 7-7. No voids were detected throughout the composite

samples. At each section view, very dense structures were observed. This has confirmed the sucessful moulding process during the mechanical testing specimens preparation.

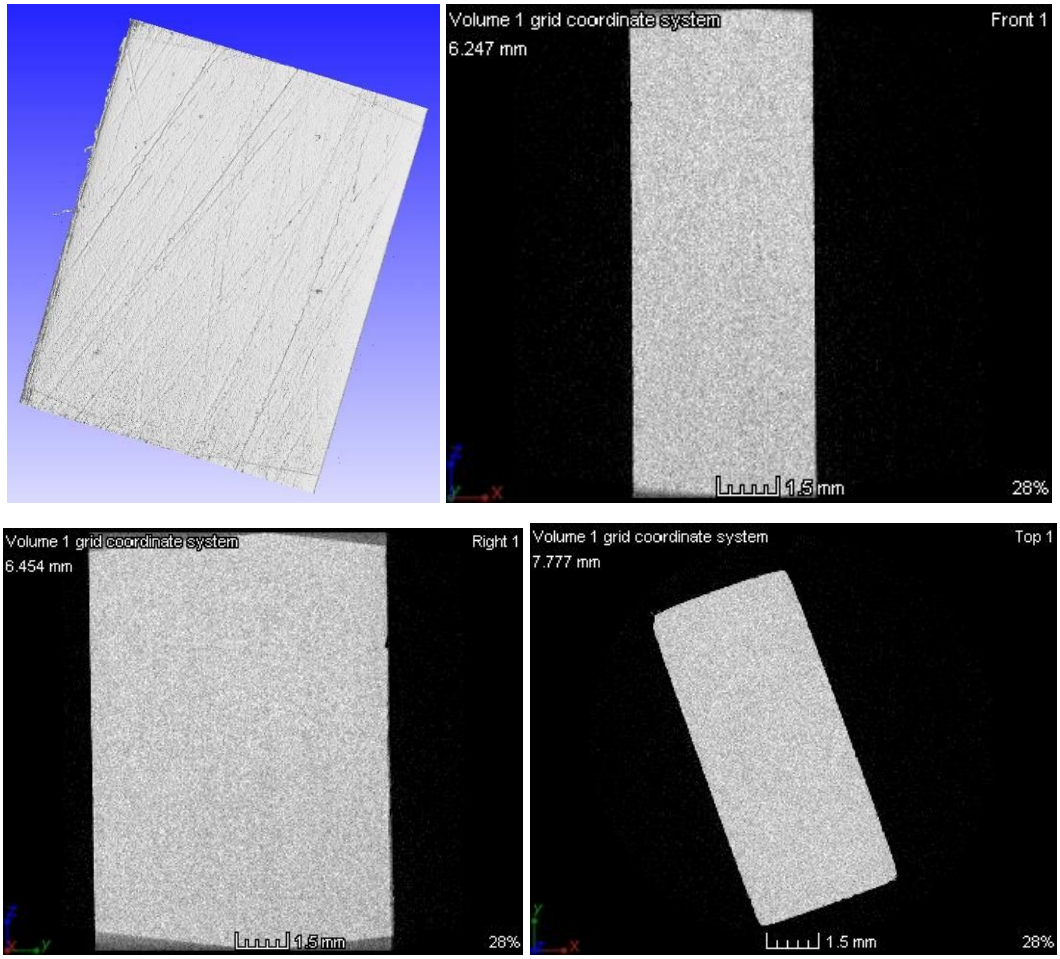

Figure 7-7 CT images showing the dense feature of different 2-D sections of the IF-WS_2/nylon 12 sample

It was also found that, by varying the contrast of the CT images for the composites, the much lower density polymer matrix (exhibiting much lower contrast) could be turned to become transparent, leaving only IF-WS_2 nanoparticles visible. Although theoretically the size of nanoparticles is undetectable with a normal Micro-CT that has a low resolution, the extremely high density of WS_2 in fact sparkled during scan and particles near each other become visible, allowing to reveal the nanoparticles distribution in the composites.

Figure 7-8 shows the distribution of nanoparticles in composites with 0.1wt% and 0.25 wt% concentrations. Identical to the EM images, the particles are very well-dispersed

throughout the entire samples, and a much denser distribution in the 0.25 wt% composites than the 0.1 wt% sample.

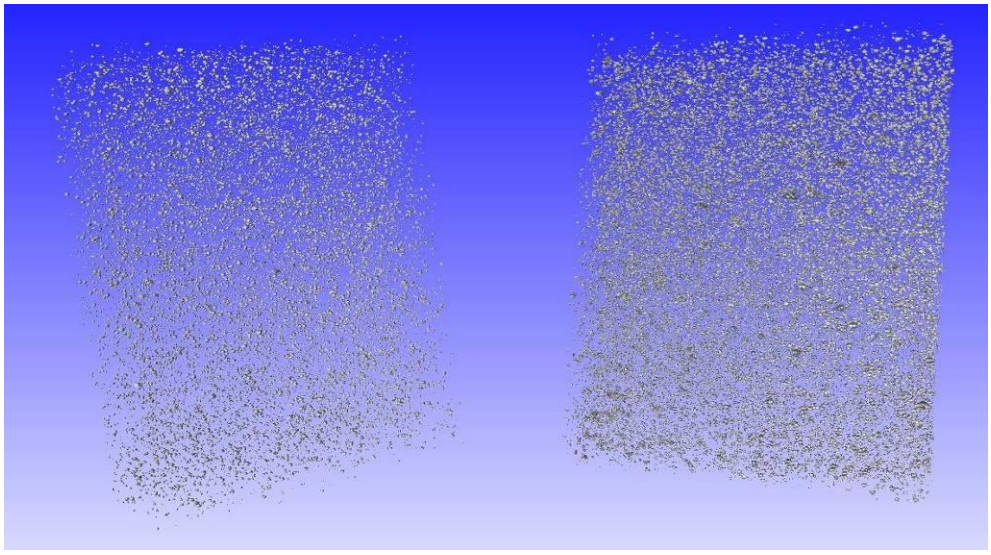

Figure 7-8 Micro-CT images showing the IF-WS_2 nanoparticle distributions of 0.1 wt% (left), and 0.25 wt% (right) within the composites

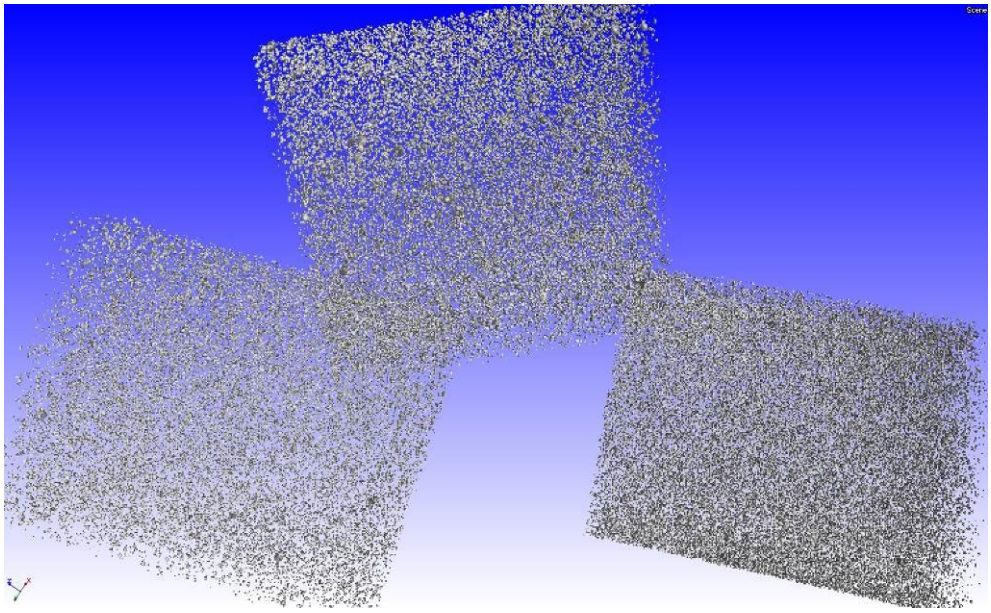

Figure 7-9 Micro-CT images showing the IF-WS_2 nanoparticle distribution of the 0.5 wt%, 2 wt%, and 4 wt% composites

Similarly, the distribution of nanoparticles for composites with 0.5 wt%, 2 wt% and 4 wt% nanoparticles is presented in Figure 7-9. Uniformly distributed nanoparticles are displayed for each composite and an increment of distribution density is visible with increased concentrations.

7.3.2 DSC and crystallization

The DSC curves for pure nylon 12 and 0.1 wt% IF-WS_2 reinforced sample have been displayed in Figure 7-10, where the melting peak appears at around 180°C, a minor exothermal peak occurs at around 353°C and a major exothermal peak at 422°C for neat nylon 12 and at 442°C for 0.1 wt%, indicating a main degradation. Several peaks were included from temperature ranging from 400°C to 500°C, while a broadened peak followed after 500°C. Similar behaviour has been recorded for composites with all different concentrations as shown in Figure 7-12.

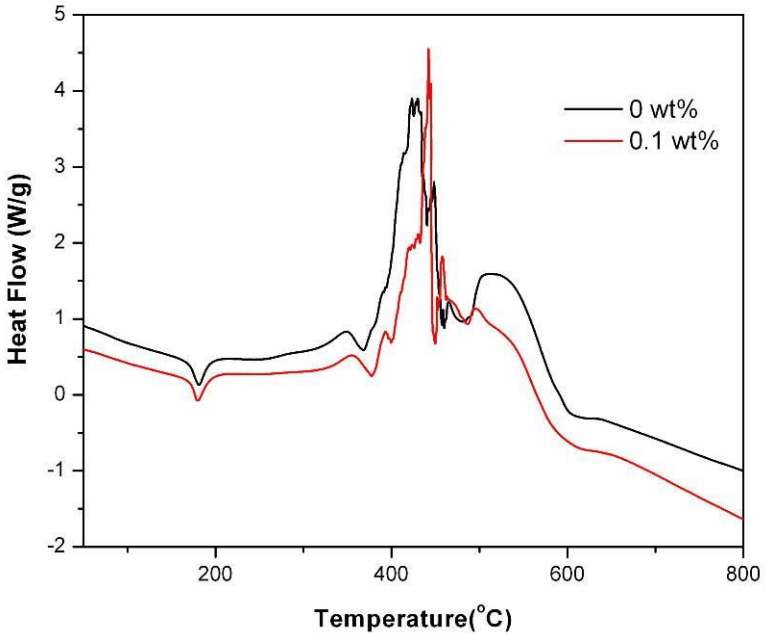

Figure 7-10 DSC curves of neat nylon and 0.1 wt% IF-WS_2/nylon 12 composite obtained in air at 10°C/min

Typically, all the DSC curves have melting peaks at around 180°C, initial exothermal peak at around 350°C and a final broad exothermal peak after 500°C. However the main exothermal peaks for all samples are very complicated, with multi-peaks exhibited in 400-500°C. This is due to the stochastic chain deformation and decomposition of nylon 12 during the oxidation process, especially the oxidation of WS_2 might involve the formation of some sulphides, which make the peaks more complex [69].

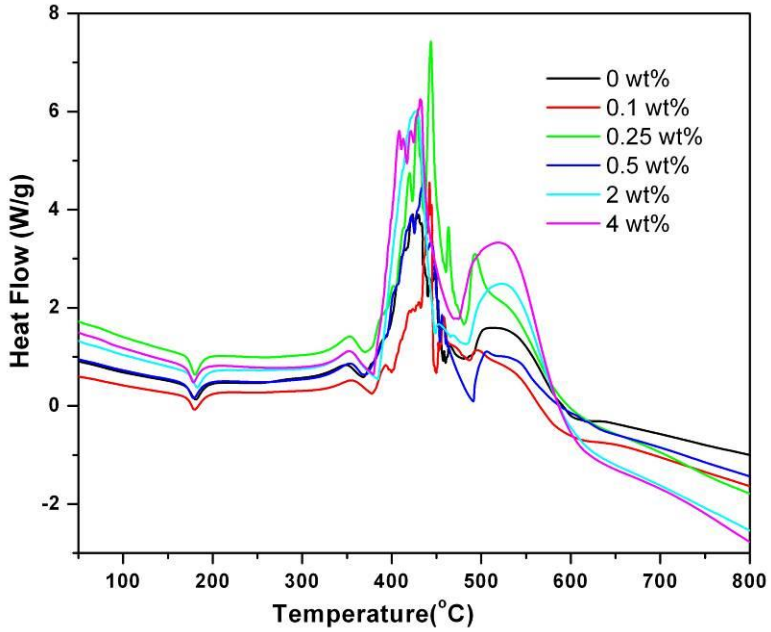

Figure 7-11 DSC curves of IF-WS_2/nylon 12 composites obtained in air at 10°C/min

Of these characteristics of DSC curve, further information could be revealed from the melting peak, which has been zoomed in and displayed separated in Figure 7-12. The area integration from melting peak represents the melting enthalpy, ΔH_m, which reflects the crystallization of a polymer. Figure 7-12 shows a very close melting temperature range from 178°C to no more than 182°C, which could be considered no change. The area integration is also more or less similar, judging from the curves.

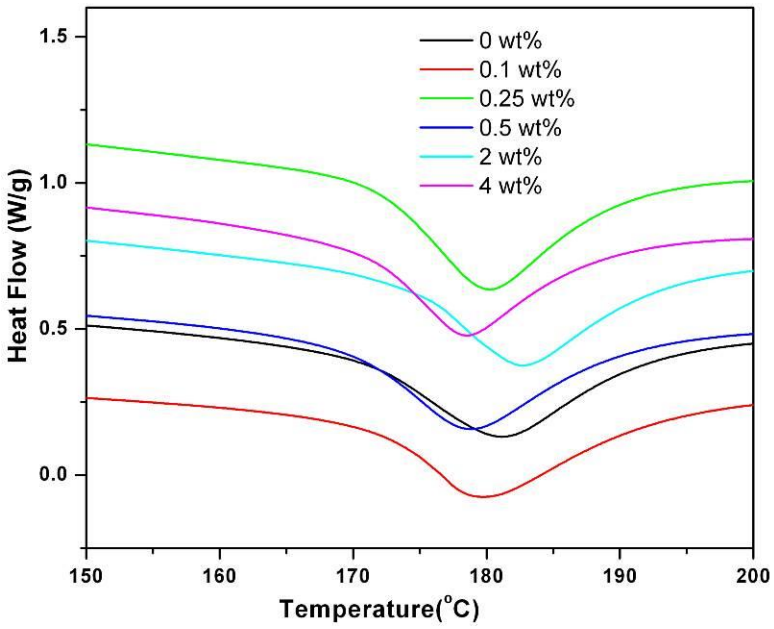

Figure 7-12 DSC curve showing the melting peaks of IF-WS_2/nylon 12 composites obtained in air at 10°C/min

Generally, the crystallization X_C of a polymer based composites could be calculated using the following equation,

$$X_C = \frac{\Delta H_m}{\Delta H_0 \times (1 - f)} \times 100 \qquad \text{Equation 7-1}$$

Where ΔH_m is the melting enthalpy measured in the heating experiments, ΔH_0 is the theoretical value of enthalpy of 100 % crystalline polymer, and f the fraction of fillers in the composites. For pure nylon 12, ΔH_0 =209.2 J/g, thus the crystallization of nylon 12 with different concentration of IF-WS_2 reinforcements could be worked out based on the DSC curves shown in Figure 7-12.

Table 7-1 summarises the melting data for IF-WS_2/nylon 12 composites, where T_m represents the melting peak temperature, ΔH_m is derived from the melting peak area and X_C is the crystallinities calculated from ΔH_m. As a comparison, the DSC data for original nylon 12 powder was also included. It shows that all the bulk materials including pure nylon 12 have a ΔH_m value around 30, and melting point around 180°C, compared to 80.4 and 187°C for nylon 12 powders respectively, thus leading to huge differences in crystallization, with around 14% in comparison with 38.4 for pure nylon 12 powder (Table 7-1).

For the bulk composites with different IF-WS_2 contents, the differences in ΔH_m, T_m and X_C could be ignored, which suggests that the crystallization of nylon 12 has not been obviously altered by incorporation of IF-WS_2. However, a remarkable decrease of crystallization from 38.4% to 14.8% has taken place after moulding nylon 12 powders into bulk sample, and this might attribute to different nucleate conditions. For nylon 12 powders, it was normally prepared through a dissolution-precipitation process, under a protected high temperature high pressure environment. Thus it is more favourable for the nucleation and recrystallization to take place, compared to the sintering process in the mould within a furnace.

Table 7-1 DSC melting data of IF-WS_2/nylon 12 composites with a heating rate of 10°C/min in air

WS_2 content (%)	ΔH_m	Melting point (T_m, °C)	Crystallization (X_C, %)
0*	80.4	187.3	38.4
0	30.89	181.11	14.8
0.1	29.92	178.03	14.3
0.25	30.04	180.03	14.4
0.5	29.38	178.72	14.1
2	30.45	182.62	14.8
4	27.18	178.32	13.5

*: original nylon 12 powder

7.3.3 TGA and thermal stability

TGA results are displayed in Figure 7-13. For IF-WS_2 nanoparticles, the oxidation in air starts from 350°C (as shown in Figure 6-41 of Chapter **6**). With regards to nanocomposites impregnated with IF-WS_2 nanoparticles, little change in thermal stability was observed. Before 450°C, the results shows that composites with 0.1 wt% and 0.25 wt% IF-WS_2 have higher oxidation temperatures than that of the pure nylon 12 matrix, and the 0.5 wt% composites only display a slight better performance than the neat matrix. When the IF-WS_2 contents were increased to 2 and 4 wt%, the composites exhibited a poorer thermal resistant behaviour compared to pure nylon 12. From 450°C onwards, the weight loss of 2 wt% and 4 wt% composites became less than composites of other concentrations, probably due to the formation of carbides, oxides and sulphides following oxidation of IF-WS_2, thus resulting in delayed weight loss than other samples from 450-550°C. After 550°C, attributing to the higher amount of residue weight of tungsten oxide from oxidation of IF-WS_2, there is a good correspondence between the residual weight and the IF contents of the sample.

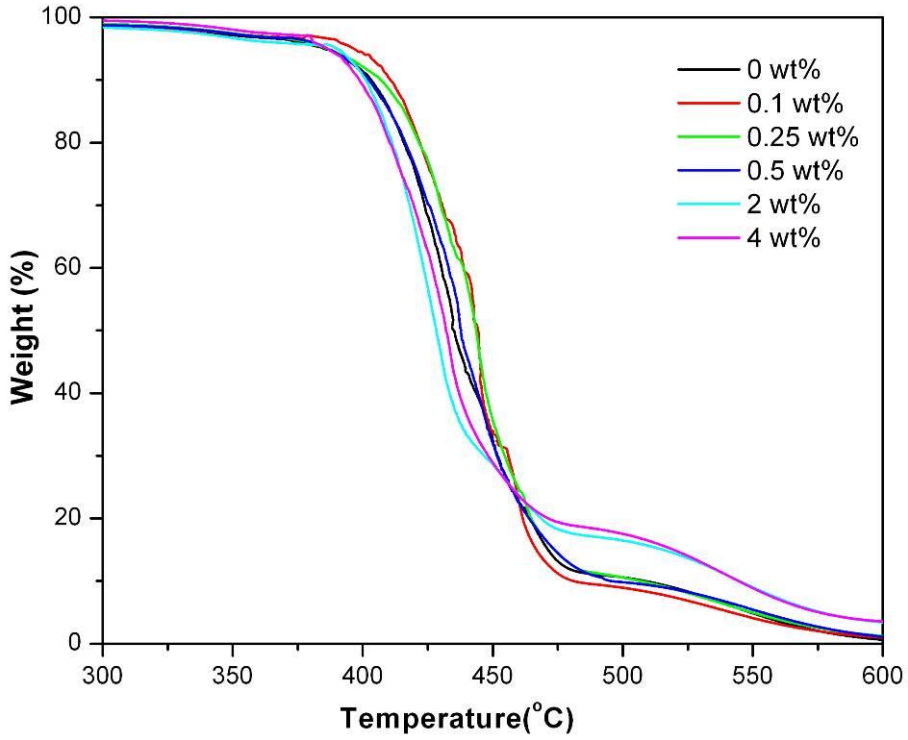

Figure 7-13 TGA curves of IF-WS_2/nylon 12 composites heated in air

For an easy comparison, the characteristic temperatures of TGA data for the composites have been summarised in Table 7-2. The displayed temperatures T_i, T_{10}, T_{50} and T_{80}, represents the initial degradation temperature obtained at 2% weight loss(T_i); temperatures for 10 and 50 and 80% weight loss (T_{10}, T_{50}, T_{80}). The initial degradation temperature ranges from 321°C for the 2 wt% sample to 350°C for the 4 wt% sample. However this might also be resulted from different moistures released by samples before the real degradation began. As also clearly seen from the TGA curves in Figure 7-13, T_{10} and T_{50} for 0.1 wt% and 0.25 wt% are higher than neat polymer, whilst other samples are almost the same or even slightly lower (eg. T_{10} for 4 wt% is 398°C, compared to 403°C for 0 wt%). However, the slight improvement of thermal stability is indeed existed, as for T_{50}, 444.3 for 0.1 wt% to 434.6 for 0 wt%. T_{80} is almost the same for all samples except for the 4 wt% one, as explained previously, and the higher IF-WS_2 content delayed the weight loss from 450°C. Same reason also accounts for the differences in T_{80}.

Table 7-2 TGA data of IF-WS_2/nylon 12 composites obtained in air with a heating rate of 10°C/min

WS_2 content (%)	Air				
	T_i(°C)	T_{10}(°C)	T_{50}(°C)	T_{80}(°C)	T_{90}(°C)
0	331.8	403.2	434.6	464.4	509
0.1	330	410.6	444.3	463.8	481
0.25	339.8	407	443.6	464.8	506.7
0.5	336.9	402.3	437.8	463.9	495.5
2	321	402.3	430.5	464.4	545
4	350.6	398.7	432	471.4	544.5

7.3.4 XRD and crystalline structure

Several crystalline structures have been defined for nylon 12. It is well accepted that the α-phase and α`-phase of nylon 12 are monoclinic, both show two characteristic reflections in XRD patterns at room temperature. Normally, the structure possessing two distinct reflections with a *d* spacing of 0.37 and 0.44 nm is designated to α-phase; while α`-phase also exhibits two crystalline peaks, though much closer to each other, compared to α-phase nylon 12 [225]. On the contrary, only one strong reflection is presented in the γ-form nylon 12, attributed to a *d* spacing at about 0.42 nm [225, 226].

To evaluate the crystalline structure of nylon 12 composites in this study, both powdered and bulk nylon 12 with IF-WS_2 nanocomposites were appraised by XRD, with results shown in Figure 7-14 to Figure 7-17.

Figure 7-14 presents XRD profiles for pure nylon 12 powders and melted nylon 12 in bulk form. As a semi-crystalline polymer, two strong crystalline peaks are presented in the XRD pattern of pure nylon 12 powder at 2θ=21.08 and 2θ=22.08 respectively, corresponding to d_{001} (0.421 nm) and d_{001} (0.402 nm) of the α`-phase of nylon 12, which is believed to be a less stable phase [226]. However only one distinct crystalline

reflection appears at 2θ=21.42 (d_{001}=0.415 nm) for the bulk pure nylon sample after sintering, attributing to a more stable γ-phase at room temperature [226, 227]. The XRD patterns of nylon 12 before and after sintering are identical to previous study, since nylon 12 powders in Yan's work were produced from dissolution and precipitation of nylon 12 pellets, the same as the commercial nylon 12 powders used in our work [228].

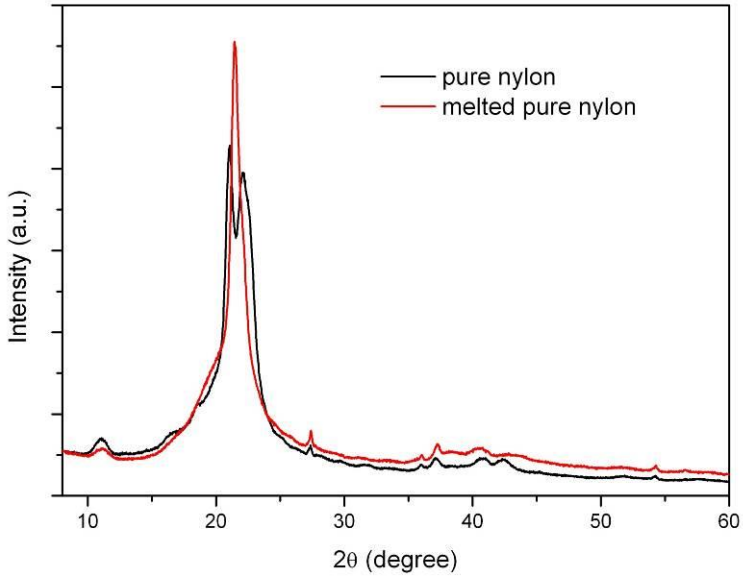

Figure 7-14 XRD patterns for powdered and melted pure nylon

Similarly, XRD patterns for powdered and melted nylon 12 with 0.1 wt% IF-WS_2 nanocomposites are shown in Figure 7-15. Compared with the profiles of pure nylon, a tiny new peak appeared at around 14.3 degree, which should correspond to (002) plane of IF-WS_2 (JCPDS No. 84-1398). The rest of XRD patterns of the composites remain the same to the pure nylon 12, with two crystalline peaks for the powder form and only one peak for the bulk. The two crystalline peaks located at 2θ=21.08 and 2θ=22.08 are closer than those located at 2θ=20.13 (d=0.44 nm) and 2θ=24 (d=0.37 nm) for α-phase, thus should also be assigned to (001) planes of the α`-phase.

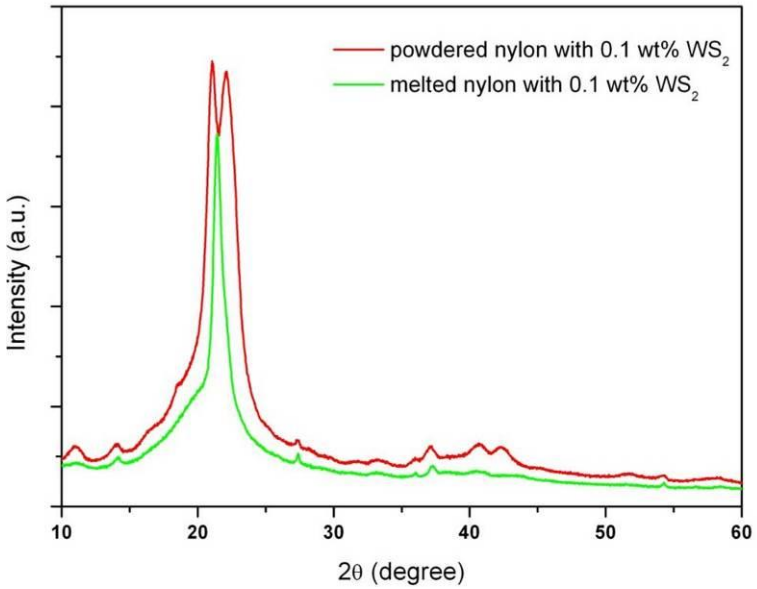

Figure 7-15 XRD patterns of powdered and melted nylon 12 reinforced with 0.1 wt% IF-WS_2

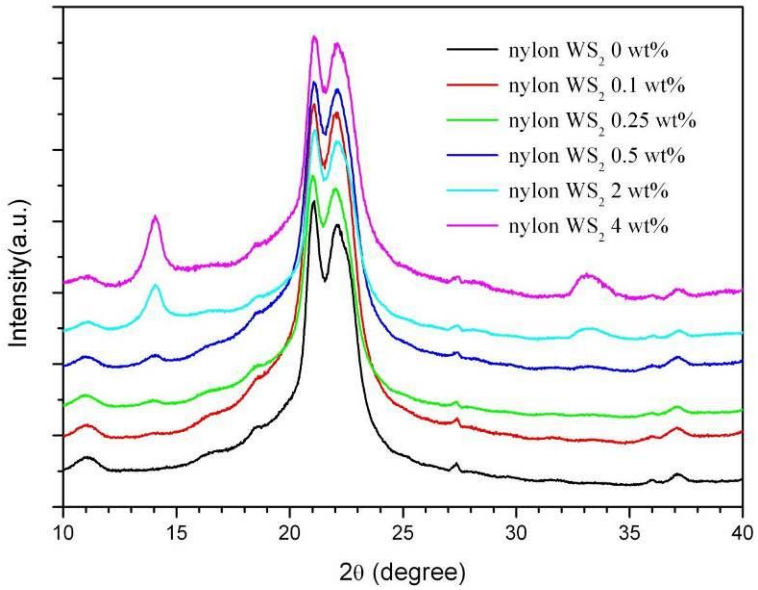

Figure 7-16 XRD profiles of powdered nylon 12 mixed with different amounts of IF-WS_2 content

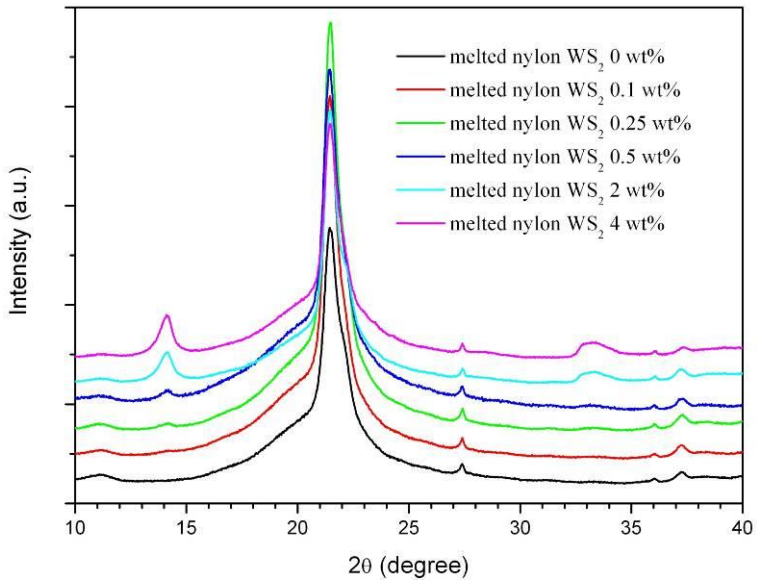

Figure 7-17 XRD profiles of melted bulk form nylon 12 reinforced with different amounts of IF-WS_2 content

Figure 7-16 and Figure 7-17 display the XRD profiles of nylon 12 with different contents of IF-WS_2 in powder and bulk form respectively.

It is notable that the composite powders, regardless the IF-WS_2 contents, have possessed identical XRD signals to the nylon 12, with two dominated peaks at 21.08 and 22.08, respectively, which are attributed to the (001) plane of the α`-phase nylon 12 particles. For all bulk nanocomposites, only one major peak at 21.4 degree was observed, with the *d* spacing of (001) plane being 0.415 nm, suggesting a stable γ phase. Due to the low content of IF-WS_2 in the composites, only the 14.3 peak and a broad peak presumably a combination of 32.7 and 33.6 appeared in the XRD pattern, and their intensities increase gradually with the amounts of content in composites, in both the powder and bulk composites, from a very tiny signal for 0.1 wt% to a vivid peak for 0.5 wt%, then to a distinct peak in 2 and 4 wt%.

It is also worthy to mention that, taking the powdered 4 wt% IF-WS_2 pattern for example as shown in Figure 7-16, the relative intensity of *d(002)* peak of IF-WS_2 at around 14.3 degree with *d(001)* peaks for nylon 12 at 21.08 and 22.08 degree are high, compared with that of the bulk composites. In other words, the peak intensity of IF-WS_2 in bulk composites is relatively weaker than that in the powder composite. The same phenomenon was observed for all other IF-WS_2 contents. It might be explained that, during the sintering process the composites powder melted and recrystallized,

many IF-WS_2 have been impregnated into the nylon 12 particles rather than distributed on their surface as do in the powdered form which have contributed to the higher XRD intensities.

Furthermore, the relative intensity for the peak at 21.4 degree for the (001) plane to other peaks of γ-phased nylon 12 (e.g. peak at around 27.5) has increased for 0.1 wt%, 0.25 wt% and 0.5 wt% IF-WS_2 samples, however decreased for 2 and 4 wt% samples (even lower than pure nylon sample with 4 wt% IF-WS_2). This intensity change has reflected a change of the γ-phase amounts in the nylon 12 samples.

7.3.5 Raman

Raman spectra of nylon 12 with all different contents of IF-WS_2, for both the powder and bulk form composites, were acquired and shown in Figure 7-18 to Figure 7-20. Figure 7-18 displays the spectra for a series of powder composites. Peaks at 350 cm^{-1} and 420 cm^{-1} should be assigned to IF-WS_2, both starting to appear from spectrum b and the intensities becoming more and more dominant in spectra c and f, as highlighted in the top left inset. All the other peaks in these spectra should be assigned to the nylon 12 particles.

From previous studies [229-231], Raman shifts of nylon 12 are assigned to different modes and defined into four main regions, which is CH_2 stretch region (900-1150 cm^{-1}), the CNH bending region (1310-1350 and 1440-1490 cm^{-1}), amide I band attributed to stretching of -C=O group located at 1638 cm^{-1} and amide III located at 1283 cm^{-1}, assigned to the CN stretch and the C=O in-plane bending of the amide group [-C(=O)-NHC-] [229-231].

An amide II band has also been defined at 1550 cm^{-1} according to -NH stretching and C=O in-plane bending, though it is very weak compared to that in a distinct FTIR [231]. The shift resulted from the stretching vibration of a –NH group appeared at 3290 cm^{-1}.

In this study, the majority of Raman shifts for nylon 12 are detected, as shown in Figure 7-18. Shifts at 2924 cm^{-1} and 2800-2900 cm^{-1} (2839 cm^{-1} and 2874 cm^{-1}) are assigned to the CH_2 asymmetric and symmetric stretching, respectively. The amide I peak appears at 1632 cm^{-1}. Shifts located at 1434 cm^{-1}, 1364 cm^{-1} and 1293 cm^{-1} are attributed to the bending, wagging and twisting of CH_2, respectively [232].

Shift for amide III occurs at 1266 cm^{-1}. The NH wagging has resulted in two peaks at 1219 cm^{-1} and 1244 cm^{-1}. There are several primary peaks at around 950-1200 cm^{-1}, which should be assigned to the CH_2 stretching mode; whilst the C-CO stretching accounts for shifts at 910 cm^{-1} and 937 cm^{-1}. CH_2 rocking might result in the peak at 715 cm^{-1}. The shift appears at 633 cm^{-1} should be defined to Amide IV (d CO) [230] and the characteristic peak for N-H out of plane bending is presented at 611 cm^{-1} [232].

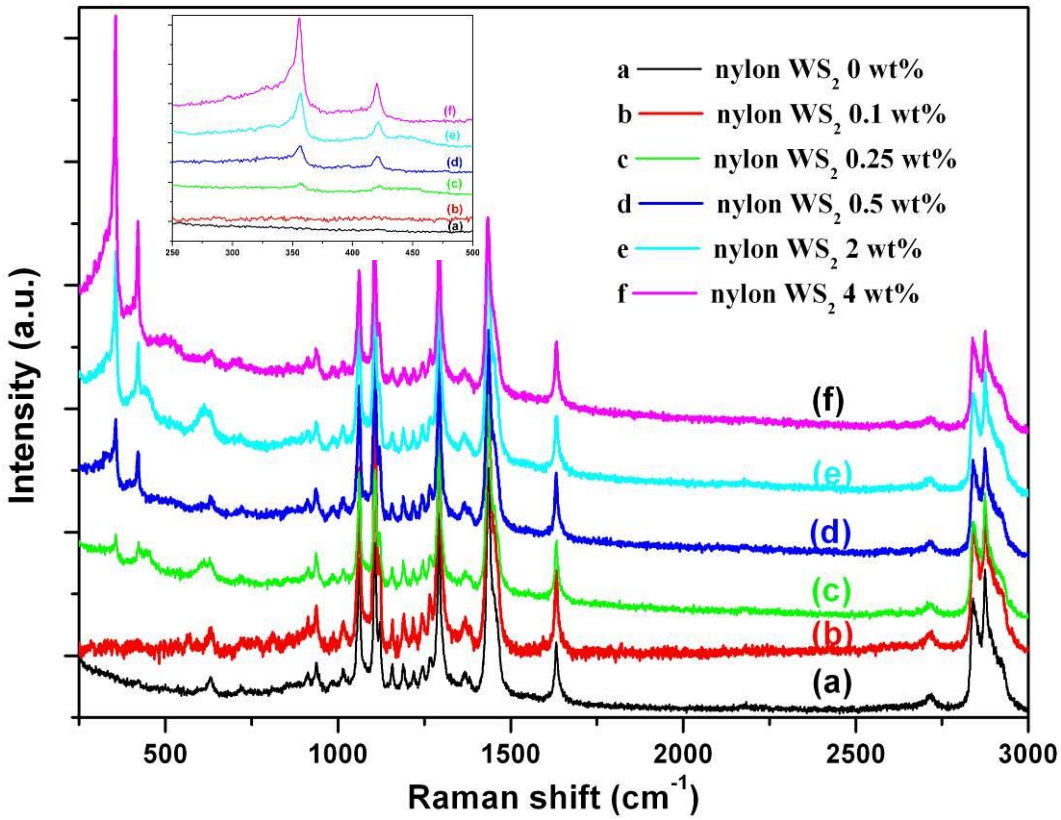

Figure 7-18 Raman spectra of IF-WS_2/nylon 12 powder composites (a, 0 wt% IF-WS_2; b, 0.1 wt% IF-WS_2; c, 0.25 wt% IF-WS_2; d, 0.5 wt% IF-WS_2; e, 2 wt% IF-WS_2; and f, 4 wt% IF-WS_2)

Table 7-3 summaries the main peak assignment of the obtained spectra, with comparison to literatures [230-234].

Table 7-3 Peak assignments for Raman vibrational modes

Band assignment	Wavenumber (cm^{-1}) experimental	Wavenumber (cm^{1}) from [230, 231]	Wavenumber (cm^{-1}) from [234]	Wavenumber (cm^{-1}) from [233]
CH_2 asymmetric stretching	2924	2923	2920	2925
CH_2 symmetric stretching	2874	2883	2888	2886
CH_2 symmetric stretching	2839	2848	2853	2850
Amide I (n C=O)	1632	1636	1634	1634
CH_2 bending	1434	1437	1440	1437
CH_2 wagging	1364	1373	1386	1374
CH_2 twisting	1293	1296	1300	1296
Amide III	1266		1253	1261
N-H wagging	1244			1240
	1219		1213	
C-C stretching	1190			
C-C stretching	1157		1131	1140
	1120	1120		1128
	1106	1107	1107	
C-C stretching	1060	1063	1064	1062
C-C stretching	1014			
	985			
C-CO stretching	937		948	948
	910			
CH_2 rocking			880	861
	715			
Amide IV (d C O)	633		628	630
Amide VI (g N-H)	611		600	580, 620

Figure 7-19 shows the Raman spectra of bulk IF-WS_2/nylon 12 nanocomposites, in comparison with powdered composites. No obvious changes were observed in the spectra for nylon 12, indicating the chain conformation of the nylon 12 particles has not

been altered after being sintered into bulk, although preferred crystalline structure occurred, as revealed by XRD patterns. For IF-WS_2, the intensities of shifts at 350 cm^{-1} and 420 cm^{-1} similarly display an ascendant order with increased content amounts. However a tiny new peak appeared at around 520 cm^{-1} for the 0.5 wt% IF-WS_2 sample in Figure 7-19d, and became more evident in Figure 7-19e and f for samples of 2 wt% and 4 wt% IF-WS_2, respectively.

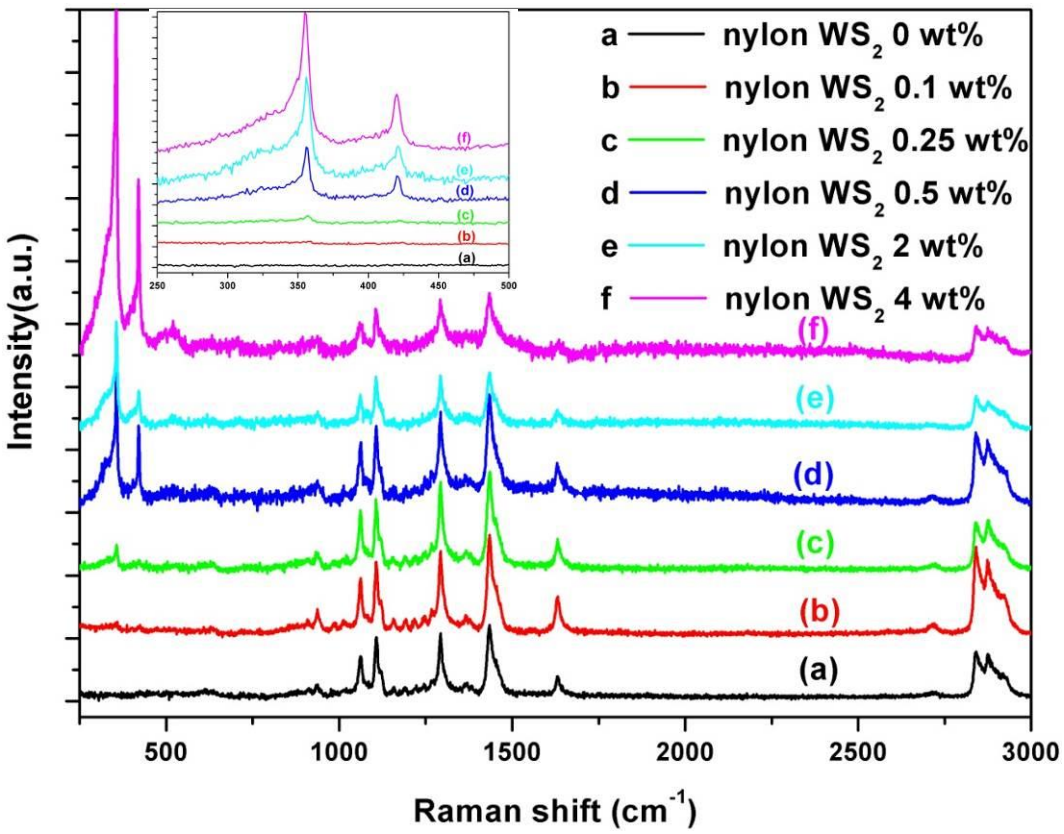

Figure 7-19 Raman spectra of bulk melted nylon 12/WS_2 composites (a, melted pure nylon 12; b, 0.1 wt% IF-WS_2; c, 0.25 wt% IF-WS_2; d, 0.5 wt% IF-WS_2; e, 2 wt% IF-WS_2; and f, 4 wt% IF-WS_2)

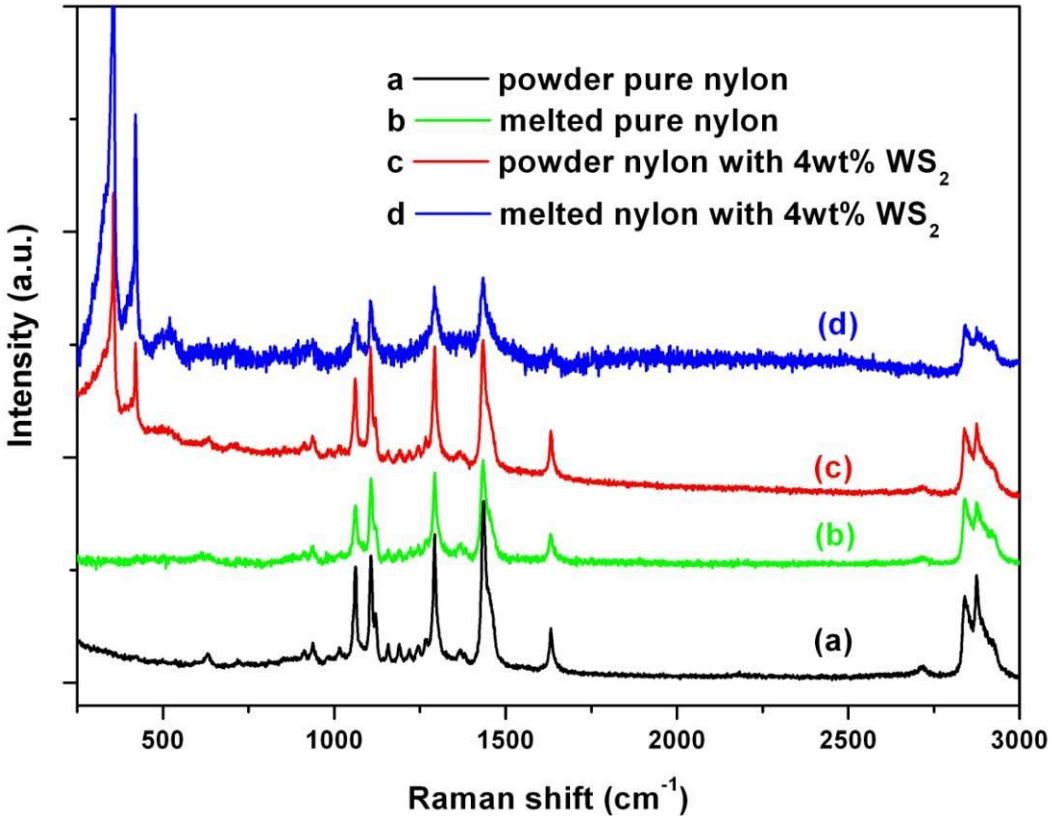

Figure 7-20 Raman spectra of a comparison of the powdered and melted IF-WS_2/nylon 12 composites (a, powdered pure nylon 12; b, melted pure nylon 12; c, powdered nylon 12 with 4 wt% IF-WS_2; and d, melted nylon 12 with 4 wt% IF-WS_2)

Figure 7-20 shows a Raman comparison between the powdered and bulk composites. No obvious change could be observed apart from the additional peak at around 520 cm^{-1} as discussed above. Furthermore, the peak at 633 cm^{-1} in bulk composites is not as sharp as that of the powder sample. This also occurred in Figure 7-18 and Figure 7-19, regardless of the IF-WS_2 content.

7.3.6 Mechanical properties

Typical stress-strain curves are displayed in Figure 7-21, and the results show that the strength and ductility have been significantly improved. From 0.1 to up to 2 wt%, an improvement of 27% in tensile strength for the 2 wt% composites, against the neat nylon 12, was obtained, however a decrease for the 4 wt% sample was also seen, though still higher than the pure nylon 12. The Young's modulus as reflected by the slope of the initial liner part of the stress-strain curve also are increased with increased IF-WS_2 contents till 2 wt%, then started to decrease for the 4 wt% sample. Similar trends were found for the strains which increased first then decreased dramatically after 2 wt%, and

the sample became brittle at 4 wt% at which the strain became as low as 13.2 and the sample was broken before yielding point. Mechanical data for IF-WS_2/nylon 12 composites were summarised in Table 7-4.

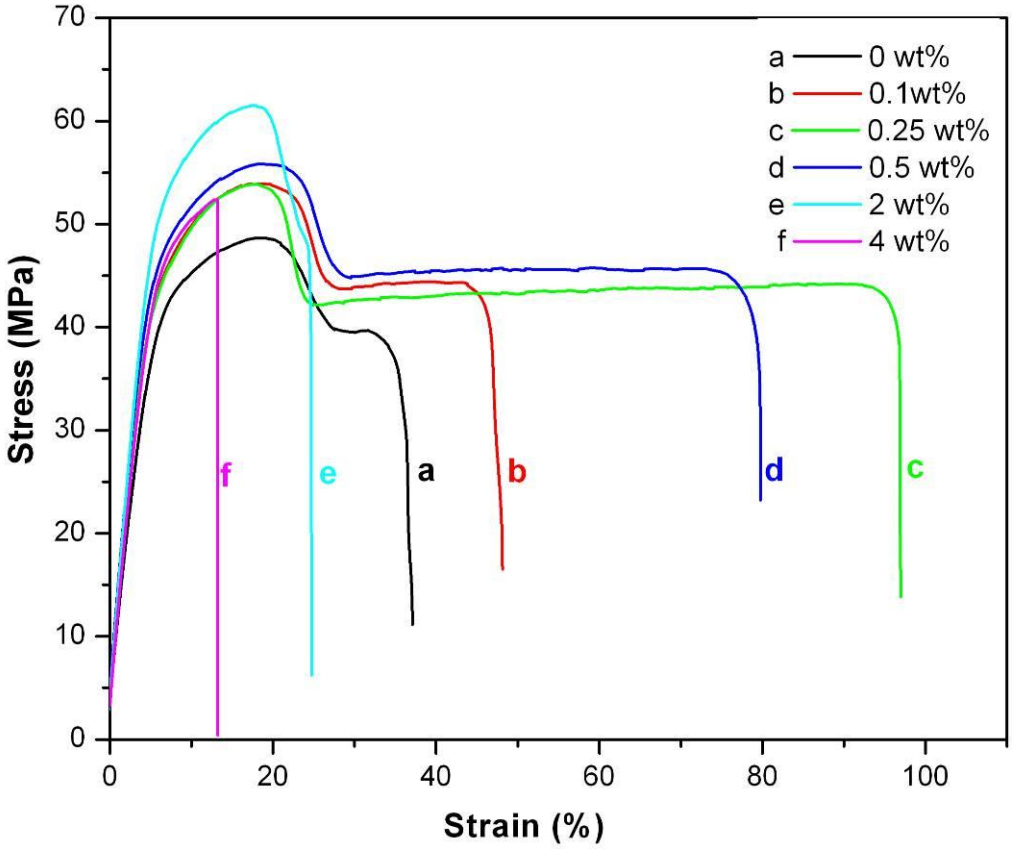

Figure 7-21 Typical tensile stress–strain curves of the IF-WS_2/nylon 12 composites as a function of IF-WS_2 content

Table 7-4 A comparison of mechanical properties of IF-WS_2/nylon 12 composites from tensile tests

WS_2 content (%)	Tensile stress (MPa)	Toughness* (MJ/m^3)	Elongation* at break (%)	Bending Stress (MPa)
0	48.7	14.86	37	67.1
0.1	53.9	21.44	48	72.2
0.25	53.9	42.42	97	78.9
0.5	55.9	36.80	79.8	78.4
2	61.5	12.56	24.7	85.6
4	52.4	5.21	13.2	79

*: Both toughness and elongation at break data are based on the tensile tests

Figure 7-22 shows the photos of the polymer composites samples after fracture from tensile tests. They are displayed in an ascendant order of the IF-WS_2 contents, 0 wt%, 0.1 wt%, 0.25 wt%, 0.5 wt%, 2 wt% and 4 wt%, respectively, from left to right.

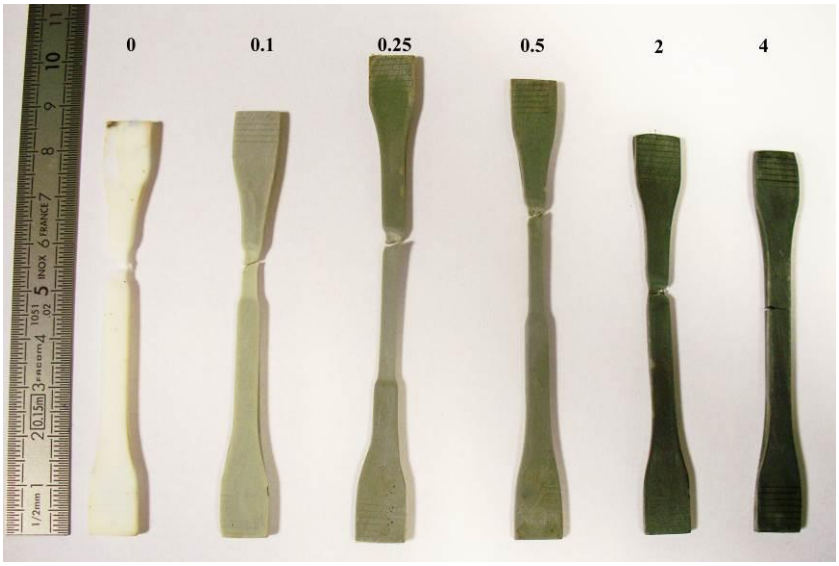

Figure 7-22 Photos of samples after pull-to-break experiments (from left to right: ruler, original nylon 12, with 0.1 wt% IF-WS_2, 0.25 wt%, 0.5 wt%, 2 wt% and 4 wt% IF-WS_2 samples after break).

Obvious necking behaviour was observed for samples of 0 to 2 wt% IF-WS_2 contents. It is noted that there is a significant increase in elongation at break for the composites with low IF-WS_2 addition up to 0.5 wt%, indicating a remarkably improved ductility. However the elongation at break started to decrease from 2 wt% samples, and became brittle for the 4 wt% samples which displayed a sharp fracture surface without any necking behaviour.

Normally, elongation at break, or in other words, ductility is a requisite to toughness. A tough material must possess high ductile performance. However, a material with high ductility would not necessarily be a tough material, without high stiffness. Defined as the ability of a material to absorb energy before fracture, toughness of materials could be evaluated by several approaches, of which the area under the stress-strain curve was used to demonstrate the toughness of the IF-WS_2/nylon 12 composites in this study. An increase was observed for nanocomposites with 0.25 wt% and 0.5 wt% IF-WS_2, which is 285% and 248% of that of neat nylon 12 respectively. As discussed above, toughness is a combination of strength and ductility, thus toughness for 2 wt% sample lower than that of the neat nylon 12, is not surprising, although it has much higher tensile strength.

As demonstrated in Section **7.3.1**, there was a sample with 2 wt% IF-WS_2 incorporated into nylon 12, in which the IF-WS_2 nanoparticles have not been properly dispersed in the matrix, as shown in Figure 7-6 (sample A), whilst the IF-WS_2 nanoparticles were uniformly distributed for sample displayed in Figure 7-5 (sample B). The stress-stain curves of both samples are shown in Figure 7-23, with curve (a) representing the poorly dispersed sample A and curve (b) representing the well-dispersed sample B. Though the same 2 wt% of IF-WS_2 has been added to the matrix, their toughness is significantly different, with sample B 236% higher than that of sample A, as 12.56 vs 5.33 MJ/m^3, irrespective of the ultimate tensile strength of 61.5 MPa against 57 MPa, and elongation at break of 24.7 % against 12.2%. From Figure 7-23a and c, it shows that sample A was broken during the elastic deformation before yielding, thus no necking behaviour was observed, which also accounts for the low elongation at break. Thus, the different dispersion status has a decisive influence on the toughness.

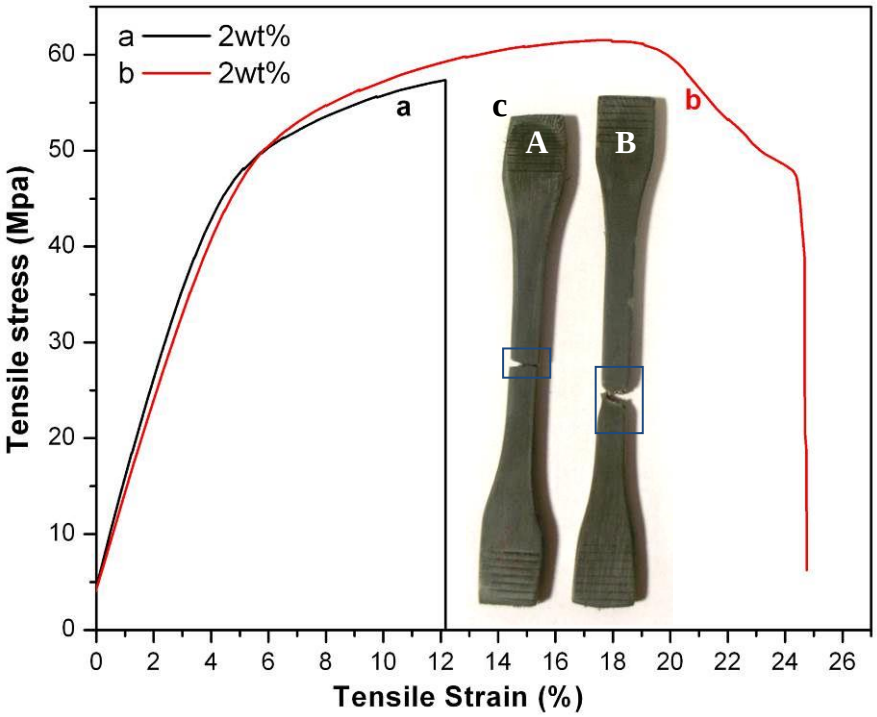

Figure 7-23 Stress–strain curves showing the tensile behaviour of nylon 12 reinforced with 2 wt% IF-WS_2 composites, with dispersion of IF-WS_2 in (b) being better than that in (a). Photos of both fractured samples are displayed in (c)

Three-point flexural test results are shown in Figure 7-24, where the bending strengths of different composites are listed in Table 7-4. Except from the 4 wt% IF-WS_2 sample, which is broken during the bending test, all other samples survived after a 22 mm deflection, exhibiting very good plastic characteristics. An increment in bending strength was clearly shown from the stress-strain curves with increased IF-WS_2 contents, from 67.2 MPa for neat nylon 12 to 85.6 MPa for the 2 wt% IF-WS_2 sample. However, a decrease is then followed, which means the system became brittle at 4 wt%, and the specimen was broken at a deflection of 13 mm, with the final bending strength of 79 MPa.

It is noteworthy that for the 4 wt% sample, a toughness value could also be worked out from the bending stress-strain curve, where a toughness modulus of 5.20 MJ/m^3 is shown, in excellent agreement with that from tensile behaviour (5.21 MJ/m^3). This shows the stable toughness performance against slow loading, a non-axial performance which is typical for particulate reinforcements. Similar comparison was not possible for other samples, as they were not broken during the bending tests, due to their good plastic performance.

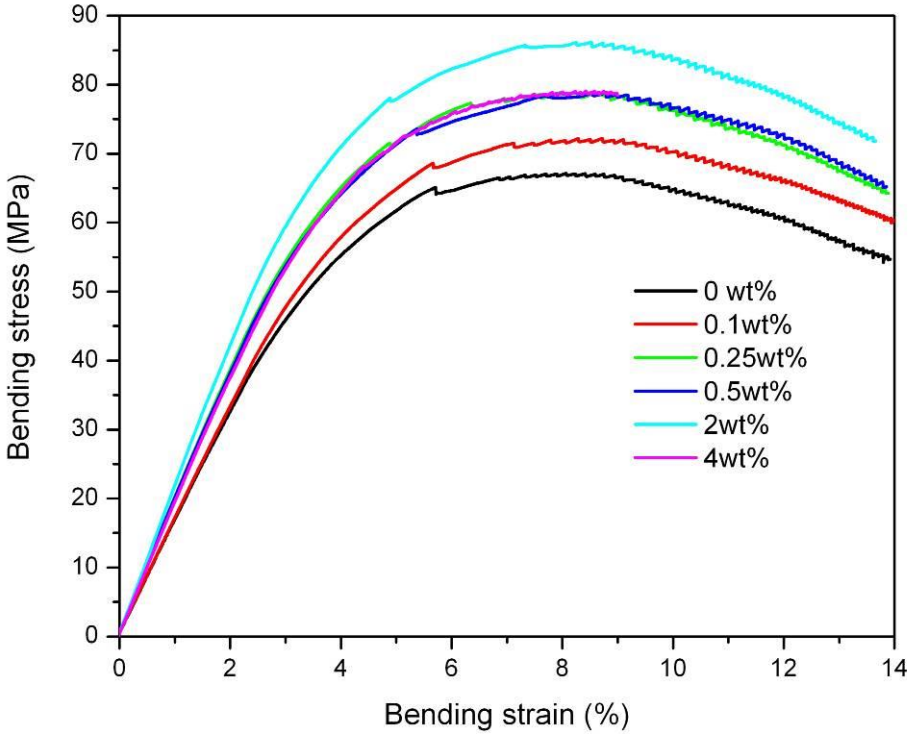

Figure 7-24 Typical bending stress–strain curves showing the flexural behaviour of composites as a function of IF-WS_2 contents

It is therefore concluded that the resulting IF-WS_2/nylon 12 composites are of high quality with regards to their mechanical properties, even the resulted neat nylon 12 has a higher tensile strength compared to other studies [235, 236], which may be due to the relatively high density, i.e. no voids as confirmed by the Micro-CT analyses (Figure 7-7).

The improvement of mechanical properties of nylon 12 reinforced with IF-WS_2 nanoparticles mainly resulted from large interfaces between the IF-WS_2 nanoparticles and the nylon 12 matrix. Under loading, the well-dispersed IF-WS_2 nanoparticles would promote the load transfer efficiency, helping to stop or delay crack propagation and leading to improved strength.

The remarkable improvement of toughness for the composites with low IF-WS_2 contents should be attributed to the high quality dispersion of IF-WS_2 nanoparticles within nylon 12 matrix, in addition to the nanoparticles themselves as an excellent shock absorber [13, 14]. However, higher percentage of IF-WS_2 in polymer would lead to agglomeration which causes local stress concentration thus resulting in lower toughness.

7.4 Conclusions

In this study, ultra-toughened nylon 12 reinforced with low volume of IF-WS_2 nanocomposites have been prepared through an efficient mixing process.

The microscopy characterisations have revealed that an excellent dispersion of IF-WS_2 nanoparticles in nylon 12 matrix was achieved, without using any surfactant. XRD analyses have confirmed that an α`-phase to a more stable γ-phase transition took place during the sintering of nylon 12, regardless the amounts of IF-WS_2 added to the matrix.

DSC data show little change on the melting temperature. The composites with lower amounts of IF-WS_2 have better thermal stability than neat polymer, whilst further increased IF-WS_2 contents decreased their thermal stability.

By incorporation of a very low IF-WS_2 content into the nylon 12 matrix, the tensile strength and bending strength have been improved by 27% and 28% respectively (2 wt%), and the toughness by 185% and 148% with 0.25 and 0.5 wt% of IF-WS_2 addition, respectively, compared to the neat polymer. The improvements of mechanical properties should be attributed to the well-dispersed nanoparticles in the polymer matrix.

Chapter 8 Conclusions and future work

8.1 Summary and conclusions

In summary, this thesis reports the synthesis of a series of tungsten related nanostructures, including tungsten oxide nanoparticles, nanowires, tungsten oxide and oxynitride nanorods, in particular the IF-WS_2 nanoparticles, by using various techniques from solvothermal to chemical vapour deposition for the oxide and nitride and rotary reaction for the sulphide. The morphologies, crystal structures of these products were characterised in detail using combined techniques. For the first time, an alternative and efficient rotary process for the large scale manufacturing of IF-WS_2 nanoparticles was designed, tested, modified and proved to be applicable to industrial application. Furthermore, a whole new class of binary phase C-WS_2 composite nanoparticles was generated, and they exhibited remarkably improved thermal stabilities. Finally, the applications of IF-WS_2 nanoparticles in reinforcing polymer matrix nanocomposites were also explored. In detail:

In Chapter 4, a completely new rotary tube furnace for nanomaterial production has been designed, machined and assembled, with all the technical requirements satisfied. The continuous feeding system and the baffled reaction tube design appear to allow this technique a true contender/alternative process for replacing the tall fluidised reactor. Further modifications and assessments confirm that this rotary furnace is capable of continuous IF-WS_2 production, and most significantly, this could be easily scaled up for industrial level production.

In Chapter 5, a number of 0D and 1D tungsten based nanomaterials has been produced through different methods. The main findings are summarised as below:

Very fine monoclinic WO_x nanoparticles within 100 nm, which make high quality precursor for IF-WS_2 synthesis, have been successfully produced by the decomposition of APT.

Ultra-fine monoclinic $W_{18}O_{49}$ nanowires have been synthesised by a solvothermal method. Nanowires with desired aspect ratios, diameters and lengths have been obtained by tuning parameters such as reaction time (2-6 h) and precursor concentrations from

0.002 to 0.004 M. With a higher precursor concentration, the resultant bundles are larger in diameter, shorter and straighter along their axis. When the reaction time is increased, the bundles become larger and longer at the beginning, while a reduction in length follows as the diameter remains unchanged. This investigation helped gain a deeper understanding of the fundamental growth of WO_x nanowires and achieve materials with desired aspect ratios.

Furthermore, our systematic research has found the morphology dependence on different solvents. Nanowires prepared from a mixed ethanol and cyclohexanol solvent possess a record high specific surface area of 275 m^2/g, nearly twice of the highest value reported so far, 152 m^2/g, for nanowires from solvent cyclohexanol alone.

Patterned WO_xN_y nanorods were generated from a WO_x nanorod precursor which was grown on a reverse-patterned W foil with Au coating, by a simple innovative and efficient W-water vapour reaction, for the first time. The size and chemical compositions of nanorods can be tailored through different reaction temperatures, time and substrate treatments. A structural evolution mechanism has been proposed to account for the interesting nanoporous structural feature of the nanorods. This research could open new routes for nanodevice construction.

Chapter 6 has demonstrated the realisation of large scale manufacture of IF-WS_2 nanoparticles, based on the built rotary system, using WO_3 precursor and H_2S reaction gas. The parameters for IF-WS_2 nanoparticles synthesis have been optimised and the quartz working tube and feeding system have been modified to further improve the productivity, reached a 50 g level of batch production. As the first alternative technique to current tall fluidised tower reaction, this technique could be more suitable for IF-WS_2 production, with high energy efficiency and low capital investment.

This thesis has further demonstrated the application of the rotary furnace for the first creation, continuously, of novel C-coated IF-WS_2 core shell structured composite nanoparticles. The C shell ranging from 2-5 nm uniformly sheathed the IF-WS_2 core, can effectively improve the thermal stability of the composites by about 70°C. This new material could find application where thermal stability is critical.

In Chapter 7, ultra-toughened composites of nylon 12 reinforced with low volume of IF-WS_2 nanocomposites have been created. The tensile strength and bending strength of

the composites have been improved by 27% and 28% respectively (2 wt%), and the toughness dramatically improved by 185% and 148% with 0.25 and 0.5 wt% of IF-WS_2 contents, respectively, compared to the neat polymer. The improvements of mechanical properties have been attributed to the well-dispersed IF-WS_2 nanoparticles in the nylon 12 matrix. Such nanocomposites could be promising for applications in structural and ballistic protections.

8.2 Recommendations for future work

Based on the results obtained, some recommendations were proposed for future work.

Ultra-thin tungsten oxide nanowires prepared from solvothermal treatment of WCl_6 in mixed cyclohexanol and ethanol solvent, possess a record surface area up to 275 m^2/g, further experiments could be carried out to validate the improved performance in sensor and electro-chromic application, for instance.

The simple innovative and efficient process for reversed pattern growth for tungsten oxide and oxynitride nanorods growth from Au-coated W foil could be extended to other nanomaterials. According to requirement in application, different patterns could be realised through Au coating preparation. Other conversions apart from nitridation, such as sulphidisation could be tried following oxide nanomaterial templates. In addition, other physical methods could also be applied to create different Au patterns, to visualise required patterned growth, such as the conventional masked sputtering etc. Furthermore, other low cost metal or metal oxides other than Au could be used for similar preventing effect for the nanorod growth.

It will be interesting to further investigate tungsten oxynitride morphology evolution, from tungsten oxide nanorods to porous tungsten oxynitride nanorods, by nitridation to nanoparticles, or by oxidation back to tungsten oxide nanorods again, to confirm the proposed evolution mechanism. For example, a simple oxidation experiment could be carried out to verify whether the nanocavities in the tungsten oxynitride nanorod would be filled by lattice expansion if the nitride were oxidised to tungsten oxide again.

The final validation of rotary furnace, with the collection system would be significant. Subsequently, this rotary furnace could be adopted for industry scale manufacturing. This innovative rotary furnace could also be used for other MX_2 (M=Mo, W; X=S, Se

etc.) IF and INT nanostructures large scale production. Furthermore, minor modification would enable this reactor effective for a wide range of gas-solid reaction, to produce various nanomaterials in large amounts, wherever agglomeration hindered the scaling up production in a static furnace.

Further studies could be focused on the synthesis of IF-WS_2 nanoparticles from reaction of APT and H_2S. A two part elements long rotary furnace with different temperature controllers should be useful, with the first part providing high temperature around 1400°C for the decomposition of APT into WO_x nanoparticles, while the second part for sulphidisation of WO_x into IF- WS_2 at around 800°C. The realisation of the proposed two parts rotary furnace is worthy for future projects, which would make the process very efficient and energy saving.

Furthermore, the CVD production of C-coated IF-WS_2 core shell structured composite nanoparticles could easily be optimised for desired thickness by tuning the parameters. Properties such as thermal, tribological, di-electrical behaviours of coated particles could be evaluated against different coating thickness, to explore potential applications for this new class of nanomaterials. Importantly, this technique could also be extended for other MX_2 type IF or INT structures such as MoS_2 ($MoSe_2$), NbS_2 ($NbSe_2$) etc., for revised performance, compared to pristine nanostructures.

The successful preparation of IF-WS_2 reinforced nylon 12 polymer nanocomposites, especially the dramatically improved toughness, inspired the motivation of using IF-WS_2 as reinforcement for other polymer matrix, particularly for structural and ballistic fibre applications.

References

1. R. Tenne, et al., *Polyhedral and cylindrical structures of tungsten disulphide.* Nature, 1992. **360**: p. 444-446.
2. L. Margulis, et al., *Nested fullerene-like structures.* Nature, 1993. **365**: p. 113-114.
3. Y. Feldman, et al., *High rate, gas phase growth of MoS_2 nested inorganic fullerenes and nanotubes.* Science, 1995. **267**: p. 222-225.
4. H. Y. Rosenfeld, et al., *Cage structures and nanotubes of $NiCl_2$.* Nature, 1998. **395**: p. 336.
5. M. Remskar, et al., *New crystal structures of WS_2: microtubes, ribbons, and ropes.* Adv. Mater., 1998. **10**(3): p. 246-249.
6. A. Rothschild, J. Sloan, and R. Tenne, *Growth of WS_2 nanotubes phases* J. Am. Chem. Soc. , 2000. **122**: p. 5169-5179.
7. L. Rapoport, et al., *Inorganic fullerene-like material as additives to lubricants: structure–function relationship.* Wear, 1999. **225-229**: p. 975-982.
8. G. Seifert, et al., *Structure and electronic properties of MoS_2 nanotubes.* Phys. Rev. Lett., 2000. **85**(1): p. 146-149.
9. R. Dominko, et al., *Dichalcogenide nanotube electrodes for Li-Ion batteries.* Adv. Mater., 2002. **14**(21): p. 1531-1534.
10. I. Kaplan-Ashiri and R. Tenne, *Mechanical properties of WS_2 nanotubes.* J. Cluster Sci., 2007. **18**(3): p. 549-563.
11. I. Kaplan-Ashiri, et al., *On the mechanical behavior of WS_2 nanotubes under axial tension and compression.* Proc. Natl. Acad. Sci., 2006. **103**(3): p. 523-528.
12. L. Rapoport, et al., *Hollow nanoparticles of WS_2 as potential solid-state lubricants.* Nature, 1997. **387**: p. 791-793.
13. Y. Q. Zhu, et al., *Shock-wave resistance of WS_2 nanotubes.* J. Am. Chem. Soc. , 2003. **125**: p. 1329-1333.
14. Y. Q. Zhu, T. Sekine, and Y. H. Li, *WS_2 and MoS_2 inorganic fullerenes- super shock absorbers at very high pressures.* Adv. Mater., 2005. **17**: p. 1500-1503.
15. Y. Q. Zhu, et al., *Shock-absorbing and failure mechanisms of WS_2 and MoS_2 nanoparticles with fullerene-like structures under shock wave pressure.* J. Am. Chem. Soc., 2005. **127**: p. 16263-16272.
16. P. J. Hogg, *Composites in Armor.* Science 2006. **314**.
17. Y. Feldman, et al., *New reactor for production of tungsten disulfide hollow onion-like (inorganic fullerene-like) nanoparticles.* Solid State Sci., 2000. **2**: p. 663-672.
18. Y. Feldman, et al., *Bulk synthesis of inorganic fullerene-like MS_2 (M=Mo, W) from the respective trioxides and the reaction mechanism.* J. Am. Chem. Soc., 1996. **118**: p. 5362-5367.
19. Y. Q. Zhu, et al., *Morphology, structure and growth of WS_2 nanotubes.* J. Mater. Chem., 2000. **10**: p. 2570-2577.
20. Y. H. Li, et al., *Novel route to WO_x nanorods and WS_2 nanotubes from WS_2 inorganic fullerenes.* J. Phys. Chem. B 2006. **110**: p. 18191-18195.

21. X. Z. Li, et al., *Photocatalytic activity of WO_x–TiO_2 under visible light irradiation.* J. Photochem. Photobiol. A, 2001. **141**: p. 209-217.
22. M. Ferroni, et al., *Microstructural characterization of a titanium–tungsten oxide gas sensor.* J. Mater. Res., 1997. **12**: p. 793-798.
23. A. Ponzoni, et al., *Nanostructured WO_3 deposited by modified thermal evaporation for gas-sensing applications.* Thin Solid Films, 2005. **490**: p. 81-85.
24. Y. M. Zhao and Y. Q. Zhu, *Room temperature ammonia sensing properties of $W_{18}O_{49}$ nanowires.* Sens. Actuators, B, 2009. **137**(1): p. 27-31.
25. Y. S. Kim, et al., *Room-temperature semiconductor gas sensor based on nonstoichiometric tungsten oxide nanorod film.* Appl. Phys. Lett., 2005. **86**(21).
26. S. H. Lee, et al., *Crystalline WO_3 nanoparticles for highly improved electrochromic applications.* Adv. Mater., 2006. **18**(6): p. 763-766.
27. P. Poizot, et al., *Nano-sized transition-metal oxides as negative-electrode materials for lithium-ion batteries.* Nature, 2000. **407**: p. 496-499.
28. O. Lev, et al., *Sol–gel materials in electrochemistry.* Chem. Mater, 1997. **9**: p. 2354-2375.
29. Y. Q. Zhu, et al., *Tungsten oxide tree-like structures.* Chem. Phys. Lett., 1999. **309**(5–6): p. 327-334.
30. G. Gu, et al., *Tungsten oxide nanowires on tungsten substrates.* Nano Lett., 2002. **2**(8): p. 849-851.
31. Y. B. Li, et al., *WO_3 nanorods/nanobelts synthesized via physical vapor deposition process.* Chem. Phys. Lett., 2003. **367**(1–2): p. 214-218.
32. H. G. Choi, Y. H. Jung, and D. K. Kim, *Solvothermal synthesis of tungsten oxide nanorod/nanowire/nanosheet.* J. Am. Ceram. Soc., 2005. **88**(6): p. 1684-1686.
33. S. B. Sun, et al., *Bundled tungsten oxide nanowires under thermal processing.* Nanotechnology, 2008. **19**(30): p. 305709 (7pp).
34. J. Polleux, et al., *Template-free synthesis and assembly of single-crystalline tungsten oxide nanowires and their gas-sensing properties.* Angew. Chem. Int. Ed., 2006. **45**(2): p. 261-265.
35. V. Chakrapani, J. Thangala, and M.K. Sunkara, *WO_3 and W_2N nanowire arrays for photoelectrochemical hydrogen production.* Int. J. Hydrogen Energy, 2009. **34**(22): p. 9050-9059.
36. J. S. Becker and R. G. Gordon, *Diffusion barrier properties of tungsten nitride films grown by atomic layer deposition from bis(tert-butylimido)bis(dimethylamido)tungsten and ammonia.* Appl. Phys. Lett., 2003. **82**(14): p. 2239-2241.
37. B. L. Park, et al., *Comparison of PECVD-WNx and CVD-TiN films for the upper electrode of Ta_2O_5 capacitors.* P. Ieee. 1998 International Interconnect Technology Conference1998. 96-98.
38. H. Tominaga and M. Nagai, *Cathode catalysts for fuel cell development: A theoretical study based on band structure calculations for tungsten nitride and cobalt tungsten nitrides.* Electrochim. Acta, 2009. **54**(26): p. 6732-6739.
39. Z. W. Yao and H. Dong, *Investigation of NO dissociation and reduction by H_2 on nanosized W_2N surface with transient-response techniques.* Appl. Surf. Sci., 2008. **255**(5, Part 1): p. 2259-2264.
40. S. Jeon, H. Kim, and K. Yong, *Deposition of tungsten oxynitride nanowires through simple evaporation and subsequent annealing.* J. Vac. Sci. Technol., B, 2009. **27**(2): p. 671-676.

41. Y. M. Zhao, et al., *Preparation and characterization of tungsten oxynitride nanowires.* J. Mater. Chem., 2007. **17**(41): p. 4436-4440.
42. N. G. Chopra, et al., *Boron nitride nanotubes.* Science, 1995. **269**: p. 966-967.
43. P. A. Parilla, et al., *The first true inorganic fullerenes?* Nature, 1999. **397**: p. 114.
44. A. Margolin, et al., *Fullerene-like WS_2 nanoparticles and nanotubes by the vapor-phase synthesis of WCl_n and H_2S.* Nanotechnology, 2008. **19**: p. 095601 (11pp).
45. X. H. Hou, C. X. Shan, and K. L. Choy, *Microstructures and tribological properties of PEEK-based nanocomposite coatings incorporating inorganic fullerene-like nanoparticles.* Surf. Coat. Technol., 2008. **202**(11): p. 2287-2291.
46. S. Brown, et al., *Bulk vs nanoscale WS_2: finite size effects and solid-state lubrication.* Nano Lett., 2007. **7**(8): p. 2365-2369.
47. G. L. Frey, et al., *Optical-absorption spectra of inorganic fullerene like MS_2 (M=Mo, W).* Phys. Rev. B, 1998. **57**(11): p. 6666-6671.
48. M. Nath, A. Govindaraj, and C. N. R. Rao, *Simple synthesis of MoS_2 and WS_2 nanotubes.* Adv. Mater., 2001. **13**: p. 283-285.
49. R. Tenne, *Advances in the synthesis of inorganic nanotubes and fullerene-like nanoparticles.* Angew. Chem. Int. Ed., 2003. **42**: p. 5124-5132.
50. M. Bar Sadan, S. G. Wolf, and L. Houben, *Bright-field electron tomography of individual inorganic fullerene-like structures.* Nanoscale, 2010. **2**(3): p. 423-428.
51. P. Ratnasamy, L. Rodrique, and A. J. Leonard, *Structural and textural studies in molybdenum sulfide systems.* J. Phys. Chem., 1973. **77**(18): p. 2242-2245.
52. J. Sloan, et al., *Defect and ordered tungsten oxides encapsulated inside 2H–WX_2 (X =S and Se) fullerene-related structures.* J. Solid State Chem., 1999. **144**: p. 100-117.
53. A. Margolin, et al., *Study of the growth mechanism of WS_2 nanotubes produced by a fluidized bed reactor.* J. Mater. Chem., 2004. **14**: p. 617-624.
54. I. Kaplan-Ashiri, et al., *Mechanical behavior of individual WS_2 nanotubes.* J. Mater. Res., 2004. **19**(2): p. 454-459.
55. O. Tevet, et al., *Nanocompression of individual multilayered polyhedral nanoparticles.* Nanotechnology, 2010. **21**(36): p. 365705 (6pp).
56. J. Tannous, et al., *Understanding the tribochemical mechanisms of IF-MoS_2 nanoparticles under boundary lubrication.* Tribol. Lett., 2011. **41**(1): p. 55-64.
57. H. Friedman, et al., *Fabrication of self-lubricating cobalt coatings on metal surfaces.* Nanotechnology, 2007. **18**(11): p. 115703, 8pp.
58. L. Rapoport, et al., *Friction and wear of fullerene-like WS_2 under severe contact conditions: friction of ceramic materials.* Tribol. Lett., 2005. **19**(2): p. 143-149.
59. O. Tevet, et al., *Friction mechanism of individual multilayered nanoparticles.* Proc. Natl. Acad. Sci. U.S.A, 2011. **108**(50): p. 19901-19906.
60. J. F. Wu, W. S. Zhai, and G. F. Jie, *Preparation and tribological properties of WS_2 nanoparticles modified by trioctylamine.* P. I. Mech. Eng. J-J-Eng., 2009. **223**(4): p. 695-703.
61. I. Lahouij, et al., *Lubrication mechanisms of hollow-core inorganic fullerene-like nanoparticles: coupling experimental and computational works.* Nanotechnology, 2012. **23**(37): p. 375701 (10pp).
62. J. Jelenc and M. Remskar, *Friction on a single MoS_2 nanotube.* Nanoscale Res. Lett., 2012. **7**(1): p. 208.
63. J. Tannous, et al., *Synthesis and tribological performance of novel $Mo_XW_{1-x}S_2$ ($0 \leqslant x \leqslant 1$) inorganic fullerenes.* Tribol. Lett., 2010. **37**(1): p. 83-92.

64. L. Rapoport, N. Fleischer, and R. Tenne, *Applications of WS_2 (MoS_2) inorganic nanotubes and fullerene-like nanoparticles for solid lubrication and for structural nanocomposites.* J. Mater. Chem., 2005. **15**: p. 1782–1788.
65. A. Katz, et al., *Self-lubricating coatings containing fullerene-like WS_2 nanoparticles for orthodontic wires and other possible medical applications.* Tribol. Lett., 2006. **21**(2): p. 135-139.
66. M. Redlich, et al., *Improved orthodontic stainless steel wires coated with inorganic fullerene-like nanoparticles of WS_2 impregnated in electroless nickel-phosphorous film.* Dent. Mater., 2008. **24**(12): p. 1640-1646.
67. G. E. Moore, *Acute inhalation toxicity study in rats – limit test,* in *Product safety laboratories*2006: Dayton, New Jersey, USA
68. L. Rapoport, et al., *Slow release of fullerene-like WS_2 nanoparticles as a superior solid lubrication mechanism in composite matrices.* Adv. Eng. Mater., 2001. **3**(1-2): p. 71-75.
69. M. Naffakh, et al., *Influence of inorganic fullerene-like WS_2 nanoparticles on the thermal behavior of isotactic polypropylene.* J. Polym. Sci., Part B: Polym. Phys., 2007. **45**(16): p. 2309-2321.
70. R. R. Sahoo and S. K. Biswas, *Microtribology and friction-induced material transfer in layered MoS_2 nanoparticles sprayed on a steel surface.* Tribol. Lett., 2010. **37**(2): p. 313-326.
71. L. Joly-Pottuz, et al., *Ultralow-friction and wear properties of IF-WS_2 under boundary lubrication.* Tribol. Lett., 2005. **18**(4): p. 477-485.
72. C. Schuffenhauer, et al., *How stable are inorganic fullerene-like particles? Thermal analysis (STA) of inorganic fullerene-like NbS_2, MoS_2, and WS_2 in oxidizing and inert atmospheres in comparison with the bulk material.* Phys. Chem. Chem. Phys., 2004. **6**(15): p. 3991-4002.
73. R. L. D. Whitby, et al., *Tungsten disulphide sheathed carbon nanotubes.* Chem. Phys. Chem., 2001. **2**(10): p. 620-623.
74. C. Dames, et al., *Low-dimensional phonon specific heat of titanium dioxide nanotubes.* Appl. Phys. Lett., 2005. **87**(3).
75. A. Rothschild, S. R. Cohen, and R. Tenne, *WS_2 nanotubes as tips in scanning probe microscopy.* Appl. Phys. Lett., 1999. **75**: p. 4025-4027.
76. P. M. Ajayan, in *Carbon Nanotubes: Preparation and Properties*, T.W. Ebbesen, Editor 1997, CRC Press, Boca Raton: Florida. p. 111.
77. C. Ballif, et al., *Preparation and characterization of highly oriented, photoconducting WS_2 thin films.* Appl. Phys. A, 1996. **62**: p. 543-546.
78. Kubota, T., et al., *Edge dispersion of supported MoS_2 and WS_2 catalysts as evaluated by using $Co(CO)_3NO$ as a probe molecule.* Appl. Catal., A, 2005. **290**: p. 17-24.
79. J. Chen, et al., *Synthesis of open-ended MoS_2 nanotubes and the application as the catalyst of methanation.* Chem. Commun., 2002(16): p. 1722-1723.
80. J. Chen, Z. L. Tao, and S. L. Li, *Lithium intercalation in open-ended TiS_2 nanotubes.* Angew. Chem. Int. Ed., 2003. **42**(19): p. 2147-2151.
81. L. Krusin-Elbaum, et al., *Room-temperature ferromagnetic nanotubes controlled by electron or hole doping.* Nature, 2004. **431**: p. 672-676.
82. S. Nordlinder, K. Edstrom, and T. Gustafsson, *The performance of vanadium oxide nanorolls as cathode material in a rechargeable lithium battery.* Electrochem. Solid-State Lett., 2001. **4**(8): p. A129-A131.

83. A. Zak, et al., *Alkali metal intercalated fullerene-like MS_2 (M= W, Mo) nanoparticles and their properties.* J. Am. Chem. Soc., 2002. **124**(17): p. 4747-4758.
84. G. Seiferta, et al., *Novel NbS_2 metallic nanotubes.* Solid State Commun., 2000. **115**: p. 635-638.
85. M. Nath, et al., *Superconducting $NbSe_2$ nanostructures.* Chem. Phys. Lett., 2003. **368**(5-6): p. 690-695.
86. C. Masarapu, L. L. Henry, and B. Q. Wei, *Specific heat of aligned multiwalled carbon nanotubes.* Nanotechnology, 2005. **16**(9): p. 1490-1494.
87. A. Zak, et al., *Growth mechanism of MoS_2 fullerene-like nanoparticles by gas-phase synthesis.* J. Am. Chem. Soc., 2000. **122**: p. 11108-11116.
88. Y. Feldman, V. Lyakhovitskaya, and R. Tenne., *Kinetics of nested inorganic fullerene-like nanoparticle formation.* J. Am. Chem. Soc., 1998. **120**(17).
89. R. Rosentsveig, et al., *WS_2 nanotube bundles and foils.* Chem. Mater., 2002. **14**(2): p. 471-474.
90. F. L. Deepak and R. Tenne, *Gas-phase synthesis of inorganic fullerene-like, structures and inorganic nanotubes.* Cent. Eur. J. Chem., 2008. **6**(3): p. 373–389.
91. N. Zink, et al., *In situ heating TEM study of onion-like WS_2 and MoS_2 nanostructures obtained via MOCVD.* Chem. Mater., 2008. **20**: p. 65-71.
92. N. Zink, et al., *Selective synthesis of hollow and filled fullerene-like (IF) WS_2 nanoparticles via metal–organic chemical vapor deposition.* Chem. Mater., 2007. **19**: p. 6391-6400.
93. X. L. Li, J. P. Ge, and Y. D. Li, *Atmospheric pressure chemical vapor deposition: An alternative route to large-scale MoS_2 and WS_2 inorganic fullerene-like nanostructures and nanoflowers.* Chem. Eur. J., 2004. **10**: p. 6163-6171.
94. Y. D. Li, et al., *Artificial lamellar mesostructures to WS_2 nanotubes.* J. Am. Chem. Soc., 2002. **124**(7): p. 1411-1416.
95. D. Vollath and D.V. Szabo, *Synthesis of nanocrystalline MoS_2 and WS_2 in a microwave plasma.* Mater. Lett., 1998. **35**: p. 236-244.
96. G. Alonso, et al., *Preparation of WS_2 catalysts by in situ decomposition of tetraalkylammonium thiotungstates.* Appl. Catal., A, 2000. **197**: p. 87-97.
97. E. B. Mackie, et al., *Production of WS_2 nanotubes by an activation method.* Adv. Mater., 2000. **12**(7): p. 495-498.
98. E. S. Vasilyeva, et al., *Synthesis of tungsten disulphide nanoparticles by the chemical vapor condensation method.* Microelectron. J. **40**(4-5): p. 687-691.
99. C. N. R. Rao and M. Nath., *Inorganic nanotubes.* Dalton Trans., 2003: p. 1-24.
100. C. N. R. Rao, et al., *Synthesis of inorganic nanomaterials.* Dalton Trans., 2007: p. 3728-3749.
101. J. G. Liu, et al., *Tuning the field-emission properties of tungsten oxide nanorods.* Small, 2005. **3**: p. 310-313.
102. C. Martin, et al., *Nb_2O_5-supported WO_3: a comparative study with WO_3/Al_2O_3.* Catal. Today, 2003. **78**: p. 365-376.
103. L. Reyes, et al., *Gas sensor response of pure and activated WO_3 nanoparticle films made by advanced reactive gas deposition.* Sens. Actuators, B, 2006. **117**(1): p. 128-134.
104. C. Bittencourt, et al., *WO_3 films modified with functionalised multi-wall carbon nanotubes: Morphological, compositional and gas response studies.* Sens. Actuators, B, 2006. **115**(1): p. 33-41.

105. A. C. Dillon, et al., *Metal oxide nano-particles for improved electrochromic and lithium-ion battery technologies.* Thin Solid Films, 2008. **516**(5): p. 794-797.
106. H. Y. Jheong, et al., *Electrochromic property of the viologen-anchored mesoporous TiO_2 films.* J. Electroceram., 2006. **17**(2-4): p. 929-932.
107. R. Tenne, et al., *Reactors for producing inorganic fullerene-like tungsten disulfide hollow nanoparticles and nanotubes* April, 2009, Yeda Research and Development Co., Ltd. (Rehovot, IL) United States
108. IsraCast, *Protecting the soldiers of tomorrow,* 2006.
109. T. Polcar, M. Evaristo, and A. Cavaleiro, *Self-lubricating W-S-C nanocomposite coatings.* Plasma Processes Polym., 2009. **6**(6-7): p. 417-424.
110. T. Hubert, H. Hattermann, and M. Griepentrog, *Sol-gel-derived nanocomposite coatings filled with inorganic fullerene-like WS_2.* J. Sol-Gel Sci. Technol., 2009. **51**(3): p. 295-300.
111. D. B. Mohan and A. Cavaleiro, *Experimental development and deposition of nanocomposite films by a hybrid dc magnetron sputtering and cluster gun technique.* Vacuum, 2009. **83**(10): p. 1257-1261.
112. C. Velasco-Santos, et al., *Chemical functionalization of carbon nanotubes through an organosilane.* Nanotechnology, 2002. **13**(4): p. 495-498.
113. M. S. P. Shaffer and A. H. Windle, *Fabrication and characterization of carbon nanotube/poly(vinyl alcohol) composites.* Adv. Mater., 1999. **11**(11): p. 937-+.
114. C. Stéphan, et al., *Characterization of singlewalled carbon nanotubes-PMMA composites.* Synth. Met., 2000. **108**(2): p. 139-149.
115. Z. X. Jin, et al., *Poly(vinylidene fluoride)-assisted melt-blending of multi-walled carbon nanotube/poly(methyl methacrylate) composites.* Mater. Res. Bull., 2002. **37**(2): p. 271-278.
116. Z. X. Jin, et al., *Dynamic mechanical behavior of melt-processed multi-walled carbon nanotube/poly(methyl methacrylate) composites.* Chem. Phys. Lett., 2001. **337**(1–3): p. 43-47.
117. R. Andrews, et al., *Fabrication of carbon multiwall nanotube/polymer composites by shear mixing.* Macromol. Mater. Eng., 2002. **287**(6): p. 395-403.
118. C. Shahar, et al., *Surface functionalization of WS_2 fullerene-like nanoparticles.* Langmuir, 2010. **26**(6): p. 4409-4414.
119. M. N. Tahir, et al., *Overcoming the insolubility of molybdenum disulfide nanoparticles through a high degree of sidewall functionalization using polymeric chelating ligands.* Angew. Chem. Int. Ed., 2006. **45**(29): p. 4809-4815.
120. J. N. Coleman, et al., *Two-dimensional nanosheets produced by liquid exfoliation of layered materials.* Science, 2011. **331**(6017): p. 568-571.
121. J. N. Coleman, *Liquid-phase exfoliation of nanotubes and graphene.* Adv. Funct. Mater., 2009. **19**(23): p. 3680-3695.
122. J. H. Hildebrand and R. L. Scott, eds. *The Solubility of Non-Electrolytes*. 3rd ed. 1950, Reinhold: New york.
123. Z. Z. Wu, et al., *Novel hexagonal MoS_2 nanoplates formed by solid-state assembly of nanosheets.* J. Cryst. Growth, 2010. **312**(12-13): p. 1973-1976.
124. L. Rapoport, et al., *Polymer nanocomposites with fullerene-like solid lubricant.* Adv. Eng. Mater., 2004. **6**(1-2): p. 44-48.
125. M. Shneider, et al., *The effect of tungsten sulfide fullerene-like nanoparticles on the toughness of epoxy adhesives.* J. Adhes. Sci. Technol., 2010. **24**(6): p. 1083-1095.

126. E. Zohar, et al., *The mechanical and tribological properties of epoxy nanocomposites with WS_2 nanotubes.* Sens. Transducers J., 2011. **21**(Special I ssue): p. 12.
127. M. Naffakh, et al., *Isothermal crystallization kinetics of isotactic polypropylene with inorganic fullerene-like WS_2 nanoparticles.* Thermochim. Acta, 2008. **472**(1-2): p. 11-16.
128. M. Naffakh, et al., *Use of inorganic fullerene-like WS_2 to produce new high-performance polyphenylene sulfide nanocomposites: Role of the nanoparticle concentration.* J. Phys. Chem. B, 2009. **113**(30): p. 10104-10111.
129. M. Naffakh, et al., *Unique nucleation activity of inorganic fullerene-like WS_2 Nanoparticles in polyphenylene sulfide nanocomposites: isokinetic and isoconversional study of dynamic crystallization kinetics.* J. Phys. Chem. B, 2009. **113**(20): p. 7107-7115.
130. M. Naffakh, et al., *Novel melt-processable poly(ether ether ketone)(PEEK)/inorganic fullerene-like WS_2 nanoparticles for critical applications.* J. Phys. Chem. B, 2010. **114**(35): p. 11444-11453.
131. M. Naffakh, A. M. Diez-Pascual, and M. A. Gomez-Fatou, *New hybrid nanocomposites containing carbon nanotubes, inorganic fullerene-like WS2 nanoparticles and poly(ether ether ketone) (PEEK).* J. Mater. Chem., 2011. **21**(20): p. 7425-7433.
132. M. Naffakh, et al., *Novel melt-processable nylon-6/inorganic fullerene-like WS_2 nanocomposites: Complex isothermal crystallization kinetics and melting behaviour.* Mater. Chem. Phys., 2011. **128**(1–2): p. 265-273.
133. M. Naffakh, et al., *Novel melt-processable nylon-6/inorganic fullerene-like WS2 nanocomposites for critical applications.* Mater. Chem. Phys., 2011. **129**(1-2): p. 641-648.
134. W. Zhang, et al., *Use of functionalized WS_2 nanotubes to produce new polystyrene/polymethylmethacrylate nanocomposites.* Polymer, 2003. **44**(7): p. 2109-2115.
135. C. S. Reddy, A. Zak, and E. Zussman, *WS_2 nanotubes embedded in PMMA nanofibers as energy absorptive material.* J. Mater. Chem., 2011. **21**(40): p. 16086-16093.
136. M. Bashouti, et al., *Alignment of colloidal CdS nanowires embedded in polymer nanofibers by electrospinning.* ChemPhysChem, 2006. **7**(1): p. 102-106.
137. A. Fahmi, T. Pietsch, and N. Gindy, *Hierarchical nanoporous structures by self-assembled hybrid materials based on block copolymers.* Macromol. Rapid Commun., 2007. **28**(24): p. 2300-2305.
138. C. Hammond, ed. *Introduction to Crystallography*. Microscopy Handbooks1990, Royal Microscopical Society, Oxford University Press, USA.
139. I. M. Watt, ed. *The Principles and Practice of Electron Microscopy*. 2nd ed. 1997, Cambridge University Press: Cambridge.
140. J. R. Ferraro and K. Nakamoto, eds. *Introductory Raman Spectroscopy*. 1994, Academic Press: Boston.
141. S. J. Rothenberg, et al., *Determination of specific surface-area by krypton adsorption, comparison of 3 different methods of determing surface-area, and evaluation of different specific surface-area standards* J. Colloid Interface Sci., 1987. **116**(2): p. 541-554.

142. E. P. Barrett, L. G. Joyner, and P. P. Halenda, *The determination of pore volume and area distributions in porous substance. 1. computations from nitrogen isotherms.* J. Am. Chem. Soc., 1951. **73**(1): p. 373-380.
143. International Organization Standardization, *ISO 178*, in *Plastic test standard: Plastics – determination of flexural properties* 2003.
144. W. Klose and A. Schinkel, *Energy and mass transport processes in the granular bed of an indirectly heated rotary kiln.* China Particuology, 2004. **2**(3): p. 107-112.
145. H. Henein, J. Brimacombe, and A. Watkinson, *Experimental study of transverse bed motion in rotary kilns.* Metall. Mater. Trans. B, 1983. **14**(2): p. 191-205.
146. J. Mellmann, *The transverse motion of solids in rotating cylinders-forms of motion and transition behavior.* Powder Technol., 2001. **118**(3): p. 251-270.
147. J. L. Pinilla, et al., *A novel rotary reactor configuration for simultaneous production of hydrogen and carbon nanofibers.* Int. J. Hydrogen Energy, 2009. **34**(19): p. 8016-8022.
148. S. L. Pirard, et al., *Motion of carbon nanotubes in a rotating drum: The dynamic angle of repose and a bed behavior diagram.* Chem. Eng. J., 2009. **146**(1): p. 143-147.
149. W. M. Yeoh, et al., *Production of carbon nanotubes from chemical vapor deposition of methane in a continuous rotary reactor system.* Chem. Eng. Commun., 2012. **199**(5): p. 600-607.
150. S. L. Pirard, J. P. Pirard, and C. Bossuot, *Modeling of a continuous rotary reactor for carbon nanotube synthesis by catalytic chemical vapor deposition.* AlChE J., 2009. **55**(3): p. 675-686.
151. J. L. Pinilla, et al., *Production of hydrogen and carbon nanofibers by thermal decomposition of methane using metal catalysts in a fluidized bed reactor.* Int. J. Hydrogen Energy, 2007. **32**(18): p. 4821-4829.
152. M. Pérez-Cabero, I. Rodríguez-Ramos, and A. Guerrero-Ruíz, *Characterization of carbon nanotubes and carbon nanofibers prepared by catalytic decomposition of acetylene in a fluidized bed reactor.* J. Catal., 2003. **215**(2): p. 305-316.
153. G. J. Finnie, et al., *Longitudinal and transverse mixing in rotary kilns: A discrete element method approach.* Chem. Eng. Sci., 2005. **60**(15): p. 4083-4091.
154. N. Gui, J. R. Fan, and K. F. Cen, *A macroscopic and microscopic study of particle mixing in a rotating tumbler.* Chem. Eng. Sci., 2010. **65**(10): p. 3034-3041.
155. R. Rutgers, *Longitudinal mixing of granular material flowing through a rotating cylinder—: Part I. Descriptive and theoretical.* Chem. Eng. Sci., 1965. **20**(12): p. 1079-1087.
156. A. A. Boateng, *Rotary kiln transport phenomena: a study of the bed motion and heat transfer*, in *Department of Metals and Materials Engineering*1993, The university of British Columbia.
157. X. Y. Liu, E. Specht, and J. Mellmann, *Slumping–rolling transition of granular solids in rotary kilns.* Chem. Eng. Sci., 2005. **60**(13): p. 3629-3636.
158. D. Kurfe, H. Hinrichsen, and I. Zimmermann, *Statistical model of the powder flow regulation by nanomaterials.* Powder Technol., 2005. **159**(2): p. 63-70.
159. W. D. Owens, et al., *Thermal analysis of rotary kiln incineration: Comparison of theory and experiment.* Combust. Flame, 1991. **86**(1-2): p. 101-114.

160. C. S. Campbell, *Granular material flows - An overview.* Powder Technol., 2006. **162**(3): p. 208-229.
161. A. Z. M. A. Abouzeid, et al., *The influence of operating variables on the residence time distribution for material transport in a continuous rotary drum.* Powder Technol., 1974. **10**(6): p. 273-288.
162. J. J. Dai, H. P. Cui, and J. R. Grace, *Biomass feeding for thermochemical reactors.* Prog. Energy Combust. Sci., 2012. **38**(5): p. 716-736.
163. D. H. Wilson and D. L. Dunnington, *Plan ahead to avoid feeding problems.* Chem. Eng.-New York, 1991. **98**(8): p. 72-81.
164. X. H. Hao, et al., *Hydrogen production from glucose used as a model compound of biomass gasified in supercritical water.* Int. J. Hydrogen Energy, 2003. **28**(1): p. 55-64.
165. E. Couteau, et al., *CVD synthesis of high-purity multiwalled carbon nanotubes using $CaCO_3$ catalyst support for large-scale production.* Chem. Phys. Lett., 2003. **378**(1–2): p. 9-17.
166. Y. M. Sun, et al., *Ultra thin tungsten nitride film growth on dielectric surfaces.* Thin Solid Films, 2004. **458**(1–2): p. 251-256.
167. Z. Liu, Y. Bando, and C. Tang, *Synthesis of tungsten oxide nanowires.* Chem. Phys. Lett., 2003. **372**: p. 179-182.
168. D. Z. Guo, et al., *Synthesis and characterization of tungsten oxide nanorods.* J. Mater. Res., 2004. **19**(12): p. 2665-3670.
169. M. J. Hudson, J. W. Peckett, and P. J. F. Harris, *A new and effective synthesis of non-stoichiometric metal oxides such as oxygen-deficient $WO_{2.72}$.* J. Mater. Chem., 2003. **13**: p. 445–446.
170. J. Pfeifer, et al., *Growth and morphology of $W_{18}0_{49}$ crystals produced by microwave decomposition of ammonium paratungstate* J. Cryst. Growth, 1996. **169**: p. 727-733.
171. J. Moon, et al., *Particle-shape control and formation mechanisms of hydrothermally derived lead titanate.* J. Mater. Res., 1999. **14**(3): p. 866-875.
172. F. R. Sale, *Heat capacities of the tungsten oxides WO_3, $W_{20}O_{58}$, $W_{18}O_{49}$ and WO_2.* Thermochim. Acta, 1979. **30**(1-2): p. 163-171.
173. S. Brunauer, P.H. Emmett, and E. Teller, *Adsorption of gases in multimolecular layers.* J. Am. Chem. Soc., 1938. **60**: p. 309-319.
174. L. G. STeoh, et al., *Sensitivity properties of a novel NO_2 gas sensor based on mesoporous WO_3 thin film.* Sens. Actuators, B, 2003. **96**(1-2): p. 219-225.
175. P. D. Yang, et al., *Generalized syntheses of large-pore mesoporous metal oxides with semicrystalline frameworks.* Nature, 1998. **396**(6707): p. 152-155.
176. Y. M. Zhao, *Production and properties of inorganic nanotubes / nanowires* 2008, University of Nottingham.
177. B. Pietruszka, et al., *High-efficiency WO_3/carbon nanotubes for olefin skeletal isomerization.* Catal. Today, 2005. **102**: p. 94-100.
178. Z. X. Lu, S. M. Kanan, and C. P. Tripp, *Synthesis of high surface area monoclinic WO_3 particles using organic ligands and emulsion based methods.* J. Mater. Chem., 2002. **12**(4): p. 983-989.
179. A. Fahmi, et al., *Functional hybrid materials.* Mater. Today, 2009. **12**(5): p. 44-50.
180. G. L. Frey, et al., *Investigations of nonstoichiometric tungsten oxide nanoparticles.* J. Solid State Chem., 2001. **162**(2): p. 300-314.

181. F. D. Hardcastle and I. E. Wachs, *Determination of the molecular structures of tungstates by Raman spectroscopy.* J Raman Spectrosc., 1995. **26**(6): p. 397-405.
182. M. F. Daniel, et al., *Infrared and Raman study of WO_3 tungsten trioxides and WO_3, xH_2O tungsten trioxide tydrates.* J. Solid State Chem., 1987. **67**(2): p. 235-247.
183. M. Boulova, et al., *High-pressure Raman study of microcrystalline WO_3 tungsten oxide.* J. Phys. Condens. Matter, 2002. **14**(23): p. 5849.
184. J. F. Marco, et al., *Chemical stability of TiN, TiAlN and AlN layers in aggressive SO_2 environments.* Surf. Interface Anal., 2005. **37**(12): p. 1082-1091.
185. C. P. Constable, J. Yarwood, and W.D. Münz, *Raman microscopic studies of PVD hard coatings.* Surf. Coat. Technol., 1999. **116–119**(0): p. 155-159.
186. Y. G. Shen, et al., *Structural properties and nitrogen-loss characteristics in sputtered tungsten nitride films.* Thin Solid Films, 2000. **372**(1–2): p. 257-264.
187. C. L. Dezelah, et al., *A low valent metalorganic precursor for the growth of tungsten nitride thin films by atomic layer deposition.* J. Mater. Chem., 2007. **17**(11): p. 1109-1116.
188. Y. Z. Tsai and J. G. Duh, *Tribological behavior of CrN/WN multilayer coatings grown by ion-beam assisted deposition.* Surf. Coat. Technol., 2006. **201**(7): p. 4266-4272.
189. C. L. Dezelah IV, et al., *Preparation and characterization of molybdenum and tungsten nitride nanoparticles obtained by thermolysis of molecular precursors.* J. Mater. Chem., 2004. **14**(21): p. 3167-3176.
190. Y. Ma, et al., *X-ray diffraction study of nanocrystalline tungsten nitride and tungsten to 31 GPa.* J. Appl. Phys., 2007. **102**(1).
191. P. Bai, W. Xing, and Z. Yan, *Synthesis and characterization of mesostructured tungsten nitride by using tungstic acid as the precursor.* J. Porous Mater., 2006. **13**(2): p. 173-180.
192. Y. G. Shen and Y. W. Mai, *Reactively sputtered WO_xN_y films.* J. Mater. Res., 2000. **15**(11): p. 2437-2445.
193. F. R. de Boer, et al., eds. *Cohesion of Metals*. 1988: Amsterdam: North Holland.
194. D. L. Chen, et al., *Novel pseudo-morphotactic synthesis and characterization of tungsten nitride nanoplates.* J. Solid State Chem., 2011. **184**(2): p. 455-462.
195. D. R. Lide, ed. *CRC Handbook of Chemistry and Physics*. 1990, CRC Press: Boca Raton.
196. A. R. Ko, et al., *Template-free synthesis and characterization of mesoporous tungsten nitride nanoplates.* Phys. Chem. Chem. Phys., 2011. **13**(28): p. 12705-12707.
197. M. Alaei, A. Rashidi, and A. Mahjoub, *Two suitable methods for the preparation of inorganic fullerene-like (IF) WS_2 nanoparticles.* Iran. J. Chem. Chem. Eng., 2009. **28**(2): p. 91-98.
198. I. Wiesel, et al., *Synthesis of WS_2 and MoS_2 fullerene-like nanoparticles from solid precursors.* Nano Res., 2009. **2**(5): p. 416-424.
199. A. Zak, et al., *Scaling up of the WS_2 nanotubes synthesis.* Fullerenes Nanotubes Carbon Nanostruct., 2011. **19**(1-2): p. 18-26.
200. A. Zak, et al., *Insight into the growth mechanism of WS_2 nanotubes in the scaled-up fluidized-bed reactor.* Nano, 2009. **4**(2): p. 91-98.
201. D. Tonti, et al., *Preparation and photoelectrochemistry of semiconducting WS_2 thin films.* J. Phys. Chem. B, 1997. **101**(14): p. 2485-2490.

202. L. Joly-Pottuz and M. Iwaki, *Superlubricity of Tungsten Disulfide Coatings in Ultra High Vacuum*, in *Superlubricity*, E. Ali and M. Jean-Michel, Editors. 2007, Elsevier Science B.V.: Amsterdam. p. 227-236.
203. R. L. D. Whitby, et al., *WS_2 nanotubes containing single-walled carbon nanotube bundles.* Appl. Phys. Lett., 2001. **79**(27): p. 4574-4576.
204. R. L. D. Whitby, et al., *Tungsten disulphide coated multi-walled carbon nanotubes.* Chem. Phys. Lett., 2002. **359**(1-2): p. 121-126.
205. W. K. Hsu, et al., *$W_xMo_yC_zS_2$ nanotubes.* Carbon, 2001. **39**(7): p. 1107-1111.
206. W. K. Hsu, et al., *C-MoS_2 and C-WS_2 nanocomposites.* Appl. Phys. Lett., 2000. **77**(25): p. 4130-4132.
207. X. F. Zhang, et al., *Carbon nanotube-MoS_2 composites as solid lubricants.* ACS Appl. Mater. Interfaces, 2009. **1**(3): p. 735-739.
208. V. Stolojan, et al., *Dielectric properties of WS2-coated multiwalled carbon nanotubes studied by energy-loss spectroscopic profiling.* Appl. Phys. Lett., 2005. **86**(6).
209. Y. Z. Jin, et al., *Large-scale synthesis and characterization of carbon spheres prepared by direct pyrolysis of hydrocarbons.* Carbon, 2005. **43**(9): p. 1944-1953.
210. G. L. Frey, et al., *Optical properties of MS_2 (M = Mo, W) inorganic fullerenelike and nanotube material optical absorption and resonance Raman measurements.* J. Mater. Res., 1998. **13**(09): p. 2412-2417.
211. J. S. Zabinski, M. S. Donley, and S. V. Prasad, *Sythesis and characterization of tungsten disulfide films grown by pulsed-laser deposition.* J. Mater. Sci., 1994. **29**(18): p. 4834-4839.
212. S. Costa, et al., *Characterization of carbon nanotubes by Raman spectroscopy.* Mater. Sci.-Poland, 2008. **26**(2): p. 433-441.
213. K. Nakamura, M. Fujitsuka, and M. Kitajima, *Disorder-induced line broadening in first-order Raman scattering from graphite.* Phys. Rev. B, 1990. **41**(17): p. 12260-12263.
214. A. C. Ferrari, *Raman spectroscopy of graphene and graphite: Disorder, electron-phonon coupling, doping and nonadiabatic effects.* Solid State Commun., 2007. **143**(1-2): p. 47-57.
215. S. Reich and C. Thomsen, *Raman spectroscopy of graphite.* Phil. Trans. R. Soc. A, 2004. **362**(1824): p. 2271-2288.
216. E. D. Obraztsova, et al., *Raman identification of onion-like carbon.* Carbon, 1998. **36**(5–6): p. 821-826.
217. D. Roy, et al., *Characterisation of carbon nano-onions using Raman spectroscopy.* Chem. Phys. Lett., 2003. **373**(1–2): p. 52-56.
218. D. Shah, et al., *Effect of nanoparticle mobility on toughness of polymer nanocomposites.* Adv. Mater., 2005. **17**(5): p. 525-528.
219. B. Q. Chen and J. R. G. Evans, *Impact strength of polymer-clay nanocomposites.* Soft Matter, 2009. **5**(19): p. 3572-3584.
220. B. X. Yang, et al., *Mechanical reinforcement of polyethylene using polyethylene-grafted multiwalled carbon nanotubes.* Adv. Funct. Mater., 2007. **17**(13): p. 2062-2069.
221. Y. S. Thio, et al., *Toughening of isotactic polypropylene with $CaCO_3$ particles.* Polymer, 2002. **43**(13): p. 3661-3674.
222. A. S. Argon and R.E. Cohen, *Toughenability of polymers.* Polymer, 2003. **44**(19): p. 6013-6032.

223. Z. Bartczak, et al., *Toughness mechanism in semi-crystalline polymer blends: II. High-density polyethylene toughened with calcium carbonate filler particles.* Polymer, 1999. **40**(9): p. 2347-2365.
224. R. Rafiq, et al., *Increasing the toughness of nylon 12 by the incorporation of functionalized graphene.* Carbon, 2010. **48**(15): p. 4309-4314.
225. C. Ramesh, *Crystalline transitions in nylon 12.* Macromolecules, 1999. **32**(17): p. 5704-5706.
226. K. Inoue and S. Hoshino, *Crystal structure of nylon 12.* J. Polym. Sci., Part B: Polym. Phys., 1973. **11**(6): p. 1077-1089.
227. S. Rhee and J. L. White, *Crystal structure and morphology of biaxially oriented polyamide 12 films.* J. Polym. Sci., Part B: Polym. Phys., 2002. **40**(12): p. 1189-1200.
228. C. Z. Yan, et al., *An organically modified montmorillonite/nylon-12 composite powder for selective laser sintering.* Rapid Prototyping Journal, 2011. **17**(1): p. 28-36.
229. H. Sato, et al., *Molecular structure, crystallinity, and morphology of uncompatibilized and compatibilized blends of polyethylene/nylon 12.* Macromol. Chem. Phys., 2003. **204**(10): p. 1351-1358.
230. P. J. Hendra, et al., *The application of Fourier transform Raman spectroscopy to the identification and characterization of polyamides: I. Single number nylons.* Spectrochim. Acta, Part A, 1990. **46**(5): p. 747-756.
231. J. S. Stephens, D. B. Chase, and J. F. Rabolt, *Effect of the electrospinning process on polymer crystallization chain conformation in nylon-6 and nylon-12.* Macromolecules, 2004. **37**(3): p. 877-881.
232. H. Baranska, A. Labudzinska, and J. Terpinski, eds. *Laser Raman Spectrometry-Analytical Applications*. ed. Ellis Horwood1987: Chichester, UK.
233. W. F. Maddams and I. A. M. Royaud, *The application of Fourier transform Raman spectroscopy to the identification and characterisation of polyamides I. Double-number nylons.* Spectrochim. Acta, Part A, 1991. **47**(9-10): p. 1327-1333.
234. C. Menchaca, et al., *In situ high-temperature Raman study of crystalline nylon 6,12 fibers gamma-irradiated in argon atmosphere*. J. Phys. Chem. Solids, 2006. **67**(9–10): p. 2111-2118.
235. N. Aït Hocine, P. Médéric, and T. Aubry, *Mechanical properties of polyamide-12 layered silicate nanocomposites and their relations with structure.* Polym. Test., 2008. **27**(3): p. 330-339.
236. I. Y. Phang, et al., *Morphology, thermal and mechanical properties of nylon 12/organoclay nanocomposites prepared by melt compounding*. Polym. Int., 2005. **54**(2): p. 456-464.

Appendix

Appendix A: drawings for the shaft of seal system

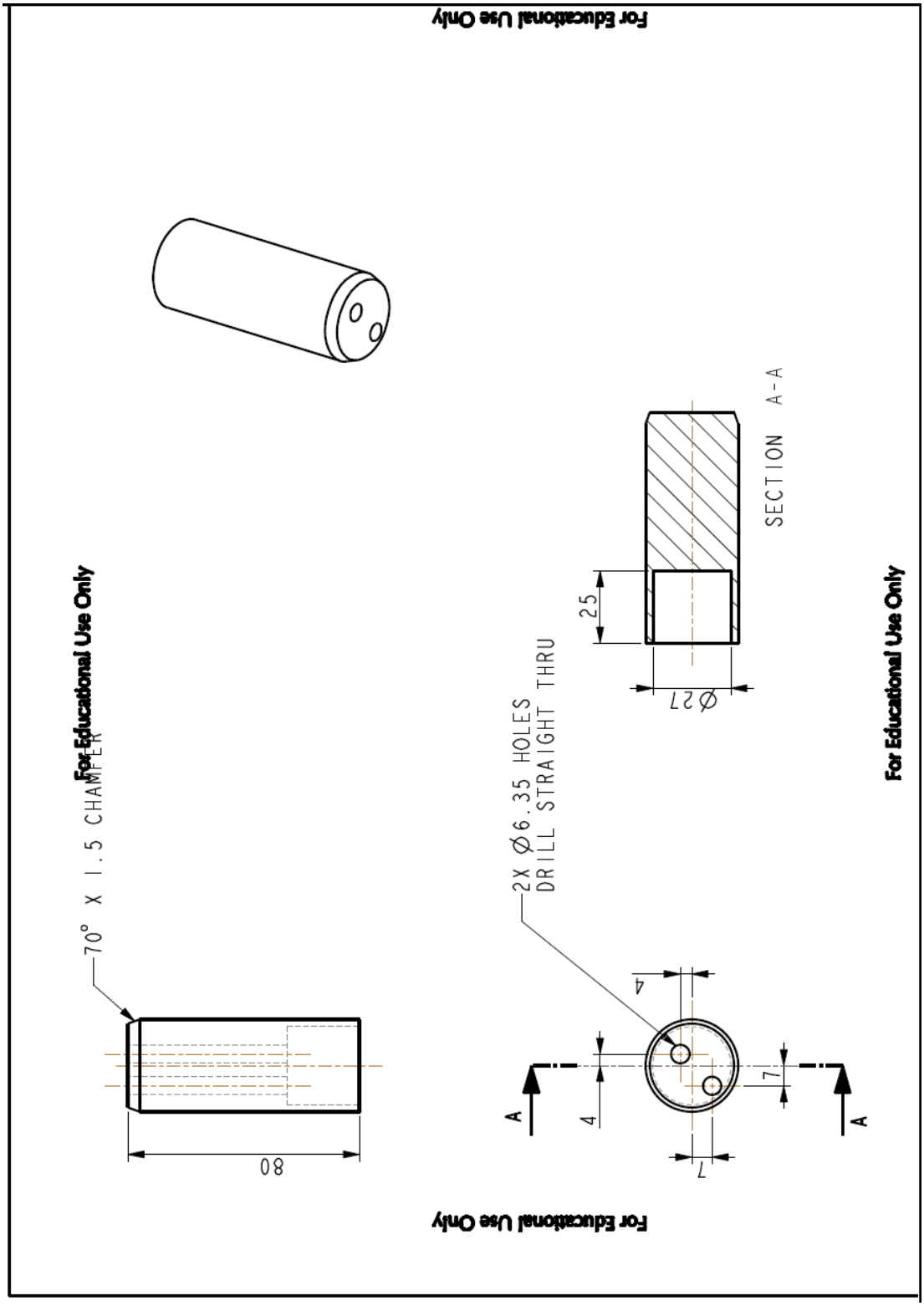

Appendix B: drawings for the housing of the seal system

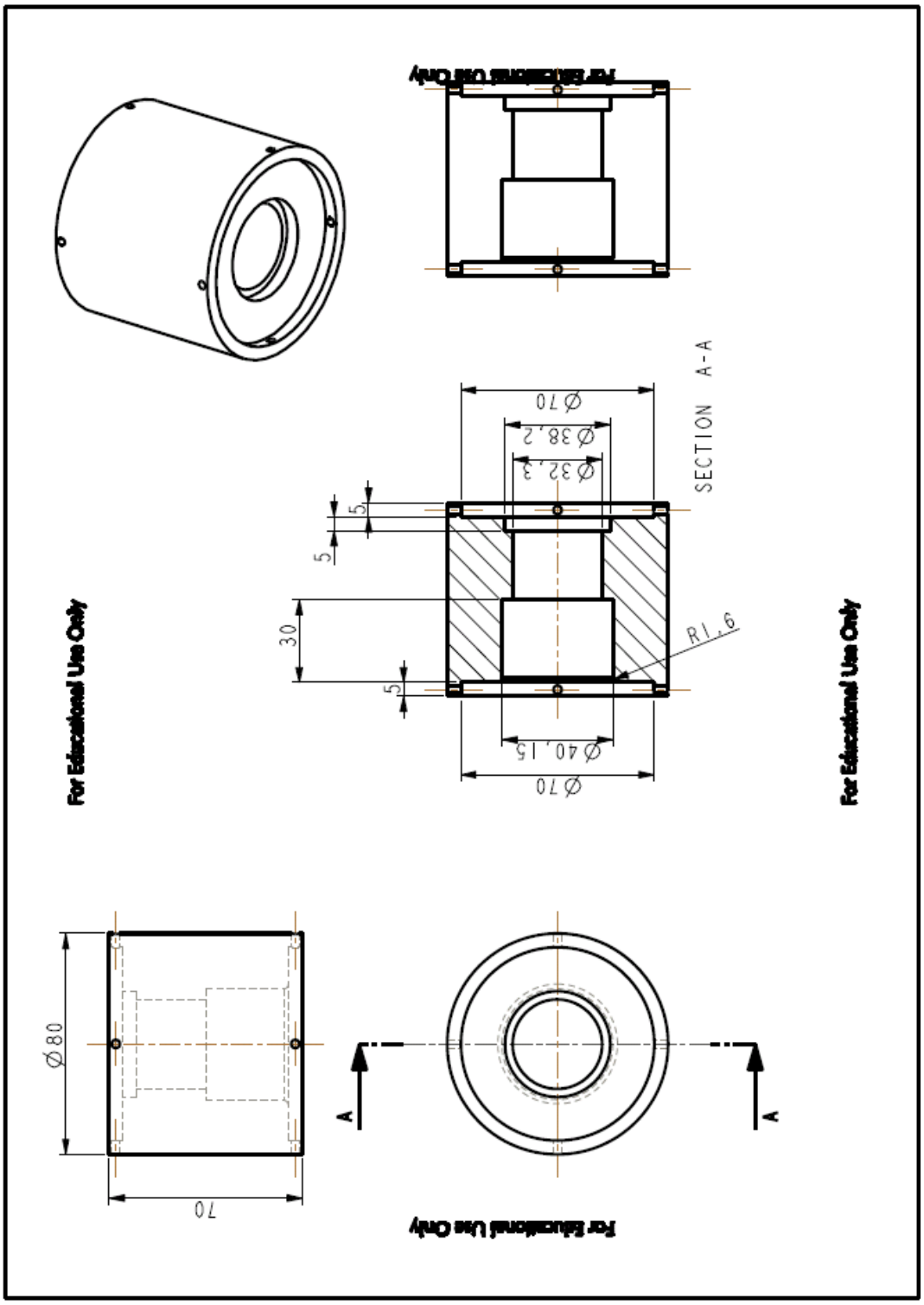

Appendix C: JCPDS card for $W_{0.62}(N_{0.62}O_{0.38})$

Pattern: PDF 01-089-4762 Radiation: 1.54060 Quality: Indexed

Formula	W0.62 (N0.62 O0.38)
Name	Tungsten Nitride Oxide
Name (mineral)	
Name (common)	

Lattice:	Cubic	**Mol. weight =**	128.75		
S.G.:	Fm-3m (225)	**Volume [CD] =**	70.86		
		Dx =	12.07		
		Dm =			
		I/Icor =	9.060		
a =	4.13800	**alpha =**			
b =		**beta =**			
c =		**gamma =**			
a/b =	1.00000	**Z =**	4		
c/b =	1.00000				

ANX: NO2
Analysis: N0.62 O0.38 W0.62
Formula from original source: W0.62 (N0.62 O0.38)
ICSD Collection Code: 76013
Minor Warning: No R factors reported/abstracted
Wyckoff Sequence: b a(FM3-M)
Unit Cell Data Source: Powder Diffraction

Structure
Publication: Acta Metall.
Detail: volume 2, page 675 (1954)
Authors: Kiessling, R., Peterson, L.
Primary Reference
Publication: Calculated from ICSD using POWD-12++

Radiation:	CuKα1	**Filter:**	Not specified
Wavelength:	1.54060	**d-spacing:**	
SS/FOM:	999.9 (0.0002,9)		

d	2θ	I	h	k	l
2.38908	37.619	999	1	1	1
2.06900	43.716	794	2	0	0
1.46300	63.541	404	2	2	0
1.24765	76.253	268	3	1	1
1.19454	80.309	110	2	2	2
1.03450	96.251	45	4	0	0
0.94932	108.470	94	3	3	1
0.92528	112.713	125	4	2	0
0.84467	131.555	104	4	2	2

Appendix D: JCPDS card for monoclinic WO_3

Pattern: PDF 00-043-1035 Radiation: 1.54060 Quality: Calculated

Formula	W O3
Name	Tungsten Oxide
Name (mineral)	
Name (common)	α-W O3

Lattice:	Monoclinic	**Mol. weight =**	231.85
S.G.:	P21/n (14)	**Volume [CD] =**	422.88
		Dx =	
		Dm =	
		I/Icor =	5.040

a =	7.29700	**alpha =**	
b =	7.53900	**beta =**	90.910
c =	7.68800	**gamma =**	
a/b =	0.96790	**Z =**	8
c/b =	1.01976		

Additional Patterns: To replace 00-024-0747
General Comments: Calculation of diffractometer peak intensities done with MICRO-POWD v. 2.2 (D. Smith and K. Smith) using default instrument broadening function (NBS Table), diffracted beam monochromator polarization correction, and atomic scattering factors corrected for anomalous dispersion. Cell parameters from Loopstra, B., Acta Crystallogr., 21 158 (1966)
Atomic positions from same source: W(1) in 4e with x=0.254, y=0.037, z=0.282; W(2) in 4e with x=0.250, y=0.023, z=0.784; O(1) in 4e with x=0.005, y=0.042, z=0.211; O(2) in 4e with x=0.993, y=0.474, z=0.218; O(3) in 4e with x=0.288, y=0.262, z=0.286; O(4) in 4e with x=0.211, y=0.259, z=0.730; O(5) in 4e with x=0.292, y=0.043, z=0.008; O(6) in 4e with x=0.279, y=0.487, z=0.993. Isotropic thermal parameters estimated as B=1.0 for each atom. Intensity threshold for <1=0.1%

Primary Reference
Publication: ICDD Grant-in-Aid
Authors: Grier, D., McCarthy, G., North Dakota State University, Fargo, North Dakota, USA.

Radiation:	CuKα1	**Filter:**	M
Wavelength:	1.54060	**d-spacing:**	
SS/FOM:	111.7 (0.006,45)		

d	2θ	I	h	k	l
5.24300	16.897	1	1	1	0
4.30900	20.596	1	1	1	1
3.84400	23.120	100	0	0	2
3.76900	23.586	97	0	2	0
3.64800	24.380	99	2	0	0
3.42400	26.002	1	0	1	2
3.38400	26.315	1	0	2	1
3.34900	26.595	19	1	2	0
3.11700	28.615	16	-1	1	2
3.08300	28.938	17	1	1	2
3.06200	29.141	1	1	2	1
2.69100	33.267	39	0	2	2
2.66700	33.575	27	-2	0	2
2.62300	34.156	62	2	2	0
2.62300	34.156	62	2	0	2
2.53400	35.394	6	-1	2	2
2.51500	35.671	6	-2	1	2
2.51500	35.671	6	1	2	2
2.49000	36.041	1	-2	2	1
2.47900	36.206	1	2	1	2
2.47300	36.297	1	2	2	1
2.43000	36.963	1	-1	0	3
2.40600	37.345	1	1	0	3
2.32900	38.628	1	-3	0	1
2.31400	38.888	1	-1	1	3
2.31400	38.888	1	3	1	0
2.30800	38.993	1	3	0	1
2.29200	39.277	1	1	1	3
2.26700	39.728	1	1	3	1
2.22600	40.491	1	-3	1	1
2.20700	40.855	1	3	1	1
2.17700	41.444	14	-2	2	2
2.15400	41.907	14	2	2	2
2.11900	42.633	1	0	2	3
2.10300	42.974	1	0	3	2
2.04400	44.279	4	3	2	0
2.02700	44.670	3	-1	3	2
2.02700	44.670	3	1	2	3
2.01600	44.927	4	1	3	2
1.99620	45.397	4	-3	1	2
1.98160	45.751	1	-3	2	1
1.96970	46.043	5	3	1	2
1.92180	47.259	9	0	0	4
1.88470	48.248	9	0	4	0
1.86220	48.869	1	0	1	4
1.84290	49.415	1	-2	2	3
1.83050	49.772	1	0	4	1
1.82900	49.816	1	-2	3	2
1.82440	49.950	24	4	0	0
1.82440	49.950	24	1	4	0
1.81530	50.217	1	2	3	2
1.81450	50.241	2	-3	2	2
1.81110	50.342	13	-1	1	4
1.79770	50.744	12	1	1	4
1.79450	50.841	9	3	2	2
1.77710	51.375	1	-1	4	1
1.77390	51.474	1	1	4	1
1.74680	52.333	1	-1	3	3
1.73340	52.768	1	-4	1	1
1.72170	53.155	1	4	1	1
1.71180	53.487	12	-2	0	4
1.71180	53.487	12	0	2	4
1.70480	53.724	8	3	1	3
1.69220	54.156	9	0	4	2
1.68920	54.260	8	2	0	4
1.67450	54.777	10	2	4	0
1.67210	54.862	1	-1	2	4
1.66900	54.972	7	-2	1	4
1.66160	55.238	1	1	2	4
1.65810	55.365	8	-4	0	2
1.65100	55.623	8	-1	4	2
1.64840	55.719	1	2	1	4
1.64590	55.811	10	1	4	2
1.64190	55.958	18	4	2	0
1.63780	56.111	15	4	0	2
1.63360	56.268	1	2	4	1
1.61940	56.806	1	-4	1	2
1.61710	56.894	1	-2	3	3
1.61040	57.153	1	-4	2	1
1.60080	57.527	1	4	1	2
1.60080	57.527	1	4	2	1
1.59780	57.645	1	-3	3	2
1.58410	58.191	2	3	3	2
1.55840	59.246	4	-2	2	4
1.54150	59.961	4	2	2	4

Appendix E: JCPDS card for 2H-WS_2

Pattern: PDF 01-084-1398 Radiation: 1.54060 Quality: Blank

Formula	W S2
Name	Tungsten Sulfide
Name (mineral)	Tungstenite-2H, syn
Name (common)	tungsten(IV) sulfide - 2H

Lattice:	Hexagonal	**Mol. weight =**	247.97
S.G.:	P63/mmc (194)	**Volume [CD] =**	106.11
		Dx =	7.76
		Dm =	
		I/Icor =	14.730

a =	3.15320	**alpha =**	
b =		**beta =**	
c =	12.32300	**gamma =**	
a/b =	1.00000	**Z =**	2
c/b =	3.90809		

ANX: AX2
Analysis: S2 W1
Formula from original source: W S2
ICSD Collection Code: 202366
Calculated Pattern Original Remarks: Molybdenite group
Significant Warning: ICSD Warning on inter-atomic distances exist
Wyckoff Sequence: f c(P63/MMC)
Unit Cell Data Source: Single Crystal

Structure
Publication: J. Solid State Chem.
Detail: volume 70, page 207 (1987)
Authors: Schutte, W.J., De Boer, J.L., Jellinek, F.
Primary Reference
Publication: Calculated from ICSD using POWD-12++

Radiation:	CuKα1	**Filter:**	Not specified
Wavelength:	1.54060	**d-spacing:**	
SS/FOM:	999.9 (0,30)		

d	2θ	I	h	k	l
6.16150	14.364	999	0	0	2
3.08075	28.959	52	0	0	4
2.73075	32.769	166	1	0	0
2.66608	33.587	235	1	0	1
2.49655	35.943	121	1	0	2
2.27409	39.599	468	1	0	3
2.05383	44.055	47	0	0	6
2.04352	44.289	27	1	0	4
1.82961	49.798	201	1	0	5
1.64140	55.977	30	1	0	6
1.57660	58.495	91	1	1	0
1.54037	60.010	28	0	0	8
1.52739	60.573	83	1	1	2
1.47961	62.746	28	1	0	7
1.40349	66.576	23	1	1	4
1.36538	68.689	13	2	0	0
1.35707	69.169	21	2	0	1
1.34164	70.080	23	1	0	8
1.33304	70.599	12	2	0	2
1.29567	72.957	51	2	0	3
1.25061	76.040	39	1	1	6
1.24827	76.208	22	2	0	4
1.23230	77.378	5	0	0	10
1.22398	78.003	15	1	0	9
1.19434	80.325	34	2	0	5
1.13704	85.291	6	2	0	6
1.12323	86.596	5	1	0	10
1.10179	88.715	39	1	1	8
1.07890	91.117	7	2	0	7
1.03645	96.011	22	1	0	11
1.03213	96.545	9	2	1	0
1.02853	96.996	14	2	1	1
1.02176	97.858	8	2	0	8
1.01794	98.353	8	2	1	2
1.00101	100.622	36	2	1	3
0.97866	103.829	3	2	1	4
0.97091	105.005	12	1	1	10
0.96682	105.639	6	2	0	9
0.96120	106.527	1	1	0	12
0.95202	108.021	29	2	1	5
0.92222	113.286	6	2	1	6
0.91481	114.711	3	2	0	10
0.91025	115.612	11	3	0	0
0.90778	116.110	5	3	0	1
0.90048	117.616	11	3	0	2
0.89550	118.675	12	1	0	13
0.89038	119.797	8	2	1	7
0.88869	120.173	4	3	0	3
0.88021	122.120	2	0	0	14
0.87294	123.870	4	3	0	4
0.86606	125.602	13	2	0	11
0.86048	127.067	4	1	1	12
0.85744	127.889	10	2	1	8
0.83777	133.697	3	1	0	14
0.83218	135.529	10	3	0	6
0.82419	138.330	8	2	1	9
0.82070	139.632	1	2	0	12